

# Optical absorption factor of solar cells for PVT systems

**Citation for published version (APA):**

Santbergen, R. (2008). *Optical absorption factor of solar cells for PVT systems*. [Phd Thesis 1 (Research TU/e / Graduation TU/e), Mechanical Engineering]. Technische Universiteit Eindhoven.  
<https://doi.org/10.6100/IR639175>

**DOI:**

[10.6100/IR639175](https://doi.org/10.6100/IR639175)

**Document status and date:**

Published: 01/01/2008

**Document Version:**

Publisher's PDF, also known as Version of Record (includes final page, issue and volume numbers)

**Please check the document version of this publication:**

- A submitted manuscript is the version of the article upon submission and before peer-review. There can be important differences between the submitted version and the official published version of record. People interested in the research are advised to contact the author for the final version of the publication, or visit the DOI to the publisher's website.
- The final author version and the galley proof are versions of the publication after peer review.
- The final published version features the final layout of the paper including the volume, issue and page numbers.

[Link to publication](#)

**General rights**

Copyright and moral rights for the publications made accessible in the public portal are retained by the authors and/or other copyright owners and it is a condition of accessing publications that users recognise and abide by the legal requirements associated with these rights.

- Users may download and print one copy of any publication from the public portal for the purpose of private study or research.
- You may not further distribute the material or use it for any profit-making activity or commercial gain
- You may freely distribute the URL identifying the publication in the public portal.

If the publication is distributed under the terms of Article 25fa of the Dutch Copyright Act, indicated by the "Taverne" license above, please follow below link for the End User Agreement:

[www.tue.nl/taverne](http://www.tue.nl/taverne)

**Take down policy**

If you believe that this document breaches copyright please contact us at:

[openaccess@tue.nl](mailto:openaccess@tue.nl)

providing details and we will investigate your claim.

# Optical Absorption Factor of Solar Cells for PVT Systems

PROEFSCHRIFT

ter verkrijging van de graad van doctor aan de  
Technische Universiteit Eindhoven, op gezag van de  
Rector Magnificus, prof.dr.ir. C.J. van Duijn, voor een  
commissie aangewezen door het College voor  
Promoties in het openbaar te verdedigen  
op dinsdag 16 december 2008 om 16.00 uur

door

Rudi Santbergen

geboren te Eindhoven

Dit proefschrift is goedgekeurd door de promotoren:

prof.dr.ir. R.J.Ch. van Zolingen  
en  
prof.dr.ir. A.A. van Steenhoven

Copromotor:  
dr.ir. C.C.M. Rindt

Copyright © 2008 by R. Santbergen

Cover design by Jorrit van Rijt, Oranje Vormgevers

All rights reserved. No part of this publication may be reproduced, stored in a retrieval system, or transmitted, in any form, or by any means, electronic, mechanical, photocopying, recording, or otherwise, without the prior permission of the author.

Printed by the Eindhoven University Press.

This work was funded by Energy research Centre of the Netherlands (ECN) and SenterNovem (project number 2020-01-13-11-004).

A catalogue record is available from the Eindhoven University of Technology Library.

ISBN: 978-90-386-1467-0

# Contents

<b>1</b>	<b>Introduction</b>	<b>1</b>
1.1	Solar energy . . . . .	1
1.2	Solar cells . . . . .	1
1.2.1	Crystalline silicon solar cells . . . . .	2
1.2.2	Thin-film solar cells . . . . .	3
1.3	The absorption factor of a PV laminate . . . . .	4
1.4	The photovoltaic/thermal collector . . . . .	6
1.4.1	PVT collector design . . . . .	6
1.4.2	PVT systems . . . . .	8
1.4.3	PVT research . . . . .	8
1.5	Objectives . . . . .	10
1.6	Outline . . . . .	10
<b>2</b>	<b>Model for the absorption factor of solar cells</b>	<b>11</b>
2.1	Introduction . . . . .	11
2.2	Reflection, refraction and absorption . . . . .	12
2.2.1	Reflection and refraction at an uncoated interface . . . . .	13
2.2.2	Reflection and refraction at a coated interface . . . . .	14
2.2.3	Absorption . . . . .	15
2.3	Optical multilayer systems . . . . .	16
2.3.1	A system with two interfaces . . . . .	16
2.3.2	A system with any number of interfaces . . . . .	18
2.4	The extended net-radiation method . . . . .	19
2.4.1	Scatter matrices . . . . .	19
2.4.2	Matrix equations . . . . .	21
2.5	Interface models . . . . .	22
2.5.1	Specular reflection model . . . . .	22
2.5.2	Phong's diffuse reflection model . . . . .	23
2.5.3	Ray tracing model for textured interfaces . . . . .	25
2.5.4	Combined model using the haze parameter . . . . .	26
2.6	Two- versus three-dimensional modelling of internal reflection . . . . .	28

2.7	Optical confinement . . . . .	30
2.8	Structure of the numerical model . . . . .	31
2.9	Conclusion . . . . .	32
<b>3</b>	<b>The absorption factor of crystalline silicon solar cells</b>	<b>35</b>
3.1	Introduction . . . . .	35
3.2	Modelling crystalline silicon solar cells . . . . .	36
3.2.1	The absorption coefficient of doped crystalline silicon . . . . .	36
3.2.2	Textured silicon surfaces . . . . .	39
3.2.3	Back contact structures . . . . .	41
3.2.4	Electrical cell efficiency . . . . .	43
3.3	Model validation . . . . .	44
3.3.1	Experimental setup . . . . .	44
3.3.2	Sample description . . . . .	45
3.3.3	Bare silicon . . . . .	46
3.3.4	Aluminium back contact . . . . .	48
3.3.5	Surface texture . . . . .	50
3.3.6	Comparison of experimental and numerical results . . . . .	54
3.4	Cell design parameters . . . . .	55
3.4.1	Reference c-Si solar cell design . . . . .	56
3.4.2	The influence of texture steepness . . . . .	57
3.4.3	The influence of wafer thickness . . . . .	58
3.4.4	The influence of emitter sheet resistance . . . . .	59
3.4.5	The influence of the back contact configuration . . . . .	60
3.4.6	The influence of metal coverage of front contact . . . . .	61
3.5	Discussion . . . . .	62
3.6	Conclusion . . . . .	65
<b>4</b>	<b>The absorption factor of thin-film solar cells</b>	<b>67</b>
4.1	Introduction . . . . .	67
4.2	Modelling thin-film solar cells . . . . .	68
4.2.1	Optical properties of semiconductor materials used in thin-film solar cells . . . . .	69
4.2.2	Transparent conductive oxides . . . . .	71
4.3	Model validation for a-Si structures . . . . .	72
4.3.1	Sample description . . . . .	73
4.3.2	Glass/ZnO:Al (sample 1) . . . . .	74
4.3.3	Glass/ZnO:Al/a-Si (sample 2) . . . . .	76
4.3.4	Glass/ZnO:Al/a-Si/Al (sample 3) . . . . .	77
4.3.5	Glass/textured ZnO:Al (sample 4) . . . . .	78
4.3.6	Glass/textured ZnO:Al/a-Si/Al (sample 5) . . . . .	79
4.3.7	Comparison of numerical and experimental results . . . . .	81

---

4.4	Simulation of the absorption factor of thin-film solar cells . . . . .	82
4.4.1	a-Si solar cell . . . . .	83
4.4.2	$\mu$ c-Si solar cell . . . . .	85
4.4.3	Micromorph silicon tandem solar cell . . . . .	86
4.4.4	a-Si/a-SiGe/ $\mu$ c-Si triple junction solar cell . . . . .	87
4.4.5	CIGS solar cell . . . . .	88
4.4.6	Cell design . . . . .	89
4.5	The effective absorption factor of thin-film solar cells . . . . .	92
4.6	Discussion and concluding remarks . . . . .	94
<b>5</b>	<b>The annual yield of PVT systems</b>	<b>97</b>
5.1	Introduction . . . . .	97
5.2	PVT collector . . . . .	98
5.2.1	Sheet-and-tube collector design and definitions . . . . .	99
5.2.2	Collector model . . . . .	101
5.2.3	Assumptions in the collector model . . . . .	104
5.2.4	Illustration of the collector model . . . . .	105
5.3	PVT systems . . . . .	107
5.3.1	System sizing of practical solar thermal system . . . . .	107
5.3.2	System model . . . . .	108
5.3.3	Assumptions in the system model . . . . .	113
5.3.4	Illustration of the system model . . . . .	114
5.4	Annual yield of PVT collectors . . . . .	117
5.4.1	The effect of cell technology . . . . .	118
5.4.2	The effect of collector sizing . . . . .	120
5.4.3	The effect of optical coatings applied to the collector . . . . .	120
5.5	PVT systems compared to separate PV and T systems . . . . .	126
5.5.1	The electrical yield of PV systems . . . . .	126
5.5.2	The thermal yield of solar thermal systems . . . . .	127
5.5.3	Relative efficiency of PVT systems . . . . .	127
5.5.4	PVT specific efficiency loss mechanisms . . . . .	129
5.5.5	Avoided primary energy . . . . .	132
5.6	Conclusion . . . . .	134
<b>6</b>	<b>Assessment of PVT systems</b>	<b>137</b>
6.1	Electrical losses . . . . .	138
6.2	Thermal losses . . . . .	142
6.3	Promising applications for PVT systems . . . . .	144
<b>7</b>	<b>Conclusions and recommendations</b>	<b>147</b>

---

<b>A Model for stratified thermal storage tanks</b>	<b>151</b>
A.1 Multinodel model . . . . .	151
A.2 Figure of merit . . . . .	152
<b>Bibliography</b>	<b>155</b>
<b>Nomenclature</b>	<b>165</b>
<b>Summary</b>	<b>169</b>
<b>Samenvatting</b>	<b>171</b>
<b>Dankwoord</b>	<b>173</b>
<b>List of publications</b>	<b>175</b>
<b>Curriculum Vitae</b>	<b>177</b>

# Introduction

## 1.1 Solar energy

Currently, humankind consumes  $15 \cdot 10^{12}$  W of primary power, 87% of which from burning fossil fuels [1]. Because of the negative environmental effects associated with the use of fossil fuels, a transition to sustainable energy sources is desirable [2]. Furthermore, because of the limited reserves of non-renewable energy sources, such as oil, coal and nuclear fuel, a transition to renewable energy sources will become necessary in the long term. A very abundant form of sustainable renewable energy is solar energy, since the sun irradiates our planet with a power of more than 8000 times the current power consumption.

The sun's energy can be harnessed in many ways. For example a photovoltaic (PV) module converts solar energy into electricity and a solar thermal collector converts solar energy into heat, e.g. for domestic hot water or room heating. A so-called photovoltaic/thermal (PVT) collector delivers both electricity and heat, with the photovoltaic cells generating the electricity and acting as the absorber for the heat at the same time. Further details will be given in section 1.4.

## 1.2 Solar cells

Solar cells, also known as photovoltaic cells, exploit the photovoltaic effect to convert light into electricity. Many different solar cell technologies exist [3]. Currently, the silicon wafer-based solar cell technology is the dominant one. In addition various types of thin-film solar cell technologies are used on a smaller scale. Finally a range of more novel solar cell concepts exists, such as the polymer and the dye sensitised solar cell concepts, which are currently in the research phase. In this thesis both sili-



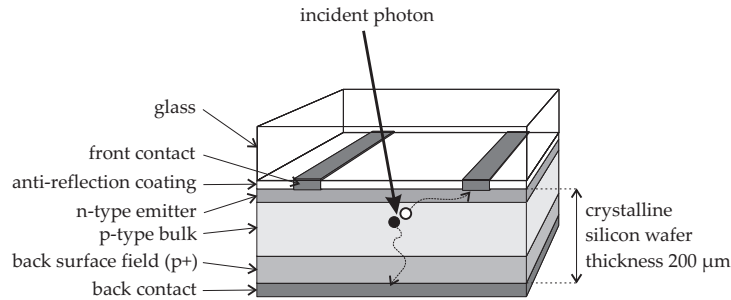


**Figure 1.1:** A schematic cross-section of a crystalline silicon solar cell.

con wafer-based and thin-film solar cells are considered. The structure and working principle of these cells is now briefly described, a more detailed description can be found in many textbooks [3, 4, 5, 6].

### 1.2.1 Crystalline silicon solar cells

The active part of the crystalline silicon (c-Si) solar cell is a crystalline silicon wafer with a typical thickness of  $200\ \mu\text{m}$  (see figure 1.1). Since crystalline silicon is a semiconductor, it can be doped to modify its electrical transport properties. The bulk of the wafer contains a uniform p-type (e.g. boron) doping. By indiffusion of n-type doping (e.g. phosphorus) a thin n-type region is created at the front. This n-type region is called the emitter and is typically only  $0.2\ \mu\text{m}$  thick. The p- and n-type regions contain relatively high concentrations of positively charged holes and negatively charged electrons, respectively. By diffusion, these so-called majority charge carriers are transported across the p-n junction until the diffusive ‘force’ is balanced by an electrostatic force. When no new electrons or holes are being created this is a stable situation with a strong electrostatic field at the p-n junction.

When the wafer is irradiated by sunlight, an incident photon with an energy larger than the bandgap can promote an electron from the valence band to the conduction band, effectively creating an electron-hole pair. The electrostatic field at the p-n junction separates the pairs by sweeping the minority charge carriers across the junction, i.e. free electrons go to the front and free holes go to the back. Unfortunately, a small part of the electron-hole pairs generated is lost by recombination, either in the bulk of the wafer or at the front or back surface. By contacting the front and back of the wafer, the separated free electrons and holes are collected and the electrical energy can be harnessed.

In practice, the contact at the front consists of a fine silver grid and the back contact can for example consist of a thin aluminium layer, alloyed to the back. The alloying process dopes the back region relatively heavily, setting up a so-called back

surface field (BSF) which reduces the loss of electron-hole pairs by recombination at the back. To reduce recombination at the front, a silicon nitride passivation layer is used, which at the same time functions as an anti-reflective (AR) coating. The cells are connected in series and encapsulated between glass and a rear-side foil to form a PV laminate. Typically, transparent ethyl vinyl acetate (EVA) is used as encapsulant, providing among others the bond between the cells and the glass plate.

Modern crystalline silicon cells are textured, i.e. the wafer is made rough, which increases the electrical efficiency in two ways. Firstly, texture improves the incoupling of solar irradiance, i.e it allows more irradiance to enter the wafer. Secondly, texture improves trapping of weakly absorbed irradiance, i.e. irradiance is refracted into oblique directions and is internally reflected inside the wafer many times with only a small chance of escape.

The performance of a solar cell is expressed by the electrical efficiency  $\eta_e$ , which is the fraction of incident energy that is converted into electrical energy. In the last decades the electrical efficiency of crystalline silicon solar cells has increased steadily and at the same time the cost of production has come down [7]. On industrial scale, the present efficiency of multicrystalline silicon solar cells ranges from 14 to 15% [8]. The comparable cell efficiencies for mono-crystalline silicon solar cells are 16 to 17% [8]. Advanced mono-crystalline silicon solar cells reach an average cell efficiency up to 22% on an industrial scale [9]. The following trends to increase the efficiency can be observed:

- a reduction of the front metallisation coverage by application of concepts like the PUM concept [10, 11, 12] and the Emitter-Wrap-Through (EWT) concept [13],
- further enhancement of light incoupling by improved texturisation [14],
- improved optical confinement by adaptation of the back contact structures [15],
- development of cell concepts with both front and back passivation [16],
- adaptation of the emitter doping profile with the trend to shallower emitters.

The reduction of wafer thickness is an important tool to reduce the required amount of silicon feedstock [8] and therefore the cost. The reduction of wafer thickness is being accelerated by the present shortage of silicon feedstock.

### 1.2.2 Thin-film solar cells

In thin-film solar cells, materials are used with an absorption coefficient being much higher than the absorption coefficient of crystalline silicon. This implies that a thickness of one or a few micrometre for the active layer is enough to obtain a reasonable efficiency. The small amount of relatively expensive material required for the active layers is an important advantage of thin-film solar cells. Important representatives

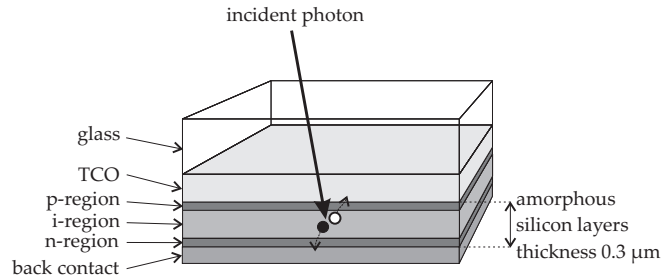


**Figure 1.2:** A schematic cross-section of a single junction amorphous silicon thin-film solar cell.

of the group of thin-film solar cells, being produced on an industrial scale, are the amorphous silicon (a-Si) based, the cadmium telluride (CdTe) and the copper indium gallium diselenide (CIGS) solar cells.

The structure of a single junction amorphous silicon solar cell is shown in figure 1.2. Because of the very short minority carrier lifetime in p- and n-type amorphous silicon, a p-i-n structure is used instead of a p-n structure, enabling direct separation of generated electron-hole pairs in an electrostatic field. In nearly all thin-film solar cells, the front contact is made of a transparent conductive oxide (TCO), e.g. aluminium doped zinc oxide (ZnO:Al). As the name suggests this material is both transparent and conductive. The TCO layer can be textured, i.e. made rough, before the subsequent layers are deposited. This improves the incoupling and trapping of irradiance in the semiconductor layer.

An industrial scale thin-film PV laminate can be produced by respectively depositing TCO, semiconductor and back contact layers on a glass substrate. By laser scribing, the laminate is divided into separate series connected cells. Typical efficiencies on an industrial scale are 6-7% for single junction or tandem amorphous silicon solar cells, 8-10% for CdTe solar cells and 10-11% for CIGS solar cells [8].

### 1.3 The absorption factor of a PV laminate

Because the absorption factor of the PV laminate, containing the crystalline silicon or thin-film solar cells, plays such an important role in the thermal efficiency of a PVT collector, some fundamental aspects of this absorption factor will be highlighted first. Solar irradiance incident on a PV laminate is either reflected, absorbed or transmitted. The absorption factor of the laminate is defined as the fraction of the incident solar irradiance that is absorbed. When this quantity is considered as a function of wavelength  $\lambda$ , it is called the spectral absorption factor  $A_\lambda$ . By weighting  $A_\lambda$  over

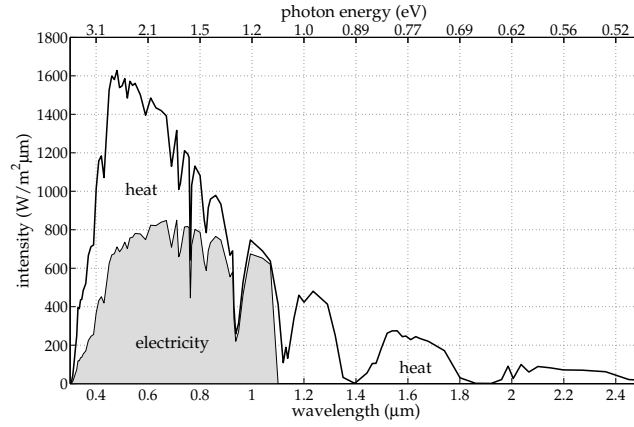


**Figure 1.3:** The AM1.5g solar spectrum [17]. The part of the spectrum that can theoretically be converted into electricity by a single junction solar cell is indicated (assuming  $E_g = 1.1$  eV, being the bandgap of crystalline silicon).

the AM1.5g solar spectrum  $G_\lambda$ , the AM1.5g absorption factor  $A$  is obtained

$$A = \frac{\int A_\lambda G_\lambda d\lambda}{\int G_\lambda d\lambda} . \quad (1.1)$$

This AM1.5g spectrum is a standardised solar spectrum given by Hulstrom [17] and is shown in figure 1.3. AM1.5 stands for Air Mass 1.5 and 'g' refers to the global spectrum, containing both direct and diffuse solar irradiance. Similarly, a spectral reflection factor  $R_\lambda$  and spectral transmission factor  $T_\lambda$  can be defined for the laminate, from which the corresponding AM1.5g reflection factor  $R$  and AM1.5g transmission factor  $T$  can be derived. From conservation of energy it follows

$$R_\lambda + A_\lambda + T_\lambda = 1 . \quad (1.2)$$

Note that most PV laminates are opaque ( $T_\lambda = 0$ ) so in that case  $A_\lambda = 1 - R_\lambda$ .

At least 90% of the surface area of a PV laminate is covered by solar cells, the remaining area consists of spacing between and around the cells. The solar cells show a wavelength dependent optical behaviour. As can be seen from figure 1.3 the AM1.5g spectrum ranges roughly from  $\lambda = 0.3$   $\mu\text{m}$  in the ultraviolet (UV) to  $\lambda = 2.5$   $\mu\text{m}$  in the infrared (IR). The photon energy  $E_{\text{ph}}$  is inversely proportional to  $\lambda$

$$E_{\text{ph}} = \frac{hc}{\lambda} , \quad (1.3)$$

where  $h$  is Planck's constant and  $c$  is the speed of light. On the second horizontal axis the photon energy is shown, which ranges from 4 eV in the UV to 0.5 eV in the IR. Only short wavelength photons, with  $E_{\text{ph}} > E_g$ , can create electron-hole

pairs and are readily absorbed in the semiconductor, with  $E_g$  being the bandgap of the semiconductor. Note that each photon can create at most one electron-hole pair, thereby expending an amount of energy equal to  $E_g$ . The excess energy ( $E_{ph} - E_g$ ) is converted into heat. On the other hand long-wavelength photons with  $E_{ph} < E_g$ , cannot create electron-hole pairs and are hardly absorbed in an intrinsic semiconductor. However, in a p- or n-type doped region these photons can be absorbed by free charge-carriers and the strength of this free-carrier absorption is proportional to the doping concentration. Note that free-carrier absorption does not generate electron-hole pairs. Also some absorption occurs in the other layers, such as glass, EVA, TCO, AR coating and back contact.

All absorbed solar energy not converted into electricity is converted into heat. The fraction of incident solar irradiance converted into heat is given by the effective absorption factor

$$A_{\text{eff}} = A - \eta_e . \quad (1.4)$$

For most solar cells the effective absorption factor  $A_{\text{eff}}$  is in the range of 60-80%.

## 1.4 The photovoltaic/thermal collector

A photovoltaic/thermal (PVT) collector delivers both electricity and heat, with the solar cells generating the electricity and acting as the absorber for the heat at the same time [18]. PVT collectors can be applied in those cases where there is a demand for both electricity and heat.

### 1.4.1 PVT collector design

A wide variety of PVT collectors exists and they are being used in a range of systems [19]. One example is the ventilated PV facade where the heated ventilation air is used for room heating. Another example is the PVT concentration system where solar cells under concentrated sunlight are actively cooled and the heat extracted is used. However, flat-plate PVT collectors are seen as the main future market product [19]. These can be either glazed or unglazed collectors and either air or a liquid can be used as a heat transporting medium.

The yield of a system with a flat-plate PVT collector was numerically investigated by de Vries [20] and by Zondag [21]. Several PVT collector designs were considered for Dutch climatological conditions. The unglazed PVT collector gives the highest electrical efficiency, but under the given conditions its thermal performance is very poor. It was concluded that the one-cover sheet-and-tube design represents a good compromise between electrical and thermal yield and manufacturability. Hence, in this thesis the focus is on this glazed sheet-and-tube design.

This design is schematically shown in figure 1.4. At the heart there is the PV laminate, generating electricity. The heat generated in the laminate is extracted by a

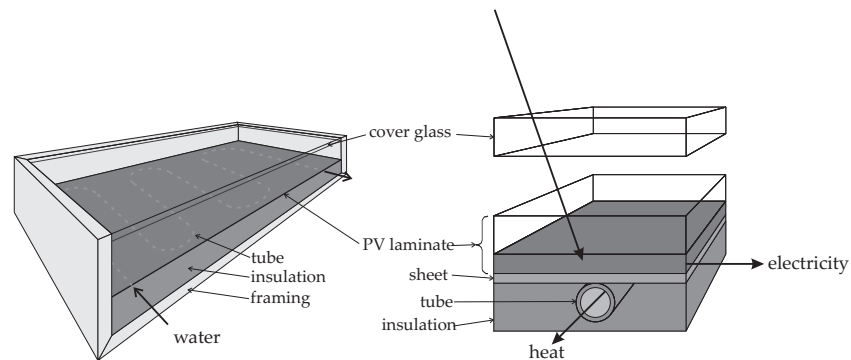


**Figure 1.4:** A one-cover flat-plate sheet-and-tube PVT collector. Incident solar irradiance is converted into both electricity and heat. Left: the complete collector. Right: A detailed cross-section.

copper sheet at the back. Connected to this sheet is a serpentine shaped tube through which water flows collecting the heat. In order to reduce heat loss to the ambient, the backside is thermally insulated and at the front there is a cover glass. The stagnant air layer provides thermal insulation. This design is similar to a glazed solar thermal collector with the spectrally selective absorber replaced by a PV laminate.

The main advantages of a PVT collector over a PV module and a solar thermal collector side-by-side are firstly a higher electrical and thermal yield per unit surface area, secondly more architectural uniformity on the roof and thirdly reduced installation costs [18]. Regarding the first point, note that equal surface area's are considered. For example, a  $2 \text{ m}^2$  PVT collector is compared to a  $1 \text{ m}^2$  PV module and a  $1 \text{ m}^2$  thermal collector side-by-side.

The *electrical* efficiency of a glazed PVT collector might be somewhat lower than the electrical efficiency of a PV module for the following reasons:

- reflection losses caused by the extra cover,
- higher cell temperatures e.g. imposed by the heat collecting fluid.

Further, the *thermal* efficiency of the PVT collector will be lower than the thermal efficiency of a solar thermal collector. The three main reasons for this are:

- lower absorption factor  $A$  of the absorber,
- extraction of electrical energy from the PV laminate, which is not available in the form of heat anymore,
- higher radiative heat loss from the absorber to the cover glass due to a higher emissivity  $\varepsilon$ .

**Table 1.1:** Typical values of the absorption factor  $A$ , the effective absorption factor  $A_{\text{eff}}$  and the emissivity  $\varepsilon$  of the spectrally selective absorber and the PV laminate.

	spectrally selective absorber	PV laminate
$A$	95%	70-90%
$A_{\text{eff}}$	95%	60-80%
$\varepsilon$	12%	85%

The three main reasons for the lower thermal efficiency are quantified in table 1.1, where the spectrally selective absorber in a solar thermal collector and the absorber in a PVT collector (i.e. the PV laminate) are compared. Note that for the PV laminate the (effective) absorption factor depends on the cell design in a complicated way, while the emissivity  $\varepsilon$ , for the temperatures considered here, is solely determined by the encapsulation of the solar cells, e.g. glass.

### 1.4.2 PVT systems

PVT collectors are combined with other elements such as inverter, pump, heat storage, etc. to form a PVT system. A simplified schematic overview of a typical PVT system for domestic hot water is shown in figure 1.5. The PVT collector supplies electricity and heat. An inverter converts direct current from the collector to alternating current which is supplied to the electricity grid. The heat is collected in a storage vessel and each time there is a demand for hot water heat is extracted from the vessel.

The heat generated by PVT systems can be used in industrial applications [22] and in several domestic applications such as domestic hot water, room heating and pool heating [23]. Each application has its specific required temperature and required amount of storage. Both can strongly affect the electrical and thermal performance of the PVT system compared to the performance of a reference system, e.g. a PV system or solar thermal system. Therefore, in order to assess the PVT collector, the application should be known and the system should be well defined. In this thesis the focus is on the medium temperature applications of domestic hot water heating and room heating.

### 1.4.3 PVT research

Over the last 30 years, a large amount of research on PVT collectors has been carried out. Zondag [19] presents an overview, both in terms of an historic overview of research projects and in the form of a thematic overview addressing the different research issues for PVT.

At the Eindhoven University of Technology, thermal and electrical models were

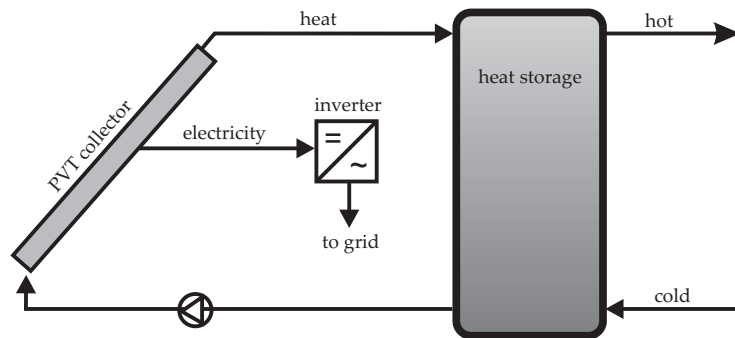


Figure 1.5: A schematic overview of a PVT system for domestic hot water.

developed by de Vries [20] to predict the efficiency of various collectors. The numerical models were validated by comparing the efficiency found numerically with the efficiency measured of a prototype PVT collector. Because the absorption factor has such a strong influence on the thermal efficiency of a PVT collector, de Vries developed an optical model for this absorption factor. To do so, de Vries used the relatively simple net-radiation method [24] and assumed planar interfaces. Other optical models for solar cells were developed by Krauter [25], Fraidenraich [26] and Lu [27]. All these models were developed for planar structures as well, and do not take into account features like texturisation and the effect of light trapping.

Both Platz [28] and Affolter [29] executed reflection measurements on a few crystalline silicon and a range of thin-film solar cells, to determine the absorption factor. Though these measurements are very valuable, they do not provide full insight in the importance of the various absorption mechanisms. In order to obtain this insight, more detailed modelling is required.

In other solar cell studies, not specifically linked to PVT applications, absorption of solar irradiance in solar cells is investigated in detail using advanced optical models in which enhanced light trapping is taken into account [30, 31, 32, 33]. Typically these models are used to calculate the optical absorption profile of the active layer, which is used as input for an electrical model determining the cell efficiency. But because the focus of these studies is on electrical efficiency, only irradiance with a photon energy near or exceeding the bandgap energy has to be, and in most cases was, considered. However, a significant part of the energy in the AM1.5g solar spectrum is located in the sub-bandgap part. For example for crystalline silicon (with  $E_g = 1.1$  eV) this is 20% of the solar energy and for amorphous silicon (with  $E_g = 1.7$  eV) this is even 35% of the solar energy. So in order to determine the absorption factor, also the absorption of sub-bandgap irradiance has to be considered. This aspect has not yet been investigated in much detail and will be one of the main subjects of this thesis.



## 1.5 Objectives

The research presented in this thesis has two main objectives. The absorption factor of solar cells is a major parameter affecting the performance of PVT systems and this parameter was not yet studied in sufficient detail for PVT applications. Therefore the first objective is to study the absorption factor of the various types of solar cell. The acquired detailed insight in the mechanisms determining this absorption factor will enable to optimise solar cells for PVT applications.

The second objective is to study the factors that determine the electrical and thermal yield of systems with PVT collectors and to understand the factors that limit these yields compared to systems with only PV modules or thermal collectors. Detailed insight in these factors, the absorption factor of solar cells being one of these, enables to optimise the yield of PVT systems.

A dedicated optical model is developed for the absorption factor of both crystalline silicon and thin-film solar cells. This model is validated by comparing numerical results with the spectral absorption factor, measured on a set of solar cell samples. Using this model, the influence of the design features of various crystalline silicon and thin-film solar cells on the absorption factor is studied in detail. The energy yield of the PVT collectors and of the PVT system as a whole is also investigated using numerical models and the factors that limit these yields are analysed.

## 1.6 Outline

In chapter 2 the optical model for simulating the absorption factor of solar cells is introduced. In chapter 3 crystalline silicon solar cells are considered and the optical model is used to simulate the absorption factor. Detailed insight is gained in the optical effects of encapsulation, texture, free-carrier absorption and back contact. The numerical results are compared with optical measurements performed on a wide range of crystalline silicon samples. In chapter 4 the absorption factor for thin-film cells such as amorphous silicon and CIGS solar cells is investigated. Attention is paid to thin-film specific optical effects such as absorption in the transparent conductive oxide and scattering of irradiance at rough interfaces. For amorphous silicon cells, the results are compared to optical measurements. In chapter 5 the PVT system model, including PVT collector model and storage tank model, is introduced. The absorption factors of the solar cells considered in the previous chapters are used as input in the system simulations. Further the effects of additional anti-reflective coatings and low-emissivity coatings on the annual yield is investigated. The electrical and thermal efficiency of PVT collector systems are compared to the efficiencies of separate PV and thermal collector systems. Based on these results, PVT systems are assessed in chapter 6 and in chapter 7 conclusions are presented.

# Model for the absorption factor of solar cells

## 2.1 Introduction

The absorption factor of solar cells plays an important role regarding the electrical and thermal performance of PVT collectors. The relevant absorption factor is the AM1.5 absorption factor  $A$ , which is the spectral absorption factor  $A_\lambda$  averaged over the solar spectrum (equation 1.1). Solar cells are spectrally selective devices, implying that the spectral absorption factor depends strongly on the wavelength. Spectrally resolved modelling of the absorption factor is important because it gives insight in the mechanisms that determine the absorption factor and it enables the study of the influence of specific design features on the absorption factor. In order to do so the model should be flexible enough to cope with these design features.

Solar cells, whether wafer-based or thin-film, are optical multilayer systems, typically consisting of 5 to 10 layers. At each interface, incident irradiance is reflected and refracted. Especially when these interfaces are non-planar or non-smooth, irradiance can be trapped inside the optical system for many passes. In solar cells this light-trapping effect is exploited to maximise absorption of solar irradiance in the active layers. This makes a solar cell a complex optical device and its absorption factor depends on a wide range of cell design parameters.

The goal of the work described in this chapter is to develop a generic numerical model for the spectral absorption factor of solar cells, based on a multilayer system approach. The model should be flexible enough to simulate this spectral absorption factor for various types of solar cell. The inputs are the optical properties of each layer and a description of how irradiance is reflected (scattered) at the interfaces.

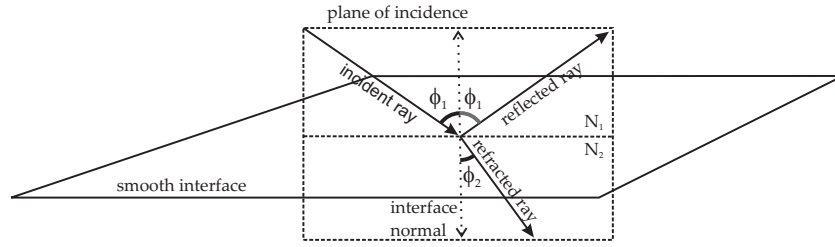


**Figure 2.1:** A ray incident on a smooth interface is reflected and refracted in a specular way. A cross-section through the plane of incidence is shown.

Reflection at a smooth interface can be described relatively simple as will be illustrated in section 2.2. In section 2.3 a multilayer system consisting of multiple smooth interfaces is considered. Many of such models can be found in literature [25, 26, 27], including the elegant net-radiation method [24]. In section 2.4 the net-radiation method is extended to incorporate the effect of light scattering. Then in section 2.5 several interface models are presented which can be used within the extended net-radiation method. In sections 2.6 to 2.8 some aspects of the model are discussed and finally in section 2.9 conclusions are drawn.

## 2.2 Reflection, refraction and absorption

In this section a smooth planar interface is considered, which reflects irradiance in a specular (i.e. mirror-like) way. Medium 1 and 2 above and below this interface respectively, are characterised by a complex refractive index

$$N = n - ik, \quad (2.1)$$

where  $n$  is the real refractive index and  $k$  is the extinction coefficient. As illustrated in figure 2.1, a ray of light is incident on the interface with an angle of incidence  $\phi_1$  (measured from the surface normal). This ray splits up in a reflected ray and a refracted ray. Both rays remain in the plain of incidence, defined by the incident ray and the interface normal vector. The angle of refraction  $\phi_2$  is given by Snell's law

$$N_1 \sin \phi_1 = N_2 \sin \phi_2. \quad (2.2)$$

In this thesis, the reflection coefficient  $r$  is defined as the ratio of the *intensities* (i.e. power densities) of the reflected beam and the incident beam, respectively. This ratio can be derived from Fresnel's equations [34]. The reflection coefficient of both a coated and an uncoated interface are considered.

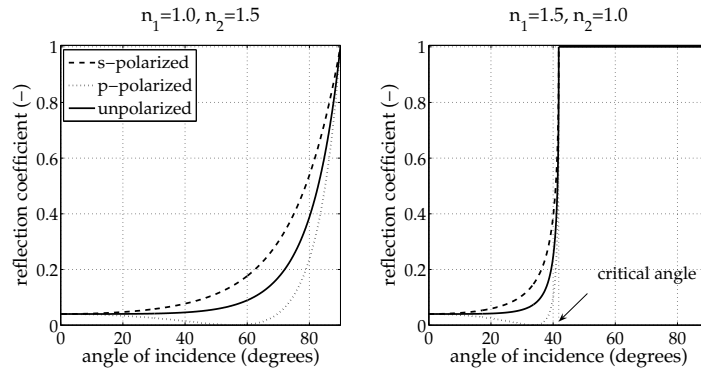


**Figure 2.2:** The reflection coefficient  $r$  as a function of the angle of incidence  $\phi_1$  for p-, s- and unpolarised irradiance. On the left a transition from a medium with a low to a medium with a high refractive index is considered. On the right the opposite transition is considered and the critical angle  $\phi_{cr}$  is indicated.

### 2.2.1 Reflection and refraction at an uncoated interface

First the most simple interface, without coating, is considered. Using a notation similar to Macleod's [34], the reflection coefficient is given by

$$r = \left| \frac{\eta_1 - \eta_2}{\eta_1 + \eta_2} \right|^2, \quad (2.3)$$

where  $\eta$  is the modified refractive index given by

$$\eta = \begin{cases} N / \cos \phi & \text{for p-polarized irradiance,} \\ N \cos \phi & \text{for s-polarized irradiance.} \end{cases} \quad (2.4)$$

Here  $\eta_1$  is determined using  $N_1$  and  $\phi_1$  and  $\eta_2$  is determined using  $N_2$  and  $\phi_2$ . The reflection coefficient depends on the polarisation state of light. More information on the polarisation states of light can be found in several textbooks [34, 35]. Direct sunlight is generally considered to be unpolarised [35], i.e. it contains equal amounts of p- and s-polarised irradiance. Note that the complex refractive index of metals contains a large imaginary component. As can be derived from equation 2.3 this explains their very high reflection coefficient. The fraction of energy in the refracted (transmitted) beam is simply given by

$$t = 1 - r. \quad (2.5)$$

These equations are illustrated in figure 2.2. In the left panel, the reflection coefficient  $r$  is given as a function of the angle of incidence  $\phi_1$  for a ray of light going from a medium with a low refractive index to a medium with a high refractive index. In the right panel the opposite transition is considered, i.e. from a high to a low

refractive index. In that case, there exists a critical angle of incidence  $\phi_{\text{cr}}$ , given by

$$\phi_{\text{cr}} = \arcsin n_2/n_1 . \quad (2.6)$$

If the angle of incidence is larger than this critical angle ( $\phi_1 > \phi_{\text{cr}}$ ), then total internal reflection occurs ( $r = 1, t = 0$ ). In solar cells the active layer often has a relatively high refractive index and therefore a small critical angle so total internal reflection is used to trap light inside this layer.

### 2.2.2 Reflection and refraction at a coated interface

The reflection coefficient of the interface between medium 1 and 2 can be reduced significantly if a thin coating is added to the interface. This coating is characterised by a thickness  $d_c$  and a refractive index  $N_c = n_c - ik_c$ . The coating is considered to be thin if its optical thickness ( $n_c d_c$ ) is smaller than the coherence length of the incident light, which is approximately  $1 \mu\text{m}$  for solar irradiance [35].

Irradiance is an electromagnetic wave and in case *thin* coatings are applied, interference occurs between the part of the wave reflected by the top of the coating and the part of the wave reflected by the bottom of the coating, as indicated in the left panel of figure 2.3. If the phase difference  $\delta$  between the two waves is equal to  $\pi$  (i.e. a half period), then destructive interference occurs at the top interface of the coating and the reflection coefficient is reduced. Note that simultaneously at the bottom interface, constructive interference will occur, increasing the transmission coefficient. This effect is exploited in anti-reflective (AR) coatings. If the refractive index of the coating lies in between the refractive indices of the neighbouring media, then the reflection coefficient of the combination of the coating and the underlying medium is given by

$$r = \left| \frac{\eta_1 - Y}{\eta_1 + Y} \right|^2 , \quad (2.7)$$

where  $Y$  can be interpreted as the ‘effective refractive index’ of this combination [34], given by

$$Y = \frac{\eta_2 \cos \delta + i\eta_c \sin \delta}{\cos \delta + i(\eta_2/\eta_c) \sin \delta} , \quad (2.8)$$

and both  $\eta_1, \eta_2$  and  $\eta_c$  are given by equation 2.4. Phase difference  $\delta$  is given by

$$\delta = \frac{2\pi N_c d_c}{\lambda \cos \phi_c} , \quad (2.9)$$

where  $\lambda$  is the (vacuum) wavelength of the irradiance and the angle of refraction in the coating  $\phi_c$  is given by Snell’s law (equation 2.2). In this way the coating can be considered as an interface with a reflection coefficient described by equation 2.7.

In the right panel of figure 2.3 the reflection coefficient of a coated interface is sketched as a function of the wavelength of the incident irradiance. A ray is considered, going from medium 1 (with refractive index  $N_1$ ) to medium 2 (with refractive

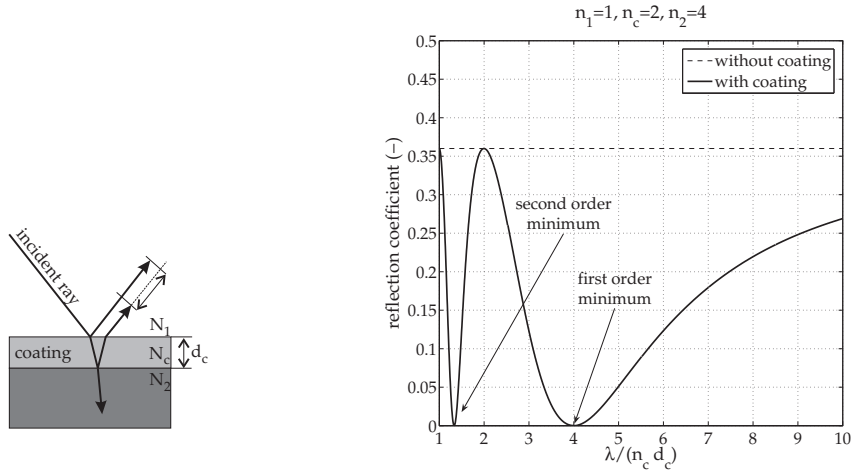


**Figure 2.3:** Left: Destructive interference occurring between waves reflected at the top and at the bottom of the coating. Right: The reflection coefficient  $r$  of a coated interface as a function of wavelength  $\lambda$ . Normally incident irradiance is considered.

index  $N_2$ ) and the ray is normally incident ( $\phi_1 = 0^\circ$ ). It is assumed that the coating has the optimum refractive index, i.e. the geometric mean of the refractive indices of the neighbouring media  $N_c = \sqrt{N_1 N_2}$ . As indicated, the first order reflection minimum occurs at wavelength  $\lambda/4 = n_c d_c$ . This reflection minimum is exploited in anti-reflective (AR) coatings, i.e. the optical thickness of the coating  $n_c d_c$  is chosen such that the reflection minimum lies in the wavelength region of interest.

### 2.2.3 Absorption

The intensity  $I$  of a ray traversing an homogeneous absorbing medium reduces exponentially [35]

$$I(x) = I(0)e^{-\alpha x}, \quad (2.10)$$

where  $I(0)$  is the initial intensity,  $x$  is the traversed distance and  $\alpha$  is the absorption coefficient. This absorption coefficient is proportional to the imaginary part of the refractive index

$$\alpha = 4\pi k/\lambda, \quad (2.11)$$

and should not be confused with the absorption *factor*  $A$  introduced in section 1.3.

## 2.3 Optical multilayer systems

Having introduced the laws of optics governing a single interface, in this section multilayer systems with smooth interfaces are considered. In order to illustrate the strength of the net-radiation method, first a simple system is considered containing only two interfaces and then the method is generalised for a system with any number of interfaces.

### 2.3.1 A system with two interfaces

As shown in figure 2.4, there are three media involved (labelled 0, 1 and 2), separated by two interfaces (labelled 1 and 2). Each medium is characterised by a refractive index  $N$ . The first and final media are semi-infinite, medium 1 (or layer 1) is characterised by a thickness  $d_1$ . It is assumed here that the thickness of this layer is much larger than the coherence length of the incident irradiance so interference effects do not occur. The layer is said to be incoherent. However, if any thin (coherent) layers would be present, they would be treated as a coating, i.e. as a part of the interface and not as a separate layer (see section 2.2.2).

Assuming specular reflection and a given angle of incidence  $\phi_0$ , the reflection coefficients  $r_1$  and  $r_2$  of interfaces 1 and 2, respectively, can be determined. The transmission coefficient  $\tau_1$  of layer 1 is defined as the fraction of irradiance remaining after a single passage through this layer

$$\tau_1 = e^{-\alpha_1 d_1 / \cos \phi_1}, \quad (2.12)$$

where  $d_1 / \cos \phi_1$  is the distance the ray has traversed in the layer. For a non-absorbing layer  $\tau = 1$  and for an opaque layer  $\tau = 0$ .

Next the spectral absorption factor  $A_\lambda$  of the system described above is considered. To be more precise,  $A_\lambda$  will in this chapter refer to the absorption factor for a *single* polarisation state and a *single* wavelength. It is understood that by taking the average of  $A_\lambda$  for both polarisation states p and s,  $A_\lambda$  is found for unpolarised irradiance and by averaging over the solar spectrum (equation 1.1) the AM1.5 absorption factor  $A$  is found. The same is true for the spectral reflection and transmission factors  $R_\lambda$  and  $T_\lambda$ .

Two methods for determining the spectral absorption factor  $A_\lambda$  of the system as a whole will be presented. Both methods are equivalent and they take into account the effect of multiple reflections, indicated in figure 2.4.

#### Cumulative method

The most straightforward strategy is to follow (trace) an incoming ray of light as sketched in the left panel of figure 2.4. At the interfaces the ray will split up in a reflected and refracted sub-ray and multiple internal reflections occur between the

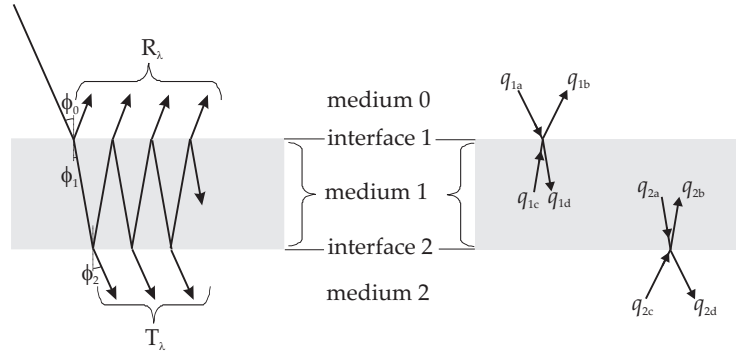


**Figure 2.4:** A cross-section of a simple multilayer system containing two interfaces. Left: the internally reflecting sub-rays considered in the cumulative method are indicated. Right: the net-radiation fluxes considered in the net-radiation method are indicated.

two interfaces. In order to determine the factors  $R_\lambda$ ,  $A_\lambda$  and  $T_\lambda$  accurately, the contribution of each sub-ray has to be considered. The infinitely many contributions can be expressed as a geometric series

$$R_\lambda = r_1 + t_1^2 \tau_1^2 r_2 \sum_{n=0}^{\infty} (r_1 r_2 \tau_1^2)^n = r_1 + \frac{t_1^2 \tau_1^2 r_2}{1 - r_1 r_2 \tau_1^2}, \quad (2.13)$$

$$T_\lambda = t_1 \tau_1 t_2 \sum_{n=0}^{\infty} (r_1 r_2 \tau_1^2)^n = \frac{t_1 \tau_1 t_2}{1 - r_1 r_2 \tau_1^2}, \quad (2.14)$$

$$A_\lambda = 1 - R_\lambda - T_\lambda, \quad (2.15)$$

where  $r$  and  $t$  are the reflection and transmission coefficients of the interfaces (equation 2.3 and 2.5) and  $\tau$  is the transmission coefficient of the layer (equation 2.12).

### Net-radiation method

Another strategy is to group the infinitely many sub-rays into net-radiation fluxes as indicated in the right panel of figure 2.4. There are four fluxes (labelled  $a$ ,  $b$ ,  $c$  and  $d$ ) per interface. For example flux  $q_{1b}$  contains all sub-rays travelling away from interface 1 in the upward direction. Because each flux contains the net-radiation, this method is called the net-radiation method [24]. It is convenient to consider the fluxes to be non-dimensional and to normalise the incident flux, i.e.  $q_{1a} = 1$ . Further it is assumed that no irradiance is incident from below the multilayer structure, i.e.



$q_{2c} = 0$ . It can be checked that the fluxes are related in the following way

$$\begin{cases} q_{1a} = 1 \\ q_{1b} = r_1 q_{1a} + t_1 q_{1c} \\ q_{1c} = \tau_1 q_{2b} \\ q_{1d} = r_1 q_{1c} + t_1 q_{1a} \\ q_{2a} = \tau_1 q_{1d} \\ q_{2b} = r_2 q_{2a} + t_2 q_{2c} \\ q_{2c} = 0 \\ q_{2d} = r_2 q_{2c} + t_2 q_{2a} . \end{cases} \quad (2.16)$$

By solving this set of linear equations, the fluxes are found and the spectral reflection, absorption and transmission factors can be found directly

$$\begin{aligned} R_\lambda &= q_{1b} \\ A_\lambda &= q_{1d} - q_{2a} + q_{2b} - q_{1c} \\ T_\lambda &= q_{2d} . \end{aligned} \quad (2.17)$$

Note that this method is equivalent with the cumulative method, but it has the advantage that the individual sub-rays do not need to be considered.

### 2.3.2 A system with any number of interfaces

When more and more layers (and interfaces) are added to the system, the path that light takes can become more and more complicated. If the cumulative method is used, a myriad of sub-rays has to be considered and their intensities summed. Schropp and Zeman [6] describe a systematic method for doing so, which is quite complex, nevertheless.

Using the net-radiation method is more straightforward. At each interface four fluxes are defined. The interfaces are labelled  $i = 1 \dots I$ , where  $I$  is the total number of interfaces. Then at each interface  $i$  the following relationships exist between the fluxes

$$\begin{cases} q_{ia} = \tau_{(i-1)} q_{(i-1)d} \\ q_{ib} = r_i q_{ia} + t_i q_{ic} \\ q_{ic} = \tau_i q_{(i+1)b} \\ q_{id} = r_i q_{ic} + t_i q_{ia} , \end{cases} \quad (2.18)$$

where again  $r$  and  $t$  are the reflection and transmission coefficients of the interfaces (equation 2.3 and 2.5) and  $\tau$  is the transmission coefficient of the layers (equation 2.12). It should be noted that there are two exceptions to equation 2.18, i.e. by definition  $q_{1a} = 1$  and because no irradiance reaches the multilayer system from the backside  $q_{Ic} = 0$ . The set of  $4I$  linear equations can be solved by applying a Gauss elimination procedure to the equations written in matrix form. The reflection,

absorption and transmission factors are given by

$$\begin{aligned} R_\lambda &= q_{1b} , \\ A_{\lambda,i} &= q_{id} - q_{(i+1)a} + q_{(i+1)b} - q_{ic} , \\ T_\lambda &= q_{Id} , \end{aligned} \quad (2.19)$$

where  $A_{\lambda,i}$  is the spectral absorption factor of layer  $i$  and the spectral absorption factor of the entire multilayer system  $A_\lambda$  is given by summing over all layers

$$A_\lambda = \sum_{i=1}^{I-1} A_{\lambda,i} . \quad (2.20)$$

## 2.4 The extended net-radiation method

The underlying assumption in the net-radiation method, described in the previous section, is that all interfaces reflect light in a specular way. However, solar cells are designed to scatter light in a *non-specular* way in order to improve the optical confinement. To be able to take this non-specular reflection into account, the net-radiation method was extended. First it will be indicated how non-specular reflection can be described mathematically by matrices, in general. Then it is explained how these matrices are used in the extended net-radiation method.

### 2.4.1 Scatter matrices

In a three-dimensional multilayer structure, a zenith angle  $\phi$  and an azimuth angle  $\theta$  are required to describe the direction of scattered irradiance. In principle the extended net-radiation method can handle three dimensions, however it is more convenient to consider a two-dimensional cross-section, keeping  $\theta$  constant. As a result, the direction of scattered irradiance can be described by zenith angle  $\phi$  only. Whether this simplification affects the accuracy of the model will be discussed in section 2.6.

A rough interface will scatter reflected and refracted (transmitted) light in various directions, as indicated in figure 2.5. The distribution of this light over the angular range between  $\phi = 0^\circ$  (being the surface normal direction) and  $\phi = 90^\circ$  (being the surface parallel direction) can be described by a so-called angular distribution function. To characterise the optical behaviour of an interface completely, four different distribution functions are required, describing the distribution of reflected or transmitted irradiance in case a ray is incident from above or below the interface (see figure 2.5). Furthermore these distribution functions may vary with varying angle of incidence. In section 2.5 it will be discussed how for various types of rough interface these distribution functions can be determined. However, in this section it is assumed that these functions are already known.

The angular range of  $0^\circ$  to  $90^\circ$  is divided into many angular intervals, typically having a width of a few degrees, and these intervals are numbered 1 to  $J$ , where  $J$

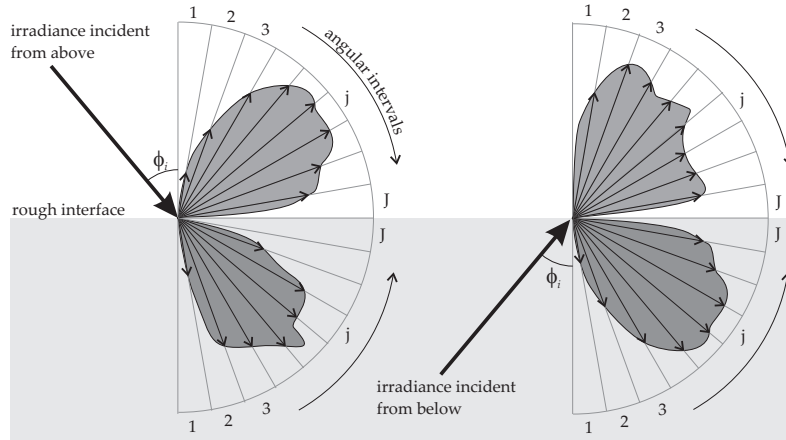


**Figure 2.5:** An incident beam of light is scattered at a rough interface. Both reflected and refracted (transmitted) light is distributed over all hemispherical directions.

is the number of angular intervals. A single ray is incident on the rough interface, with angle of incidence  $\phi_i$ . The angular distribution of the *reflected* irradiance is considered. By integrating the distribution function of the reflected irradiance over a single reflection interval  $j$ , the fraction of irradiance scattered into this interval can be determined. In fact, this can be done for each reflection interval  $j = 1 \dots J$ . Then by scanning through all angles of incidence  $\phi_i$  (where  $i = 1 \dots J$  indicates the angular interval corresponding to the incident ray), the reflection matrix  $r^+$  can be constructed. Element  $r_{i,j}^+$  indicates the fraction of the irradiance incident from interval  $i$  scattered into interval  $j$ . In a similar way a transmission matrix  $t^+$  can be constructed. Also for irradiance incident from *below* the interface, reflection and transmission matrices  $r^-$  and  $t^-$  can be constructed. If  $J$  is the number of angular intervals, then the matrices  $r^+$ ,  $t^+$ ,  $r^-$  and  $t^-$  will be  $J \times J$  matrices. Note that typically an angular resolution corresponding to  $J \approx 30$  is sufficient and that it can be convenient to vary this resolution from layer to layer, as will be explained in section 2.5.1.

The use of these matrices is now illustrated. Instead of a single incident ray, some angular distribution of incident irradiance is considered. This distribution of incident irradiance over the angular intervals can be expressed as a  $J \times 1$  matrix, called the incident flux vector,  $q_{in}$ . By multiplying the incident flux vector with the scatter matrix  $r^+$ , the *reflected* flux vector is acquired

$$q_{ref} = r^+ \cdot q_{in} . \quad (2.21)$$

The reflected flux vector contains the distribution of reflected irradiance. Similarly, the *transmitted* flux vector can be found

$$q_{tr} = t^+ \cdot q_{in} , \quad (2.22)$$

containing the angular distribution of transmitted irradiance. Would the incident irradiance have come from below the interface, the matrices  $r^-$  and  $t^-$  would have to be used.

### 2.4.2 Matrix equations

In the net-radiation method (see section 2.3.2) a set of equations was solved to determine the net-radiation fluxes  $q$  of the multilayer system. In a similar way, in the extended net-radiation method, flux-vectors  $q$  are defined. At each interface  $i$  there are four flux vectors  $q_{ia}$ ,  $q_{ib}$ ,  $q_{ic}$  and  $q_{id}$ . They are related in the following way

$$\begin{cases} q_{ia} = \tau_{(i-1)} q_{(i-1)d} \\ q_{ib} = r_i^+ q_{ia} + t_i^- q_{ic} \\ q_{ic} = \tau_i q_{(i+1)b} \\ q_{id} = r_i^- q_{ic} + t_i^+ q_{ia} \end{cases} \quad (2.23)$$

where  $r^+$ ,  $t^+$ ,  $r^-$  and  $t^-$  are the scatter matrices introduced in section 2.4.1. For each layer there is a layer transmittance matrix  $\tau$ , which is a diagonal matrix describing for each angular interval the fraction of irradiance that is transmitted (equation 2.12). Note the similarity between equations 2.18 and 2.23. Two fluxes are not given by equation 2.23, because no irradiance enters the multilayer system from the backside  $q_{ic} = 0$  and  $q_{1a}$  is the incident flux vector, representing the angular distribution of the incident irradiance. It is again convenient to consider all fluxes as dimensionless vectors and to normalise the incident flux  $q_{1a}$  as to have the sum of all its elements equal to unity

$$\sum_{j=1}^J q_{1a}^j = 1, \quad (2.24)$$

where the sum is over all angular intervals indicated by the superscript  $j$ .

By solving the set of linear equations (equation 2.23), the unknown fluxes are found. The first step in solving is to write the matrix equations in block matrix form, i.e. the scatter matrices are used as building blocks to construct a larger block matrix. The final step is to apply a Gauss elimination procedure to this block matrix resulting in the numerical values for all the fluxes.

The spectral reflection, absorption and transmission factors are then given by

$$R_\lambda = \sum_{j=1}^J q_{1b}^j, \quad (2.25)$$

$$A_{\lambda,i} = \sum_{j=1}^J \left( q_{id}^j - q_{(i+1)a}^j + q_{(i+1)b}^j - q_{ic}^j \right), \quad (2.26)$$

$$T_\lambda = \sum_{j=1}^J q_{Td}^j. \quad (2.27)$$

In this case  $R_\lambda$  and  $T_\lambda$  can be called the *hemispherical* spectral reflection and transmission factor because irradiance reflected and transmitted in all hemispherical directions is considered. Again  $A_{\lambda,i}$  is the spectral absorption factor of layer  $i$  and by summing over all layers in the multilayer system, the overall spectral absorption factor is found.

## 2.5 Interface models

In the previous section it was explained how the spectral reflection, absorption and transmission factor of a multilayer structure with rough interfaces can be determined using scatter matrices in the extended net-radiation method. In this section the following models to determine these scatter matrices are presented: the specular reflection model (section 2.5.1), Phong's diffuse reflection model (section 2.5.2) and the ray tracing model for textured interfaces (section 2.5.3). Each model describes a specific type of light-scattering encountered in solar cells. In section 2.5.4 it is demonstrated how different scatter models can be combined for modelling the type of light-scattering encountered frequently in thin-film solar cells.

### 2.5.1 Specular reflection model

One example of a specularly reflecting interface is the top surface of an encapsulated solar cell, i.e. the smooth interface between air and glass. In figure 2.6 such a smooth interface is shown and the angular intervals are indicated. Light incident from angular interval  $i$ , is reflected into reflection interval  $j = i$ . In case of perfect specular reflection, no light is reflected into neighbouring intervals. As a result the scatter matrix  $r^+$  is a diagonal matrix. The diagonal elements  $r_{i,i}$  are the reflection coefficients given by equation 2.3, using the central angle  $\phi_i$  as angle of incidence.

In the middle panel of figure 2.6 the *refraction* of light going from a medium with a low, to a medium with a high refractive index is shown. For now it is assumed that the distribution of angular intervals above and below the interface is the same. Then light incident from angular interval  $i$ , is refracted into a different interval  $j < i$ , closer to the surface normal. A transmission matrix  $t^+$  could be constructed, each element  $t_{i,j}$  describing the fraction of irradiance incident from interval  $i$  that is refracted into interval  $j$ . However, defining a different set of angular intervals below the interface has some advantages, as will be explained next.

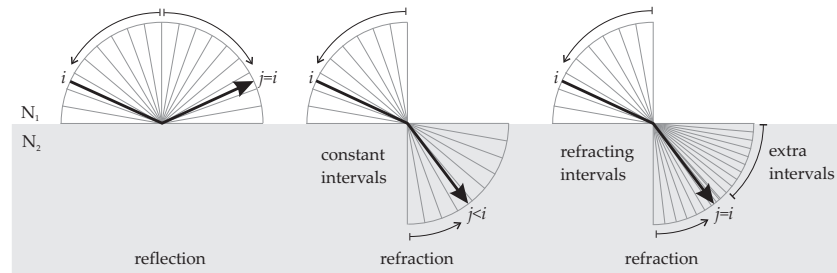


**Figure 2.6:** A cross-section of a specularly reflecting interface indicating reflection (left) and refraction (right). For refraction both the case with fixed angular intervals and refractive propagation of angular intervals is shown.

### Refractive propagation of angular intervals

In the extended net-radiation method the angular range from  $0^\circ$  to  $90^\circ$ , can be subdivided into angular intervals differently in each layer. Above the interface, angular intervals are defined and below the interface a new set of angular intervals can be constructed. Burgers [10] points out that it is convenient to propagate the angular intervals in a ‘refractive’ way, as will be explained next. Consider the incident rays bounding angular interval  $i$ . After refraction these rays can be used to form the interval boundary of interval  $j = i$  below the interface. In the same way each interval above the interface can be propagated to the next layer. By this way of creating new intervals, all irradiance incident in interval  $i$  is automatically refracted into interval  $j = i$ . As a result, the transmission matrices  $t$  are simply diagonal matrices, with the transmission coefficients  $t$  on the main diagonal. This makes the transmission matrices for specular reflection more easy to construct, simplifying the extended net-radiation method.

However, when going to an optically more dense medium (i.e. with a higher refractive index), extra intervals should be created beyond the critical angle as indicated in the right panel of figure 2.6. The other way round, when going to a less dense medium, intervals are removed accordingly (not shown). As a result, the number of angular intervals varies from layer to layer, being highest in the media with the highest refractive index. This is very convenient because in optically dense layers a higher angular resolution is required as refraction tends to ‘squeeze’ the angular distribution of irradiance towards the surface normal.

### 2.5.2 Phong’s diffuse reflection model

One example of a diffusely reflecting interface could be the alloyed aluminium back contact in a crystalline silicon solar cell. In order to describe this type of reflection, Phong’s model for diffuse reflection [36] has been used in some optical solar cell models [10, 37]. This is an empirical model for the angular distribution  $I(\phi)$  of re-

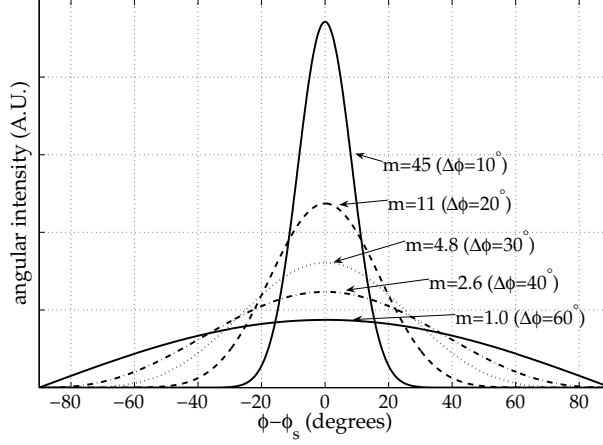


**Figure 2.7:** The distribution of scattered irradiance given by Phong's model for various opening angles  $\Delta\phi$ .

flected irradiance

$$I(\phi) = c \cdot \cos^m(\phi - \phi_s), \quad (2.28)$$

where  $c$  is the normalisation constant,  $m$  is the Phong exponent and  $\phi_s$  is the angle of specular reflection. In figure 2.7 the distribution is sketched and it can be seen that  $I(\phi)$  is distributed smoothly around the specular direction and the width of this distribution depends on the Phong exponent  $m$ . By variation of this parameter, the 'diffuseness' of reflection can be varied from diffuse to specular. A related parameter is the opening angle

$$\Delta\phi = \arccos\left(\frac{1}{2} \left(\frac{1}{m}\right)\right). \quad (2.29)$$

Note that  $\Delta\phi = 0^\circ$  corresponds to specular reflection and  $\Delta\phi = 60^\circ$  corresponds to Lambertian diffuse reflection.

Phong's model gives only the *distribution* of reflected irradiance, it does not give the fraction of the incident irradiance that is reflected, i.e. the reflection coefficient  $r$  is not given. A possible assumption is that the reflection coefficient of a diffusely reflecting interface is identical to the reflection coefficient of a smooth interface, given by equation 2.3. The normalisation constant  $c$  in equation 2.28 can then be adjusted to the reflection coefficient  $r$ ,

$$c = r / \int \cos^m(\phi - \phi_s) d\phi \quad (2.30)$$

In the same way the distribution of *refracted* irradiance can be given by Phong's model. Then in equation 2.28,  $\phi_s$  is the angle of specular *refraction* and in equation 2.30, normalisation constant  $c$  is adjusted to  $t = 1 - r$ .

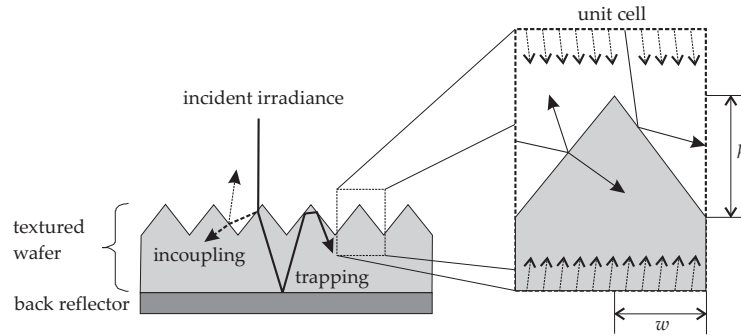


**Figure 2.8:** Left: A cross-section of a textured wafer, where improved incoupling and trapping of irradiance are indicated. Right: Ray tracing inside a unit cell, where feature height  $h$  and width  $w$  are indicated.

For an incident beam with a given angle of incidence  $\phi_i$ , Phong's model is used to determine the distribution of scattered irradiance over the angular intervals. This information is used to construct column  $i$  of the scatter matrices  $r^+$  and  $t^+$ . This procedure is repeated for all angles of incidence to complete these scatter matrices. The scatter matrices  $r^-$  and  $t^-$ , characterising the optical behaviour of the interface with respect to irradiance coming from below, are constructed in a similar way.

### 2.5.3 Ray tracing model for textured interfaces

Another type of interface that can be found in solar cells is the textured interface. In most crystalline silicon solar cells the wafer is textured, resulting in more or less regular protrusions at the wafer surface with a typical dimension of  $10\ \mu\text{m}$  [38]. Optically this texture has two effects. Firstly, if the texture is steep enough then any light that is reflected initially, is reflected sideways and will hit a neighbouring protrusion. In this way, light has a second chance of entering the wafer and incoupling of light is improved (see figure 2.8). Secondly, light that has entered the wafer is refracted into oblique directions. This increases the optical path length travelled through the wafer, increasing the absorption factor especially for weakly absorbed irradiance. Provided the texture dimensions are much larger than the wavelength of the incident irradiance, geometrical optics applies and ray tracing can be used to determine the path of this irradiance.

Ray tracing is a flexible optical tool and is used in many optical models for solar cells [37, 39, 40, 41, 42]. However, in all cases the rays are traced through the complete multilayer structure. This requires a great number of rays in order to arrive at a good statistical average. The strength of the extended net-radiation method lies in the fact that at each interface the most appropriate scatter model can be used and that the computationally expensive ray tracing is only used at those interfaces where ray



tracing is required.

In order to construct the scatter matrices, a unit cell with periodic boundaries is used, as shown in the right panel of figure 2.8. The unit cell contains a single feature of a certain width  $w$  and height  $h$ . As an example a simple zigzag feature is shown, however other features, such as the parabolic feature that will be introduced in section 3.2.2, can be used as well. Because of the periodic boundary conditions, this single feature is effectively repeated infinitely. A set of rays is released at random points above the interface under a well defined zenith angle  $\phi$ . These rays are traced as they are reflected and refracted until they leave the top or bottom of the unit cell. The information regarding direction and relative intensity of the rays leaving the top of the unit cell is used to construct scatter matrices  $r^+$ . At the same time, the data corresponding to the rays leaving the unit cell at the bottom is used to construct  $t^+$ .

The scatter matrices  $r^-$  and  $t^-$  characterise the optical behaviour of the interface with respect to irradiance coming from below. These matrices are constructed in a similar way, however the rays to be traced are incident from the *bottom* of the unit cell, as indicated in figure 2.8.

#### 2.5.4 Combined model using the haze parameter

Each model described previously can be used to calculate scatter matrices capturing a specific type of light-scattering encountered in solar cells. However, to capture the light scattering frequently encountered at the rough interfaces of thin-film solar cells, two of the models considered previously have to be combined, as will be explained next.

In thin-film solar cells a transparent conductive oxide (TCO) layer is present which is often textured. The resulting texture is generally very fine, with a roughness  $\sigma$  of approximately 100 nm. This roughness is comparable to or smaller than the wavelength of incident irradiance. As a result, the electromagnetic wave properties of irradiance become apparent and geometric optics is no longer applicable. An exact approach would be to solve Maxwell's equations [43] at the interface rigorously. However, this is quite involved. The description in terms of a haze parameter is a simple approximation frequently found in literature [31, 44].

In this description it is assumed that an incident ray is partly reflected in a specular way and partly in a diffuse way. A parameter called 'haze'  $H$  is defined as the ratio between the diffusely reflected part and the total reflected part. Haze in transmission is defined as the ratio between the diffusely transmitted part and the total transmitted part. According to the scalar scatter theory [45], haze can be described by

$$H(\lambda) = 1 - \exp \left[ - \left( \frac{2\pi(n_1 - n_2)\sigma}{\lambda} \right)^2 \right], \quad (2.31)$$

where  $\lambda$  is the wavelength,  $\sigma$  the roughness of the interfaces and  $n_1$  and  $n_2$  are the

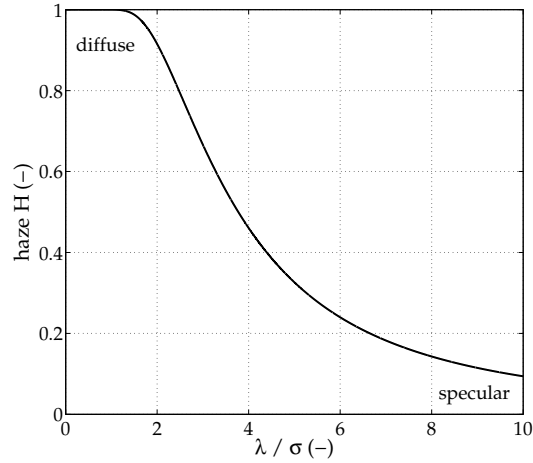


Figure 2.9: Haze  $H$  as a function of normalised wavelength  $\lambda/\sigma$ .

refractive indices above and below the interface, respectively. In figure 2.9,  $H(\lambda)$  is sketched as a function of the wavelength normalised with respect to this roughness  $\sigma$ . It can be seen that short wavelength irradiance is mostly scattered diffusely and the longer wavelength irradiance is affected by the texture to a lesser extent and is mainly reflected in a specular way.

Schulte [46] has shown experimentally, that the angular distribution of the diffuse part can be approximated using ray tracing. This is surprising because theoretically geometrical optics cannot be applied to these length-scales. Since a mixture of specular and diffuse reflection occurs at these finely textured interfaces, the scatter matrices are constructed from both the specular matrix  $\mathbf{r}_{\text{spec}}^+$  and the texture matrix  $\mathbf{r}_{\text{tex}}^+$ , described earlier. Haze is used as a weighting parameter

$$\mathbf{r}_{\text{haze}}^+ = H\mathbf{r}_{\text{tex}}^+ + (1 - H)\mathbf{r}_{\text{spec}}^+, \quad (2.32)$$

where  $\mathbf{r}^+$  can also be replaced by  $\mathbf{t}^+$ ,  $\mathbf{r}^-$ , and  $\mathbf{t}^-$ . In this way for short wavelengths ( $H \approx 1$ ) the interface behaves as a textured interface, while for longer wavelengths ( $H \approx 0$ ) it behaves as a smooth interface. In between these two extremes there is a gradual transition. Roughness  $\sigma$  is the parameter that determines the wavelength range where this transition occurs.

## 2.6 Two- versus three-dimensional modelling of internal reflection

In this section it is discussed to what extent three-dimensional effects in internal reflection can be captured by the two-dimensional optical model introduced in this chapter. The numerical model is two-dimensional (2D) in the sense that a 2D cross-section of a multi-layer is considered. Almost every optical effect that occurs in real solar cells can be captured by a 2D model. However, care should be taken when modelling internal reflection, e.g. light trapped in the c-Si wafer of a c-Si solar cell. The high refractive index of c-Si results in a relatively small critical angle of  $17^\circ$  (assuming  $n = 3.42$ ). Irradiance hitting the surface from the inside under an angle larger than the critical angle undergoes total internal reflection. This means that a ray can escape only if it is inside the loss-cone. However, the 2D and 3D situation are different with respect to the fraction of irradiance that escapes the silicon wafer.

This can be quantified by considering the fraction  $F$  of the hemisphere occupied by a loss cone with a critical angle  $\phi_{\text{cr}}$ . In two dimensions,  $F$  is given by

$$F_{2\text{D}} = \frac{2\phi_{\text{cr}}}{\pi}, \quad (2.33)$$

while in three dimensions,  $F$  is given by

$$F_{3\text{D}} = 1 - \cos \phi_{\text{cr}}. \quad (2.34)$$

If light would be distributed uniformly over all hemispherical directions, then the chance of escape would be approximately proportional to  $F$ . Because  $F_{2\text{D}} > F_{3\text{D}}$ , in the 2D situation more light would escape than in the 3D situation. An escape factor  $f_{\text{esc}}$  (having a value between 0 and 1) can be introduced in the 2D model, by which the chance of escape is multiplied to correct for the 3D effects. Note that  $f_{\text{esc}} = 1$  means that no correction is made. The ratio between  $F_{2\text{D}}$  and  $F_{3\text{D}}$  can be used as a first order estimate for  $f_{\text{esc}}$

$$f_{\text{esc}} \approx \frac{F_{3\text{D}}}{F_{2\text{D}}} = \frac{\pi(1 - \cos \phi_{\text{cr}})}{2\phi_{\text{cr}}}. \quad (2.35)$$

This function increases monotonically from 0 to 1 if  $\phi_{\text{cr}}$  is increased from  $0^\circ$  to  $90^\circ$ . In the practical case of light trapped in a c-Si wafer (where  $\phi_{\text{cr}} = 17^\circ$ ) it follows  $f_{\text{esc}} \approx 0.23$ .

This effect was analysed in more detail by comparing the chance of escape through a textured silicon/air interface in both a 2D and 3D version of the ray-tracing model described in section 2.5.3. As shown in the left panel of figure 2.10, the situation is kept as simple as possible, i.e. the interface is characterised by fixed refractive indices at both sides ( $n_{\text{Si}} = 3.42$  and  $n_{\text{air}} = 1$ ) and a zigzag (2D) or pyramid (3D) texture with a steepness  $\gamma$  of  $41^\circ$ . Rays incident on the textured interface are released

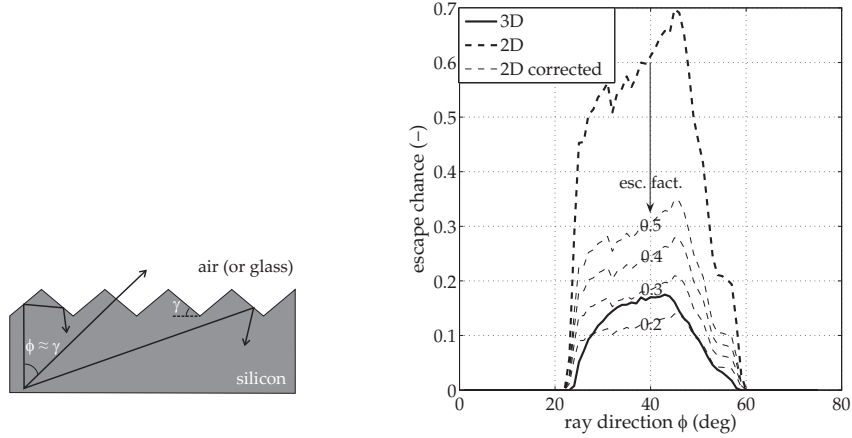


**Figure 2.10:** Left: Three rays reflected by the back contact under different zenith angles  $\phi$ , reaching the textured front of the wafer. Only the ray having a zenith angle close to the texture steepness, i.e. deviating less than the critical angle, has a chance of escaping. Right: The escape chance as a function the ray's initial zenith angle  $\phi$ , for a 3D situation (solid line) and a 2D situation with various escape factors (dashed lines)

at a random point *below* the interface, with a random azimuth but under a well defined zenith angle  $\phi$  (i.e. angle with the vertical direction). The fraction of rays that is transmitted by the interface and can escape is analysed.

In the right panel of figure 2.10 the escape chance is plotted as a function of the ray's initial zenith angle  $\phi$ . It can be seen that the 2D model (dashed line) and the 3D model (solid line) agree on the part of the angular domain for which total internal reflectance occurs, i.e. having an escape chance of zero. It turns out that only rays having a zenith angle close to the texture steepness, i.e. deviating less than the critical angle, have a chance of escaping. However, as expected, the 2D escape chance is much higher than the 3D escape chance. To incorporate this 3D effect in the 2D model the escape factor  $f_{\text{esc}}$  is introduced which reduces the escape chance. It turns out that for this particular textured interface, using an escape factor of 0.2 to 0.3 in the 2D model gives the best fit with the results from the 3D model. This is in line with the estimate of  $f_{\text{esc}} \approx 0.23$  given earlier.

As can be seen from equation 2.35, the escape factor is a function of the critical angle. Therefore the value of the escape factor that has to be used in the 2D model may vary from case to case. Furthermore, equation 2.35 is only an estimate and some details not captured by this equation, like the shape and steepness of the texture, may affect  $f_{\text{esc}}$  as well.

## 2.7 Optical confinement

In this section the effect of optical confinement, i.e. trapping light inside a layer, is illustrated. Some modelling aspects are discussed as well. To illustrate the effect, a 300  $\mu\text{m}$  thick layer having a high refractive index  $n$  is considered. It is convenient to assume  $n = 3.42$ , corresponding to the refractive index of c-Si (for  $\lambda > 1.4 \mu\text{m}$ ). Assuming for example a transmittance  $\tau = 0.99$ , the layer is very transparent, i.e. in a single pass 99% of the light is transmitted and only 1% is absorbed. Light is normally incident ( $\phi = 0^\circ$ ) on this layer from the front. The front interface is smooth and at the back there is a perfect reflector, not absorbing any light. However, the mode of reflection by the back side is varied.

In case the back side reflects all light specularly, most light reflected by the back is able to escape the layer. In that case light makes only two passes through the wafer (one down and one up) and because approximately 1% of the light is absorbed in each pass, the absorption factor of this layer is 0.02.

Because of the high refractive index, the critical angle for this layer is only  $17^\circ$ . So if the back reflector scatters light outside the critical angle, this light undergoes total internal reflection and can be trapped for multiple passes, increasing the path length and therefore the absorption factor of the layer. One way to scatter light is by means of a textured back side. A texture profile with a steepness  $\gamma$  can be assumed at the back. In figure 2.11, the absorption factor of the layer is shown as a function of steepness  $\gamma$  for a zigzag profile (dashed line) and for a parabolic profile (dotted line). In case  $\gamma < 2^\circ$ , the shallow texture does not reflect light sufficiently obliquely to cause light trapping. If  $\gamma$  is increased to  $10^\circ$ , more light is reflected outside the critical angle and is trapped for at least two more passes. Whether a trapped ray of light can escape after a second, third or higher order reflection, depends in a complicated way on the part of the texture that is hit by the ray. Especially the local slope of the texture at the point of impact is of great importance. Because the zigzag texture and the parabolic texture are different in this respect, they cause a somewhat different degree of optical confinement and therefore a different absorption factor, as can be seen in figure 2.11. It can be seen that for  $\gamma > 10^\circ$  the absorption factor no longer increases, but starts to oscillate with increasing steepness. This indicates that increasing the steepness further does not necessarily improve light trapping.

A second way to scatter light is by means of micro-roughness. Since this roughness is smaller than the wavelength of light, the geometrical optics used in ray tracing does not apply. For some types of back reflector found in solar cells, a further complication is that very little is known about their microscopic topography. This makes it difficult to arrive at a physical model for the angular distribution of light scattered by such a back side.

However, in case of such a microrough back reflector, Phong's model described in section 2.5.2 can be used. This is an empirical model, giving a simple expression

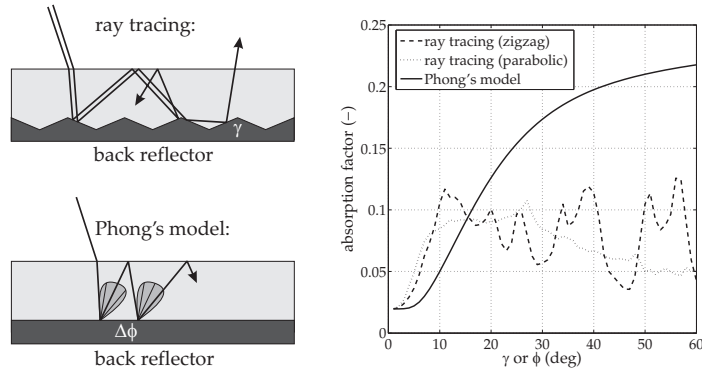


**Figure 2.11:** The absorption factor of a weakly absorbing layer ( $\tau = 0.99$ ) with a perfectly reflecting back side. Different angular distributions of light reflected by the back side are considered. Both the ray tracing model with steepness  $\gamma$  and Phong's model with opening angle  $\Delta\phi$  are used.

for the angular distribution of scattered light, with one parameter: opening angle  $\Delta\phi$ . It should be emphasised that Phong's model is used as an *effective* description of scattered light. The real angular distribution of light scattered by a microrough back side may deviate from Phong's distribution, however the effect of optical confinement can be captured very well, using Phong's model for the back side.

This is shown in figure 2.11. Phong's model is used to describe diffuse reflection by the back side. The absorption factor is plotted as a function of opening angle  $\Delta\phi$  (solid line). In case  $\Delta\phi < 4^\circ$ , hardly any light is scattered outside the critical angle and  $A = 0.02$  as for the specularly reflecting back side. But if  $\Delta\phi$  is increased, more light is scattered outside the critical angle and reflected internally. Because optical confinement is improved,  $A$  increases. For  $\Delta\phi = 60^\circ$ ,  $A$  has increased to as much as 0.22, which is more than a ten-fold increase in absorption factor with respect to the case with a specularly reflecting back side. Because such a high degree of optical confinement can be described using Phong's model, it is a powerful effective description of light scattering at the microrough back side of a solar cell.

## 2.8 Structure of the numerical model

In section 2.5 it was explained how for each interface in the multilayer structure, four scatter matrices can be generated. The sub-routine for creating the scatter matrices is at the heart of the model and is shown in more detail in figure 2.12. Depending on the type of light scattering, one of the following interface models is used: specular reflection, Phong's model for diffuse reflection, ray tracing or the combined model. The angular intervals are considered one by one as indicated by the angular interval

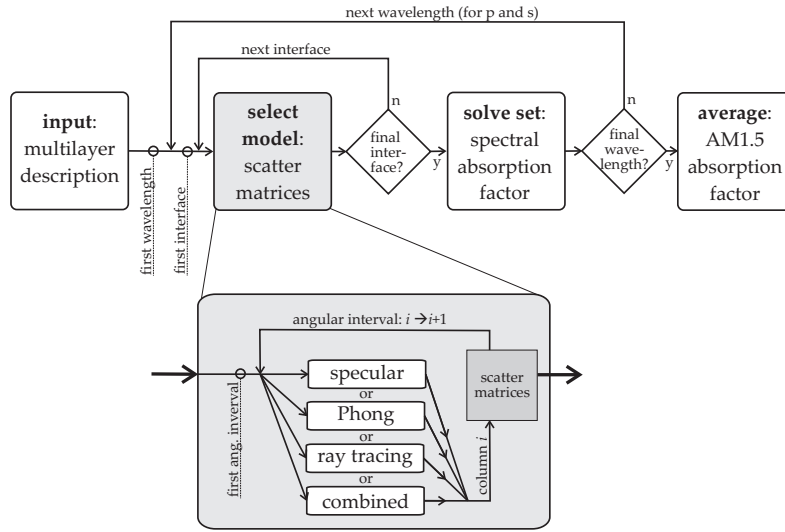


**Figure 2.12:** A flowchart for the complete optical model. Separate loops for the interfaces and for the wavelengths are indicated.

loop. As explained in section 2.4.1, each angular interval corresponds to a single column in the scatter matrices.

Using the ‘interface loop’, the matrices of all interfaces are combined in a large set of linear equations. This set is solved to find the spectral absorption factor of the structure as a whole. However, this is the spectral absorption factor  $A_\lambda$  for one polarisation state and at one wavelength  $\lambda$ . In general, the optical properties of the layers will vary as a function of wavelength. Hence the complete model contains a ‘wavelength-loop’, performing the routine once for p- and once for s-polarisation at each wavelength in the AM1.5 spectrum. After going through every wavelength, the loop terminates and the AM1.5 absorption factor  $A$  is calculated by averaging over the solar spectrum (equation 1.1).

## 2.9 Conclusion

Solar cells are complex optical devices, consisting of multiple layers. In this chapter it was shown that the net-radiation method is a very convenient method for tackling the optics of multilayer systems. The important effect of multiple reflections is taken into account by considering net-radiation fluxes. Since the classical net-radiation method can be used for smooth interfaces only, it was extended to handle rough interfaces as well. Rough interfaces are indispensable in modern solar cells and their optical behaviour is characterised by scatter matrices. To generate scatter matrices for each type of interface that can be encountered in solar cells, existing models are

imported into the optical model. In this way a flexible and efficient optical model is obtained which is very well suited for determining the spectral absorption factor of a wide range of solar cells.





# The absorption factor of crystalline silicon solar cells

## 3.1 Introduction

Currently, the wafer based crystalline silicon (c-Si) solar cell technology continues to be the dominant solar cell technology with a market share of more than 90% [8]. It is foreseen that the c-Si solar cell technology (including ribbon and thin-film c-Si) will remain to play an important role in the medium (2020) and long (2030) term [7]. The working principle was already described briefly in section 1.2.1.

C-Si solar cells are being used in the absorbers of PVT collectors. The thermal efficiency of these collectors is determined to a large extent by the AM1.5 absorption factor of the c-Si cells used. However, for sub-bandgap solar irradiance (i.e. for  $\lambda > 1.1 \mu\text{m}$ ) the spectral absorption factor of c-Si solar cells has not been studied in sufficient detail. It is relevant to do so because as much as 20% of the energy in the AM1.5 solar spectrum is contained in this part of the spectrum.

The goal of the work described in this chapter is to gain insight in the absorption mechanisms occurring in c-Si solar cells, to determine their AM1.5 absorption factor and to explore the limits in optimising c-Si solar cells for PVT applications. This analysis is performed using the optical model described in chapter 2.

First some aspects of modelling c-Si solar cells are highlighted in section 3.2. In section 3.3 the numerical model is validated by comparing the numerical results to results of optical measurements carried out on a set of c-Si samples. Then in section

3.4 the numerical model is used to investigate the influence of cell design parameters on the absorption factor of the cell. In section 3.5 a few typical c-Si solar cell designs are considered and it is discussed how the current technological development of the c-Si solar cell affects the absorption factor. Finally in section 3.6 some general conclusions are presented.

## 3.2 Modelling crystalline silicon solar cells

In this section some modelling aspects that are specific to c-Si solar cells are highlighted. Especially the optical properties of structures present at the front and the back of the solar cell are considered. It is discussed how these structures can be modelled using the optical model described in chapter 2. Note that at first only the active area of the c-Si cell is considered, i.e. without the front contact grid. In section 3.4.6 the effect of the front contact grid is looked into.

### 3.2.1 The absorption coefficient of doped crystalline silicon

Because c-Si is a semiconductor, its absorption coefficient  $\alpha$  will vary over many orders of magnitude with varying wavelength  $\lambda$ . For intrinsic (i.e. undoped) c-Si,  $\alpha(\lambda)$  is given as the solid line in figure 3.1 [47]. It can be seen that  $\alpha$  decreases strongly with increasing wavelength. Short-wavelength photons ( $\lambda < 1.0 \mu\text{m}$ ) have an energy larger than the (indirect) bandgap. These photons are able to create electron-hole pairs and are readily absorbed by the c-Si. However, long-wavelength photons ( $\lambda > 1.2 \mu\text{m}$ ) cannot generate electron-hole pairs and are hardly absorbed. Photons in the transition region ( $1.0 < \lambda < 1.2 \mu\text{m}$ ) are weakly absorbed, i.e. are only absorbed after having travelled some distance in the c-Si material.

Intrinsic silicon is a poor conductor, but the addition of doping reduces the resistivity. By adding n- or p-type doping to a semiconductor, ‘free’ electrons or holes are introduced. These free charge carriers can absorb photons by free-carrier absorption (but electron-hole pairs are not generated) [4]. Hence the absorption coefficient of silicon is a function of n- and p-type doping concentration  $c_n$  and  $c_p$ . Green [4] gives the following expression for the free-carrier absorption coefficient

$$\alpha_{\text{fc}} = 2.6 \cdot 10^{-18} c_n \lambda^3 + 2.7 \cdot 10^{-18} c_p \lambda^2, \quad (3.1)$$

where  $\alpha_{\text{fc}}$  is given in  $\text{cm}^{-1}$ ,  $\lambda$  in  $\mu\text{m}$  and  $c_n$  and  $c_p$  in  $\text{cm}^{-3}$ .

In a c-Si solar cell, typically n-type doping can be found in the approximately  $0.2 \mu\text{m}$  thin emitter layer at the front of the wafer. An emitter is commonly characterised by its sheet resistance  $R_{\text{sheet}}$ . Note that the sheet resistance describes the resistance in the plane of a thin sheet between the opposite sides of a square and for this reason  $R_{\text{sheet}}$  is expressed in units  $\Omega_{\square}$ . The doping concentration  $c_n$  of the emitter is a function of  $z$ , where  $z$  is the wafer normal coordinate and  $z = 0$  corresponds to the

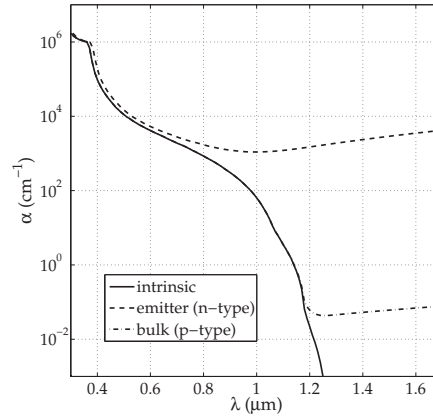


**Figure 3.1:** The absorption coefficient of c-Si as a function of wavelength for intrinsic silicon [47], p-type silicon with typical bulk doping concentration of  $1.0 \cdot 10^{16} \text{ cm}^{-3}$  and n-type silicon with typical emitter doping concentration of  $3.3 \cdot 10^{20} \text{ cm}^{-3}$  [4].

wafer's front surface. Bisschop [48] has determined this  $c_n(z)$  for various phosphorus emitters using stripping Hall measurements. These profiles have a maximum doping concentration  $c_0$  near the surface and typically  $c_0 = 3.3 \cdot 10^{20} \text{ cm}^{-3}$ . In this case the sheet resistance of the emitter is not so much controlled by  $c_0$  which hardly varies, but mainly by the depth of the doping profile.

In this thesis only the *amount* of free-carrier absorption is of interest and the exact shape of the absorption profile is of less concern. Because  $\alpha_{fc}$  is linear in doping concentration (see equation 3.1), the amount of free-carrier absorption depends only on the so-called areal doping concentration

$$C_n \equiv \int c_n(z) dz, \quad (3.2)$$

where  $c_n(z)$  is the doping concentration profile. Doping concentration profiles of emitters with a sheet resistance ranging from 22 to 57  $\Omega_{\square}$  were reported by Bisschop [48]. The areal doping concentrations of these emitters were determined by integrating the doping profiles. In figure 3.2 the areal concentrations found in this way are plotted versus the sheet resistance for the emitters measured by Bisschop. On a physical basis one would expect that the areal concentration of charge carriers is approximately proportional to the sheet conductance and therefore inversely proportional to the sheet resistance. The following inverse relation between  $C_n$  and  $R_{\text{sheet}}$  was found to fit the experimental data reasonably well

$$C_n = \frac{1.1 \cdot 10^{17} \Omega_{\square} \text{cm}^{-2}}{R_{\text{sheet}}}, \quad (3.3)$$

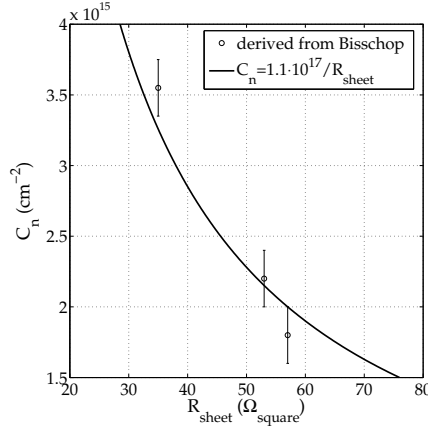


**Figure 3.2:** The areal concentration of free-charge carriers in the emitter  $C_n$  versus the emitter sheet resistance  $R_{\text{sheet}}$  as measured by Bisschop [48] (circles) and the fitted inverse relation (solid line).

as can be seen from the solid line in figure 3.2.

The optical model (described in chapter 2) uses uniform layers, each characterised by a refractive index  $n$  and an absorption coefficient  $\alpha$ . In order to model the effect of free-carrier absorption by the emitter, the emitter is represented in the model as a separate layer with uniform doping concentration  $c_0 = 3.3 \cdot 10^{20} \text{ cm}^{-3}$ . In the model, the areal concentration  $C_n$  of the emitter is controlled through an effective thickness of the emitter layer. This effective thickness, being specific to free-carrier absorption, is defined as

$$d_{e,fc} = C_n / c_0 . \quad (3.4)$$

Note that  $d_{e,fc}$  should not be confused with the conventional definition of emitter thickness, i.e. the physical depth of the n-type region, being the depth at which the n-type concentration falls below the bulk doping concentration.

Not the areal concentration  $C_n$ , but the sheet resistance  $R_{\text{sheet}}$  is the quantity normally used to specify the emitter. Therefore a relation between  $d_{e,fc}$  and  $R_{\text{sheet}}$  would be more convenient. By substituting equation 3.3 into equation 3.4 and taking  $c_0 = 3.3 \cdot 10^{20} \text{ cm}^{-3}$  the required relationship is found

$$d_{e,fc} = \frac{3.5 \mu\text{m}\Omega_{\square}}{R_{\text{sheet}}} . \quad (3.5)$$

For typical emitters with a sheet resistance of 50 to 70  $\Omega_{\square}$  the corresponding  $d_{e,fc}$  is 70 to 50 nm.

In figure 3.1,  $\alpha(\lambda)$  is shown for c-Si with the typical n-type doping concentration found in emitters of  $3.3 \cdot 10^{20} \text{ cm}^{-3}$ . It can be seen that such a high doping concentration increases  $\alpha$  to above  $10^3 \text{ cm}^{-1}$  for all wavelengths. Besides the emitter, the bulk

of the wafer is doped. Typically, wafers are used with a bulk resistivity of  $1.5 \Omega\text{cm}$ . This corresponds to a p-type doping concentration in the bulk of  $1.0 \cdot 10^{16} \text{ cm}^{-3}$ . This is more than four orders of magnitude less than the doping concentration in the emitter. For this doping concentration  $\alpha(\lambda)$  is also shown in figure 3.1. It can be seen that at these low concentrations the effect of free-carrier absorption is relatively small, increasing  $\alpha$  to only  $0.1 \text{ cm}^{-1}$  for sub-bandgap irradiance.

In the emitter relatively strong free-carrier absorption occurs in a thin region while in the bulk of the wafer free-carrier absorption is only weak but occurs over the entire depth of the wafer. The areal concentration  $C_n$  indicates the relative importance of free-carrier absorption in the emitter versus free-carrier absorption in the bulk. For the uniform bulk doping this is simply the product of  $c_p$  and the wafer thickness of say  $200 \mu\text{m}$ , resulting in  $C_p = 2.0 \cdot 10^{14} \text{ cm}^{-2}$ . This is still one order of magnitude less than the areal concentration of a typical emitter ( $C_n = 2.0 \cdot 10^{15} \text{ cm}^{-2}$ ), indicating that free-carrier absorption in the emitter is dominant over free-carrier absorption in the bulk.

### 3.2.2 Textured silicon surfaces

Commonly, the c-Si wafers used for solar cells are textured, i.e. the wafer surface is roughened, resulting in roughness dimensions in the order of  $10 \mu\text{m}$  [38]. A detailed view of a typical texture is shown in the left panel of figure 3.3. The function of this texture is twofold. Firstly, incoupling of sunlight is improved, i.e. a larger fraction of the incident light enters the wafer and reflection losses are reduced. Secondly, by means of refraction, the light entering the wafer is scattered into oblique directions. This helps to trap weakly absorbed light inside the wafer. Both effects increase the absorption in the wafer significantly and therefore the electrical cell efficiency as well.

Texture can be applied by wet chemical etching. The surface morphology of this texture depends on the etch composition, temperature and duration of etching. Alkaline etchants act anisotropically upon silicon, i.e. dependent on crystallographic orientation. When applied to mono-crystalline silicon wafers having a suitable crystallographic orientation, this results in a steep pyramid texture over the complete wafer surface, which improves incoupling of light very efficiently. However, an alkaline etch is not very suitable for multicrystalline silicon wafers with crystallographic orientations varying between the various crystallites in the wafer. Therefore multicrystalline silicon wafers typically undergo an acid etch process. Acid etchants act isotropically upon silicon, resulting in rounded or pitted textures, regardless of the crystallographic orientation. In the left panel of figure 3.3, an electron microscopic picture is shown of this texture after an etch exposure somewhat longer than commonly used in industrial processes. The rounded features, though somewhat less pronounced, are representative for the textures currently used in industry on multi-crystalline silicon solar cells [49, 50]. More details are given by Hylton [38].

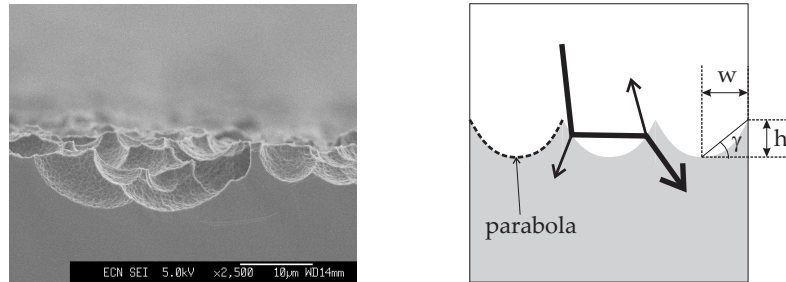


**Figure 3.3:** Left: A detailed view of the rounded texture on a silicon wafer resulting from an acid etch (courtesy of Hylton [38]). Right: A two-dimensional periodic parabolic profile as used in the numerical model. Three periods are shown and steepness  $\gamma$  is indicated.

Because the presence of texture affects the optical behaviour of the solar cell very much, its optical effects are taken into account by the optical model described in chapter 2. Since the dimensions of this texture ( $\approx 10 \mu\text{m}$ ) are typically one order of magnitude larger than the wavelength of solar irradiance ( $\approx 1 \mu\text{m}$ ), ray tracing can be used to model light scattering by the textured surface. A simplified two-dimensional representation of the surface morphology is the parabolic profile shown in the right panel of figure 3.3. This profile is used in the optical model. The effective steepness  $\gamma$  is a model parameter defined by

$$\tan \gamma = h/w, \quad (3.6)$$

where  $h$  and  $w$  are the feature height and width, respectively. Note that because ray tracing is based on geometrical optics, for a given texture profile only steepness  $\gamma$  is important (i.e. the ratio of  $h$  and  $w$ ) and not the absolute value of  $h$  and  $w$ . Besides steepness  $\gamma$ , the shape of the texture profile can be important. For example a parabolic profile will reflect and refract light differently than a zigzag profile of the same steepness. Though this results in a somewhat different angular distribution of scattered irradiance, similar degrees of incoupling and optical confinement can be obtained with different texture profiles, as was shown in section 2.7. The required degree of texturisation (i.e. the steepness) will be different for different texture profiles. Because the parabolic profile resembles the pitted structure of silicon surfaces textured by means of an acid texture etch, the parabolic profile will be used for the simulation of these surfaces.

From the microscopic images published by Hylton [38] (shown in the left panel of figure 3.3) it can be seen that height  $h$  and width  $w$  of these texture features are comparable. Therefore the texture steepness will be approximately  $45^\circ$ . A ray tracing analysis was used to find the relation between the steepness  $\gamma$  of the parabolic profile and the corresponding hemispherical reflection factor  $R_\lambda$ . These numerical results were compared to the measured  $R_\lambda$  of the front and back side of several wafers that

were textured using a similar acid etch. For a steepness of  $41^\circ$ , the numerical  $R_\lambda$  corresponds to the  $R_\lambda$  measured for the front side of the wafer and for a steepness of  $32^\circ$ , the numerical  $R_\lambda$  corresponds to the  $R_\lambda$  measured for the back side of the wafer. Therefore  $\gamma_{\text{front}} = 41^\circ$  and  $\gamma_{\text{back}} = 32^\circ$  will be used to model the front and back surfaces of all textured wafers used in this thesis, unless stated otherwise.

### 3.2.3 Back contact structures

First of all, the back contact of a solar cell has to be a good electrical contact, i.e. having a low contact resistance, and has to have a low effective surface recombination velocity. Secondly, it has to be highly reflective to reflect as much weakly absorbed light as possible back into the active layer, giving photons an extra chance to generate electron-hole pairs. A diffusely reflecting back contact is preferred over a specularly reflecting one as diffusely reflected light is generally better trapped inside the wafer.

#### Alloyed aluminium

In industry, the back contact is frequently applied to the c-Si wafer by screen printing of aluminium followed by an alloy step. The goal of the alloying process is to obtain a low contact resistance and well passivated back contact, i.e. with a low effective surface recombination velocity. In practice this is done by screen printing aluminium (Al) paste to the back of the wafer and then heating the wafer for a few seconds at a temperature of about  $800^\circ\text{C}$ , being well above the melting temperature of Al ( $660^\circ\text{C}$ ), but far below the melting temperature of silicon ( $1410^\circ\text{C}$ ). As the Al melts, the silicon (Si) of the back of the wafer is dissolved in the melt, up to a mass fraction of about 30wt%. During cooling down, Si is again secreted from the melt until at the eutectic temperature a melt with the eutectic composition (12wt% Si) is formed. This melt solidifies in the eutectic composition. Details about the alloying process are given by Lölgen [51].

The end result of the alloying process is indicated in figure 3.4. At the back of the silicon wafer there is an approximately  $10\ \mu\text{m}$  thick layer of secreted Si which is Al doped rather heavily ( $c_p = 10^{18}\ \text{cm}^{-3}$ , being the solid solubility at the solidification temperature). This forms the  $p^+$  layer which sets up the back surface field (BSF) required for a low effective surface recombination velocity. Below this layer there is the Al/Si alloy of eutectic composition. Because the Al/Si alloy is opaque, any layer(s) present below this layer do not have to be taken into account in the optical model for the c-Si solar cell with the alloyed Al back contact. Because the BSF passivates the back surface, the effective surface recombination velocity is reduced to about  $1000\ \text{cm/s}$  [51, 52]. Since the interfaces between the different layers have acquired some micro roughness, light is reflected in a diffuse way.

In the optical model described in chapter 2, the  $p^+$  layer and the alloyed layer can be modelled separately. Some additional free-carrier absorption will take place



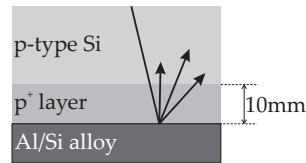


Figure 3.4: Detailed view of the aluminium alloyed back contact.

in the  $p^+$  layer. This can be modelled by representing this layer in the model as a separate layer at the back of the wafer with a modified absorption coefficient given by equation 3.1. This approach is very similar to the one used for the emitter at the front of the wafer.

The refractive index  $n$  and extinction coefficient  $k$  of the eutectic Si/Al alloy layer were interpolated from the optical properties of pure Si [47] and pure Al [53]. Using  $n$  and  $k$  obtained in this way in equation 2.3, it is found that the alloy ( $r = 0.87$ ) is less reflective than pure Al ( $r = 0.92$ ). If free-carrier absorption in the  $p^+$  layer is also taken into account, the back contact becomes effectively even less reflective ( $r = 0.83$ ). These back contact reflection coefficients are theoretical values for  $\lambda = 1.2 - 1.6 \mu\text{m}$  and do not take into account the effect of roughness. To what extent these values approach the experimental values will be discussed in section 3.3.4.

The effect of light scattering by the back contact can be simulated using Phong's model (described in section 2.5.2) or using the ray-tracing model (described in section 2.5.3). In section 2.7 it was evaluated to what extent these methods are suitable for describing diffuse reflection at the back side of a silicon wafer. Both methods can be used as an effective description, however it was concluded that especially in case of diffuse light scattering, e.g. caused by microroughness, Phong's model is more suitable.

### More advanced back contact structures

The cell design based on the use of an alloyed Al back contact is a frequently used state-of-the-art c-Si solar cell design. There is a strong tendency to thinner and thinner wafers for cost reasons and to cope with silicon feedstock shortage. However, if the alloyed Al back contact is applied to thinner wafers, the difference in expansion coefficient of silicon and aluminium leads to too much bow. Furthermore, the use of thinner wafers implies that the influence of both the effective rear side surface recombination velocity and the reflectivity of the rear side of the solar cell becomes more and more important. This means that because of the moderate effective surface recombination velocity and the moderate reflectivity the concept of a total area alloyed Al back contact needs to be abandoned.

One way to obtain a low surface recombination velocity is to passivate the back of the solar cell with a passivating thin film (e.g.  $\text{Si}_3\text{N}_4$ ,  $\text{SiO}_2$  or  $\text{Al}_2\text{O}_3$ ) and to combine

this with an open back contact [16]. Because these thin films are transparent, the rear side reflectivity is also determined by the (encapsulation) materials present below the solar cell. In order to gain some insight in the optical properties of a back surface configuration with white Tedlar<sup>®</sup> as a reflector, the spectral reflection factor of a polished c-Si wafer encapsulated in a glass/EVA/c-Si/EVA/Tedlar<sup>®</sup> configuration was investigated. By fitting the measured reflection curve  $R_\lambda$ , the optical properties of the open back surface of the c-Si wafer were extracted. For  $r_{\text{back}} \approx 0.60$  and  $\Delta\phi \approx 10^\circ$  a good agreement was found (not shown). Note that a double sided polished wafer was used in the experiment. Because all interfaces are smooth, no light is scattered obliquely and the value found for  $r_{\text{back}}$  corresponds to irradiance normally incident on the interface, i.e.  $\phi = 0^\circ$ . In real cells, some light will also reach the open back side of the wafer under a more oblique angle and total internal reflection may occur, effectively increasing  $r_{\text{back}}$ . Therefore the value of  $r_{\text{back}} \approx 0.60$  should be interpreted as a minimum value. In practice, the back contact structure is more complicated, because of the presence of the passivating oxide. In addition also in this configuration attempts will be made to make the reflectivity as high as possible, among others by enhancement of the reflectivity of white Tedlar<sup>®</sup>.

Another way to obtain a back contact structure with a low effective surface recombination is to combine a passivating oxide (e.g. SiO<sub>2</sub>) with a metallic reflector. Kray [15] shows that in this case very high reflection coefficients can be obtained, i.e.  $r_{\text{back}} = 0.94 - 0.99$  with a sandwich of silicon oxide and aluminium. On textured wafers their diffuseness of reflection  $\Delta\phi = 15^\circ$ . In such a structure ohmic contacts can be obtained by local laser firing.

### 3.2.4 Electrical cell efficiency

In section 3.4, the effect of several cell design parameters on the AM1.5 absorption factor will be investigated. It is relevant to know the effect on the electrical solar cell efficiency as well. The optical model itself does not calculate this electrical efficiency. It does, however, calculate the optical absorption profile of the active layer. This absorption profile can be imported into solar cell device model PC1D [30], which in turn can determine the desired electrical efficiency. PC1D solves the semiconductor transport equations, taking into account the generation, recombination and transport of electrons and holes in the active layer.

The required input parameters for PC1D are related to the structure and material quality of the solar cell device. Some of these parameters are introduced here because they will play a role in section 3.4. The bulk minority carrier lifetime  $\tau_b$  is related to the diffusion recombination length

$$L = \sqrt{D\tau_b}, \quad (3.7)$$

where  $D$  is the minority carrier diffusion coefficient of 25 cm<sup>2</sup>/s [4]. Typical values, that can be obtained for very well bulk passivated multicrystalline wafers, are  $\tau_b =$

100  $\mu\text{s}$  and consequently  $L = 500 \mu\text{m}$ . Of course an as high as possible  $\tau_b$  and  $L$  are desirable because it corresponds to a lower recombination rate in the bulk of the active layer.

A measure for recombination occurring at the front or back surface of the wafer is the surface recombination velocity  $S$ . To take into account both recombination occurring at and *near* the surface, the *effective* surface recombination velocity is used  $S_{\text{eff}}$  [5]. A typical value for the alloyed aluminium back contact is  $S_{\text{eff}} = 1000 \text{ cm/s}$  [51, 52], while a back contact passivated with an oxide has a lower  $S_{\text{eff}}$  of typically 100  $\text{cm/s}$  [52].

### 3.3 Model validation

In order to gain insight in the validity of the optical model, the model is validated by comparing its numerical results to results of optical measurements carried out on a set of c-Si samples. In section 3.3.1 the experimental set-up is described and in section 3.3.2 a brief overview is given of the c-Si samples used. In sections 3.3.3 to 3.3.5 numerical and experimental results are compared and finally in section 3.3.6 the validity of the model is discussed.

#### 3.3.1 Experimental setup

The AM1.5 absorption factor could be determined directly from a calorimetric measurement [54]. However, this does not give the required spectrally resolved information. This information can be obtained by measuring the spectral reflection factor  $R_\lambda$  and the spectral transmission factor  $T_\lambda$  optically and determining the spectral absorption factor indirectly using  $A_\lambda = 1 - R_\lambda - T_\lambda$ .

Hemispherical reflection and transmission factors have to be measured, containing both direct and diffuse contributions. The solar energy department of Energy research Centre of the Netherlands (ECN) has the experimental setup for measuring these hemispherical reflection and transmission factors. ECN has made this setup available for the optical experiments described in this thesis. The setup consists of a Labsphere RTC 060 SF integrating sphere. The inside of this sphere is coated with Spectrafect<sup>®</sup> making the inside highly reflective. To measure  $R_\lambda$ , the sample is placed at port 2 (see left panel of figure 3.5). A light source irradiates the sample through port 1 and all light reflected by the sample is collected by the sphere. The intensity inside the sphere is proportional to  $R_\lambda$  and is measured as a function of wavelength by an Instrument Systems spectro-radiometer. To measure the transmission factor  $T_\lambda$ , the sample is placed at port 1 and port 2 is closed (see right panel of figure 3.5). In this way all transmitted light is collected by the sphere. The hemispherical  $R_\lambda$  and  $T_\lambda$  can be determined with a 1% absolute inaccuracy for  $0.33 < \lambda < 1.6 \mu\text{m}$ .

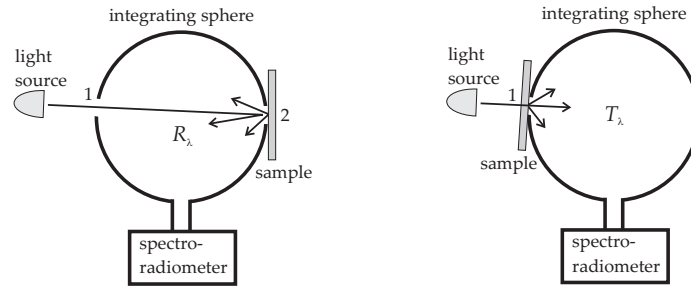


**Figure 3.5:** The integrating sphere setup. To measure the hemispherical reflection factor  $R_\lambda$  the sample is placed at port 2 (left) and to measure the hemispherical transmission factor  $T_\lambda$  the sample is placed at port 1 and port 2 is closed (right).

**Table 3.1:** The c-Si samples for the measurement of the spectral reflection  $R_\lambda$  and transmission  $T_\lambda$  factors.

nr	material	thickness	surface	emitter	ARC	back contact
1	mono	485 $\mu\text{m}$	polished	-	-	-
2	mono	485 $\mu\text{m}$	polished	47 $\Omega_\square$	-	-
3	mono	485 $\mu\text{m}$	polished	-	-	Al evaporated
4	mono	485 $\mu\text{m}$	polished	-	-	Al screenpr. & alloyed
5	multi	325 $\mu\text{m}$	textured	-	-	-
6	multi	318 $\mu\text{m}$	textured	62 $\Omega_\square$	-	-
7	multi	309 $\mu\text{m}$	textured	62 $\Omega_\square$	yes	-
8	multi	325 $\mu\text{m}$	textured	62 $\Omega_\square$	yes	Al screenpr. & alloyed

### 3.3.2 Sample description

A complete c-Si solar cell is a complex optical device in which several optical effects occur simultaneously. In order to validate the model, a set of samples was prepared at the solar energy department of Energy research Centre of the Netherlands (ECN). These samples have a gradually increasing complexity. In this way one optical effect is introduced at a time and it can be checked whether this effect is captured by the model. Note that the set of samples contains both mono-crystalline and multicrystalline silicon samples. Both are forms of c-Si and have identical optical properties. Next a brief description of sample 1 to 8 is given of which the details are summarised in table 3.1.

Samples 1 to 4 are made of Czochralski mono-crystalline silicon wafers of approximately 500  $\mu\text{m}$  thick, with a boron p-type doping concentration of approximately  $1.0 \cdot 10^{16} \text{ cm}^{-3}$  resulting in a resistivity of 1.5  $\Omega\text{cm}$ . The wafers are polished resulting in smooth surfaces. Sample 1 is a bare wafer. Sample 2 has a phosphorus emitter of 47  $\Omega_\square$  at the front. Sample 3 has aluminium evaporated at the back. The alu-

minium layer is completely opaque. Note that this is not a typical back contact and this sample is only used to investigate the reflection coefficient of a smooth Si/Al interface. Sample 4 has a standard screenprinted and alloyed aluminium back contact as described in section 3.2.3.

Samples 5 to 8 are approximately 300  $\mu\text{m}$  thick, textured multicrystalline silicon wafers. The wafers have a boron p-type doping concentration of approximately  $1.0 \cdot 10^{16} \text{ cm}^{-3}$  resulting in a resistivity of 1.5  $\Omega\text{cm}$ . They were textured by means of the standard acid texture etch [14], resulting in the pitted surface texture described in section 3.2.2. Samples 6, 7 and 8 have a phosphorus emitter of 62  $\Omega\Box$  at the front. Samples 7 and 8 have an added PECVD silicon nitride ( $\text{Si}_3\text{N}_4$ ) anti-reflective coating with a thickness of typically 80 nm at the front. Sample 8 has a screenprinted and alloyed aluminium back contact. This final sample resembles a complete c-Si solar cell, except that the front metallisation is not yet added.

### 3.3.3 Bare silicon

In the following sections the spectral reflection factor  $R_\lambda$  and transmission factor  $T_\lambda$  measured for samples 1 to 8 will be compared to the results of the optical model, starting with the relatively simple bare silicon samples, samples 1 and 2.

#### Polished wafer (sample 1)

In the left panel of figure 3.6,  $R_\lambda$  and  $T_\lambda$  are shown for the bare polished wafer (sample 1). In fact  $1 - R_\lambda$  is plotted so the vertical distance in between  $1 - R_\lambda$  and  $T_\lambda$  corresponds to the spectral absorption factor  $A_\lambda = 1 - R_\lambda - T_\lambda$ . Measurement results are indicated by symbols ( $\circ$ ,  $\nabla$ ). The measurements have an inaccuracy of only 1% absolute and error bars are not indicated since their size is comparable to the size of the symbols. The numerical results are indicated by lines. As can be seen for sample 1 the numerical results agree very well with the experiments.

This measurement illustrates that for  $\lambda < 1.0 \mu\text{m}$  the wafer is opaque ( $T_\lambda = 0$ ) while for  $\lambda > 1.2 \mu\text{m}$  the wafer is transparent ( $A_\lambda \approx 0$ ). The bulk doping concentration is too low to cause significant free-carrier absorption. The increase in  $R_\lambda$  for  $\lambda > 1.2 \mu\text{m}$  is caused by the transparency of the wafer, allowing irradiance to be reflected internally by the back surface, i.e. the back surface becomes 'visible'. Both front and back surface were modelled as smooth surfaces.

Because the agreement between numerical and experimental results is very good, two things can be concluded. Firstly, that polished wafer surfaces can indeed be modelled as specularly reflecting surfaces and secondly that the optical properties of c-Si reported by Green [47] used in the model are very accurate.

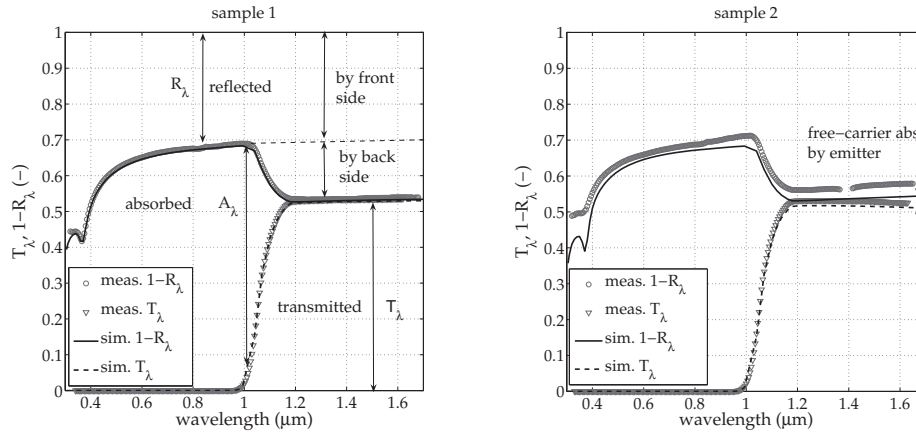


**Figure 3.6:** Measured and simulated  $1 - R_\lambda$  and  $T_\lambda$  as a function of  $\lambda$  for a polished wafer (sample 1, left) and for a polished wafer with emitter (sample 2, right).

### Emitter (sample 2)

In the right panel of figure 3.6,  $R_\lambda$  and  $T_\lambda$  are shown for sample 2. This sample has an emitter with a sheet resistance of  $47 \Omega_\square$ , but apart from that is identical to sample 1. As explained in section 3.2.1 the emitter is modelled as a single layer with an n-type doping concentration of  $3.3 \cdot 10^{20} \text{ cm}^{-3}$ . Using the sheet resistance of  $47 \Omega_\square$  in equation 3.5 it follows that in the model a thickness  $d_{e,fc}$  should be used of 74 nm.

For the transmission curve shown in the right panel of figure 3.6 there is a good agreement between simulation and experiment. However, for the reflection curve some small differences can be observed. For  $\lambda < 0.4$  the measured reflection factor is 0.50, while the simulated reflection factor remains close to the value of 0.43 (also found for sample 1). Apparently, the high doping concentration not only causes free-carrier absorption of infrared irradiance, it also affects the refractive index ( $n$  or  $k$ ) in the blue part of the spectrum. This optical effect, possibly caused by a kind of bandgap narrowing [55], was not taken into account in the model.

In the wavelength region  $0.4 < \lambda < 1.0 \mu\text{m}$ , the reflection curve deviates 2 to 3% from the simulated curve and from the reflection curves of samples 1, 3 and 4 (see left panel of figure 3.6 and figure 3.7), though this is not expected. Probably some residual oxide remained on sample 2 after indiffusion of the emitter. This residual oxide may have reduced the reflection coefficient of the wafer's front surface slightly. If it is assumed that the oxide has reduced the reflection coefficient of the front surface by 2.5% uniformly over the spectrum, then the measurement results can be corrected by simply increasing  $R_\lambda$  by 2.5% (not shown). In that case, for  $0.4 < \lambda < 1.0 \mu\text{m}$  a good agreement is found with the numerical results. At the same time, a small amount of absorption remains for  $\lambda > 1.2 \mu\text{m}$  which is comparable to the amount found in

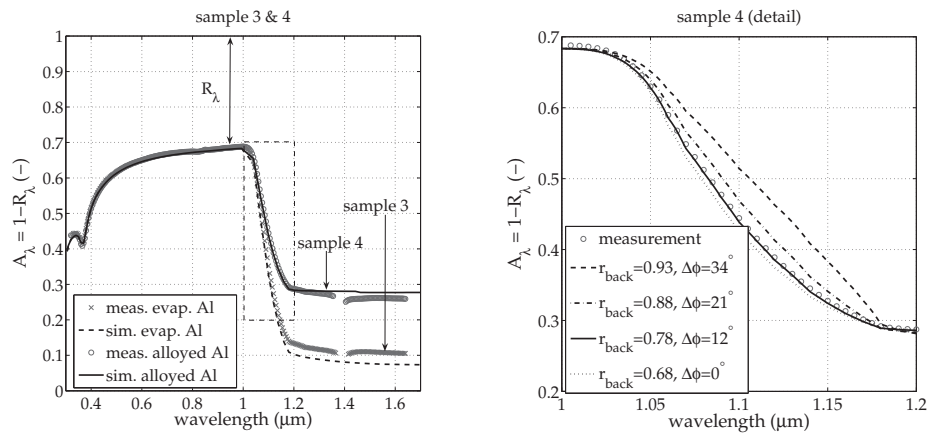


**Figure 3.7:** Measured and simulated  $A_\lambda = 1 - R_\lambda$  as a function of  $\lambda$  for a polished wafer with evaporated aluminium at the back (sample 3) and with an alloyed aluminium back contact (sample 4), both shown in the left panel. Right: A detailed view of the the ‘slope’ corresponding to sample 4 with various fits of  $r_{\text{back}}$  and  $\Delta\phi$ .

the simulation. This remaining absorption can be attributed to free-carrier absorption and is indicated by the arrow. Since compared to the previous sample only an emitter was added, this confirms that a detectable amount of free-carrier absorption occurs in the emitter.

### 3.3.4 Aluminium back contact

Samples 3 and 4 have aluminium at the back. Because  $T_\lambda = 0$ , only  $A_\lambda = 1 - R_\lambda$  is shown in figure 3.7. Short wavelength irradiance ( $\lambda < 1.0 \mu\text{m}$ ) does not reach the back of the wafer so in this part of the graph,  $R_\lambda$  is the same as for sample 1 without aluminium.

#### Evaporated aluminium (sample 3)

In the left panel of figure 3.7 the measurement results are shown for sample 3 with evaporated Al at the back. It can be seen that for  $\lambda > 1.2 \mu\text{m}$   $A_\lambda$  is only 0.11 ( $R_\lambda = 0.89$ ) because of the high reflectance of the back interface. As already mentioned in section 3.2.3, the theoretical reflection coefficient of a Si/Al interface is quite high, approximately 0.92 for  $\lambda = 1.2 - 1.6 \mu\text{m}$ . If this value is used in the simulations in combination with specular reflection a reasonable agreement is found with the experimental results. For  $\lambda = 1.2 - 1.6 \mu\text{m}$  the measured  $R_\lambda$  is only 3% lower, indicating that the reflection coefficient of the silicon/evaporated aluminium interface is only slightly less than the theoretical value.



#### Alloyed aluminium back contact (sample 4)

In the left panel of figure 3.7,  $A_\lambda$  is also shown for the sample with an alloyed aluminium back contact (sample 4). It can be seen clearly that, compared to sample 3,  $A_\lambda$  is increased from 0.11 to 0.29 (or  $R_\lambda$  is reduced from 0.89 to 0.71) for  $\lambda > 1.2 \mu\text{m}$ . This increase in  $A_\lambda$  has two causes. Firstly the alloyed back contact is less reflective and secondly it scatters reflected light diffusely. If light is scattered diffusely, a part will be reflected internally at the front surface and remains trapped inside the wafer.

It is expected that both effects are responsible for the observed increase in  $A_\lambda$ . In section 2.7 it was shown that Phong's model for diffuse reflection is most suitable to provide an effective description of the diffuse reflection by the back contact. Therefore this model will be used in the analysis of the alloyed aluminium back contact. As described in section 2.5.2, Phong's model has two parameters: the reflection coefficient  $r_{\text{back}}$  and the diffuseness of reflection  $\Delta\phi$ . In the wavelength range  $\lambda = 1.2 - 1.6 \mu\text{m}$ ,  $A_\lambda$  increases if in the numerical model  $r_{\text{back}}$  is reduced or  $\Delta\phi$  is increased. Both parameters can be varied independently and they are to some degree exchangeable, at least for  $\lambda = 1.2 - 1.6 \mu\text{m}$ . Burgers [10], however, points out that the proper combination of  $r_{\text{back}}$  and  $\Delta\phi$  can be found by closer inspection of  $A_\lambda$  in the *near* infrared region ( $\lambda = 1.0 - 1.2 \mu\text{m}$ ). This wavelength region is characterised by a strong decrease in  $A_\lambda$  because the wafer becomes more and more transparent with increasing wavelength. Four curves of  $A_\lambda$ , that all fit the experimental data for  $\lambda = 1.2 - 1.6 \mu\text{m}$ , clearly deviate in the near infrared region, as shown in the right panel of figure 3.7. As observed by Burgers, a larger  $\Delta\phi$  results in an increase of  $A_\lambda$  in the 'slope'. Using a least squares fit, the combinations that best fits the measured  $A_\lambda$  was found. An excellent fit was found for  $r_{\text{back}} = 0.78$  and  $\Delta\phi = 12^\circ$ . This indicates that this particular alloyed Al back contact can be described using Phong's model and this combination of optical back contact parameters  $r_{\text{back}}$  and  $\Delta\phi$ .

In section 3.2.3 it was shown that a sharp Si/Al interface is highly reflective ( $r = 0.92$ ). An alloyed Al back contact was expected to be less reflective because of free-carrier absorption in the  $p^+$  layer and the optical properties of the Si/Al alloy. Not taking into account the effects of roughness on  $r_{\text{back}}$  it was estimated that  $r_{\text{back}} = 0.83$ . This theoretical estimate turns out to be close to the value found in the measurement ( $r_{\text{back}} = 0.78$ ). This indicates that the relatively low value of  $r_{\text{back}}$  can be explained to a large extent by the free-carrier absorption in the  $p^+$  layer and the optical properties of the Si/Al alloy.

Burgers [10] also reports  $r_{\text{back}} = 0.78$  for an alloyed aluminium back contact. However, he finds a more diffuse reflection,  $\Delta\phi = 45^\circ$ . Note that  $\Delta\phi$  is determined by the roughness of the back interface. This may be affected by the state of the back surface of the wafer (polished or textured) before alloying. Also the alloying temperature and time may affect this roughness. Nonetheless it can be concluded that  $r_{\text{back}} = 0.78$  seems to be a very representative reflection coefficient for Al alloyed back contacts.



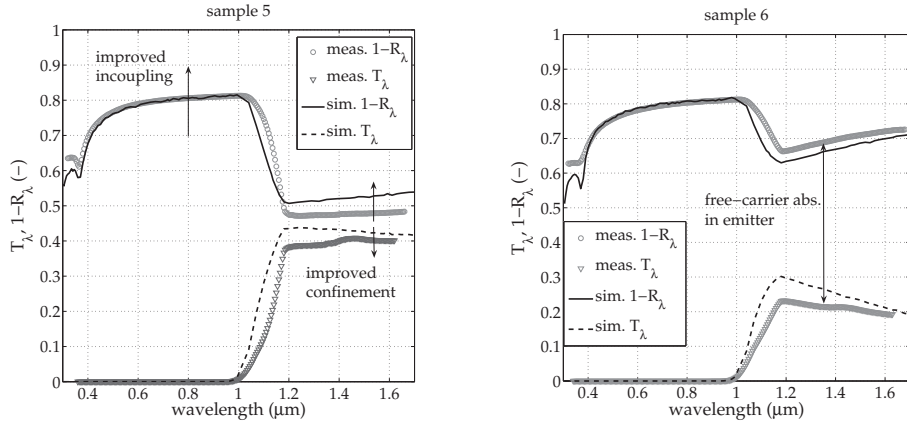


**Figure 3.8:** Measured and simulated  $1 - R_\lambda$  and  $T_\lambda$  as a function of  $\lambda$  for a textured wafer (sample 5, left) and for a wafer with both texture and an emitter (sample 6, right).

### 3.3.5 Surface texture

Samples 5 to 8 have textured surfaces. The effect of this texture is again investigated by spectral reflection and transmission measurements. The results are compared with results obtained by simulation. Unless stated otherwise, the textured surfaces at the front and back of the wafer are represented in the numerical model by parabolic profiles having a steepness of  $41^\circ$  and  $32^\circ$ , respectively. These values were derived from optical experiments as indicated in section 3.2.2. Emitter, anti-reflective (AR) coating and back contact will be introduced one by one.

#### Bare textured wafer (sample 5)

Sample 5 is a bare textured wafer, without emitter, AR-coating or back contact. When the measured spectral reflection and transmission factors (left panel of figure 3.8) are compared to those of the bare polished sample (sample 1 shown in the left panel of figure 3.6), the two effects of texture can be seen. Firstly, in the opaque regime ( $\lambda < 1.0 \mu\text{m}$ )  $R_\lambda$  is reduced as a result of improved incoupling (as indicated). Secondly, in the transparent regime ( $\lambda > 1.2 \mu\text{m}$ )  $A_\lambda$  has increased as a result of the increased path-length caused by the improved optical confinement (indicated as well).

It can be seen that both effects of texture, i.e. improved incoupling and optical confinement, are also found numerically. If texture is represented by a different profile, such as a zigzag profile, then there is less agreement between model and measurement (not shown). This confirms that besides the steepness, the shape of the texture profile is important as well.

**Emitter (sample 6)**

Sample 6 is identical to sample 5 with a phosphorous emitter with a sheet resistance of  $62 \Omega_{\square}$  added. From the optical measurement results (right panel of figure 3.8) it can be seen that for  $\lambda < 1.0 \mu\text{m}$  there is no difference with the previous sample. However, for  $\lambda > 1.2 \mu\text{m}$ ,  $A_{\lambda}$  has increased tremendously because of free-carrier absorption in the emitter (indicated by the arrow). Note that though this absorption mechanism increases the absorption in the active area of the solar cell, the electrical efficiency does not increase since no additional electron-hole pairs are generated.

Similar to the experiments, the model results show that the addition of an emitter results in a large increase in  $A_{\lambda}$  for  $\lambda > 1.2 \mu\text{m}$ . Because the textured surfaces trap light for many passes, the effect of free-carrier absorption has increased drastically (compare sample 2 in the right panel of figure 3.6 and sample 6 in right panel of figure 3.8).

**Anti-reflective coating (sample 7)**

Sample 7 is identical to sample 6, except that an  $\text{Si}_3\text{N}_4$  AR-coating was added to the front. From the experimental results shown in the left panel of figure 3.9 it can be seen that for  $\lambda \approx 0.7 \mu\text{m}$  the coating reduces  $R_{\lambda}$  to very low values (the first order reflection minimum is indicated). This is a well known interference effect exploited by AR-coatings. This effect is modelled with a coating thickness of 84 nm and good agreement is found. There is a small deviation between the numerical and experimental  $R_{\lambda}$  for  $\lambda \approx 0.4 \mu\text{m}$ . This deviation is partly caused by the optical effect of the high doping concentration in the emitter already observed for samples 2 and 6.

The deviation may also be partly caused by the fact that for  $\lambda \approx 0.4 \mu\text{m}$  the optical properties of the  $\text{Si}_3\text{N}_4$  AR-coating in this particular sample deviate from the optical properties used in the numerical model. The  $\text{Si}_3\text{N}_4$  coating used in sample 7 was produced by means of plasma enhanced chemical vapour deposition (PECVD) and also in the numerical model the optical properties of  $\text{Si}_3\text{N}_4$  deposited by PECVD are used. These optical properties were provided by Hoex [56]. However, a number of properties of the coating are influenced by the deposition conditions [57]. Often a  $\text{Si}_3\text{N}_4$  coating with better passivating properties is obtained at the cost of a higher parasitic absorption of ultraviolet irradiance [57]. The data used in the numerical model correspond to a coating having relatively low parasitic absorption, while in the coating used in sample 7, the parasitic absorption is apparently somewhat higher.

**Back contact (sample 8)**

Sample 8 is similar to sample 7, but with an alloyed aluminium back contact added. This back contact is opaque, so  $T_{\lambda} = 0$  and only  $A_{\lambda} = 1 - R_{\lambda}$  is shown in the right panel of figure 3.9. Irradiance with  $\lambda < 1.0 \mu\text{m}$  does not reach the back-contact, so that part of the graph is similar to the graph of sample 7 without back-contact.

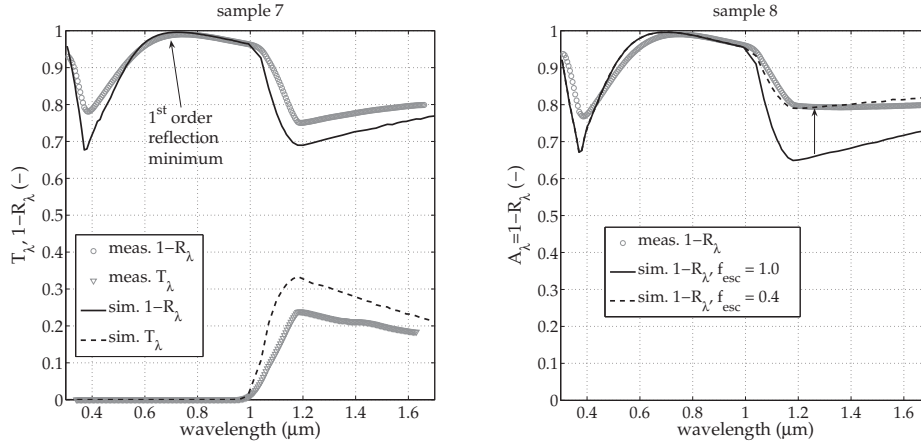


**Figure 3.9:** Measured and simulated  $1 - R_\lambda$  and  $T_\lambda$  as a function of  $\lambda$  for a textured wafer with emitter and  $\text{Si}_3\text{N}_4$  AR-coating (sample 7, left) and with aluminium alloyed back contact (sample 8, right).

The focus here will be on the remaining part of the graph. It can be seen from the measurement of sample 8 that  $A_\lambda = 0.80$  for  $\lambda > 1.2 \mu\text{m}$ .

Since the textured and AR-coated front surface of sample 8 is identical to the one of sample 7, this front surface was modelled in the same way, i.e. a parabolic texture profile ( $\gamma = 41^\circ$ ) with a  $\text{Si}_3\text{N}_4$  coating ( $d = 84 \text{ nm}$ ). The alloyed Al back contact is modelled in the same way as the alloyed Al back contact of the polished wafer (sample 4), i.e. using Phong's model with the parameters  $r_{\text{back}} = 0.78$  and  $\Delta\phi = 12^\circ$ . The results of this simulation are shown as the solid line in the right panel of figure 3.9. As can be seen, the model gives  $A_\lambda = 0.65$  (at  $\lambda = 1.2 \mu\text{m}$ ) and  $A_\lambda = 0.75$  (at  $\lambda = 1.7 \mu\text{m}$ ), which is 0.05-0.15 below the measured value. Apparently, in the sample light is confined better than the model predicts.

To bring the model results into agreement with the measurements one could argue that reflection by the back contact should be modelled more diffuse, i.e.  $\Delta\phi$  should be increased in the model. This was tested and as expected this improves optical confinement somewhat. But even the assumption of a perfectly diffuse reflecting back contact ( $\Delta\phi = 60^\circ$ ) raises  $A_\lambda$  only to 0.70-0.80, which is still below the measured value.

One could also argue that the reflection coefficient used in the model is too high. Reducing  $r_{\text{back}}$  increases absorption in the back contact and increases  $A_\lambda$  for  $\lambda > 1.2 \mu\text{m}$ . However, to reach the measured value ( $A_\lambda = 0.80$ ), a very low back contact reflection coefficient has to be assumed, i.e.  $r_{\text{back}} = 0.45$ . Since the alloyed Al back contact of sample 4 was shown to have  $r_{\text{back}} = 0.78$ , the much lower value for this sample does not seem to be realistic.

Alternatively, it could be argued that the description of the back contact in terms

of Phong's model (described in section 2.5.2) should be replaced by a description in terms of a texture (as described in section 2.5.3). After all, a textured wafer is used and some texture is known to be present at the backside of the wafer before the back contact is added. Possibly after alloying the aluminium back contact, the reflection by the back contact should still be described using the texture model as was done for samples 5, 6 and 7. As shown in section 2.7, the mathematical description of reflection by the back contact in terms of a texture of moderate steepness and a description using Phong's model can give similar results. Also when simulating sample 8 it was found that Phong's model and the texture model are to some extent equivalent when used to model the back contact. This was explained in more detail in section 2.7. However, describing the back contact in terms of a texture does not bring the numerical results into closer agreement with the experimental results.

It appears that numerical modifications of the optical back contact parameters alone cannot bring the degree of optical confinement into agreement with the degree of optical confinement found experimentally. However, the front surface of the wafer also affects the degree of optical confinement. In section 2.6 it was described that when considering optical confinement by the textured front surface of the wafer, there is a significant difference between a two-dimensional (2D) and a three-dimensional (3D) description. As described in section 2.6, in the numerical model, which is essentially 2D, an escape factor  $f_{\text{esc}}$  was introduced to compensate for 3D effects in light trapping. This is a reduction factor (between 0 and 1) for the amount of light that escapes the wafer at the front. Up till now this 3D correction was not used (i.e.  $f_{\text{esc}} = 1$ ). However, for the sample considered here (sample 8) light trapping between the textured front and alloyed Al back is very efficient and 3D effects become important. To be able to describe this effect numerically the 3D correction is used by reducing the  $f_{\text{esc}}$  in the optical model.

If the original back contact description (Phong's model with  $r_{\text{back}} = 0.78$  and  $\Delta\phi = 12^\circ$ ) is used in combination with an escape factor of 0.4 for the front surface, a very good agreement is found. This result is shown as the dashed line in the right panel of figure 3.9. Based on equation 2.35, a somewhat lower escape factor of approximately 0.23 is to be expected for light trapped in a c-Si wafer (see section 2.6). However, this is a rough estimate based on the assumption of a uniform angular distribution of irradiance. Furthermore, in reality the escape factor can be affected by additional parameters, such as the exact profile of the surface texture. Apparently for this particular configuration, using an escape factor of 0.4 in the numerical model is sufficient to obtain a degree of optical confinement comparable to the degree of confinement found in sample 8.

Light trapping is essentially a 3D effect. The 2D model used in this thesis is quite successful in describing light trapping if a correction factor (escape factor  $f_{\text{esc}}$ ) is introduced. However, this extra parameter is not known a priori and has to be derived by fitting the numerical results to the experimental results. Note that in textured

samples 5, 6 and 7 some 3D effects may occur. Not having made a small correction in the simulations of these samples may explain the observed small deviation between experimental and numerical results for  $\lambda > 1.0\mu\text{m}$  (see figure 3.8 and the left panel of 3.9). However, the effect of  $f_{\text{esc}}$  will of course be most prominent in sample 8, in which the combination of texture with the diffusely reflecting back contact leads to effective light trapping.

### 3.3.6 Comparison of experimental and numerical results

In figures 3.6 to 3.9 the *spectral* absorption factors  $A_\lambda$  determined experimentally and numerically, were shown for samples 1 to 8. By averaging  $A_\lambda$  over the AM1.5 solar spectrum, the (AM1.5) absorption factor  $A$  is obtained (see equation 1.1). In table 3.2 an overview is given of both the absorption factor derived from the experimental results and the absorption factor derived from the numerical results. It can be seen that the absorption factor of a bare polished wafer (sample 1) is measured to be only 49.5%. Because of reduction of reflective losses (by texture, AR-coating and light trapping) and by additional absorption (in emitter and back contact), the absorption factor increases to as much as 90.2% for sample 8. This is a complete cell except from front contact metallisation grid and encapsulation.

The numerical model is based on the laws of (geometrical) optics. The textured front surface of the wafer is modelled using a texture model. In this model texture was represented by a parabolic profile and ray-tracing is used to describe the improved incoupling and scattering of reflected and refracted light. Phong's model for diffuse reflection is used as an effective model for describing light scattering by the alloyed Al back contact. For  $\lambda > 1.0\ \mu\text{m}$  trapping of irradiance inside the wafer is an important effect, of which the three-dimensional nature is taken into account using an escape factor.

Experimentally the spectral reflection factor  $R_\lambda$  and transmission factor  $T_\lambda$  can be determined very accurately, having an inaccuracy of only 1% absolute. The spectral absorption factor  $A_\lambda = 1 - R_\lambda - T_\lambda$  is obtained by combining  $R_\lambda$  and  $T_\lambda$  and therefore has an inaccuracy of 2%. In case of an opaque back contact this inaccuracy is 1%, because in that case no transmission measurement is required.

It was demonstrated that the optical model captures the important optical effects encountered in c-Si solar cells. However, some simplifying assumptions were necessary, e.g. representing the textured surface by a parabolic profile. This may have introduced some deviations with respect to the experimental results. A deviation of a second kind may be introduced by the fact that some of the required numerical input parameters are not known with sufficient accuracy. These parameters were determined by inverse modelling, i.e. fitting the numerical results to the experimental results. For example the reflective properties of the alloyed aluminium back contact ( $r_{\text{back}}$  and  $\Delta\phi$ ) were determined using the experimental results of sample 4. Also the required escape factor was determined using the results of sample 8.

**Table 3.2:** The numerical and the corresponding measured AM1.5 absorption factor A. For numerical results marked with \*, an escape factor of 0.4 was used.

nr	description	$A_{\text{num}}(\%)$	$A_{\text{exp}}(\%)$
1	bare polished c-Si wafer	49.2	$49.5 \pm 2.0$
2	#1 + emitter ( $47 \Omega_{\square}$ )	49.9	$51.7 \pm 2.0$
3	#1 + evaporated back contact	51.7	$52.7 \pm 1.0$
4	#1 + alloyed back contact	55.9	$55.9 \pm 1.0$
5	#1 + texture (acid etch)	63.3	$64.1 \pm 2.0$
6	#5 + emitter ( $62 \Omega_{\square}$ )	69.6	$71.4 \pm 2.0$
7	#6 + AR-coating ( $\text{Si}_3\text{N}_4$ )	82.7	$85.8 \pm 2.0$
8	#7 + alloyed back contact (Al)	87.8	$90.2 \pm 1.0$
		90.0*	

The overall result of this approach is that the AM1.5 absorption factors determined numerically deviate only 3% or less from the AM1.5 absorption factors determined experimentally. For sample 8, which is a close representation of a complete c-Si solar cell, after compensating for the 3D effects by means of an escape factor, the deviation is even reduced to less than 1%. The remaining deviation originates mainly from the blue part of the solar spectrum ( $\lambda \approx 0.38 \mu\text{m}$ ) where the optical properties of heavily doped silicon and of the  $\text{Si}_3\text{N}_4$  coating deviate slightly from the values used in the model. Because in general there is a good agreement between the optical model and experiment it can be concluded that the model is a valid tool for gaining insight in the absorption mechanisms of c-Si solar cells and for studying the effect of cell design parameters on the AM1.5 absorption factor.

### 3.4 Cell design parameters

The cell design described in section 3.3, based on the use of a textured c-Si wafer with an aluminium alloyed back contact, is a frequently used state-of-the-art c-Si solar cell design. The optical model will be used to gain more insight in the relative importance of the different absorption mechanisms in this cell design. It is important to know the influence on the absorption factor of design parameters, such as the steepness of the texture, the sheet resistance of the emitter and the thickness of the wafer.

As was explained in section 3.2.3, the concept of using an alloyed aluminium back contact is less compatible with thinner wafers and will probably not be used any more in the medium term. Therefore the absorption factor of a number of cells with an alternative back contact structure will be studied as well.

The surface area of a c-Si solar cell consist of up to 8% front contact metallisation.

There is a tendency to reduce this metal coverage. First the active area absorption factor is considered and in section 3.4.6 the effect of metal coverage on the absorption factor of the complete cell area is discussed.

### 3.4.1 Reference c-Si solar cell design

In this section the reference c-Si solar cell design is defined that will be used in the analysis of the effect of design parameters on the AM1.5 absorption factor. Because the presence of the encapsulation of a cell will turn out to play an important role, encapsulated solar cells are considered, unless indicated differently. Crystalline silicon cells in a solar module are encapsulated in the following way: glass / EVA / cell / EVA / TPT-foil, where EVA stands for Ethyl Vinyl Acetate, TPT stands for Tedlar®-polyester-Tedlar®. The reference configuration shown in figure 3.10 has a 3 mm low iron content glass cover and a 200  $\mu\text{m}$  EVA layer. The optical properties of EVA were derived from spectral reflection and transmission measurements on a glass/EVA/glass sandwich, prepared for this purpose. The optical properties of the glass used in this sandwich were determined as well. In the simulations low iron content glass developed for solar cell applications (with properties slightly differing from the glass in the sandwich) was used [58].

The solar cell considered here is the textured c-Si solar cell with an alloyed Al back contact. This cell is modelled using the parameters obtained in section 3.3. The texture at the front surface of the c-Si wafer is modelled as a parabolic profile with a steepness of  $41^\circ$ . An anti-reflective coating ( $\text{Si}_3\text{N}_4$ , 84 nm thin) and an emitter ( $R_{\text{sheet}} = 57 \Omega_{\square}$ ) are also present at the front. The alloyed Al back contact is modelled using Phong's model with a reflection coefficient  $r_{\text{back}} = 0.78$  and diffuseness  $\Delta\phi = 12^\circ$ . 3D effects in light trapping are taken into account by means of an escape factor  $f_{\text{esc}} = 0.40$ . Note that because the back contact is opaque the layers behind the cell do not need to be modelled optically.

In figure 3.10 the spectral absorption factor  $A_{\lambda}$  is indicated for each layer in the reference configuration separately. The remaining white area represents  $R_{\lambda}$ . It can be seen that for short-wavelength solar irradiance ( $\lambda < 1.1 \mu\text{m}$ ) the band-to-band absorption is dominant, while for long-wavelength solar irradiance free-carrier absorption in the emitter and absorption by the back contact are dominant. Smaller fractions of the AM1.5 spectrum are absorbed in the glass cover, in EVA and in the AR-coating. Also indicated in the figure are the AM1.5 weighted absorption factors of the individual layers. Note that these values were obtained by averaging the spectral results over the AM1.5 spectrum which has the highest spectral intensity in the visible part of the spectrum (see figure 1.3). The AM1.5 absorption factor for this reference configuration is the sum of all contributions from the individual layers, which amounts to 90.7%. This implies that only 9.3% of the incident solar irradiance is reflected.



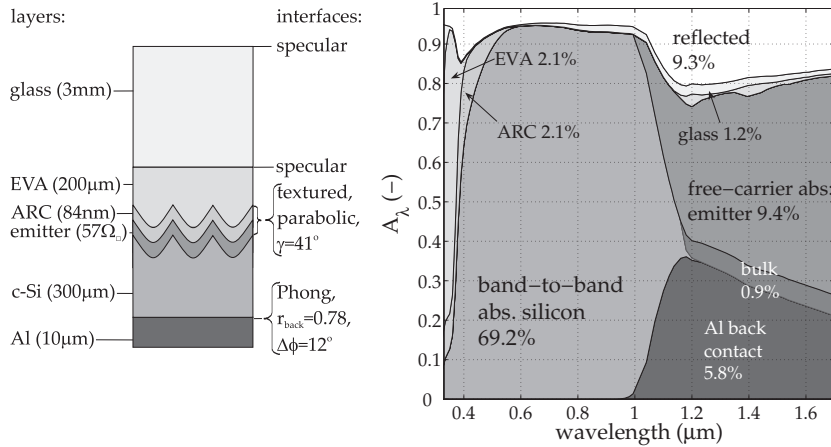


**Figure 3.10:** Area plot of the spectral absorption factor  $A_\lambda$  for each layer of the reference configuration. The AM1.5 absorption factors are also given for each layer separately. The total AM1.5 absorption factor is 90.7%.

### 3.4.2 The influence of texture steepness

In this section the effect of texture steepness on the AM1.5 absorption factor  $A$  is investigated. Etch recipes are being developed with the aim of obtaining a steeper surface texture to further improve incoupling of incident light [14].

Two optical paths exist that lead to improved incoupling of light into the wafer: the direct and the indirect path. In case of the direct path, already mentioned in section 3.2.2, reflected light hits a neighbouring protrusion directly (see also figure 3.3). This direct path is only available in case of steep texture  $\gamma > 25^\circ$ . As pointed out by Hylton [38], for encapsulated cells there is an indirect path as well, illustrated in figure 3.11. Light reflected obliquely by the textured wafer will return to the glass/air interface under an angle larger than the critical angle and will undergo total internal reflection. This also guarantees a second chance of entering the wafer. Note that this indirect path is only available in encapsulated cells, but requires a less steep texture, i.e.  $\gamma > 10^\circ$ .

Steepness  $\gamma$  of the parabolic texture profile at the front of the wafer of the reference configuration was varied numerically. All other cell design parameters remain unchanged. For the case with encapsulation, the effect on  $A$  is shown in figure 3.11 (solid line). If no texture is present ( $\gamma = 0^\circ$ ), reflection losses are high, resulting in a low absorption factor ( $A = 84.9\%$ ). However, if  $\gamma$  increases to above  $10^\circ$ , the indirect path (described above) becomes available and  $A$  starts to increase. For  $\gamma = 10 - 25^\circ$ , there is a strong increase in  $A$  to above 90%. Increasing  $\gamma$  to more than  $25^\circ$  will cause a transition from the indirect to the direct path, but this results in only a small further



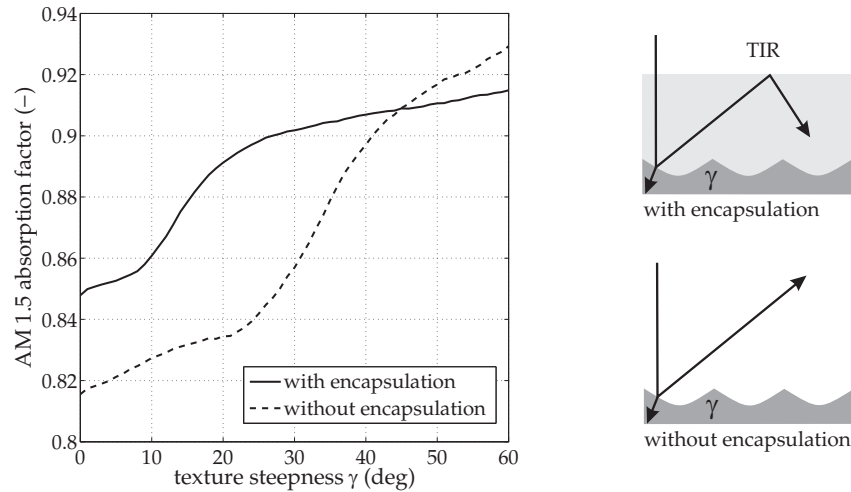


**Figure 3.11:** The AM1.5 absorption factor  $A$  as a function of the steepness  $\gamma$  of the texture at the front of the c-Si wafer for both an encapsulated and unencapsulated configuration. The effect of light trapping by total internal reflection (TIR) inside the encapsulation is shown on the right.

increase of  $A$ .

This is in contrast with a cell which has no encapsulation to trap reflected irradiance (i.e. no indirect path). This case was investigated numerically as well and the results are shown as the dashed line in figure 3.11. As can be seen for  $\gamma = 0^\circ$ ,  $A$  is only 81.6%. This is lower than for the encapsulated cell because no light is absorbed in glass or EVA.  $A$  remains low up to  $\gamma = 25^\circ$  and then increases sharply because the direct path becomes available. The cell without encapsulation has the advantage that there is no glass surface that reflects light. As a result  $A$  increases to above 92% for  $\gamma > 50^\circ$ . So it can be concluded that in general a steeper texture results in higher absorption factor. However, the effectiveness of a certain texture depends very much on the presence of encapsulation.

### 3.4.3 The influence of wafer thickness

As already mentioned in section 1.2.1, the reduction of the wafer thickness is an important tool to reduce the required amount of silicon feedstock and so the cost of the c-Si solar cell. The effect of the reduction of wafer thickness on the AM1.5 absorption factor was investigated numerically. The reference configuration was taken as starting point and the wafer thickness was varied between 20 and 500  $\mu\text{m}$ , keeping all other parameters constant, initially. In the left panel of figure 3.12 the AM1.5 absorption factor  $A$  is plotted as a function of wafer thickness (solid line).

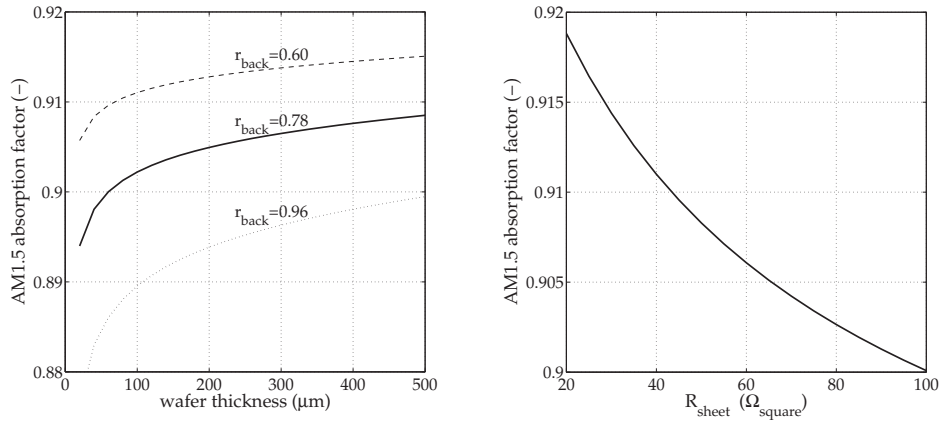


**Figure 3.12:** The AM1.5 absorption factor  $A$  for the encapsulated reference configuration. Left: as a function of wafer thickness (at  $R_{\text{sheet}} = 57 \Omega_{\square}$ ). Right: as a function of emitter sheet resistance (at  $r_{\text{back}} = 0.78$ ).

It can be seen that in case of an alloyed Al back contact ( $r_{\text{back}} = 0.78$ ) a reduction of wafer thickness from 300 to 100  $\mu\text{m}$ , decreases  $A$  by only 0.5%. The modest sensitivity of the absorption factor to variation of wafer thickness is caused by the fact that most irradiance in the solar spectrum (i.e. the part with  $\lambda < 1.0 \mu\text{m}$ ) is absorbed in the first pass through the wafer. It requires at least two passes (one down and one up) to escape the wafer. Only a fraction of the long wavelength irradiance can make two or more passes and potentially escape. The more the wafer thickness is reduced, the larger this fraction becomes. However, because light trapping is very efficient, the amount of irradiance that escapes increases only slightly. A significant decrease of  $A$  will occur only if the wafer is made extremely thin, i.e. thinner than 50  $\mu\text{m}$ .

The effect of wafer thickness was also studied in the cases of a less reflective ( $r_{\text{back}} = 0.60$ ) or a more reflective ( $r_{\text{back}} = 0.95$ ) back contact. It can be seen that the cell with the more reflective back contact is somewhat more sensitive to variations in wafer thickness because more light is reflected by this back contact and has a chance to escape.

#### 3.4.4 The influence of emitter sheet resistance

Most c-Si solar cells produced presently have a sheet resistance of approximately 60  $\Omega_{\square}$  and in the quest for higher electrical efficiencies, there is a tendency to increase this to 80  $\Omega_{\square}$  and higher. Since a significant part of long-wavelength irradiance is absorbed by free-carrier absorption in the emitter, the effect of emitter sheet resistance on the AM1.5 absorption factor  $A$  is investigated. As explained in section 3.2.1, a cell with a higher sheet resistance has a lower areal doping concentration, resulting

in less free-carrier absorption and therefore in a lower AM1.5 absorption factor. The relation between the sheet resistance  $R_{\text{sheet}}$  and the effective emitter thickness  $d_{e,fc}$  used in the model is given by equation 3.5.

In the right panel of figure 3.12 the AM1.5 absorption factor  $A$  is shown as a function of sheet resistance. In case the emitter would be omitted,  $A = 87.9\%$  (not shown). An emitter increases this to between 90.3% (at  $80 \Omega_{\square}$ ) and 91.1% (at  $40 \Omega_{\square}$ ). It can be concluded that it is possible in principle to increase the absorption factor of the c-Si solar cell by reducing the sheet resistance of the emitter. However, because the limited gain in absorption factor will not outweigh the anticipated reduction in electrical efficiency, this does not seem to be a very practical approach.

### 3.4.5 The influence of the back contact configuration

The influence of the back reflection coefficient  $r_{\text{back}}$  and the diffuseness of reflection  $\Delta\phi$  on both the AM1.5 absorption factor  $A$  and the electrical efficiency  $\eta_e$  was studied. Initially this was done for a 300  $\mu\text{m}$  thick wafer with a bulk minority carrier lifetime of 23  $\mu\text{s}$  (corresponding to a diffusion recombination length of about 250  $\mu\text{m}$ ) and an effective rear surface recombination velocity of 1000  $\text{cm/s}$ . As explained in section 3.2.4, in order to determine the electrical efficiency, the optical absorption profiles determined by the optical model were exported to solar cell device model PC1D [30]. The results are shown in figure 3.13. In the left panel the effect on  $A$  is shown. It can be seen that a low  $r_{\text{back}}$  (much absorption in the back contact) and a high  $\Delta\phi$  (efficient light trapping) result in the highest  $A$ . In the right panel the effect on  $\eta_e$  is shown. It can be seen that increasing  $r_{\text{back}}$  from 0.60 (point A) to 0.95 (point C) increases  $\eta_e$  by 0.2%. This is a relatively low sensitivity to  $r_{\text{back}}$  and is caused by the fact that the diffusion recombination length is smaller than the thickness of the wafer.

Therefore the influence of the back reflection coefficient  $r_{\text{back}}$  on the electrical efficiency was studied for several combinations of wafer thickness, bulk minority carrier lifetime and effective rear surface recombination velocity as indicated in table 3.3. Two values of  $\tau_b$  were selected: one of a passivated multicrystalline silicon wafer from the recent past (23  $\mu\text{s}$ ) and one of a very well bulk passivated multicrystalline silicon wafer (100  $\mu\text{s}$ ). Especially in the case of thinner wafers, the effective rear surface recombination velocity will become more important. Also here two values were considered: 1000  $\text{cm/s}$  for an alloyed aluminium back contact [51, 52] and 100  $\text{cm/s}$  for a back surface passivated with an oxide [52]. This value may drop for industrial processes in future because lower values have already been demonstrated at the research stage [57].

As expected (see table 3.3) the influence of the reflectivity  $r_{\text{back}}$  on the cell efficiency becomes larger in case of good material quality and low effective rear surface recombination velocity. In the best case  $\eta_e$  increases by 0.4% if  $r_{\text{back}}$  is increased from 0.60 to 0.95.

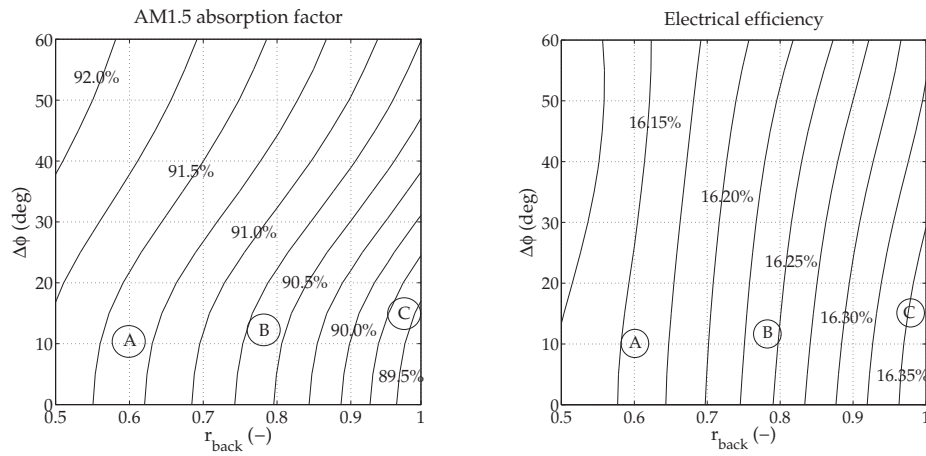


**Figure 3.13:** The AM1.5 absorption factor  $A$  (left) and electrical efficiency (right) for the reference configuration as a function of both back contact reflection coefficient  $r_{\text{back}}$  and diffuseness of reflection  $\Delta\phi$ . The standard alloyed aluminium back contact structure (point B) and an open-back contact structure with a low reflectivity (lower limit) (point A) and the back contact structure with a metal reflector (point C) are indicated.

### 3.4.6 The influence of metal coverage of front contact

Up till now only the active cell area was considered. However, a part of the solar cell can be covered by the front contact grid. So in order to determine the absorption factor of the entire solar cell ( $A_{\text{cell}}$ ) a weighted average is taken of the active (ac) area absorption factor and the front contact grid (gr) area absorption factors,

$$A_{\text{cell}} = a_{\text{ac}}A_{\text{ac}} + a_{\text{gr}}A_{\text{gr}}, \quad (3.8)$$

where  $A$  is the absorption factor and  $a$  is the relative surface area. Here the absorption factor of the encapsulated reference configuration is taken as active area absorption factor, i.e.  $A_{\text{ac}} = 90.7\%$ . The spectral absorption factor of the screen printed silver front metallisation is used as grid area absorption factor  $A_{\text{gr}}$ . Because, on a microscopic scale screen printed silver is porous, its optical properties deviate from the bulk optical properties of silver. Therefore the spectral reflection factor of screen printed silver was measured by Burgers [59]. By integrating these results over the AM1.5 solar spectrum, it was found that  $A_{\text{gr}} = 22.7\%$ . In case of a standard H-pattern grid, i.e. parallel fingers connected by two or three busbars, the relative grid area  $a_{\text{gr}}$  is approximately 8.0%. As a result  $A_{\text{cell}}$  is reduced to 85.3%.

Because any cell area covered by the front contact grid does not generate electricity, there is a tendency to reduce the relative grid area  $a_{\text{gr}}$ . In Pin-Up Module (PUM) cells [11] the surface area of the front grid is reduced significantly because no busbars are required. In these cells current is fed through a limited number of holes

**Table 3.3:** The active area electrical cell efficiency for a low ( $r_{\text{back}} = 0.60$ ) and a highly reflective ( $r_{\text{back}} = 0.95$ ) back contact. The comparison is made for various combinations of wafer thickness  $d$ , bulk minority carrier lifetime  $\tau_b$  and effective rear surface recombination velocity  $S_{\text{eff}}$ .

$d(\mu\text{m})$	$\tau_b(\mu\text{s})$	$S_{\text{eff}}(\text{cm/s})$	$\eta_e(\%)$	
			$r_{\text{back}} = 0.60$	$r_{\text{back}} = 0.95$
300	23	1000	16.16	16.35
300	100	1000	16.90	17.13
300	100	100	17.70	18.19
100	23	1000	15.95	16.30
100	100	1000	16.24	16.61
100	100	100	17.44	17.87

**Table 3.4:** An overview of the relative grid coverage  $a_{\text{gr}}$  for different encapsulated c-Si cells and the resulting cell absorption factor  $A_{\text{cell}}$ . In all cases  $r_{\text{back}} = 0.78$  and  $\Delta\phi = 12^\circ$  is assumed.

	$a_{\text{gr}}$	$A_{\text{cell}}$
H-pattern	8.0%	85.3%
PUM	4.5%	87.6%
EWT	0.0%	90.7%

in the cell and collected at the back of the cells. Since the grid coverage is reduced to only 4.5%,  $A_{\text{cell}}$  is increased to 87.6%. Reduction of  $a_{\text{gr}}$  is pushed to extremes in Emitter Wrap Through (EWT) cells [13]. Because the emitter is fed through the wafer at a large number of spots no metal front grid is required at all and as a result  $A_{\text{cell}} = A_{\text{ac}} = 90.7\%$ . An overview is given in table 3.4.

### 3.5 Discussion

In the previous section the sensitivity of the AM1.5 absorption factor to individual cell design parameters was studied. In the light of the ongoing technological solar cell developments, interesting cell designs are considered in this section. These technological developments are mainly driven by a quest for higher electrical efficiency and a reduction in cost. For photovoltaic/thermal (PVT) applications a high absorption factor is desirable as well, but this is not yet a driver because the PVT market is still extremely small compared to the PV market. Encapsulated cells are considered here. The optical model described in chapter 2 is again used to determine their AM1.5 absorption factor, both on active area and on cell level. By exporting the op-

**Table 3.5:** An overview of the different textured c-Si cell concepts and the resulting cell absorption factor  $A_{\text{cell}}$  and electrical efficiency  $\eta_{e,\text{cell}}$  for encapsulated cells. Cell marked with '1' have no texture, cells marked with '2' have an AR-coating on the glass.

cell	front contact	$d$ ( $\mu\text{m}$ )	$r_{\text{back}}$ (-)	$A_{\text{act}}$ (%)	$A_{\text{cell}}$ (%)	$\tau_e$ ( $\mu\text{s}$ )	$S_{\text{eff}}$ (cm/s)	$\eta_{e,\text{act}}$ (%)	$\eta_{e,\text{cell}}$ (%)	$A_{\text{eff}}$ (%)
A <sup>1</sup>	H-pat.	300	0.78	84.4	<b>79.8</b>	23	1000	15.76	<b>14.50</b>	65.3
B	H-pat.	300	0.78	90.7	<b>85.3</b>	23	1000	16.24	<b>14.94</b>	70.4
C	PUM	300	0.78	90.7	<b>87.6</b>	23	1000	16.24	<b>15.51</b>	72.1
D	PUM	200	0.78	90.5	<b>87.4</b>	23	1000	16.25	<b>15.52</b>	71.9
E	PUM	100	0.78	90.3	<b>87.3</b>	23	1000	16.30	<b>15.57</b>	71.7
F	PUM	300	0.95	89.0	<b>86.0</b>	23	1000	16.34	<b>15.60</b>	70.4
G	PUM	100	0.60	91.5	<b>88.4</b>	100	1000	17.44	<b>16.66</b>	71.7
H	PUM	100	0.78	90.3	<b>87.3</b>	100	1000	17.64	<b>16.85</b>	70.5
I	PUM	100	0.95	89.0	<b>85.0</b>	100	100	17.87	<b>17.07</b>	67.9
J	EWT	300	0.78	90.7	<b>90.7</b>	23	100	16.24	<b>16.24</b>	74.5
K	EWT	200	0.78	90.5	<b>90.5</b>	23	100	16.25	<b>16.25</b>	74.3
L	EWT	100	0.78	90.3	<b>90.3</b>	23	100	16.30	<b>16.30</b>	74.0
M	EWT	100	0.60	91.5	<b>91.5</b>	100	100	17.44	<b>17.44</b>	74.1
N	EWT	100	0.78	90.3	<b>90.3</b>	100	100	17.64	<b>17.64</b>	72.7
O	EWT	100	0.95	89.0	<b>89.0</b>	100	100	17.87	<b>17.87</b>	71.1
P <sup>2</sup>	EWT	100	0.60	93.8	<b>93.8</b>	100	100	17.99	<b>17.99</b>	75.9
Q <sup>2</sup>	EWT	100	0.78	92.9	<b>92.9</b>	100	100	18.22	<b>18.22</b>	74.7
R <sup>2</sup>	EWT	100	0.95	91.6	<b>91.6</b>	100	100	18.66	<b>18.66</b>	72.9

tical absorption profiles to PC1D, the electrical efficiency is determined as well. An overview of the cell designs considered and the corresponding design parameters is given in table 3.5.

All cells produced on industrial scale nowadays are textured. It can be seen that texturisation has significantly increased both the electrical cell efficiency and the absorption factor (compare H-pattern cells A and B). The currently ongoing reduction in front contact grid coverage is increasing both the electrical efficiency and absorption factor further (compare cell the H-pattern cell B, the PUM cell C and the EWT cell J). The reduction of wafer thickness only has a minor effect (compare the PUM cells C, D and E or the EWT cells J, K and L having various thicknesses, at  $\tau_b = 23 \mu\text{s}$  used in these cases). However, the absorption factor and electrical efficiency of thin cells become more sensitive to variations of the back contact parameters  $r_{\text{back}}$  and  $S_{\text{eff}}$ .

It is expected that besides the alloyed Al back contact (with  $r_{\text{back}} = 0.78$ ), other back contact configurations will become important in the near future. Two types

of back contact with improved surface passivation were considered in section 3.4.5. One type is the back contact structure with a passivating oxide and a metallic reflector, having a high reflection coefficient ( $r_{\text{back}} = 0.95$ ). The other type is the back contact structure with a passivating oxide and an open-back contact structure. In this analysis it is assumed that  $r_{\text{back}} = 0.60$ . This value needs to be regarded as a minimum, because attempts will be made to improve this reflection coefficient, among others by enhancing the reflectivity of white Tedlar<sup>®</sup>. It can be seen that a high  $r_{\text{back}}$  is beneficial for the electrical efficiency, but reduces the absorption factor somewhat (compare the PUM cells G, H and I or the EWT cells M, N and O having various  $r_{\text{back}}$ ).

Finally the effect of an additional anti-reflective (AR) coating on top of the glass is investigated. The AR-coating considered here is a single layer porous SiO<sub>2</sub> coating, deposited by a dip-coating technique [60]. It can be seen that because reflection losses are reduced even further, both the absorption factor and the electrical efficiency are increased significantly. In case  $r_{\text{back}} = 0.95$  (cell R) the highest electrical cell efficiency is reached ( $\eta_{\text{e,cell}} = 18.66\%$ ) and in case  $r_{\text{back}} = 0.60$  (cell P) the highest absorption factor is reached ( $A_{\text{cell}} = 93.8\%$ ). Note that this is an extremely high absorption factor, even approaching the absorption factor of the black absorber in a solar thermal collector with an absorption factor of 95%.

The final column of table 3.5 shows the effective absorption factor  $A_{\text{eff}}$  which is defined as

$$A_{\text{eff}} = A_{\text{cell}} - \eta_{\text{e,cell}}, \quad (3.9)$$

and represents the fraction of incident irradiance that is absorbed by the cell, but not converted into electricity. Note that  $\eta_{\text{e,cell}}$  is the electrical cell efficiency at Standard Test Conditions, i.e. at a cell temperature of 25° and under the global AM1.5 solar spectrum with an intensity of 1000 W/m<sup>2</sup>.  $A_{\text{eff}}$  is the fraction of incident irradiance that is converted into heat. This is an important parameter in PVT applications. It can be seen that  $A_{\text{eff}}$  varies from 65.3% for the classical H-pattern cell without texture (cell A) to 72.9-75.9% for the modern textured EWT cells with an AR coating on the glass (cells P, Q and R). So the reasoning that if the cell's electrical efficiency is increased there will be less energy available in the form of heat is not always true. In general it can be said that measures taken to reduce reflection losses (i.e. texturing, reduction of front contact metallisation and application of AR coatings) even *increase*  $A_{\text{eff}}$  because in absolute terms  $A_{\text{cell}}$  is increased even more than  $\eta_{\text{e,cell}}$  (see equation 3.9). This can be understood because the extra photons that are absorbed are partly converted into electricity and partly into heat. However, if the cell's efficiency is increased by reducing recombination or by applying a more reflective back contact, then it is true that  $A_{\text{eff}}$  is reduced. This can happen in two ways: by a reduction of  $A_{\text{cell}}$  and/or by an increase in  $\eta_{\text{e,cell}}$ .

## 3.6 Conclusion

The numerical model described in chapter 2 was validated by comparing the numerical results to measured spectral reflection and transmission factors over a broad wavelength range. All important effects are captured by the optical model. Improved incoupling by texture can be described very well by the two-dimensional texture model and reflection by an alloyed Al back contact can be described very well by Phong's model for diffuse reflection. In the two-dimensional model a so-called escape factor is required to model trapping of sub-bandgap irradiance in the silicon wafer correctly.

Most irradiance is absorbed by band-to-band absorption in the c-Si wafer. The effect of free-carrier absorption in the very thin emitter turned out to be an important absorption mechanism for long-wavelength solar irradiance. Some additional absorption occurs in glass, EVA, AR-coating and back contact. As a result the AM1.5 absorption factor of the active area of today's c-Si solar cell is quite high, i.e. 90.7%. The sensitivity of this number to variations in texture steepness, wafer thickness, emitter strength and back contact reflection parameters was quantified. Trapping of irradiance inside the encapsulation turned out to be important. This implies that when analysing the performance of a certain texture, the effect of encapsulation should be taken into account.

The AM1.5 absorption factor of c-Si solar cells was also investigated in light of their ongoing improvement in the quest to achieve a higher electrical efficiency at lower cost. In photovoltaic/thermal applications a high *effective* absorption factor is desirable to obtain a high thermal efficiency. It was found that applying a more reflective back contact increases the electrical efficiency but reduces the effective absorption factor. However, measures taken to reduce reflection losses at the front of the cell (i.e. texturing, reduction of front contact metallisation and application of AR coatings) not only increase the electrical efficiency, but also increase the effective absorption factor. The overall trend is an increase in effective absorption factor towards values of 73 to 76% for textured EWT cells with an AR-coating on the glass. A range is given here because different back contact designs are considered. It is unlikely that the effective absorption factor will increase beyond the maximum value of 76% because this is only possible if either the reflective losses or the electrical efficiency is reduced. A further reduction of reflective losses is hardly possible because an AM1.5 absorption factor of 94% has been reached. This is approaching the AM1.5 absorption factor of the spectrally selective absorber used in a solar thermal collector, being 95%.





# The absorption factor of thin-film solar cells

## 4.1 Introduction

As already mentioned in the introduction (section 1.2.2), besides the currently dominant c-Si wafer based solar cell technology, various thin-film solar cell technologies exist. At present the market share of the thin-film solar cell technologies is less than 10%, but might grow to 20% by 2010 and to 30% in the long term [61]. The inherent advantage of these thin-film solar cell technologies is that a far less amount of expensive semiconductor material needs to be used. This implies that on the long run thin-film solar cell technologies have the potential to extend the learning curve concerning cost reduction beyond the point that may be reached by c-Si solar cell technology [62]. A condition to do so will probably be that the efficiencies are sufficiently high.

The thermal efficiency of a photovoltaic/thermal (PVT) collector with thin-film solar cells depends to a large extent on the AM1.5 absorption factor of these cells. The absorption of sub-bandgap irradiance in thin-film solar cells is relevant for the overall AM1.5 absorption factor, but was not studied in sufficient detail so far. The goal of the work described in this chapter is to gain insight in the absorption mechanisms occurring in thin-film solar cells and to determine the AM1.5 absorption factor for various types of thin-film solar cells. This analysis is performed using the optical model described in chapter 2.

In section 4.2 the different types of thin-film solar cells are introduced and the optical properties of the materials used are summarised. In section 4.3 the numerical model is validated by comparing the numerical results to results of optical measure-

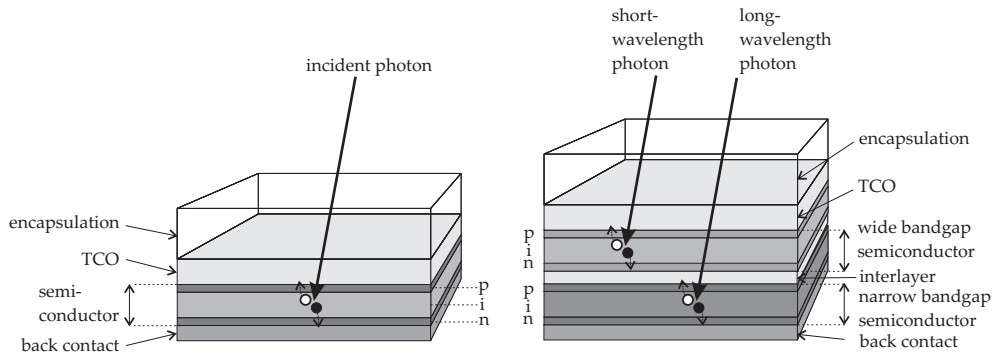


**Figure 4.1:** An example of a single junction thin-film solar cell (left) and a tandem thin-film solar cell (right).

ments carried out on a set of amorphous silicon thin-film samples. In section 4.4 the numerical model is used to determine the absorption factor of other types of thin-film cells, such as the micromorph silicon tandem cell and the copper indium gallium diselenide cell. In section 4.5 the results are discussed and finally in section 4.6 some general conclusions are presented.

## 4.2 Modelling thin-film solar cells

The structure of a single junction thin-film solar cell is indicated in the left panel of figure 4.1. This thin-film solar cell has an active part of typically less than a few micrometres thick, consisting of one or more semiconductor materials. Semiconductor materials frequently used in thin-film solar cells are amorphous silicon (a-Si), an amorphous silicon/germanium (a-Si/Ge) alloy, micro crystalline silicon ( $\mu\text{c-Si}$ ), copper indium gallium diselenide (CIGS), cadmium sulphide (CdS) and cadmium telluride (CdTe). As indicated, the electrons and holes generated in the semiconductor are collected as good as possible by the back contact and the transparent conductive oxide (TCO) respectively.

Besides the single junction solar cell, multi-junction thin-film solar cells have been developed. In the right panel of figure 4.1, the structure of a so-called tandem solar cell is shown. This tandem cell has two semiconductor layers. Generally two different semiconductor materials are used, each one characterised by a different bandgap energy  $E_g$ . As indicated in the figure, the semiconductor with the larger bandgap  $E_{g1}$  is used as top layer and the semiconductor with the smaller bandgap  $E_{g2}$  ( $E_{g2} < E_{g1}$ ) is used as bottom layer. In this way, short wavelength photons with a photon energy  $E_{ph} > E_{g1}$ , are mainly absorbed in the top layer. The longer wavelength photons with  $E_{g2} < E_{ph} < E_{g1}$  are transmitted by this top layer and mainly absorbed by the bottom layer. Because this tandem cell is a series connection of two solar cells

utilising different parts of the solar spectrum, a higher electrical efficiency can be obtained.

Because thin-film solar cells can consist of many layers, they are very complex optically. Also the fact that layer thicknesses or interface roughnesses can have dimensions comparable to or smaller than the wavelength of solar irradiance, makes it very challenging to model the optical behaviour of thin-film solar cells accurately. Nonetheless, optical models for thin-film solar cells have been developed to determine the absorption profile for calculating the electrical performance [6, 33, 63, 64]. However, because sub-bandgap solar irradiance does not play a role in the generation of electricity, the absorption of this part of the solar spectrum has not yet been studied extensively.

The optical model developed and described in chapter 2 is very suitable to analyse optical systems containing many layers. Because the optical model allows each interface to be modelled individually, the model is flexible enough to capture the complex optical behaviour of thin-film solar cells. The optical model has been validated and used for c-Si cells in chapter 3. The same approach is used for thin-film solar cells as well. However, some specific aspects being relevant specifically for thin-film solar cells, will be highlighted first. In section 4.2.1 the optical properties of various semiconductor materials used in thin-film solar cells are summarised. Section 4.2.2 is devoted to the textured transparent conductive oxide. Both the optical properties and the way of modelling are presented.

### 4.2.1 Optical properties of semiconductor materials used in thin-film solar cells

#### Amorphous silicon

Among the commercially available thin-film solar cell technologies, the amorphous silicon (a-Si) technology is the most important one in terms of production and installation [8]. The word ‘amorphous’ indicates that, as opposed to c-Si, the atoms in a-Si show no long range order. Because of the different arrangement of atoms, the electrical and optical properties of a-Si are very different from those of c-Si. For example the dangling bonds, present in high concentrations in a-Si, act as recombination centres, reducing the minority carrier lifetime. In solar cell applications *hydrogenated* amorphous silicon (a-Si:H) is used because hydrogen atoms passivate the dangling bonds. Note that often the term ‘a-Si’ is used when ‘a-Si:H’ is meant, also in this thesis.

In the left panel of figure 4.2 the refractive index  $n$  and in the right panel the absorption coefficient  $\alpha$  of a-Si are shown that are used in the optical model. a-Si has a high bandgap energy of 1.7 eV (slightly dependent on the hydrogen content) [6] corresponding to a small threshold wavelength of 730 nm. It can be seen from the rapidly decreasing absorption coefficient, that irradiance with a wavelength larger

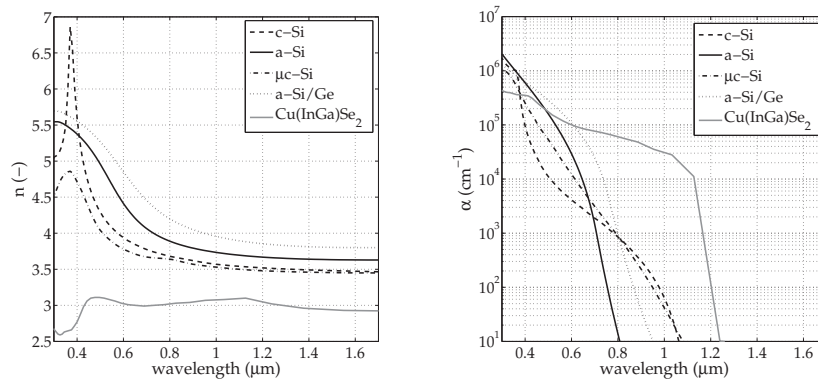


**Figure 4.2:** The refractive index  $n$  (left) and absorption coefficient  $\alpha$  (right) of the semiconductors used in thin-film solar cells (a-Si [65],  $\mu\text{c-Si}$  [65], a-Si/Ge alloy [65], and  $\text{Cu(InGa)Se}_2$  [66]). The properties of c-Si [47] are given for comparison.

than this threshold wavelength is hardly absorbed. Because of the relatively large bandgap and the corresponding low threshold wavelength, a relatively large part of the AM1.5 solar spectrum is not absorbed by a-Si.

#### Amorphous silicon/germanium alloy

A-Si is deposited using plasma enhanced chemical vapour deposition (PECVD). By introducing germanium (Ge) during deposition, an amorphous silicon/germanium (a-Si/Ge) alloy is formed. By increasing the Ge content, the bandgap of the a-Si/Ge alloy can be decreased. In figure 4.2 the optical properties of an a-Si/Ge alloy with a bandgap of 1.5 eV are shown. With respect to a-Si, the graph of the absorption coefficient has shifted to higher wavelengths and the refractive index has increased somewhat.

#### Micro-crystalline silicon

If during deposition of a-Si, conditions such as  $\text{H}_2/\text{SiH}_4$ -dilution ratio, substrate temperature and layer thickness are favourable, silicon crystallites with dimensions of tens of nanometres are formed [67]. This form of silicon is called micro-crystalline silicon ( $\mu\text{c-Si}$ ). In figure 4.2 the refractive index and the absorption coefficient of  $\mu\text{c-Si}$  are shown. It can be seen that optically  $\mu\text{c-Si}$  is more similar to c-Si than to a-Si.

#### Copper indium gallium diselenide

An alternative semiconductor material, not based on Si, is copper indium gallium diselenide ( $\text{Cu(InGa)Se}_2$  or CIGS). Because indium can be substituted with gallium

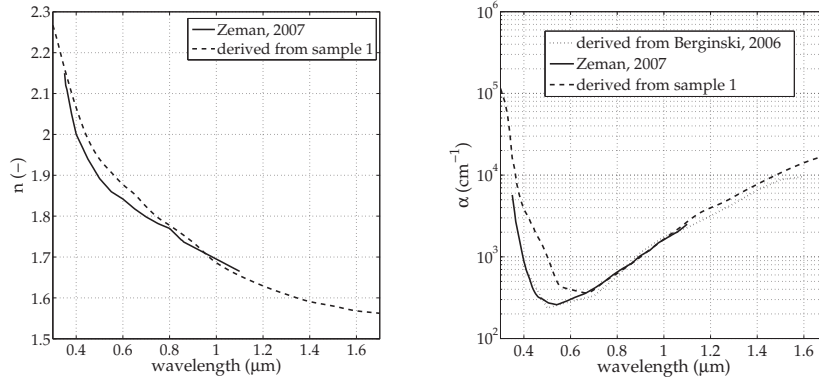


**Figure 4.3:** The refractive index  $n$  (left) and absorption coefficient  $\alpha$  (right) of aluminium doped zinc oxide as derived from measurements by Berginski [68], as provided by Zeman [65] and as derived from measurements of sample 1 (which will be introduced in section 4.3).

and vice versa, the composition can be expressed as  $\text{Cu}(\text{In}_{1-x}\text{Ga}_x)\text{Se}_2$ , where  $x$  is between 0 and 1 and represents the relative gallium content. The bandgap of CIGS increases with increasing relative gallium content  $x$ . For solar cell applications, CIGS with  $x = 0.2$  is used because this gives the highest electrical efficiencies. Therefore this composition will be considered here as well. The optical properties obtained from Alonso [66] are shown in figure 4.2. Because of the relatively small bandgap of 1.2 eV, this semiconductor has a high absorption coefficient remaining larger than  $10^4 \text{ cm}^{-1}$  up to a wavelength of 1.1  $\mu\text{m}$ .

## 4.2.2 Transparent conductive oxides

As shown in figure 4.1, at the front and the back of the semiconductor layer, contact layers are present to collect the holes and electrons respectively. To prevent ohmic losses as much as possible, these layers require a high conductivity. At the back side typically a metal layer is used, which serves both as electrical contact and as an optical reflector. As front contact, a layer is required which is not only conductive, but transparent as well. Transparent conductive oxides (TCO's) exist, such as (indium) tin oxide and zinc oxide, meeting both requirements. The conductivity of these TCO's can be improved by adding a suitable dopant.

### Optical properties

For solar cell applications aluminium doped zinc oxide (ZnO:Al) is the state-of-the-art TCO. Berginski [68] has studied the conductivity, the transparency and the surface topography of magnetron sputtered ZnO:Al. In this study it was found that an

increased doping level improves the TCO's conductivity, but at the same time reduces the transparency for the near infrared part of the solar spectrum. Berginski has measured the transmittance of ZnO:Al layers having doping concentrations of  $1.1 \cdot 10^{20} \text{ cm}^{-3}$ ,  $2.7 \cdot 10^{20} \text{ cm}^{-3}$  and  $3.8 \cdot 10^{20} \text{ cm}^{-3}$ . From these transmittance curves the corresponding absorption coefficients were derived. The curve corresponding to the doping concentration of  $3.8 \cdot 10^{20} \text{ cm}^{-3}$  is shown in the right panel of figure 4.3 and corresponds nicely with the absorption coefficient provided by Zeman [65]. The mechanism responsible for absorption in the near infrared is free-carrier absorption. Characteristic for free-carrier absorption is the increase of its strength with increasing wavelength. This explains the increase in  $\alpha$  that can be observed for  $\lambda > 0.7 \text{ }\mu\text{m}$  in the right panel of figure 4.3.

Zeman has provided the data corresponding to the refractive index  $n$ , shown in the left panel of figure 4.3 as well. In section 4.3, sample 1 will be introduced containing a ZnO:Al layer. Using this sample the optical properties ( $n$  and  $\alpha$ ) of ZnO:Al were determined. These results are also shown in figure 4.3 and agree quite well with the existing data. In the numerical simulations that will be described in section 4.3 the optical properties derived from sample 1 will be used.

### Surface topography

After deposition, the initially smooth TCO film is textured by wet-chemical etching. Berginski [68] reports that depending on doping level and substrate temperature, different postetching surface topographies appear. Using scanning electron microscopy and atomic force microscopy, Berginski analysed the surface topographies. A root-mean-squared (rms) surface roughnesses  $\sigma$  of approximately 100 nm can be obtained. At the same time this texture can have a steepness  $\gamma$  of  $17^\circ$  to  $32^\circ$ .

Because the rms roughness  $\sigma$  is comparable to the wavelength  $\lambda$  of solar irradiance, the optical model uses haze parameter  $H$  when modelling the rough TCO surface.  $H$  is defined as the fraction of incident light that is scattered and is a function of  $\sigma/\lambda$ . As described in section 2.5.4, when modelling textured TCO surfaces, haze parameter  $H$  is used as weighting parameter for scattered light. Texture steepness  $\gamma$  is a parameter determining the angular distribution of the scattered light. In section 4.3.5 the optical effects of the parameters  $\sigma$  and  $\gamma$  are studied in more detail.

## 4.3 Model validation for a-Si structures

The optical model described in chapter 2 has already been validated for c-Si cells, as described in section 3.3. However, the optical behaviour of the interfaces and layers encountered in *thin-film* solar cells may be very different. Therefore the model is validated separately for thin-film solar cells in this section. This is done by comparing numerical results to results of reflection and transmission measurements performed

**Table 4.1:** Overview of the samples used. The approximate thickness of each layer is given in brackets in micrometres. The ZnO:Al layers marked with an asterisk were etched after deposition resulting in a rough surface.

nr	description
1	glass(690)/ZnO:Al(1)
2	glass(690)/ZnO:Al(1)/a-Si(0.45)
3	glass(690)/ZnO:Al(1)/a-Si(0.45)/Al(0.30)
4	glass(690)/ZnO:Al(1)*
5	glass(690)/ZnO:Al(1)* /a-Si(0.45)/Al(0.30)

on a set of thin-film solar cell samples. A description of the samples will be given in section 4.3.1. The integrating sphere set-up used for the measurements was already described in section 3.3.1.

The required input parameters for the numerical simulations are the optical properties and the thickness of the layers and the scattering parameters of the interfaces. For thin-film solar cells (much more than for c-Si cells) the difficulty when comparing numerical results to experimental results, is that some numerical input parameters are not known with sufficient accuracy. For example layer thicknesses have to be known within a few nanometres to describe interference effects correctly. Also the optical properties of some deposited layers may vary slightly, depending on the exact deposition conditions. For this reason some parameters have to be verified by means of inverse modelling, i.e. fitting numerical results to the experimental results by varying the unknown parameter.

### 4.3.1 Sample description

The samples used were made at the Delft Institute of Microsystems and Nanoelectronics (DIMES) and their composition is summarised in table 4.1. The samples are of increasing complexity, i.e. sample 1 is relatively simple and sample 5 is more complex, resembling a complete a-Si solar cell. This was done to gain more insight in the optical effects occurring in thin-film solar cells, which in this way are introduced one at the time. The first three samples have relatively smooth interfaces and these samples are used to verify the optical properties of the layers and they serve as a reference for the remaining samples. The remaining samples have rough interfaces, just like the real thin-film solar cells, and these samples are used to verify the light-scattering behaviour of the interfaces.

All samples were deposited on a substrate of low-iron content glass [69] with a thickness of 690  $\mu\text{m}$ . Sample 1 consists of a glass substrate on which an approximately 1  $\mu\text{m}$  thick layer of ZnO:Al was deposited by means of magnetron sputtering. The usual texture etch after deposition of the ZnO:Al layer was omitted, keeping the



ZnO:Al surface relatively smooth [68]. Sample 2 is identical to sample 1 with an approximately  $0.45 \mu\text{m}$  thick layer of a-Si deposited on top of the ZnO:Al layer. The a-Si layer was deposited by Radio Frequency Plasma-Enhanced Chemical Vapour Deposition (RF-PECVD). Sample 3 is identical to sample 2 but with a  $0.30 \mu\text{m}$  thick Al back contact deposited on the a-Si layer using an electron beam evaporator.

Sample 4 consists of a glass substrate with an approximately  $1 \mu\text{m}$  thick layer of ZnO:Al deposited (as sample 1). However, after deposition the ZnO:Al layer underwent a texture etch. As described in section 4.2.2, this results in a very rough ZnO:Al surface with a roughness of approximately  $100 \text{ nm}$  [68]. This sample is used to gain insight in the optical behaviour of the rough ZnO:Al surface. Finally, sample 5 is identical to sample 4, but with an approximately  $0.45 \mu\text{m}$  thick layer of a-Si and a  $0.30 \mu\text{m}$  thick Al back contact deposited on top of the rough ZnO:Al layer. Because the a-Si layer is very thin, it is expected that the roughness of the ZnO:Al/a-Si interface is transferred to the a-Si/Al interface [70]. Note that sample 5 contains the same layers as sample 3, but the interfaces are different, i.e. sample 5 has rough interfaces. This final sample 5 is very similar to a typical a-Si solar cell. However, to simplify the fabrication of the sample and the analysis of the results, no p- and n-type regions were included. Therefore the sample is not electrically active, but this is not required for our purposes here.

### 4.3.2 Glass/ZnO:Al (sample 1)

In the left panel of figure 4.4, the spectral reflection factor  $R_\lambda$  and spectral transmission factor  $T_\lambda$  are shown for the ZnO:Al layer deposited on the glass substrate (without texture etch). As before,  $1 - R_\lambda$  and  $T_\lambda$  are plotted so the spectral absorption factor  $A_\lambda = 1 - R_\lambda - T_\lambda$  can be identified as well (as indicated in the figures). The experimental results are indicated by symbols ( $\circ$ ,  $\nabla$ ) and the numerical results by lines.

It can be seen that both the experimental reflection and transmission curves show many oscillations. These oscillations are caused by interference in the ZnO:Al layer, which has a thickness of approximately  $1 \mu\text{m}$ . As described in section 2.2.2, the optical model also takes into account these interference effects. The wavelength at which a specific reflection minimum or maximum occurs is proportional to the thickness of the layer. However, if the optical thickness of a layer exceeds the coherence length of the light source, the amplitude of the oscillations is being attenuated. The glass substrate is too thick to cause any interference.

For  $0.45 < \lambda < 0.90 \mu\text{m}$  the sample is very transparent ( $T_\lambda = 0.75 - 0.90$ ). However, below  $\lambda < 0.45 \mu\text{m}$  the ZnO:Al is much less transparent. For  $\lambda > 0.90 \mu\text{m}$ ,  $T_\lambda$  gradually decreases with increasing  $\lambda$  as a result of free-carrier absorption in the ZnO:Al layer. The strength of this free-carrier absorption depends on the doping level of the ZnO:Al used. By integrating  $A_\lambda$  over the solar spectrum an AM1.5 absorption factor of 17% is found. Because the low-iron content glass substrate is

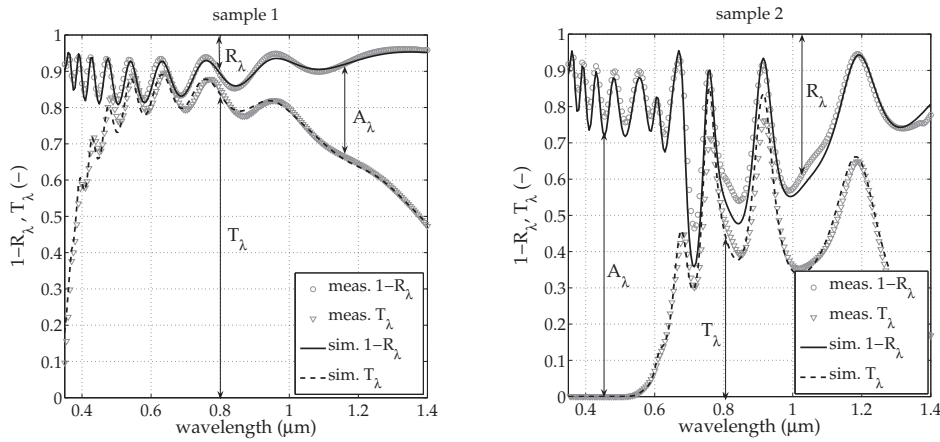


**Figure 4.4:** Measured and simulated  $1 - R_\lambda$  and  $T_\lambda$  as a function of  $\lambda$  for a glass substrate with ZnO:Al (sample 1, left) and for a glass substrate with ZnO:Al and a-Si (sample 2, right).

known to have an absorption factor of less than 1%, nearly all absorption can be attributed to the ZnO:Al layer.

In the numerical simulation of sample 1 the approximately  $1 \mu\text{m}$  ZnO:Al layer is treated as a coherent layer in which optical interference occurs. Because the sample has not been etched, the surfaces are relatively smooth [68] and therefore in the model specular reflection is assumed. The exact thickness and optical properties of this particular ZnO:Al layer are not known in detail, but will be derived from the measurement. As a starting point the approximate thickness of  $1 \mu\text{m}$  and the optical properties provided by Zeman [65] are used. Using this data in the model there is qualitative agreement, but the numerical results deviate from the measurement results in two ways (not shown). Firstly, the oscillations found in the simulation do not exactly coincide with the measured ones. Secondly, the model predicts somewhat less absorption for  $\lambda < 0.60 \mu\text{m}$ .

To investigate how these deviations of the numerical results from the experimental results could be reduced by using more accurate numerical parameters, a parameter variation analysis was performed. The thickness  $d$  and the optical properties  $n(\lambda)$  and  $\alpha(\lambda)$  of the ZnO:Al layer were varied in the numerical model. As shown in the left panel of figure 4.4, an excellent agreement can be found for both  $R_\lambda$  (solid line) and  $T_\lambda$  (dashed line). This was achieved by assuming a smaller ZnO:Al thickness of  $0.85 \mu\text{m}$  and modified optical properties.

In figure 4.3 the modified optical properties  $n(\lambda)$  and  $\alpha(\lambda)$  (dashed line) are compared to the original data by Zeman [65] (solid line). The refractive index hardly required any modification, while the absorption coefficient had to be increased somewhat for  $\lambda < 0.6 \mu\text{m}$ . In literature it is reported that the doping level of ZnO:Al

can affect the absorption coefficient of ZnO:Al in both the short-wavelength end of the solar spectrum (through the Burnstein-Moss shift [71]) and in the infrared part (through free-carrier absorption [72]). Also deposition conditions such as substrate temperature are known to affect the absorption coefficient [73]. This might explain the higher than expected absorption coefficient for  $\lambda < 0.6 \mu\text{m}$ . Because the ZnO:Al layers in samples 1 to 5 are deposited under the same conditions,  $n(\lambda)$  and  $\alpha(\lambda)$  derived from sample 1 will also be used to simulate samples 2 to 5.

### 4.3.3 Glass/ZnO:Al/a-Si (sample 2)

$R_\lambda$  and  $T_\lambda$  measured for the glass/ZnO:Al/a-Si sample are shown in the right panel of figure 4.4. Compared to the results of the previous sample two main differences can be observed. Firstly, the amplitude of the oscillations has increased and their spectral position has changed, caused by simultaneous interference in both the ZnO:Al and a-Si layer. Secondly, for  $\lambda < 0.55 \mu\text{m}$  the sample has become opaque ( $T_\lambda = 0$ ), which is caused by the high absorption coefficient of a-Si at these wavelengths.

In the numerical model both the ZnO:Al layer and the a-Si layer are treated as coherent layers. For ZnO:Al the optical properties derived from sample 1 are used (shown as the dashed line in figure 4.3), without making any further adjustments. For a-Si the optical properties shown in figure 4.2 are used as provided by Zeman [65]. The spectral position of the oscillations (i.e. the wavelengths at which the reflection and transmission minima and maxima occur) depends on the exact layer thickness. The layer thicknesses used in the numerical model were varied slightly to find the best possible fit to the measured results. The very good fit shown in the right panel of figure 4.4 was found for  $d_{\text{ZnO}} = 0.80 \mu\text{m}$  and  $d_{\text{a-Si}} = 0.48 \mu\text{m}$ . These are plausible values because the thickness of the ZnO:Al layer is close to the value found for sample 1 ( $0.85 \mu\text{m}$ ) and the thickness of the a-Si layer is close to the specified value ( $\approx 0.45 \mu\text{m}$ ). Not only the spectral position, but also the amplitude of every oscillation observed in the experimental results matches very well to the oscillations found numerically for both  $R_\lambda$  and  $T_\lambda$ .

It should be emphasised that this good agreement was found by simply assuming specular reflection at every interface. This confirms that the ZnO:Al layer deposited without subsequent etching is relatively smooth. Further, the ZnO:Al and a-Si layers can apparently be treated as a stack of coherent layers in which optical interference occurs, albeit their optical thickness is slightly larger than the coherence length of the light source. Finally, it can be concluded that the optical properties for ZnO:Al (derived from sample 1) and a-Si (provided by Zeman [65]) used in the optical model closely match the optical properties of ZnO:Al and a-Si in sample 2.

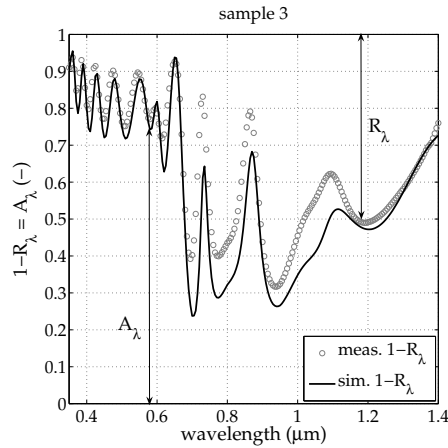


**Figure 4.5:** Measured and simulated  $1 - R_\lambda$  and  $T_\lambda$  as a function of  $\lambda$  for a glass substrate with ZnO:Al, a-Si and Al layers and smooth interfaces (sample 3).

#### 4.3.4 Glass/ZnO:Al/a-Si/Al (sample 3)

In figure 4.5 the results are given for sample 3 (glass/ZnO:Al/a-Si/Al). Since the added Al back contact is opaque, only  $1 - R_\lambda = A_\lambda$  is shown. For  $\lambda < 0.7 \mu\text{m}$ ,  $A_\lambda$  is very similar to the  $A_\lambda$  of the previous sample. Longer wavelength irradiance that would have been transmitted in the previous sample is now partly absorbed in the back contact and partly reflected by it.

The numerical results are very similar to the measurement results. The thicknesses used in the simulation are  $d_{\text{ZnO}} = 0.78 \mu\text{m}$ ,  $d_{\text{a-Si}} = 0.49 \mu\text{m}$  and  $d_{\text{Al}} = 0.30 \mu\text{m}$ . No modification of the optical properties were required.

Though the numerical results agree quite well with the experimental results for most of the spectrum, in the wavelength region  $0.7 < \lambda < 1.2 \mu\text{m}$  the numerical model over predicts  $R_\lambda$  by about 10% absolute. This is most likely caused by the fact that in reality the back contact is somewhat less reflective than predicted by the model. A second cause could be that the deposited back contact is slightly rough, giving rise to some light being reflected diffusely and being trapped inside the a-Si layer. In the model specular reflection was assumed.

Since all interfaces are still relatively smooth, the majority of irradiance reflected by the back contact can escape the configuration and is lost. As a result  $A_\lambda$  is relatively low, especially for  $\lambda > 0.7 \mu\text{m}$ , resulting in a relatively low AM1.5 absorption factor of 71% (based on the measurement results). This is already an indication that in order to obtain a high AM1.5 absorption factor, some form of light trapping is required.

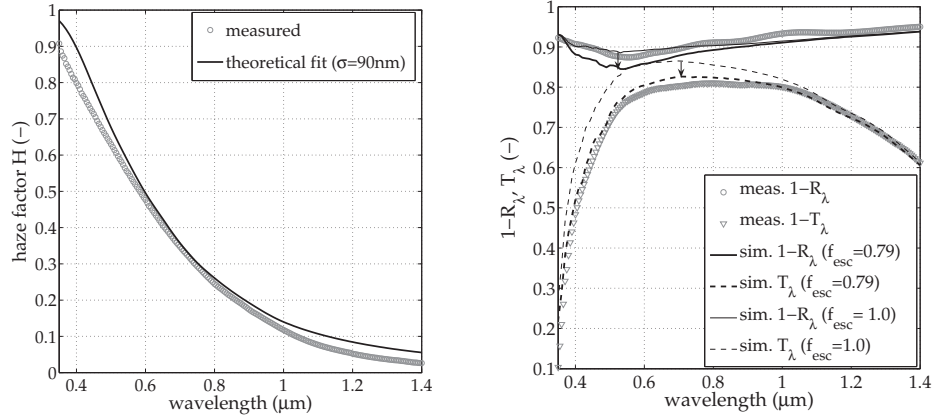


**Figure 4.6:** Glass substrate with rough ZnO:Al (sample 4). Left: Measured and theoretical haze parameter  $H$  as a function of  $\lambda$ . Right: Measured and simulated  $1 - R_\lambda$  and  $T_\lambda$  as a function of  $\lambda$ . Both the simulations with  $f_{\text{esc}} = 1.0$  (no correction) and with  $f_{\text{esc}} = 0.79$  (best fit) are shown.

#### 4.3.5 Glass/textured ZnO:Al (sample 4)

Sample 4 consists of a glass substrate on which a  $1 \mu\text{m}$  thick ZnO:Al layer was deposited, just like sample 1. However, unlike sample 1, the ZnO:Al layer of sample 4 has been textured by wet chemical etching. The parameters required to describe light-scattering by the textured surface will be derived from the measurements considered here. First the roughness  $\sigma$  is derived from a measurement of the haze parameter.

Haze parameter  $H$  in transmission is defined as the ratio of the diffuse transmission factor and the hemispherical transmission factor. The procedure for measuring the *hemispherical* transmission factor was described in section 3.3.1. As indicated in figure 3.5, port 2 is closed to detect both directly and diffusely transmitted light. However, for sample 4 an additional transmission measurement was performed in which port 2 of the integrating sphere is opened. In this way all light transmitted directly (without being scattered) leaves the integrating sphere through port 2 and only the diffusely transmitted light is detected. In the left panel of figure 4.6,  $H$  derived from the transmission measurements of sample 4 is shown as a function of wavelength. It can be seen that for short wavelength irradiance,  $H$  is close to 1, indicating that nearly all transmitted short wavelength light is transmitted diffusely, i.e. scattered by the rough ZnO:Al surface. With increasing wavelength,  $H$  decreases rapidly and for long-wavelength irradiance  $H$  is close to 0. This indicates that most long wavelength irradiance is transmitted directly, without being scattered by the rough ZnO:Al surface.

In section 2.5.4 a relationship between  $H(\lambda)$  and surface roughness  $\sigma$  was presented. By substituting  $\sigma = 90$  nm, a very good fit with the measured  $H(\lambda)$  was obtained (see left panel of figure 4.6). This roughness is close to the expected value for this sample. It can also be concluded that as expected the empirical relationship for  $H(\lambda)$  is applicable to the rough ZnO:Al surface in thin-film solar cells. Therefore this relationship is used in the optical model described in chapter 2.

The measured spectral reflection factor  $R_\lambda$  and transmission factor  $T_\lambda$  of sample 4 are shown in the right panel of figure 4.6. Compared to the results of sample 1 (shown in the left panel of 4.4) the main difference is the absence of oscillations, indicating that no interference occurs in the textured ZnO:Al layer. The rough ZnO:Al surface scatters light in different directions. In terms of electromagnetic waves this means that the fixed phase difference between the waves combining at the top or bottom interface of the ZnO:Al layer is lost. Consequently no interference will occur. Because light is trapped in the rough ZnO:Al layer somewhat better than in the smooth ZnO:Al layer of sample 1, the AM1.5 absorption factor has increased from 17% to 20% (both derived from the measurements).

Two parameters regarding the rough ZnO:Al interface remain unknown: texture steepness  $\gamma$ , and escape factor  $f_{\text{esc}}$ . By numerically varying both parameters, the best fit for both  $R_\lambda$  and  $T_\lambda$  was found in case  $f_{\text{esc}} = 0.79$  and  $\gamma = 23^\circ$ . In the right panel of figure 4.6 the numerical results are shown for both  $f_{\text{esc}} = 1.0$  (no correction) and for  $f_{\text{esc}} = 0.79$  (best fit) to illustrate the effect of  $f_{\text{esc}}$  (indicated by the arrow in the right panel of figure 4.6). The steepness  $\gamma$  used is plausible because it falls within the range of  $17^\circ$ - $32^\circ$ , given by Berginski [68].

The critical angle for the ZnO:Al/air interface (i.e. for light reaching the back surface of the sample) is  $27$ - $39^\circ$  (depending on the wavelength). Because the texture steepness is smaller than this critical angle, this rough interface transmits most of the light and a small amount of light is trapped. Knowing this, the relatively high value of  $0.79$  found for the escape factor can be explained by the fact that the angular distribution of light reaching the textured interface is more unidirectional than distributed uniformly over all directions. For unidirectional irradiance a 2D model is sufficient and  $f_{\text{esc}} = 1$  is appropriate. For the other extreme case in which light would be distributed uniformly, the escape factor could be estimated using equation 2.35, giving  $f_{\text{esc}} \approx 0.43$ . It turns out that the value of  $f_{\text{esc}}$  required here ( $0.79$ ) is in between the extreme values, as should be the case.

### 4.3.6 Glass/textured ZnO:Al/a-Si/Al (sample 5)

In figure 4.7 the results of sample 5 (glass/textured ZnO:Al/a-Si/Al) are shown. Compared to sample 3 without texture, two differences can be observed. Firstly, the measured interference pattern in the spectral reflection and transmission curves has changed. The oscillations that were visible in sample 3 for  $\lambda < 0.7$   $\mu\text{m}$  have disappeared almost completely, but for longer wavelengths oscillations are still vis-

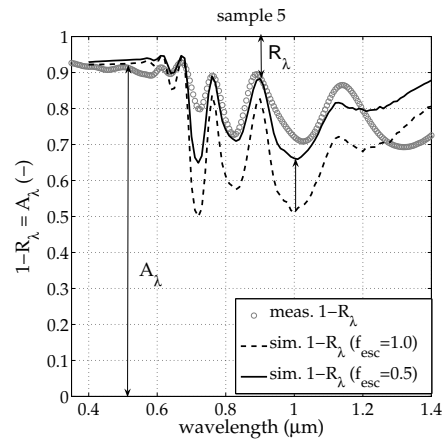


**Figure 4.7:** Measured and simulated  $1 - R_\lambda$  and  $T_\lambda$  as a function of  $\lambda$  for a glass substrate with ZnO:Al, a-Si and Al, having rough interfaces (sample 5).

ible. Secondly,  $A_\lambda$  has increased significantly. This is caused by optical confinement of irradiance scattered at the textured ZnO:Al interface. Note that irradiance is not trapped only inside the a-Si layer, but also in the glass and ZnO:Al layers. As a result absorption in each layer has increased and the AM1.5 absorption factor has increased to as much as 86%.

From the analysis of sample 4 it is known that no interference occurs in the ZnO:Al layer with a rough surface. The remaining oscillations then have to be attributed to interference in the a-Si layer. However, the interfaces of the a-Si layer are rough as well, which seems to rule out interference in this layer. But unlike the ZnO:Al layer, which is smooth on the glass side, both interfaces of the a-Si layer have a similar topography. Because the roughness at the ZnO:Al/a-Si interface is transferred to the a-Si/Al interface, the slope of the first interface matches the slope of the second interface at each point. Under these conditions interference can theoretically occur and judging from the oscillations it actually does occur. Therefore, in the simulation it was assumed that the ZnO:Al layer is incoherent but the a-Si layer is coherent. The textured interfaces are modelled with a steepness of  $23^\circ$  and a roughness of 90 nm. In figure 4.7 (dashed line) the numerical results are shown. As can be seen, the simulated oscillations and the measured ones only occur at those wavelengths where a-Si is transparent, confirming that the ZnO:Al and the a-Si layer can be considered to be incoherent and coherent respectively.

The resulting increase in  $A_\lambda$  with respect to the smooth sample (sample 3) is also found in the simulation (compare the solid line in figure 4.5 with the dashed line in figure 4.7). However, for  $\lambda > 0.7 \mu\text{m}$  the increase of  $A_\lambda$  is less than the experimental increase, indicating that the amount of optical confinement is somewhat underestimated by the model. As discussed in section 2.6, this underestimation is



related to the two-dimensionality of the model and can be corrected by introducing an escape factor. This escape factor increases the *internal* reflection coefficient of the a-Si/ZnO:Al interface, effectively enhancing optical confinement. In section 3.3.5 the approach of using an escape factor was shown to be successful in describing optical confinement in c-Si solar cell samples. The measurement results are used to calibrate the model. It was found that if the chance of irradiance escaping the configuration is reduced to half of its original value (i.e.  $f_{\text{esc}} = 0.5$ ), a much better agreement with the experimental results can be found (solid line figure 4.7). Nonetheless, still some deviations can be observed which could not be reduced any further. On average these deviations are 4%. When considering the AM1.5 absorption factor, positive and negative deviations partly cancel, resulting in a 1% difference between measurement and simulation.

Note that as explained in section 2.6, the required escape factor at a certain interface depends on the refractive indices of the media at both sides of the interface. Therefore it is not surprising that the escape factor used for the ZnO:Al/air interface of sample 4 does not correspond to the escape factor used for the a-Si/ZnO:Al interface of sample 5. Based on the assumption of a uniform angular distribution of light reaching the interface and a critical angle of approximately  $26^\circ$ , equation 2.35 gives  $f_{\text{esc}} \approx 0.35$ . The somewhat higher value of 0.5 found here can be explained probably from the fact that the angular distribution of light scattered by the back contact is not completely uniform.

### 4.3.7 Comparison of numerical and experimental results

In table 4.2 an overview is given of the AM1.5 absorption factors found numerically and experimentally. It can be seen that the glass/ZnO:Al sample already absorbs 17% of the spectrum. Note that this value strongly depends on the ZnO:Al doping level. The addition of an a-Si layer and an Al back contact increases  $A$  to 71%. Textured ZnO:Al causes much more light to be trapped, increasing  $A$  to 86%

In general a good agreement between numerical and experimental results can be obtained by adjusting layer thicknesses numerically. But with increasing complexity of the samples, the deviation increases inevitably. An escape factor was introduced at the rough a-Si/ZnO:Al (or ZnO:Al/air) interface to take into account the 3D effects of light scattering. It can be concluded that the optical model captures most optical effects occurring in thin film solar cells. Therefore the model is a valid tool for gaining insight in the absorption mechanisms occurring in thin films solar cells and to determine the AM1.5 absorption factor for various types of thin film solar cells.



**Table 4.2:** The numerical and the corresponding measured AM1.5 absorption factor  $A$  of sample 1 to 5. The escape factor used in the numerical model is also indicated.

nr	description	$f_{\text{esc}}$	$A_{\text{num}}$	$A_{\text{exp}}$
1	glass/ZnO:Al	1.00	16.4%	16.8%
2	glass/ZnO:Al/a-Si	1.00	50.2%	54.4%
3	glass/ZnO:Al/a-Si/Al	1.00	64.0%	70.7%
4	glass/textured ZnO:Al	1.00	17.0%	19.5%
		0.79	19.3%	19.5%
5	glass/textured ZnO:Al/a-Si/Al	1.00	81.0%	86.0%
		0.50	87.0%	86.0%

#### 4.4 Simulation of the absorption factor of thin-film solar cells

In this section five important types of thin-film solar cells are considered. For these cells both the spectral absorption factor and the AM1.5 absorption factor are determined by numerical simulation. The cell designs considered are based as much as possible on the design of thin-film solar cells produced on industrial scale, either now or in the near future. Each cell design contains a low iron content glass superstrate of 3 mm thickness on which a 0.8  $\mu\text{m}$  thick TCO of ZnO:Al is deposited. The optical properties of ZnO:Al and the parameters for describing scattering of light at a rough ZnO:Al surface, derived from the measurements in section 4.3, are used in the simulations. These are the refractive index  $n$  and the absorption coefficient  $\alpha$  given as the dashed lines in figure 4.3 and a roughness of 90 nm and a texture steepness of 23°.

On the rough ZnO:Al surface, one or multiple active semiconductor layers are deposited. It is assumed that the roughness and steepness is transferred from the rough ZnO:Al surface to all subsequent interfaces. In each type of thin-film solar cell, different semiconductor layers are applied. However, in all cases the final layer in the cell structure is the back surface reflector consisting of aluminium (Al) or even more reflective silver (Ag). The optical properties of Al and Ag are given by Palik [53]. To obtain a realistic degree of light-trapping numerically, an escape factor of 0.5 (as found in section 4.3) is used in all simulations presented in this section, unless stated otherwise.

The experimental results presented in section 4.3 showed that interference occurs in the a-Si layer. Theoretically the intensity of this interference depends on the optical thickness of the layer and on the coherence length of the light source. It is questionable whether this interference will occur also if the sample is exposed to

sunlight, having a coherence length of approximately  $1 \mu\text{m}$  [35]. For this reason it is assumed in the simulations presented in this section that no interference occurs in any of the semiconductor layers. The effect of the absence of interference is that the observed oscillations in the spectral absorption factor disappear. However, the AM1.5 weighted absorption factor is affected less than 1% by the absence of interference in the semiconductor layer.

#### 4.4.1 a-Si solar cell

The a-Si solar cell structure considered here is based on the structure given by Lechner [74]. In figure 4.8 schematic cross-sections are shown. On top of the ZnO:Al layer a thin (10 nm) p-type a-SiC layer, a 300 nm intrinsic a-Si layer and a thin (30 nm) n-type a-Si layer are deposited respectively, followed by the back surface reflector (BSR). The optical properties of a-Si provided by Zeman [65], found to be accurate in section 4.3, are used again in this simulation.

In order to illustrate that within a single solar cell technology a wide range of absorption factors can exist, three different a-Si thin-film solar cell structures are considered. The first structure has an Al BSR and no optical confinement. The second structure has an Al BSR as well, but a good optical confinement. The third structure has a more reflective Ag BSR and good optical confinement. The case of *no* optical confinement is simulated having all interfaces smooth and  $f_{\text{esc}} = 1$ , while the cases of good optical confinement is simulated having the interfaces are rough, with the parameters given in the introduction of section 4.4. In figure 4.8 the numerical results are shown in an area plot of the spectral absorption factor for each layer versus the wavelength  $\lambda$ . The percentages given in the figure are the AM1.5 weighted absorption factors.

In the first case (shown at the top of figure 4.8) there is no optical confinement, in combination with an Al BSR. It can be seen that for  $0.40 < \lambda < 0.75 \mu\text{m}$  most irradiance is absorbed in the a-Si layer, resulting in an AM1.5 absorption factor of 25.5% for this layer. However, for  $\lambda > 0.75 \mu\text{m}$  the a-Si layer hardly absorbs any irradiance. Because the interfaces do not scatter any irradiance, the long-wavelength irradiance that is reflected by the BSR can escape the cell largely unhindered. Note that with increasing wavelength, free-carrier absorption in the ZnO:Al layer rapidly becomes more important resulting in a relatively high AM1.5 absorption factor of 22.8% for the ZnO:Al layer. Nonetheless, as much as 33.9% of the AM1.5 spectrum is reflected, resulting in an AM1.5 factor of the cell as a whole of only 66.1%.

Practical solar cells will have some form of optical confinement. The effect of this is shown in the second and third case. If optical confinement is good, while maintaining the Al BSR (shown in the centre of figure 4.8), light is trapped for multiple passes. This increases the absorption in every layer, increasing the AM1.5 absorption factor of the cell as a whole to 88.5%.

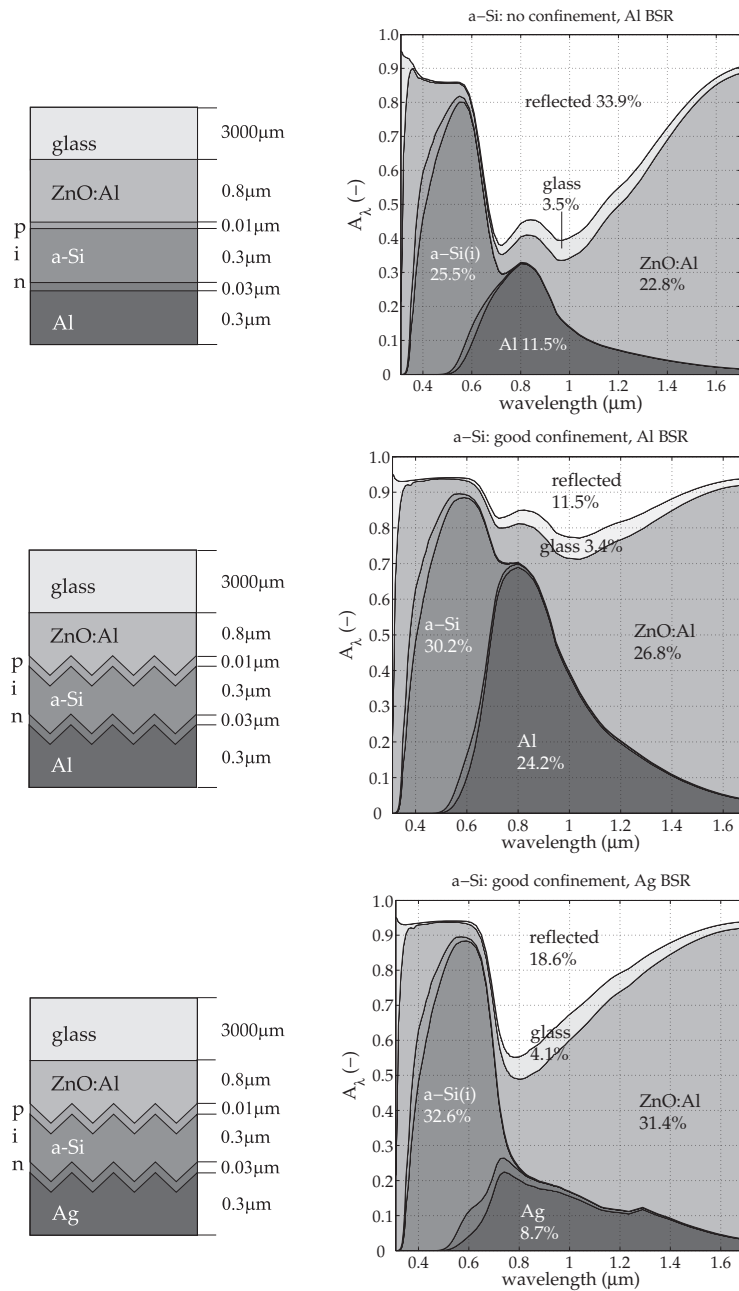


**Figure 4.8:** Area plot of the spectral absorption factor  $A_\lambda$  for each layer of the a-Si solar cell. Top: No optical confinement (smooth interfaces and  $f_{\text{esc}} = 1$ ) and an aluminium BSR ( $A = 66.1\%$ ). Centre: Good optical confinement and an aluminium BSR ( $A = 88.5\%$ ). Bottom: Good optical confinement and a silver BSR ( $A = 81.4\%$ ). The percentages given are AM1.5 absorption factors.

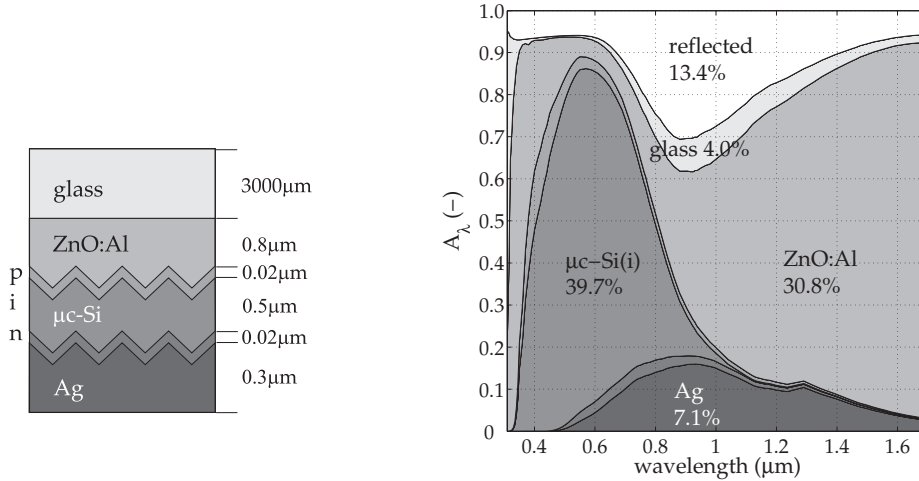


**Figure 4.9:** Area plot of the spectral absorption factor  $A_\lambda$  for each layer of the  $\mu\text{c-Si}$  silicon solar cell. The AM1.5 absorption factors are also given for most layers separately. The total AM1.5 absorption factor is 86.6%.

Alternatively, the Al BSR can be replaced by a more reflective, but also somewhat more expensive Ag BSR. As can be seen, compared to the Al BSR, less light is absorbed in the BSR and more is reflected, reducing the AM1.5 absorption factor to 81.4%. However, as a result of reduced absorption by the BSR, more light is absorbed in the active a-Si layer as well. Because this is beneficial for the electrical efficiency, there is a trend towards the more reflective BSR's. For this reason, the remaining cell technologies are primarily considered having a highly reflective Ag BSR. A more detailed discussion regarding the BSR's of thin-film solar cells will be given in section 4.4.6.

#### 4.4.2 $\mu\text{c-Si}$ solar cell

The  $\mu\text{c-Si}$  solar cell structure considered here is based on the structure given by Krč [31]. In the left panel of figure 4.9 a schematic cross-section is shown. This configuration is similar to the previous configuration with an Ag BSR and good optical confinement, but with the a-Si replaced by  $\mu\text{c-Si}$ . The intrinsic layer has a thickness of 500 nm, and both the p- and n-type layers are 20 nm thick. The optical properties of intrinsic and doped  $\mu\text{c-Si}$  were obtained from Springer [64] and Zeman [65] respectively.

In the right panel of figure 4.9 the numerical results are shown in an area plot of the spectral absorption factor for each layer versus the wavelength  $\lambda$ . These results are similar to the results of the a-Si cell with an Ag BSR. However, it can be seen

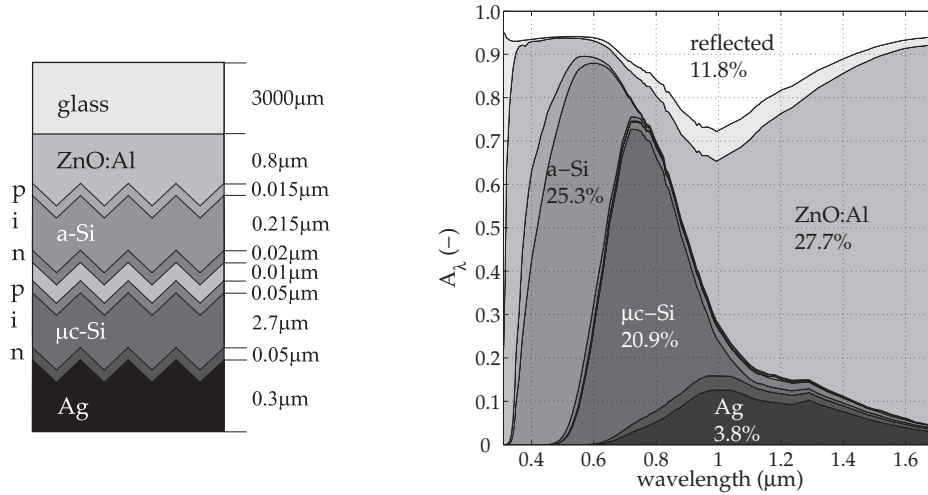


**Figure 4.10:** Area plot of the spectral absorption factor  $A_\lambda$  for each layer of the micromorph silicon solar cell. The AM1.5 absorption factors are also given for most layers separately. The total AM1.5 absorption factor is 88.2%.

that the  $\mu\text{-Si}$  layer absorbs a somewhat broader part of the solar spectrum. This is because of the smaller bandgap of  $\mu\text{-Si}$  compared to  $\text{a-Si}$  and the resulting high absorption coefficient for a larger part of the solar spectrum, shown in the right panel of figure 4.2. The AM1.5 absorption factor of the  $\mu\text{-Si}$  layer is 39.7% and for the complete cell 86.6%.

#### 4.4.3 Micromorph silicon tandem solar cell

A very promising thin-film cell technology is the so-called micromorph silicon tandem solar cell technology, consisting of a  $\mu\text{-Si}$  p-i-n structure deposited on top of an  $\text{a-Si}$  p-i-n structure. The micromorph silicon tandem cell considered here is based on the structure given by Krč [75]. In the left panel of figure 4.10 a schematic cross-section is shown. The ZnO:Al interface and all subsequent interfaces have a roughness of 90 nm and an Ag BSR is used. Because this design is in fact a stack of two cells connected in series, the top and bottom cell should generate equal photocurrents to achieve the maximum electrical efficiency. For this reason the  $\mu\text{-Si}$  bottom cell (2.7  $\mu\text{m}$ ) is much thicker than the  $\text{a-Si}$  top cell (250 nm). Between the top and bottom cell there is a so-called interlayer, consisting of undoped ZnO. The function of this interlayer is to improve optical confinement in the top cell.

In the right panel of figure 4.10 the numerical results are shown. It can be seen that for  $0.35 < \lambda < 0.60 \mu\text{m}$  most irradiance is absorbed in the  $\text{a-Si}$  top cell. As this top cell gets more transparent with increasing wavelength, more irradiance is

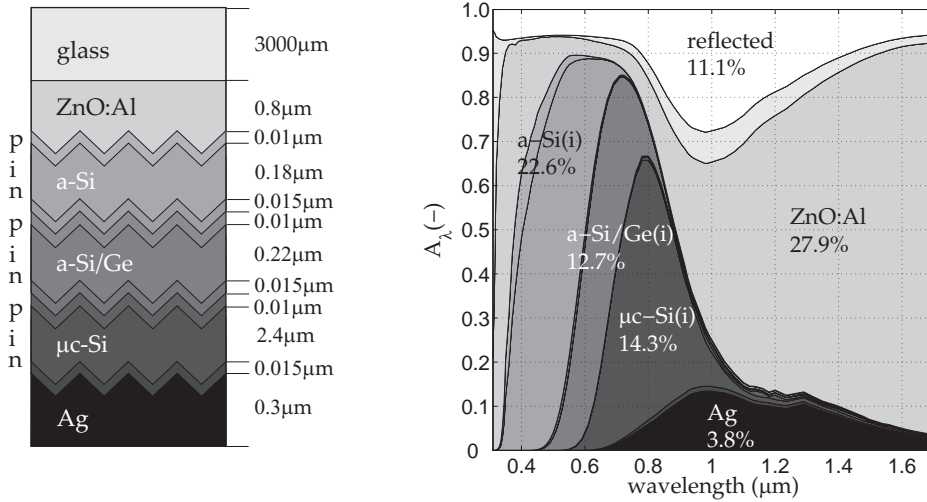


**Figure 4.11:** Area plot of the spectral absorption factor  $A_\lambda$  for each layer of the triple junction solar cell. The AM1.5 absorption factors are also given for most layers separately. The total AM1.5 absorption factor is 88.9%.

absorbed in the bottom cell. Therefore, for  $0.60 < \lambda < 0.90 \mu\text{m}$  most irradiance is absorbed in the  $\mu\text{c-Si}$  bottom cell. This illustrates nicely that the top and bottom cell each utilise different parts of the solar spectrum to potentially obtain higher cell efficiencies. For even larger wavelengths, the bottom cell becomes transparent as well and irradiance is mainly absorbed in ZnO:Al. The AM1.5 absorption factor of the a-Si layer is 25.3% and of the  $\mu\text{c-Si}$  layer 20.9%. The AM1.5 absorption factor of this cell as a whole is 88.2%.

#### 4.4.4 a-Si/a-SiGe/ $\mu\text{c-Si}$ triple junction solar cell

An even more advanced cell design than the tandem cell design considered before is the triple junction solar cell consisting of a-Si, a-SiGe and  $\mu\text{c-Si}$ . A schematic cross-section is shown in the left panel of figure 4.11. The rough interfaces have a roughness of 90 nm and an Ag BSR is used. Compared to the tandem cell, a third p-i-n structure was added between the a-Si top cell and the  $\mu\text{c-Si}$  bottom cell. This middle cell is based on an alloy of a-Si and germanium (Ge). By adjusting the Ge content, the bandgap energy of the alloy can be controlled. The alloy used in this type of triple junction cell has a bandgap energy lying in between the bandgap energies of a-Si and  $\mu\text{c-Si}$ . The optical properties of the alloy were obtained from Zeman [65] and are shown in figure 4.2. The design of the triple junction cell considered here is based on the design given by Krč [70]. The intrinsic layers in the top, middle and bottom cell

have a thickness of 0.18  $\mu\text{m}$ , 0.22  $\mu\text{m}$  and 2.4  $\mu\text{m}$  respectively. The thickness of each p-layer is 10 nm and of each n-layer is 15 nm.

In the right panel of figure 4.11 the numerical results are shown. It can be seen that the top, middle and bottom cell in the stack each absorb a different part of the solar spectrum. The irradiance transmitted by the a-Si layer is absorbed partly by the a-Si/Ge layer and the irradiance transmitted by both the a-Si and the a-Si/Ge layers is absorbed partly by the  $\mu\text{c-Si}$  layer. Longer wavelength irradiance ( $\lambda > 1.0 \mu\text{m}$ ) is hardly absorbed by any of the active layers and reaches the silver back surface reflector. Because light trapping is very efficient, most of this irradiance does not escape the cell but is absorbed by ZnO:Al. The AM1.5 absorption factors of the a-Si, a-Si/Ge and  $\mu\text{c-Si}$  layer are 22.6%, 12.7% and 14.3% respectively. The AM1.5 absorption factor of the cell as a whole is 88.9%.

#### 4.4.5 CIGS solar cell

An alternative cell design not based on Si, is the copper indium gallium diselenide (Cu(InGa)Se<sub>2</sub> or CIGS) solar cell. As already mentioned in section 4.2.1, the bandgap of CIGS increases with increasing relative gallium content  $x$ . For solar cell applications CIGS with  $x = 0.2$  is used because this gives the highest electrical efficiencies. This semiconductor material will be considered in this section, having a bandgap of 1.2 eV. The corresponding optical properties of CIGS obtained from Alonso [66], shown in figure 4.2, are used in the optical model. The optical properties of CdS, which is used as a window layer, were obtained from Sandoval-Paz [76].

The design used here is a somewhat theoretical design to have a configuration comparable to the configurations considered for the previous technologies. That is the reason that a silver back contact is assumed for now. In practice the CIGS and CdS layer in CIGS solar cells are deposited on a molybdenum coated glass substrate and the TCO is then the final layer, as described by Shafarman and Stolt [77]. Molybdenum is used instead of silver or aluminium, because a good ohmic contact with CIGS can be obtained [78]. A schematic cross-section of the solar cell used for the simulation is shown in the left panel of figure 4.12. The thickness of the CdS window layer is 50 nm and the thickness of the CIGS layer itself is 2  $\mu\text{m}$ . From an optical point of view, the design is almost identical to the practical design described by Shafarman and Stolt [77], the main difference being that silver is used instead of molybdenum.

In the right panel of figure 4.12 the numerical results are shown. It can be seen that the CIGS layer absorbs most irradiance up to a wavelength of 1.2  $\mu\text{m}$ . As a result the AM1.5 absorption factor of the CIGS layer is as much as 65.6%. The ZnO:Al layer absorbs most of the longer wavelength irradiance resulting in an AM1.5 absorption factor of 20.6% for this layer. Consequently, the AM1.5 absorption factor of the cell as a whole is 93.5%, which is by far the highest value obtained for all the cell technologies considered.

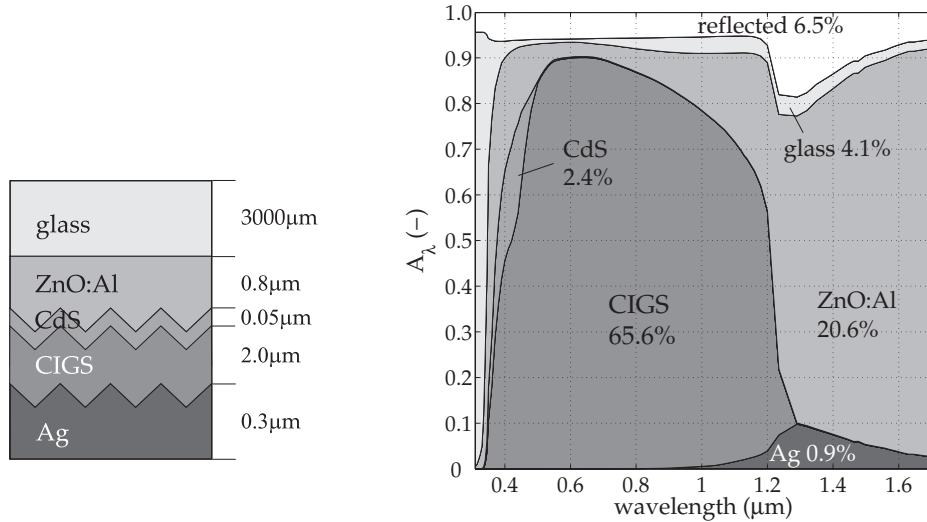


**Figure 4.12:** Area plot of the spectral absorption factor  $A_\lambda$  for each layer of the CIGS solar cell. The AM1.5 absorption factors are also given for each layer separately. The total AM1.5 absorption factor is 93.5%.

In practice a molybdenum back contact would have been used, which is much less reflective than both silver or aluminium. The simulation was repeated with an molybdenum back contact. Because only very little solar irradiance penetrates the CIGS layer and reaches the back contact, the results are hardly affected by the type of back contact. A molybdenum back contact would absorb 4.0% of the incident irradiance, increasing the AM1.5 absorption factor slightly from 93.5% to 94.0%.

Though it will generally reduce the electrical efficiency, it is possible to reduce the relative gallium content to  $x = 0$ . In that case copper indium diselenide (CIS) is obtained having an even smaller bandgap of 1.0 eV. The corresponding AM1.5 absorption factors are slightly higher, i.e. 94.2% and 94.3% for a silver and a molybdenum back contact respectively.

#### 4.4.6 Cell design

In this section it is discussed how the choice of semiconductor, the degree of light trapping and the back surface reflector affect the AM1.5 absorption factor of thin-film solar cells.



### Semiconductor bandgap

The AM1.5 absorption factor of the thin-film solar cell types considered above range from 81.4% for the a-Si cell to 93.5% for the CIGS cell. Because the layer thickness and interface properties of glass, ZnO:Al layer and back reflector were kept identical for all cell types, these differences in AM1.5 absorption factor are caused by differences in the semiconductor layers. Especially the bandgap energy of the semiconductor is important. Short-wavelength photons with an energy larger than the bandgap are readily absorbed in the semiconductor and the chance is very small that these photons are reflected by the back surface reflector and escape the cell. On the other hand, long-wavelength photons with an energy smaller than the bandgap are hardly absorbed in the semiconductor and are absorbed relatively weakly by free-carrier absorption in the TCO (ZnO:Al) layer. Despite efficient light-trapping, the chance that these photons are reflected by the back surface reflector and escape the cell is much larger. With this in mind it can be understood that a thin-film solar cell containing a layer with a small-bandgap semiconductor absorbs a larger part of the solar spectrum resulting in a larger AM1.5 absorption factor.

### Light-trapping

Because in thin-film solar cells the active layers are very thin, weakly absorbed irradiance can escape relatively easy if no efficient light-trapping scheme is used. The light trapping scheme normally used in thin-film cells consists of interfaces with texture to transmit incoming light as much as possible but reflect outgoing light internally.

In order to illustrate the importance of light-trapping, the simulations are repeated assuming poor light-trapping. Numerically the roughness of the interfaces is reduced to 0 which allows more irradiance to escape the cell. Light trapping is not completely turned off because the escape factor of 0.5 was maintained. The AM1.5 absorption factors for the cells with poor light-trapping are given in table 4.3. It can be seen that if light is trapped poorly in an a-Si cell, it has an AM1.5 absorption factor of only 67.5%. This is 13.9% less than in the reference case where light is trapped. This is in contrast with the CIGS cell, of which the AM1.5 absorption factor decreases by only 1.4% if light trapped poorly. It turns out that in the CIGS cell most irradiance is absorbed in the first pass through the active layer and to obtain a high absorption factor, efficient light trapping is less important.

### Back surface reflector

The influence of the back surface reflector *configuration* on the absorption factor will be considered now. In order to obtain a high electrical efficiency the reflection coefficient of the back surface reflector (BSR) should be as high as possible. Typically aluminium or silver BSR's are used. An aluminium BSR is cheaper than a silver

**Table 4.3:** The AM1.5 absorption factor  $A$  of the five thin-film cell types considered, with an Ag back contact and either poor or good optical confinement.

	Poor confinement			Good confinement		
	$\sigma$ (nm)	$f_{esc}$	$A$	$\sigma$ (nm)	$f_{esc}$	$A$
a-Si	0	0.5	67.5%	90	0.5	81.4%
$\mu$ c-Si	0	0.5	69.9%	90	0.5	86.6%
a-Si/ $\mu$ c-Si	0	0.5	77.7%	90	0.5	88.2%
a-Si/a-SiGe/ $\mu$ c-Si	0	0.5	78.7%	90	0.5	88.9%
CIGS	0	0.5	92.1%	90	0.5	93.5%

**Table 4.4:** The AM1.5 absorption factor of the thin-film cell types considered above, with the back contact structures Al, ZnO/Al, Ag and ZnO/Ag.

	Al	ZnO/Al	Ag	ZnO/Ag
a-Si	88.5%	84.0%	81.4%	78.8%
$\mu$ c-Si	90.4%	88.0%	86.6%	85.3%
a-Si/ $\mu$ c-Si	89.6%	88.3%	88.2%	87.6%
a-Si/a-SiGe/ $\mu$ c-Si	91.1%	89.3%	88.9%	88.0%
CIGS	93.5%	93.5%	93.5%	93.5%

one, however an aluminium BSR is less reflective than silver, especially for near infrared irradiance. To increase the reflection coefficient, a thin layer of undoped ZnO can be added between the semiconductor and the metal. The optical thickness of this ZnO layer is chosen such that constructive interference occurs in the top of the coating to maximise the reflection coefficient. The ZnO layer can be considered as a reflective coating, with a working principle similar to the working principle of an anti-reflective coating described in section 2.2.2. However, to obtain constructive instead of destructive interference the ideal reflective coating has an optical thickness of  $\lambda/2$  instead of  $\lambda/4$ .

Aluminium has the lowest reflection coefficient, followed by ZnO/Al, Ag and ZnO/Ag, respectively. In the numerical simulations presented above an Ag BSR was assumed. In table 4.4 the AM1.5 absorption factors are given for the same cells but with the other BSR's as well. It can be seen that the AM1.5 absorption factor of the a-Si solar cell is very sensitive to the reflection coefficient of the BSR. In case of the highly reflective ZnO/Ag BSR the AM1.5 absorption factor is 78.8%, while for the somewhat less reflective Al BSR the AM1.5 absorption factor is 88.5%. Because in the CIGS cell only a small amount of irradiance reaches the BSR, the AM1.5 absorption factor of this cell is not very sensitive to variations in BSR.

**Table 4.5:** Typical electrical cell efficiencies for the thin-film solar cell technologies considered in this chapter.

technology	$\eta_e$ (%)	source
a-Si	7	[8, 7]
$\mu\text{c-Si}$	8	[8]
a-Si/ $\mu\text{c-Si}$	11	[75, 79]
a-Si/a-SiGe/ $\mu\text{c-Si}$	15	[75]
CIGS	11	[8]

## 4.5 The effective absorption factor of thin-film solar cells

In section 4.4, the AM1.5 absorption factor  $A$  was considered for different thin-film solar cell technologies. In this section, the electrical efficiency  $\eta_e$  is considered as well. As already mentioned in section 1.3,  $A$  and  $\eta_e$  are defined as the fractions of incident solar irradiance that are absorbed and converted into electricity, respectively. For the thermal efficiency of a PVT collector the effective absorption factor ( $A_{\text{eff}} = A - \eta_e$ ) is the most relevant cell parameter.  $A_{\text{eff}}$  represents the fraction of incident solar irradiance that is converted into heat.

In this section,  $A_{\text{eff}}$  will be investigated for the configurations already presented in section 4.4 having an aluminium or silver back surface reflector and good or poor optical confinement. In order to determine  $A_{\text{eff}}$ , an estimate is required of the electrical efficiency  $\eta_e$ . For each of the thin-film solar cell technologies typical cell efficiencies are given in table 4.5. Note that for a-Si,  $\mu\text{c-Si}$  and CIGS current industrial scale efficiencies are reported, while for the more novel tandem and triple junction cells, laboratory scale efficiencies are reported which might be obtained in the future on industrial scale as well [7].

By varying the degree of optical confinement or the reflection coefficient of the back surface reflector (BSR) of a thin-film solar cell, not only the cell's absorption factor  $A$  is affected, but its electrical efficiency  $\eta_e$  is affected as well. It is assumed here that the electrical efficiencies given in table 4.5 correspond to solar cells having good optical confinement and a reflective silver BSR. In case of poor optical confinement or a less reflective aluminium back contact, the electrical efficiency will decrease somewhat. In this section it is assumed that  $\eta_e$  is proportional to  $A_{\text{act}}$ , the sum of the absorption factor of all *active* semiconductor layers in the cell. In case of multi-junction cells, the matching of the current between the top and bottom cell is not considered. Because in absolute terms the decrease of  $\eta_e$  will turn out to be small compared to the variations in  $A$ , it is justified to use this somewhat crude assumption when determining  $A_{\text{eff}}$ .

In table 4.6 the results are shown. For the a-Si thin-film solar cell technology, configuration Ib is the reference configuration, having good optical confinement and

**Table 4.6:** The absorption factor ( $A$ ), electrical efficiency ( $\eta_e$ ) and effective absorption factor ( $A_{\text{eff}}$ ) of five different thin-film solar cell technologies. Configurations having good or poor optical confinement (con.) and having an Ag or an Al back surface reflector (BSR) are considered.

conf.	technology	con.	BSR	$A$ (%)	$A_{\text{act}}$ (%)	$\eta_e$ (%)	$A_{\text{eff}}$ (%)
Ia	a-Si	poor	Ag	67.5	28.5	6.1	61.4
Ib	a-Si	good	Ag	81.4	32.6	7.0	74.4
Ic	a-Si	good	Al	88.5	30.2	6.5	82.0
IIa	$\mu\text{c-Si}$	poor	Ag	69.9	31.2	6.3	63.6
IIb	$\mu\text{c-Si}$	good	Ag	86.6	39.7	8.0	78.6
IIc	$\mu\text{c-Si}$	good	Al	90.4	34.3	6.9	83.5
IIIa	a-Si/ $\mu\text{c-Si}$	poor	Ag	77.7	40.7	9.7	68.0
IIIb	a-Si/ $\mu\text{c-Si}$	good	Ag	88.2	46.2	11.0	77.2
IIIc	a-Si/ $\mu\text{c-Si}$	good	Al	89.6	44.3	10.5	79.1
IVa	a-Si/a-SiGe/ $\mu\text{c-Si}$	poor	Ag	78.7	43.7	13.2	65.5
IVb	a-Si/a-SiGe/ $\mu\text{c-Si}$	good	Ag	88.9	49.6	15.0	73.9
IVc	a-Si/a-SiGe/ $\mu\text{c-Si}$	good	Al	91.1	45.5	13.8	77.3
Va	CIGS	poor	Ag	92.1	64.6	10.8	81.3
Vb	CIGS	good	Ag	93.5	65.6	11.0	82.5
Vc	CIGS	good	Al	93.5	65.6	11.0	82.5

a reflective Ag BSR. As already shown in section 4.4, this configuration has  $A = 81.4\%$  and combined with  $\eta_e = 7\%$  (see table 4.5) this gives  $A_{\text{eff}} = A - \eta_e = 74.4\%$ . So for this configuration 74.4% of the incident solar irradiance is converted into heat.

If optical confinement is poor (configuration Ia), more near- and sub-bandgap irradiance is lost by reflection, reducing the overall absorption factor ( $A$ ) to 67.5%. The absorption factor of the active layer  $A_{\text{act}}$  is reduced as well, i.e. from 32.6% to 28.5%. Assuming a reduction of  $\eta_e$  proportional to the reduction of  $A_{\text{act}}$ , it is found  $\eta_e = 6.1\%$  and consequently  $A_{\text{eff}} = 61.4\%$ .

If optical confinement is good but a less reflective Al BSR is used (configuration Ic), more irradiance is absorbed by the BSR, increasing  $A$  to 88.5%. However, because less irradiance is absorbed in the active layer,  $A_{\text{act}}$  is reduced (with respect to configuration Ib) and therefore  $\eta_e$  is reduced as well. As a result of both the increase of  $A$  and the decrease of  $\eta_e$ ,  $A_{\text{eff}}$  has increased to as much as 82.0%. For all cell technologies (except for CIGS) the same trends can be observed:

- If optical confinement is poor,  $A_{\text{eff}}$  is relatively low (61-68%).
- By improving the optical confinement,  $A_{\text{eff}}$  increases to 74-78% with Ag BSR.
- In case a less reflective Al BSR is used instead of an Ag BSR,  $A_{\text{eff}}$  increases

further to as much as 77-84%, but the electrical efficiencies drop by 0.5 to 1.2% absolute.

Note that the increase in  $A_{\text{eff}}$  is primarily caused by an increase in  $A$ . The increase of  $\eta_e$  in case of improvement of optical confinement and the decrease of  $\eta_e$  in case of application of a less reflective BSR, being both in the order of 1% absolute, are of secondary importance to  $A_{\text{eff}}$ . Because of the low bandgap of CIGS, the CIGS thin-film solar cells have a very high  $A_{\text{eff}}$  of 81-82%, regardless of the degree of optical confinement and the type of BSR.

## 4.6 Discussion and concluding remarks

The numerical model described in chapter 2 has been validated for thin-film solar cells by comparing results of optical simulations with spectral reflection and transmission factors measured for a set of amorphous silicon based test samples. Most important effects turn out to be captured by the optical model quite well over a broad wavelength range. Scattering of light by rough surfaces, having a roughness of approximately 90 nm, can be described successfully using the haze parameter. As was the case for the crystalline silicon solar cells, also for thin-film solar cells a so-called escape factor is required to model trapping of sub-bandgap irradiance.

For the five thin-film solar cell technologies considered, the spectral absorption factor was determined by means of numerical simulation. It turns out that most short-wavelength irradiance ( $E_{\text{ph}} > E_g$ ) is absorbed by band-to-band absorption in the semiconductor layer(s). Longer wavelength irradiance ( $E_{\text{ph}} < E_g$ ) is hardly absorbed in the semiconductor, but is either absorbed by free-carrier absorption in the transparent conductive oxide, absorbed by the back contact, or lost by reflection. Here the bandgap  $E_g$  of the semiconductor determines at which wavelength the transition occurs. In case a semiconductor having a low bandgap is applied, this transition occurs at larger wavelengths. Because this reduces reflection loss of near infrared irradiance, this results in a higher AM1.5 absorption factor for the cell as a whole.

For solar cells applied in a photovoltaic/thermal collector, both a high electrical efficiency and a high AM1.5 absorption factor are desirable. The ongoing developments aim at improving optical confinement, resulting in an increase of both the electrical efficiency and the absorption factor. Therefore this is beneficial on both fronts.

More reflective back surface reflectors are being developed as well. However, regarding the reflection coefficient of the back surface reflector, there is a trade-off between the electrical efficiency and the absorption factor. A more reflective back surface reflector will increase the electrical efficiency somewhat but will reduce the absorption factor.

**Table 4.7:** The AM1.5 absorption factor  $A$ , the cell efficiency  $\eta_e$  and the effective absorption factor  $A_{\text{eff}}$  for various solar cell types. Both current and expected future values are given.

	$A$ (%)	$\eta_e$ (%)	$A_{\text{eff}}$ (%)
<b>c-Si</b>			
H-pattern (current)	85	15	70
PUM (current)	87	16	71
PUM (future)	87	18	69
EWT (near future)	90	17	73
2020 design	91	20	71
2030 design	91	25	66
<b>a-Si based thin film</b>			
current	88	9	79
2020 design	89	12	77
2030 design	89	15	74
<b>CIGS thin film</b>			
current	93	11	82
2020 design	93	15	78
2030 design	93	17	76

If one considers those thin-film cells that have a relatively good spectral utilisation (a-Si/ $\mu\text{c-Si}$ , a-Si/a-SiGe/ $\mu\text{c-Si}$  and CIGS) then the absorption factor is in the range of 88 to 93% (see table 4.7). Taking into account the current cell efficiencies, the corresponding  $A_{\text{eff}}$  ranges from 79 to 82%. In future cell designs, the absorption factor  $A$  will hardly increase any further because both the light incoupling and the optical confinement are already quite good. The cell efficiencies will increase however. Taking into account the cell efficiencies for the various solar cell technologies as predicted in the Strategic Research Agenda [7], one finds an  $A_{\text{eff}}$  of 77-78% by the year 2020 and 74-76% by the year 2030 for thin-film solar cells, see table 4.7.

The effective absorption factor of  $A_{\text{eff}}$  that can be expected for thin-film solar cells will continue to be significantly higher than for crystalline silicon solar cells because also in future the electrical efficiencies of thin-film solar cells will continue to be significantly lower compared to those of crystalline silicon solar cells, see table 4.7.



# The annual yield of PVT systems

## 5.1 Introduction

In chapters 3 and 4, insight was gained in the effective absorption factor of crystalline silicon and thin-film solar cells. The effective absorption factor, defined as the fraction of incident solar energy converted into heat (see equation 1.4), is an important parameter regarding the thermal efficiency of photovoltaic/thermal (PVT) solar collectors. As described in section 1.4, these PVT collectors deliver both electricity and heat, with the solar cells generating the electricity and acting as the thermal absorber at the same time. The heat is transferred as much as possible to a heat-transporting medium to be used effectively, e.g. for domestic tap water heating.

Using the insight gained in previous chapters, the electrical and thermal efficiencies of systems with PVT collectors are investigated in this chapter. Additionally, more insight is gained in the specific loss mechanisms that are inherent to PVT collectors. One of the tools used here is the comparison of the electrical and thermal efficiency of a PVT collector system with a separate PV system (generating electricity only) and a solar thermal collector system (generating heat only). The insight gained is used to investigate how the electrical and thermal efficiencies of PVT collector systems can be optimised.

Which efficiency loss mechanism is dominant depends very much on the operating conditions. An important operating condition is the temperature level of the heat transporting medium which in turn depends on the application for the heat, e.g. pool heating, room heating, domestic hot water or industrial processes. The siz-



ing of system components around the PVT collector will turn out to be important as well. Therefore not the efficiency of just the PVT collector, but the efficiency of the system as a whole needs to be considered. Because weather conditions, such as solar irradiance and ambient temperature, vary in daily and annual cycles, *annual* system efficiencies will be considered.

In this chapter the focus is on the glazed sheet-and-tube PVT collector design. Thermally this design is based on the design of the glazed solar thermal collector, frequently applied at moderate latitudes e.g. Central and Northern Europe. Medium temperature applications (30-60 °C) of domestic hot water and room heating for a single-family household are considered. Dutch climatological conditions will be used in the analysis. Note that an analysis of the economical or energy payback time of PVT systems is outside the scope of this thesis.

De Vries has developed three PVT collector models with varying degree of complexity: a three-dimensional time dependent model, a two-dimensional steady state model and a one-dimensional steady state model [20]. By comparing these models to experimental results, he concluded that the one-dimensional steady state model is accurate enough for annual yield simulations. The PVT collector model used in this thesis is based on this one-dimensional steady state model.

De Vries [20] and Zondag [21, 80] also performed annual yield simulations for several PVT collector designs in Dutch climatological conditions. Others have studied the annual yield of PVT collectors for a range of systems designs and climatological conditions [81, 82, 83]. As indicated above, in this thesis the focus will be on the glazed sheet-and-tube collector in Dutch climatological conditions, previously studied by de Vries and Zondag. However, the more accurate solar cell absorption factors derived in chapters 3 and 4 are used and the model for heat storage has been improved. In addition, the energy loss mechanisms are studied in relation to system sizing. The optical model described in chapter 2 is used to investigate the feasibility of applying optical coatings to the PVT collector.

In section 5.2 the sheet-and-tube PVT collector design is introduced and the thermal model of this collector by Zondag will be highlighted. In section 5.3, PVT systems for domestic hot water and for combined domestic hot water and room heating and the corresponding models are introduced. In section 5.4 the numerical results regarding the annual yield of PVT systems are presented and in section 5.5 this yield is compared to the yield of separate photovoltaic and thermal systems. Finally in section 5.6 some conclusions are presented.

## 5.2 PVT collector

A wide variety of PVT collectors exists and they are being used in a range of systems [19]. One example is the ventilated PV facade where the heated ventilation air is used for room heating. Another example is the PVT concentration system where

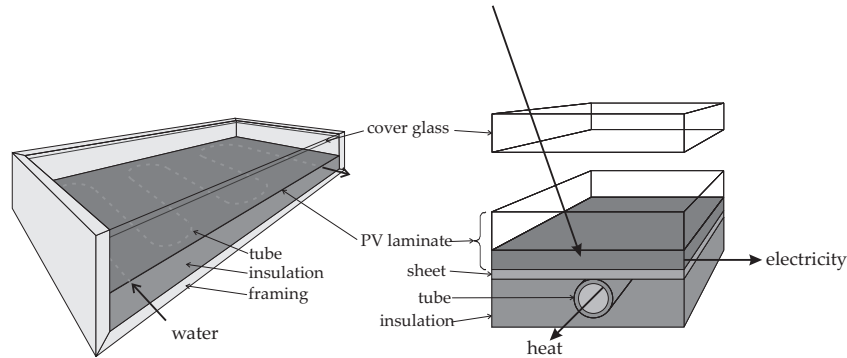


**Figure 5.1:** A one-cover flat-plate sheet-and-tube PVT collector, converting incident solar irradiance into both electricity and heat. Left: the complete collector. Right: A detailed cross-section.

solar cells under concentrated sunlight are actively cooled and the heat extracted is used. However, flat-plate PVT collectors are seen as the main future market product [19]. These can be either glazed or unglazed collectors and either air or a liquid can be used as a heat transporting medium. Zondag concluded that under Dutch climatological conditions, the one-cover sheet-and-tube design represents a good compromise between electrical and thermal yield [21]. Therefore, in this thesis the focus is on this glazed sheet-and-tube design, using water as heat transporting medium.

### 5.2.1 Sheet-and-tube collector design and definitions

The sheet-and-tube design is schematically shown in figure 5.1. At the heart there is the PV laminate, generating electricity. The heat generated in the laminate is extracted by a copper sheet at the back. Connected to this sheet is a serpentine shaped tube through which water flows collecting the heat. In order to reduce heat loss to the ambient, the backside is thermally insulated and at the front there is a cover glass. The stagnant air layer provides thermal insulation. This design is similar to a glazed solar thermal collector with the spectrally selective absorber replaced by a PV laminate.

#### Thermal efficiency

The thermal efficiency of the collector is defined as the fraction of the incident solar irradiance that is extracted from the collector by the flow of water through the tube

$$\eta_{\text{th}}^{\text{col}} \equiv \frac{P_{\text{w}}^{\text{col}}}{P_{\text{sun}}^{\text{col}}}, \quad (5.1)$$

where  $P_w^{\text{col}}$  is the thermal power extracted by the water and  $P_{\text{sun}}^{\text{col}}$  is the incident solar power, given by

$$P_{\text{sun}}^{\text{col}} = a^{\text{col}} I_{\text{sun}} , \quad (5.2)$$

where  $a^{\text{col}}$  is the aperture area of the collector and  $I_{\text{sun}}$  is the power density of incident solar irradiance above the cover glass. The power extracted by the flow of water through the tube is given by

$$P_w^{\text{col}} = \phi_c c_w (T_{w,\text{out}}^{\text{col}} - T_{w,\text{in}}^{\text{col}}) , \quad (5.3)$$

where  $\phi_c$  is the mass flow rate and  $c_w$  is the specific heat of water and  $T_{w,\text{in}}^{\text{col}}$  and  $T_{w,\text{out}}^{\text{col}}$  are the temperature of the water flowing into and out of the collector, respectively.

### Absorption factor and electrical efficiency

In previous chapters the absorption factor and electrical efficiency were considered on *cell* level. In this section these parameters are considered on the level of the *collector*. Therefore it has to be taken into account that several cells are brought together in a PV laminate, which is placed behind a cover glass. In case c-Si solar cells are used in the PV laminate, the cells are connected in series and form a string. In order to provide room for the electrical connections and to prevent a short circuit, there is a spacing of a few millimetre between the cells mutually and space between the cells and the edge of the laminate. The total surface area of the collector  $a^{\text{col}}$  therefore consists of cell area  $a^{\text{cell}}$  and spacing area  $a^{\text{space}}$ . The packing density of the laminate is defined as the fraction collector area taken up by cells,

$$\rho = \frac{a^{\text{cell}}}{a^{\text{col}}} . \quad (5.4)$$

Typically the packing density for c-Si cells is approximately 0.9. For thin-film solar cells the same packing density is assumed.

The AM1.5 absorption factor of the PV laminate in the collector  $A^{\text{col}}$  is the relevant absorption factor when it comes to the thermal efficiency of the collector. This absorption factor is given by

$$A^{\text{col}} = \tau^* (\rho A^{\text{cell}} + (1 - \rho) A^{\text{space}}) , \quad (5.5)$$

where  $\tau^*$  is the effective transmittance of the cover glass,  $A^{\text{cell}}$  is the AM1.5 absorption factor of the cell which was discussed in chapters 3 and 4 in great detail and  $A^{\text{space}}$  is the absorption factor of the spacing. Through the spacing between c-Si cells the rear-side foil used for encapsulating the cells is visible. In most PV applications *white* Tedlar<sup>®</sup> is used in the rear-side foil to reflect as much light as possible. A small part of this reflected light may reach the cell (e.g. after internal reflection at the glass/air interface) and be converted into electricity. However, in PVT applications where a high absorption factor is desirable, a black rear material is normally used,

absorbing most irradiance falling between the cells. The AM1.5 absorption factor of the spacing area was found to be 93.5%. This value was determined by measuring the spectral reflection factor of a sandwich of glass, EVA and a black Tedlar® rear-side foil.

The effective transmittance of the cover glass  $\tau^*$  appears in equation 5.5 to take into account the fact that some light is not transmitted by the cover glass and does not reach the PV laminate.  $\tau^*$  also takes into account the effect of multiple reflections between the laminate and the cover glass and its value is determined using the optical model described in chapter 2. In case of a low iron content cover glass,  $\tau^*$  has a typical value of 92% and in case anti-reflective coatings are applied to both sides of the cover glass, this value increases to 96.5%.

The electrical efficiency of the collector is defined as the fraction of the incident irradiance that is converted into electricity. For now Standard Test Conditions (STC) are assumed, i.e. a cell temperature of 25 °C, a solar irradiance of 1000 W/m<sup>2</sup> and the standard AM1.5 solar spectrum. The effect of other than standard conditions will be discussed in section 5.2.2.

Because some irradiance is not transmitted by the cover glass and because irradiance absorbed in the spacing between the cells is not converted into electricity, the electrical STC efficiency of the collector  $\eta_e^{\text{col,STC}}$  is smaller than the electrical STC efficiency of the cells used  $\eta_e^{\text{cell,STC}}$ , i.e.

$$\eta_e^{\text{col,STC}} = \tau^* \rho \eta_e^{\text{cell,STC}} . \quad (5.6)$$

### 5.2.2 Collector model

As mentioned in section 5.1, de Vries developed a one-dimensional model [20]. This model is a modified version of a steady-state thermal model for thermal collectors, developed by Hottel and Whillier [84], being widely used for thermal collectors.

De Vries incorporated electricity production in his one-dimensional model, making the model suitable for PVT collectors as well [20]. Zondag refined this model further and used it to analyse the performance of several flat plate PVT collector designs [21, 80]. For the work presented in this chapter, the thermal part of this refined model was used without modifications. Below, the working principles of this model are given briefly. For details, please refer to the original publications [20, 80].

#### Thermal model

The objective of the model is to determine the thermal efficiency of a solar thermal PVT collector  $\eta_{\text{th}}^{\text{col}}$ . The incident power is simply given by equation 5.2. The task of the model therefore is to simulate the heat flows inside the collector in order to determine how much of the heat generated in the absorber (i.e. the PV laminate) is transferred to the water flowing through the tube and how much is lost to the ambient.

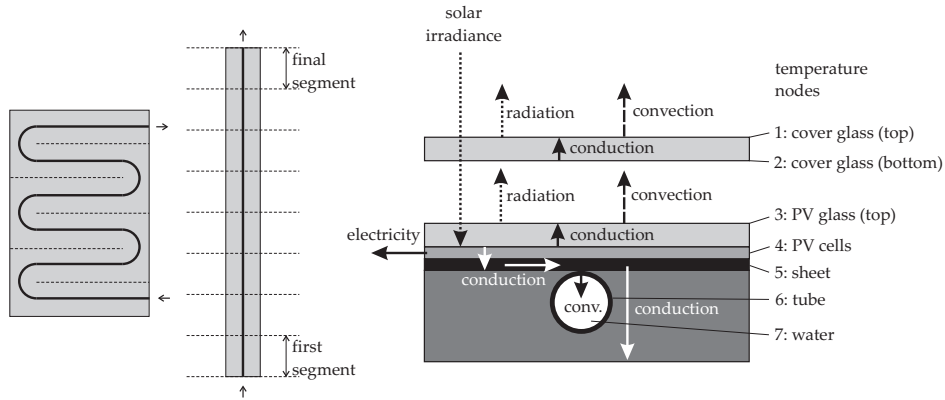


**Figure 5.2:** Left: A simplification of the model by straightening the serpentine tube and thereby ‘stretching out’ the collector. Cross-section of the stretched out PVT collector with the energy flows and temperature nodes in the thermal model indicated.

The problem is simplified by ‘stretching’ the serpentine geometry of the tube to a straight tube as indicated in the left panel of figure 5.2. This stretched out collector is then divided into a number of segments and the heat flow in each segment is analysed. The cross-section of a single segment is shown in the right panel of figure 5.2. The temperature nodes used in the model are indicated in the figure. These are the top and bottom of the cover glass, the top of the PV laminate, the PV cells, the sheet, the tube wall and the water inside the tube. The heat resistance between each node is determined, taking into account heat transport by convection, radiation and conduction (indicated by the arrows in the right panel of figure 5.2). Nusselt relations are used to describe heat transport by natural and forced convection. Weather conditions, like solar irradiance, ambient temperature, sky temperature (for radiation) and wind speed and the temperature of the water flowing in the tube when entering the segment are used as boundary conditions. By solving the energy balance at each node in a single segment, the heat fluxes are determined. The heat flux going to the water is used to determine the temperature increase of the water going through the segment.

The inflowing water temperature of the *first* segment is the given collector inflow temperature  $T_{w,in}^{col}$ . By solving the energy balances in the first segment the temperature is calculated of the water leaving this first segment and entering the second segment. By consecutively solving the heat balances in every segment, the temperature of the water leaving the collector  $T_{w,out}^{col}$  is determined. By substituting  $T_{w,in}^{col}$  and  $T_{w,out}^{col}$  into equation 5.3 the thermal power extracted from the collector  $P_w^{col}$  is determined. By substituting this into equation 5.1 the thermal collector efficiency  $\eta_{th}^{col}$  is calculated.

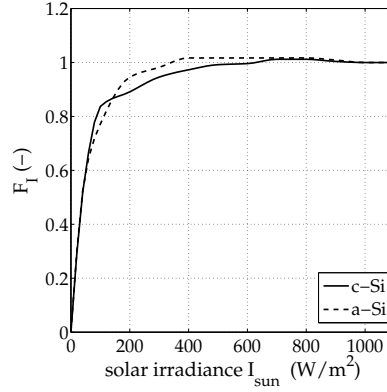


Figure 5.3: The solar irradiance factor  $F_I$  as a function of  $I_{\text{sun}}$ .

### Electrical model

The objective of the electrical model is to determine the actual electrical efficiency of the PVT collector. This model is connected to the thermal model because the electrical power generated by the PV cells is an important parameter in the energy balance in the thermal model. Note that the electrical energy extracted from the cells, is not available anymore in the form of heat. Furthermore, the cell temperature  $T_{\text{cell}}$  determined by the thermal model is an important parameter for determining the actual electrical efficiency  $\eta_e^{\text{col}}$ . This efficiency is a function of both the cell temperature  $T_{\text{cell}}$  and of the actual irradiance  $I_{\text{sun}}$  and can be approximated by

$$\eta_e^{\text{col}} = \eta_e^{\text{col,STC}} F_I F_T, \quad (5.7)$$

where  $\eta_e^{\text{col,STC}}$  is the collector's electrical efficiency at STC, given by equation 5.6 and  $F_I$  and  $F_T$  describe the dependence of the electrical efficiency on  $I_{\text{sun}}$  and  $T_{\text{cell}}$ . In figure 5.3,  $F_I$  is shown versus  $I_{\text{sun}}$ . This is an empirical curve that depends on the precise cell technology that is considered.

Within the practical temperature range  $F_T$  can be considered to be linear,

$$F_T = 1 + \beta(T_{\text{cell}} - 25 \text{ } ^\circ\text{C}), \quad (5.8)$$

where  $\beta$  is the temperature coefficient for electrical efficiency. For c-Si cells  $\beta = -0.0045 \text{ } /^\circ\text{C}$  [23] and for a-Si cells  $\beta = -0.002 \text{ } /^\circ\text{C}$  [23], indicating that the electrical efficiency c-Si cells is more sensitive to cell temperature.

### 5.2.3 Assumptions in the collector model

#### Temperature dependence

It is assumed that the absorption factor of the cells  $A^{\text{cell}}$  is independent of cell temperature. The absorption factors used here were calculated in chapter 3 and 4 using the optical properties of the semiconductors at a temperature of 27 °C (300 K). However, in a glazed PVT collector the operational cell temperature can range roughly from 0 to 150 °C.

As measured by Rajkanan [85], the bandgap of c-Si at 143 °C has shifted to larger wavelengths by about 0.04  $\mu\text{m}$ , compared to c-Si at 27 °C. Using the optical properties of c-Si at 143 °C instead of at 27 °C in the numerical model for determining the absorption factor, it is found that the absorption factor increases by only 0.5% absolute as a result of the bandgap shift. Because in the typical temperature range mentioned above this effect is relatively small, the temperature dependence of the absorption factor is not taken into account.

#### Collector lay-out

PVT systems with collector areas of 3, 6, 12 and 24  $\text{m}^2$  will be considered in this thesis. It is assumed that a single collector has a surface area of 3  $\text{m}^2$ . To obtain the areas given above, 1, 2, 4 or 8 collectors are connected in series. It is assumed that the outflow temperature of one collector is the inflow temperature of the next one.

An important issue in PVT collectors is the heat transfer between the PV cells and the heat conducting sheet at the back. An as high as possible heat transfer is desirable to maximise the electrical and thermal efficiencies. The PV laminate can be glued to the sheet or the sheet can be laminated together with the cells. A relatively low heat transfer coefficient of 45  $\text{W}/\text{m}^2\text{K}$  was measured by de Vries [20] in case of a glued PV laminate. Zondag [21] calculates that by using a thin layer of heat conducting glue, a heat transfer coefficient as high as 500  $\text{W}/\text{m}^2\text{K}$  can be obtained theoretically. In this thesis an intermediate heat transfer coefficient of 120  $\text{W}/\text{m}^2\text{K}$  is assumed.

The sheet is normally made of copper and has a serpentine shaped copper tube soldered to it. The effective heat resistance along the sheet to the tube is mainly determined by the thickness of the copper sheet and the spacing of the tube. In this thesis a sheet thickness of 0.2 mm, a tube diameter of 10 mm and a spacing of 10 cm is assumed, resulting in an effective heat transfer coefficient of about 200  $\text{W}/\text{m}^2\text{K}$ .

Finally there is a heat resistance between the wall of the tube and the water. In case the flow through the tube is laminar, then heat transfer coefficient is only 86  $\text{W}/\text{m}^2\text{K}$ , but in most cases considered in this thesis, the flow will be turbulent, corresponding to a high heat transfer coefficient of about 700  $\text{W}/\text{m}^2\text{K}$ .

The heat transfer from cell to sheet to tube to water can be represented by heat resistances connected in series and the corresponding overall or effective transfer coefficient  $h_{\text{eff}}$  ranges from 40  $\text{W}/\text{m}^2\text{K}$  in case of laminar flow to 70  $\text{W}/\text{m}^2\text{K}$  in case

**Table 5.1:** The default weather conditions and collector characteristics used as input for the collector simulations presented in this section.

Weather conditions		Collector characteristics	
ambient temp.	$T_{\text{amb}} = 20 \text{ }^\circ\text{C}$	lam. absorption factor	$A^{\text{col}} = 0.80$
sky temperature	$T_{\text{sky}} = 10 \text{ }^\circ\text{C}$	lam. emissivity	$\varepsilon = 0.90$
wind speed	$v_{\text{wind}} = 2.0 \text{ m/s}$	lam. electrical STC eff.	$\eta_e^{\text{col,STC}} = 0.15$
solar irradiance	$I_{\text{sun}} = 750 \text{ W/m}^2$	specific flow rate	$\phi_s = 10 \text{ kg/m}^2\text{h}$
		collector inlet temp.	$T_{\text{win}}^{\text{col}} = 20 \text{ }^\circ\text{C}$

of turbulent flow. The temperature difference between the cells and water is given by  $\Delta T = q_{\text{cw}}/h_{\text{eff}}$ , where  $q_{\text{cw}}$  is the heat flux from cell to water. In case of high solar irradiance ( $1000 \text{ W/m}^2$ ) and low reduced temperature ( $T_{\text{red}} = 0 \text{ }^\circ\text{Cm}^2/\text{W}$ ) the heat flux  $q_{\text{cw}}$  can reach high values of typically  $500 \text{ W/m}^2$ . In these circumstances the  $\Delta T$  will be  $13 \text{ }^\circ\text{C}$  in case of laminar flow and  $7 \text{ }^\circ\text{C}$  in case of turbulent flow.

#### 5.2.4 Illustration of the collector model

In order to gain some insight in the thermal collector model, some aspects are illustrated. The weather conditions and collector characteristics used here, are summarised in table 5.1.

##### Specific flow rate

The water flow rate  $\phi_c$  used in a thermal collector is normally chosen proportional to the collector surface area  $a^{\text{col}}$ . The specific flow rate  $\phi_c/a^{\text{col}}$  is then kept constant. In the left panel of figure 5.4 the temperature of the water versus the relative distance along the tube is plotted for various specific flow rates. It can be seen that for a very low specific flow rate of  $1.0 \text{ kg/m}^2\text{h}$ , the water in the tube rapidly heats up and approaches a temperature of  $100 \text{ }^\circ\text{C}$ . For this collector and under these weather conditions, this is the water temperature at which the amount of solar energy absorbed is exactly balanced by the amount of energy lost to the ambient.

For higher specific flow rates, the water leaves the collector before it can reach  $100 \text{ }^\circ\text{C}$ . Because the average water temperature is lower, less heat is lost to the ambient and a higher thermal efficiency is obtained. However, multiple passes through the collector may be required to reach the desired temperature level.



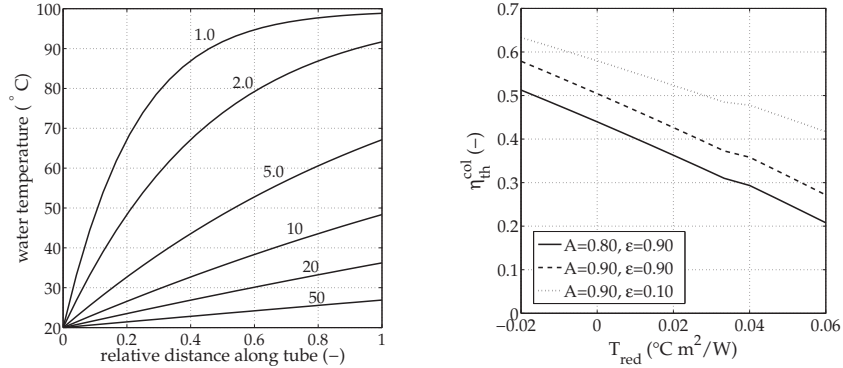


**Figure 5.4:** Numerical results obtained from the collector model. Left: Water temperature along the collector tube for various specific flow rates (expressed in  $kg/m^2h$ ). Right: Thermal collector efficiency  $\eta_{th}^{col}$  at a specific flow rate of  $10 kg/m^2h$  as a function of reduced temperature  $T_{red}$  for three different combinations of PV laminate absorption factor and emissivity.

### Reduced temperature

The reduced temperature is defined as,

$$T_{red} = \frac{T_{w,in}^{col} - T_{amb}}{I_{sun}}, \quad (5.9)$$

where  $T_{w,in}^{col}$  is the collector inflow temperature,  $T_{amb}$  is the ambient temperature and  $I_{sun}$  is the solar irradiance. In the previous section a reduced temperature of  $0^{\circ}C/(W/m^2)$  was considered. In case of a higher reduced temperature, the thermal efficiency of the collector will deteriorate because more heat is lost to the ambient. This was simulated by increasing the collector inflow temperature. The results are shown as the solid line in the right panel of figure 5.4. It can be seen that for higher reduced temperatures the collector efficiency is lower. The thermal collector efficiency versus  $T_{red}$  is often used to characterise the performance of a certain collector.

If the absorption factor of the PV laminate is increased from 0.80 to 0.90, this increases the thermal efficiency uniformly (dashed line in the right panel of figure 5.4). The effect of additionally reducing the emissivity of the laminate from 0.90 to 0.10 increases the thermal efficiency as well. Furthermore the slope of the curve has become less negative (dotted line), making the thermal efficiency somewhat less sensitive to  $T_{red}$ .

## 5.3 PVT systems

The PVT solar collector converts sunlight into both electricity and heat. However, because the sun is an intermittent energy source, there may be a temporal mismatch between the supply and demand of energy. Therefore a form of energy storage, forming a buffer between supply and demand, may be useful.

Electrical energy can be stored in batteries. However, in grid-connected applications, the public electricity grid can serve as a virtual storage. Electrical energy generated by the PVT collector can be supplied to the grid at one time and energy can be extracted again from the grid at a later time. An inverter is required to convert the direct current from the solar cells into alternating current at 230 V that can be supplied to the grid. Also for the collected heat some form of storage is required. In domestic applications heat is mostly stored as sensible heat, e.g. as hot water in a storage vessel. All this illustrates that a PVT *system* can contain other elements such as inverter and storage tank, besides PVT collectors.

Two types of PVT system will be considered here: a PVT collector system for domestic hot water and a PVT collector system for combined domestic hot water and room heating (shown in figure 5.5). The systems are subjected to Dutch climatological conditions and typical Dutch single-family household heat demands for domestic hot water and room heating are assumed. Glazed sheet-and-tube PVT collectors are considered facing south under an inclination of  $45^\circ$ .

The correct sizing of the different elements in the PVT system is important for obtaining a good system efficiency. Especially collector area and heat storage capacity in relation to the heat demand play an important role. Therefore first the sizing of practical solar thermal systems is discussed briefly. Then the PVT system model is introduced and finally this model is illustrated for one particular case.

### 5.3.1 System sizing of practical solar thermal system

#### Domestic hot water

Solar domestic hot water systems typically have a collector area of 4 to 6 m<sup>2</sup> [86]. The volume of the storage tank is generally chosen such that the tank can contain the heat demand of one or two days. The demand for domestic hot water of a single-family household is about 150 l per day. Therefore typical storage volumes of 200 to 300 l are encountered in practice [86]. Having a larger than standard storage volume would hardly improve the annual thermal system efficiency.

#### Combined domestic hot water and room heating

Solar thermal collector systems for combined domestic hot water and room heating typically have a collector area of about 12 m<sup>2</sup> [86]. The heat demand for room

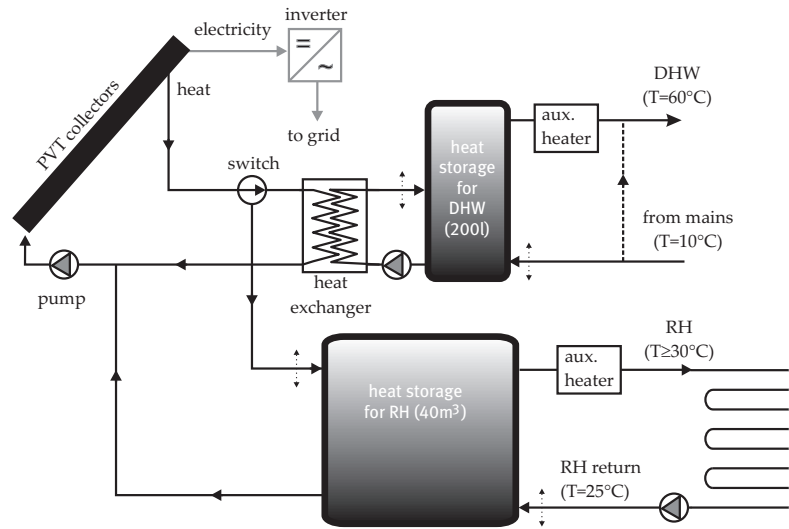


**Figure 5.5:** Schematic overview of the PVT system for combined domestic hot water and room heating. Dotted vertical arrows indicate variable inflow height of water into the storage tanks.

heating exists mainly in winter, when heat supply by the collectors is lowest. Therefore, in the ideal case the storage volume should be large enough to contain a large part of the annual heat demand. A heat storage containing tens of cubic metres of water would be required to store the total heat demand of the entire heating season. Because this is unpractically large, typical systems have a storage tank of about 1000 l [86]. Although less typical, in practice storage volumes of tens of cubic metres per household are encountered in seasonal heat storage for district room heating [87].

### 5.3.2 System model

The standard PVT system for domestic hot water considered in this thesis, has a collector surface area of 6 m<sup>2</sup> in combination with a 200 l storage tank. The standard PVT system for combined domestic hot water and room heating considered in this thesis, has a collector surface area of 12 m<sup>2</sup> in combination with a 200 l storage tank for domestic hot water and a 40 m<sup>3</sup> storage tank for room heating (see figure 5.5). Note again that this large storage volume is less typical and represents an extreme case. For both systems also half and double collector areas will be considered, however each time the tank volume and heat demand is kept constant.

The system model consists of the collector model (introduced in section 5.2.2), a heat storage tank model, an inverter model and a control strategy. Input for the collector model are the weather data and the collector inflow temperature from the storage tank  $T_{w,in}^{col}$ . Input of the heat storage tank model is the heat demand and the

inflow temperature from the collector  $T_{in}^{tank}$ .

Because the annual electrical and thermal efficiencies are required, the system performance during an entire year has to be modelled. To do so, the year is subdivided into time intervals of 15 minutes, during which weather conditions and heat demand are assumed to remain constant. Note that because the heat content of the tank(s) is not known at start of the simulation, multiple years are simulated to obtain a steady state, i.e. having the heat content of the tanks equal at the start and end of the year. The control strategy will be described first. Subsequently the weather conditions, the heat demand, the inverter model and the heat storage model, used in the PVT system model, will be introduced.

### Control strategy

To maximise the thermal yield and to keep the temperature level within the required range, a control strategy is normally implemented. The control strategy used in this thesis will now be explained.

In the system for domestic hot water, there is only one 200 l storage tank. To prevent contamination with the bacterium of the species *Legionella pneumophila* in this domestic hot water tank, the water extracted should be heated to at least 60 °C. An auxiliary heater is normally present to guarantee this temperature level. In times of high solar irradiance, the water in the tank could become much hotter and the water extracted from the tank is mixed with cold water (indicated by the dashed line in figure 5.5) to keep the supplied tap water at a constant temperature of 60 °C. To prevent boiling, the collector may heat the water up to a level of at most 95 °C. If this level is exceeded, the collector pump is stopped and no more heat is extracted from the collector. Under this condition, known as stagnation, the temperature in the collector can exceed 150 °C.

In the system for combined domestic hot water and room heating, the 200 l domestic hot water tank has priority, i.e. will be loaded first, as long as it has a temperature of less than 60 °C. If this is not the case then the coolest tank has priority, which in most cases will be the 40 m<sup>3</sup> tank for room heating. In this case the pump is only stopped if *both* tanks have reached their maximum allowed temperature of 95 °C. In all systems, another criterium to stop the pump is in case the reduced temperature  $T_{red}$  exceeds 0.1. Pumping water through the collector under these conditions would most likely only cool the water down.

### Weather data

The weather data of a test reference year (TRY) from de Bilt in the Netherlands [88] are used with the collector model. This data contains the hourly values of the ambient temperature, solar irradiance and wind speed of the complete year. The corresponding sky temperature was derived from this data. The data of the test reference

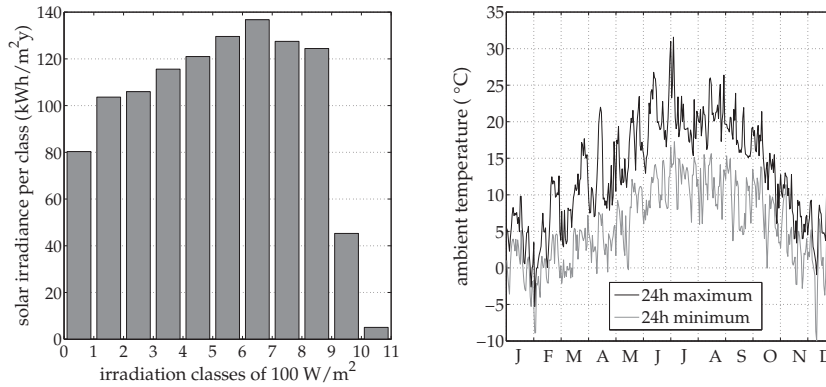


**Figure 5.6:** Illustration of the weather data for the test reference year. Left: Annual irradiation per irradiation class of  $100 \text{ W/m}^2$ . Right: Daily maximum and minimum temperatures during the year.

year does not correspond to one year in particular, but it is statistically representative for the Dutch climate.

The irradiance for a south facing plane with an inclination of  $45^\circ$  is  $1100 \text{ kWh/m}^2\text{y}$ . In the left panel of figure 5.6, the annual total solar irradiance per irradiance class is shown. Each class corresponds to an intensity interval having a width of  $100 \text{ W/m}^2$ . It can be seen that solar irradiance can reach an intensity of  $1000\text{--}1100 \text{ W/m}^2$ , however most irradiance is received having a lower intensity. In the right panel of figure 5.6, the daily maximum and minimum ambient temperature are illustrated. The seasonal cycle is clearly visible with maximum temperatures roughly ranging from  $0^\circ \text{C}$  in winter to  $25^\circ \text{C}$  in summer.

### Heat demand

For the domestic hot water heat demand, a standard withdrawal pattern is used, consisting of a withdrawal of  $117 \text{ l}$  of water per day at  $60^\circ \text{C}$  [89]. After correcting for the heat loss in the pipes between storage tank and water tap, the effective hot water withdrawal is  $139 \text{ l}$  of water per day at  $60^\circ \text{C}$  [90]. This daily pattern is repeated for every day of the year, amounting to an annual thermal energy demand of  $2960 \text{ kWh}$  ( $10.6 \text{ GJ}$ ). This demand is distributed as shown in the left panel of figure 5.7.

For the room heating demand, the demand of the Novem reference dwelling is used in the model [91]. This room heating demand is typical for a single-family town house built in 1999, in Dutch climatological conditions. The distribution of the room heating demand over the year is shown in the right panel of figure 5.7. It can be seen that there is a significant room heating demand from November till March. The annual heat demand for room heating is  $2990 \text{ kWh}$  ( $10.8 \text{ GJ}$ ) which is comparable to

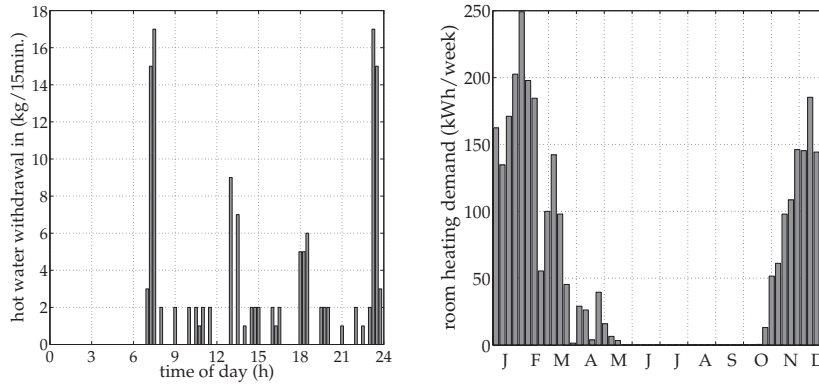


**Figure 5.7:** Left: Daily heat demand for domestic hot water heat on a 15 minute basis. The demand of 139 l/day corresponds to 2960 kWh/y. Right: Annual heat demand for room heating on a weekly basis. Total heat demand is 2990 kWh/y.

the annual heat demand for domestic hot water.

### Inverter

The inverter has a maximum input power  $P_{\max}^{\text{inv}}$  for converting direct current to alternating current. When the inverter is operating between  $0.25 \cdot P_{\max}^{\text{inv}}$  and  $P_{\max}^{\text{inv}}$ , the efficiency of the inverter is about 94%. For lower input power, the inverter is much less efficient. The inverter efficiency curve used in the model, shown in the left panel of figure 5.8, is based on the curve of a commercially available inverter [92]. The inverter size  $P_{\max}^{\text{inv}}$  has to be chosen such that a maximum overall system efficiency is obtained, in principle. Because in this thesis different collector areas and PV technologies are used, a somewhat simple approach is used: in each simulation  $P_{\max}^{\text{inv}}$  is chosen to be equal to the peak power of the installed laminates.

Additionally, the power loss due to the electrical resistance in the cabling between the collector and inverter is taken into account. The resistance of the cabling is such that during peak power 2% of the electric power is lost due to ohmic loss.

### Heat storage tank model

As indicated in the right panel of figure 5.8, the energy content of the storage tank is affected by two flows. At one side there is the collector loop, with a flow rate  $\phi_c$ , taking water from the bottom of the tank and returning it at an elevated temperature. At the other side there is the demand loop, with a flow rate  $\phi_d$ , taking water from the top of the tank and returning the same amount at a reduced temperature. Note that in practice it is compulsory to separate the water of both loops by means of a heat

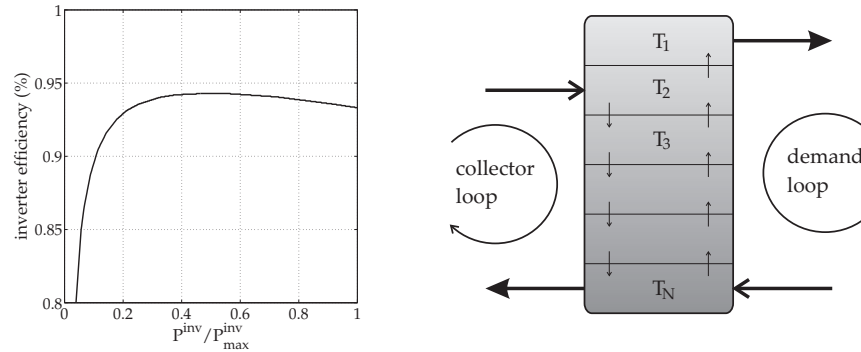


**Figure 5.8:** Left: Efficiency of the inverter as a function of relative input power  $P^{inv}/P_{max}^{inv}$ . Right: Schematic overview of the stratified heat storage tank divided into segments of uniform temperature. Inter-segment flows are indicated.

exchanger. Here it is assumed that this heat exchanger is located outside the tank on the collector side and is perfect in terms of effectiveness.

Heat storage tanks are designed to avoid mixing of water of different temperatures to maintain good thermal stratification. Having a stratified tank instead of a tank of uniform temperature has two advantages. Firstly, the water extracted at the demand side (top) has a relatively high temperature, so less auxiliary heating is required. Secondly, the water extracted at the collector side (bottom) has a relatively low temperature, which is beneficial for the efficiency of the collector (see section 5.2). Therefore the degree of the stratification is an important system parameter.

Van Berkel [93] has studied stratification inside a heat storage tank both numerically and experimentally. He uses a figure of merit (FOM) for indicating the degree of stratification. The definition of FOM is given in appendix A and theoretically FOM ranges from 1 for a perfectly stratified tank to 0.63 for a fully mixed tank. In practice various storage tank designs exist with varying degree of stratification. Both storage tanks used in the model are assumed to have a degree of stratification which is in between fully mixed and perfectly stratified.

Because a complete computational fluid dynamics (CFD) model of the storage tank is computationally very expensive, simplified storage tank models have been developed, of which the multinode model is frequently used [94]. In this model the storage tank is divided into  $N$  segments, each segment being characterised by a temperature  $T_n$ , with  $n = 1 \dots N$ . As a result of buoyancy effects, water entering a stratified tank will rise or descend to match its density and thereby its temperature. In the numerical model it is assumed that water enters the tank in the segment of best matching temperature, which helps to maintain good stratification in the tank. If the collector loop and/or the demand loop are active, water flows from one segment to

the next as indicated by the vertical arrows in the right panel of figure 5.8. Given an initial temperature distribution and inflow temperatures, the temperature distribution a small time step later can be determined by solving the energy balances. More details of the multinode model are given in appendix A.

The temperature of the water coming from the collector depends on the weather conditions and is therefore variable. In the tank for domestic hot water, the water extracted at the demand side is replenished by water from the mains, which is assumed to have a constant temperature of 10 °C. In the storage tank for room heating the demand loop is closed and water returning from the load is assumed to have a fixed temperature of 25 °C. Note that because the return temperature is fixed, the amount of heat extracted for room heating is controlled in the numerical model by the flow rate.

The choice of the number of segments  $N$  in the model determines the degree of stratification. The simplest case with only one tank segment  $N = 1$  corresponds to a fully mixed tank of uniform temperature (FOM=0.63). The limiting case of  $N \rightarrow \infty$  corresponds to a perfectly stratified tank (FOM=1). The exact relationship between  $N$  and FOM is given in appendix A. According to Duffie [84], the case with  $N = 3$  (FOM=0.78) represents a reasonable compromise between the two extreme cases. Therefore in this thesis  $N = 3$  is used for both the domestic hot water tank and the room heating tank.

Heat loss from the tank to the ambient is taken into account as well and the following assumptions are made. Both tanks are cylindrical with a height-to-radius ratio of 3. The domestic hot water tank is located in a room of 20 °C while the big room heating tank is underground and surrounded by a temperature of 10 °C. The heat loss is proportional to the surface area of the tank and inversely proportional to the thickness of the thermal insulation layer. For the 200 l domestic hot water tank an insulation thicknesses of 5 cm is used, resulting in a heat loss of 1.0 W/K. For the 40 m<sup>3</sup> room heating tank an insulation thicknesses of 30 cm is used, resulting in a heat loss of 5.7 W/K.

### 5.3.3 Assumptions in the system model

#### Angle of incidence

The absorption factor used in the model (given by equation 5.5) is the absorption factor derived under the assumption of normally incident irradiance ( $\phi = 0^\circ$ ). However, in reality the sun moves across the sky and most of the time irradiance is not normally incident but comes in under an angle. In case there is cloud coverage, irradiation is more diffuse and irradiance is more distributed over all directions. Also in that case most irradiance is not incident from the normal direction.

Using the 'normal incident' absorption factor introduces an error. To estimate the error introduced by this simplification, the absorption factor of a PV laminate was



determined as a function of the angle of incidence. It was found that for angles of incidence between 0 and 60° the absorption factor is more or less constant. Only for larger angles of incidence the reflection factor increases significantly and as a result the absorption factor decreases. This means that using the 'normal incidence' absorption factor only introduces a significant error in cases of very oblique irradiance. The error in annual yield introduced by this simplification was investigated by assuming all irradiance (consisting of a direct and a diffuse component) is incident from the direction of the sun. By determining the angle between the direction of the sun and the collector surface normal for each time step, a corrected absorption factor was determined and used in each time step of the simulation of the annual yield. The annual yield determined in this way is about 5%<sub>rel</sub> lower compared to the simulation in which the fixed 'normal incident' absorption factor was used. It is therefore estimated that by keeping the absorption factor fixed, the annual yield is overestimated by at most 5%<sub>rel</sub>.

### Solar spectrum

A similar simplification was used regarding the solar spectrum. The absorption factor of the absorber of a PVT collector was derived under the assumption of an AM1.5g spectrum. It represents the solar spectrum for clear sky conditions in case the sun is 42° above the horizon. It is a global spectrum, containing both direct and diffuse irradiance. Though this is a widely used standard spectrum, in reality the spectrum will vary somewhat with the elevation of the sun and the atmospheric conditions. The absorption factor of solar cells was determined using AM $x$  solar spectra, where Air Mass number  $x$  ranges from 1.5 to 5.6. It was found that the absorption factor of c-Si solar cells is not very sensitive to a variation of the Air Mass number. Because the variations are less than 1%<sub>rel</sub>, it is justified to use a single absorption factor derived under the assumption of an AM1.5g spectrum.

### 5.3.4 Illustration of the system model

In order to gain some insight in the PVT system model, this model is illustrated for one particular PVT system. A system for combined domestic hot water and room heating is considered. Note that in this illustration a PVT collector surface area of 24 m<sup>2</sup> is used, which is twice the standard surface area for this application. The characteristics of the collector are given in table 5.1. This system is modelled during one year, using the weather conditions and heat demand described in section 5.3.2.

### Storage tank temperature

The left panel of figure 5.9 shows the temperature of the water in the small domestic hot water tank and in the big room heating tank during a cloudless day in May (May

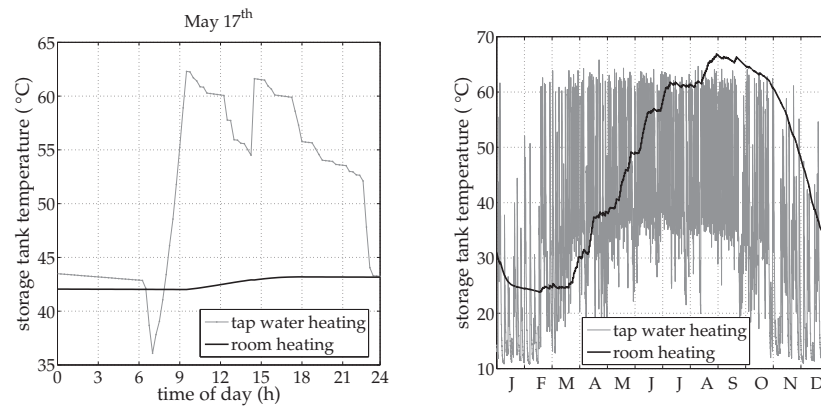


**Figure 5.9:** The water temperature in the 200 l domestic hot water tank and the 40 m<sup>3</sup> room heating tank in a system with a 24 m<sup>2</sup> PVT collector. Left: During a cloudless day in May (May 17 of the TRY). Right: During the whole test reference year.

17 of the TRY). Note that because the tanks are divided into multiple segments having a different temperature, the average water temperature is plotted. At midnight (0h) the temperature in the domestic hot water tank is around 44 °C. In the morning first some heat is extracted (see domestic hot water demand in figure 5.7), but after sunrise the PVT collectors cause the small tank to heat up within a few hours to the desired temperature of 60 °C. After this temperature has been reached, the heat supply switches to the big room heating tank for the rest of the daytime, thereby heating the 40 · 10<sup>3</sup> kg of water in this tank by about 1.2 °C. Around 14h the heat supply is briefly switched back to the small tank of which the temperature after the extraction of heat has fallen below 55 °C. Note that to prevent the system from switching too often, a hysteresis of 5 °C is used, explaining why the switch back to the domestic hot water tank occurs at 55 °C and not at 60 °C. Around 22h (after sunset) heat is again extracted from the domestic hot water tank, bringing its temperature back to 44 °C.

The right panel of figure 5.9 shows the same temperatures during the entire test reference year. It can be seen that on many days from mid-February till October the domestic hot water tank can be heated to the desired temperature level of 60 °C. On the days that this is not the case the auxiliary heater is used. From March till August the heat supply regularly exceeds the demand for domestic hot water, so the heat supplied during the second part of the day can be used to heat the big room heating tank. As a result this tank gradually heats up until at the end of August a maximum temperature of 67 °C is reached. From November (the start of the room heating season, see right panel of figure 5.7) till mid-January, the heat required for room heating is withdrawn from the room heating tank until its temperature drops below

25 °C. For the remaining part of the room heating season, the energy is supplied by the auxiliary heater.

### Solar fraction and thermal system efficiency

By summing the energy withdrawn from the tanks during the test reference year, it is found that the contribution of the collector to domestic hot water  $E_{\text{th,dhw}}^{\text{col}} = 1920$  kWh/y and to room heating  $E_{\text{th,rh}}^{\text{col}} = 1600$  kWh/y. The solar fraction  $SF$  is defined as the fraction of the demand for heat that is supplied by the collector,

$$SF = \frac{E_{\text{th}}^{\text{col}}}{E^{\text{dem}}}, \quad (5.10)$$

where  $E^{\text{dem}}$  is the annual heat demand. For the system considered above the domestic hot water solar fraction is 65% and the room heating solar fraction is 54%, resulting in an overall solar fraction of 59%. The remaining fraction is supplied by the auxiliary heater(s). Note that in most cases it is not economical to size a solar thermal system to have a solar fraction of 100%, as will be demonstrated in the next section.

The annual thermal system efficiency is defined as

$$\eta_{\text{th}}^{\text{sys}} = \frac{E_{\text{th}}^{\text{col}}}{E^{\text{sun}}}, \quad (5.11)$$

where  $E^{\text{sun}}$  is the solar energy annually incident on the collector, which is 1100 kWh/y for every square metre of collector surface area. For the system considered above,  $\eta_{\text{th}}^{\text{sys}} = 13\%$ . Compared to the PVT *collector* efficiency (see section 5.2.2), the system efficiency is relatively low. However, as will be demonstrated next, this is a consequence of the relatively large collector area of 24 m<sup>2</sup> used in this system.

The annual *electrical* system efficiency is defined as

$$\eta_{\text{e}}^{\text{sys}} = \frac{E_{\text{e}}^{\text{col}}}{E^{\text{sun}}}, \quad (5.12)$$

where  $E_{\text{e}}^{\text{col}}$  is the annual electrical system yield. In the PVT system considered here,  $E_{\text{e}}^{\text{col}} = 2970$  kWh and the corresponding annual electrical system efficiency, is 11.3%. Note that in this thesis all *system* efficiencies are by definition given on an annual basis.

### Sizing of the collector

In the left panel of figure 5.10, the effect of varying the collector surface area is shown. Note that the storage volume and thermal demand is kept constant, i.e. is independent of the collector surface area. The annual yield for domestic hot water, room

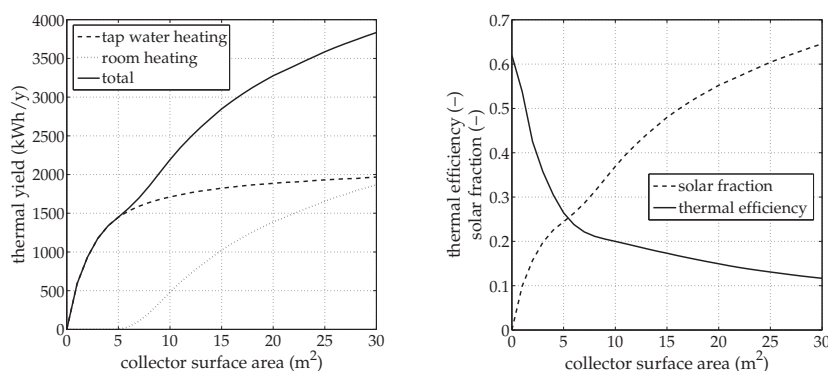


**Figure 5.10:** Left: the annual thermal yield of a PVT system for domestic hot water and room heating, as a function of collector area. Right: the corresponding overall solar fraction and thermal system efficiency. Fixed storage tank volumes are considered.

heating and the total thermal yield are shown. Not surprisingly, more heat is generated if a larger collector surface area is used. Note that in systems with a collector surface area of less than  $5 \text{ m}^2$ , all heat supplied by the collector is used for domestic hot water, which has priority over room heating. Only for larger collector surface area, the room heating part of the system is useful in combination with the  $40 \text{ m}^3$  storage tank.

In the right panel of figure 5.10, the corresponding solar fraction and thermal system efficiency are plotted. It can be seen that in order to achieve a solar fraction close to 1, a very large collector area would be required. However, this inherently corresponds to higher storage temperatures and more heat loss from especially the room heating tank, reducing the thermal efficiency. Therefore in practice the system is usually not sized to a solar fraction of 1, but to a lower solar fraction e.g. 0.5. This explains the practical system sizing discussed in section 5.3.1, on which the sizing of systems considered in this thesis is mainly based.

## 5.4 Annual yield of PVT collectors

In the previous section, the model for the annual yield of PVT systems has been illustrated. The properties of the PV laminate, such as absorption factor and electrical efficiency at Standard Test Conditions, are important input parameters for this model. In section 5.4.1 insight will be gained in the annual yield of systems with PVT collectors with various PV cell technologies. This is done by using the absorption factor and electrical efficiency for several cell technologies as input for the annual yield model. In section 5.4.2 the effect of the collector surface area on both the electrical

**Table 5.2:** The electrical efficiency and absorption factor of four cell technologies, both on cell level (as obtained from tables 3.5 and 4.6) and on collector level.

	Cell level		Collector level	
	$\eta_e^{\text{cell,STC}}$ (%)	$A^{\text{cel}}$ (%)	$\eta_e^{\text{col,STC}}$ (%)	$A^{\text{col}}$ (%)
c-Si PUM	15.52	87.4	12.97	81.0
c-Si EWT	16.25	90.5	13.58	83.5
a-Si	7.00	81.4	5.80	74.9
CIGS	11.00	93.5	9.11	86.0

and thermal yield is looked into. Finally, in section 5.4.3 it is investigated whether the yield can be increased by applying optical coatings on the PV laminate and/or on the cover glass of the PVT collector.

#### 5.4.1 The effect of cell technology

The cell technology used in the PVT collector determines the electrical efficiency and the (effective) absorption factor of the laminate and therefore the annual electrical and thermal yield of the system. In chapter 3 and 4 the electrical efficiency and absorption factor were investigated at *cell* level. However, the yield model requires the electrical efficiency and absorption factor at *collector* level. The spacing between and around the cells in the PV laminate and the fact that the laminate is placed below a cover glass should be taken into account, as discussed in section 5.2.1

PV laminates with the following PV cells will be considered in this section:

- c-Si PUM cells (cell D in table 3.5),
- c-Si EWT cells (cell K in table 3.5),
- thin-film a-Si cells (cell Ib in table 4.6),
- thin-film CIGS cells (cell Vb in table 4.6).

In the left part of table 5.2, the electrical efficiency and absorption factor are given at cell level, as obtained from tables 3.5 and 4.6. Equations 5.5 and 5.6 are used to determine the corresponding parameters at *collector* level, taking into account the effect of the cover glass and the packing density of the cells. In the right part of the table the results are given. These values will be used as input for the annual yield model.

First the reference PVT system for domestic hot water is considered, having a 6 m<sup>2</sup> PVT collector and a 200 l storage tank. For each of the four cell technologies the annual electrical and thermal yield is shown in table 5.3. It can be seen that the cell technology with the highest electrical efficiency at Standard Test Conditions (i.e.

**Table 5.3:** Results of the yield model for the four cell technologies considered for a PVT system for domestic hot water with a PVT collector area of 6 m<sup>2</sup>.

	$E_e^{\text{col}}$ (kWh/y)	$E_{\text{th}}^{\text{col}}$ (kWh/y)	$\eta_e^{\text{sys}}$ (%)	$\eta_{\text{th}}^{\text{sys}}$ (%)	$SF_{\text{DHW}}$ (%)
c-Si PUM	655	1599	9.96	24.3	54.3
c-Si EWT	683	1626	10.39	24.7	55.2
a-Si	321	1595	4.88	24.3	54.1
CIGS	450	1712	6.84	26.0	58.1

**Table 5.4:** Results of the yield model for the four cell technologies considered for a PVT system for combined domestic hot water and room heating with a PVT collector area of 12 m<sup>2</sup>.

	$E_e^{\text{col}}$ (kWh/y)	$E_{\text{th,DHW}}^{\text{col}}$ (kWh/y)	$E_{\text{th,RH}}^{\text{col}}$ (kWh/y)	$\eta_e^{\text{sys}}$ (%)	$\eta_{\text{th}}^{\text{sys}}$ (%)	$SF_{\text{DHW}}$ (%)	$SF_{\text{RH}}$ (%)
c-Si PUM	1332	1814	739	10.13	19.4	61.6	24.7
c-Si EWT	1390	1834	799	10.57	20.0	62.6	26.7
a-Si	645	1813	722	4.90	19.3	61.6	24.2
CIGS	922	1893	994	7.01	22.0	64.3	33.3

the c-Si EWT cell technology) also gives rise to the highest annual electrical yield (683 kWh/y). Note that because the a-Si cell has the least negative temperature coefficient, its annual electrical efficiency (4.88%) deviates least from the efficiency at Standard Test Conditions (5.80%), in relative terms. The cell technology with the highest absorption factor (i.e. the CIGS cell technology), gives rise to the highest thermal yield (1712 kWh/y). The corresponding solar fractions  $SF_{\text{DHW}}$  are given in the final column. This indicates that a 6 m<sup>2</sup> PVT collector with a 200 l storage tank can supply 54-58% of the heat demand for domestic hot water.

For the same four cell technologies, a second system was simulated as well. This is the reference system for combined domestic hot water and room heating with a 12 m<sup>2</sup> PVT collector and a 200 l storage tank for domestic hot water and a 40 m<sup>3</sup> storage tank for room heating. Compared to the previous system the collector surface area has doubled, however the heat demand has doubled as well, because the system is now used also for room heating. The results are shown in table 5.4. The thermal system yields are given for domestic hot water and room heating separately. It can be seen that most heat is used for domestic hot water, having solar fractions of 62-64%. Relatively little solar heat is available for room heating which has a solar fraction of 24-33%. Compared to the previous system (see table 5.3) the thermal system efficiency is somewhat lower because the room heating tank stores heat less efficiently. However, because it is possible to switch to this mostly relatively cool room heat-

**Table 5.5:** Electrical and thermal system efficiency and solar fraction for a PVT systems for domestic hot water (collector area 3, 6 and 12 m<sup>2</sup>) and combined domestic hot water and room heating (collector area 6, 12 and 24 m<sup>2</sup>). All collectors have c-Si PUM cells.

area	Domestic hot water			Combined DHW & RH		
	3 m <sup>2</sup>	6 m <sup>2</sup>	12 m <sup>2</sup>	6 m <sup>2</sup>	12 m <sup>2</sup>	24 m <sup>2</sup>
$\eta_e^{sys}$ (%)	10.34	9.96	9.53	10.25	10.13	9.84
$\eta_{th}^{sys}$ (%)	34.5	24.3	14.6	24.1	19.4	14.0
$SF_{DHW}$	38.5	54.3	65.3	52.8	61.6	67.2
$SF_{RH}$	-	-	-	0.9	24.7	57.0

ing tank, the system on average is operated at a somewhat lower temperature and therefore the *electrical* system efficiencies are slightly higher than the corresponding efficiencies in table 5.3.

#### 5.4.2 The effect of collector sizing

In this section the effect of collector sizing is investigated. The systems considered above with the c-Si PUM cell technology is used for this purpose. With respect to the surface areas used in the reference systems (6 m<sup>2</sup> for domestic hot water and 12 m<sup>2</sup> for combined domestic hot water and room heating) half and double surface areas are considered here as well. The sizes of the storage tanks are kept fixed at 200 l and 40 m<sup>3</sup>, respectively. The results are shown in table 5.5. It can be seen that the larger systems have a higher solar fraction as expected, however, because they operate at a higher temperature, both the thermal and the electrical efficiency are lower. Note that from these results it can be seen that for the given storage tank sizes it is not useful to use a 6 m<sup>2</sup> collector for combined domestic hot water and room heating, because in that case the room heating tank is hardly heated up to a usable temperature level, resulting in a room heating solar fraction of less than 1%.

#### 5.4.3 The effect of optical coatings applied to the collector

Having determined the annual yield of PVT systems with PVT collectors of varying surface area, it is investigated next to which extent the yield can be increased by applying optical coatings to the PVT collector. Both low-emissivity coatings and anti-reflective coatings will be considered.

##### Low-emissivity coatings

A normal PV laminate is not spectrally selective. Its emissivity is determined by the emissivity of the glass encapsulating the cells, being approximately 85%. This

implies that in a PVT collector, besides convection, radiation is an important means of heat transport from the PV laminate to the cover glass. Part of the heat transported is subsequently lost to the ambient.

Low-emissivity coatings are frequently applied in double glazed windows to reduce heat loss by radiation. In double glazed windows an as low as possible parasitic absorption in the visible part of the spectrum is desirable. As described by Granqvist [95], both metals and doped semiconductor coatings can be used as low-emissivity coating in double glazed windows. If low-emissivity coatings are applied on the PV laminate in a PVT collector, an as low as possible parasitic absorption in the near infrared part of the spectrum is required as well, to maintain a good electrical efficiency. Because of the much lower absorption in the near infrared, the doped semiconductor coatings are more suitable than the metal coatings. The most important examples of doped semiconductor coatings are tin oxide, indium tin oxide and zinc oxide. Fluor doped tin oxide (SnO:F) is widely used for low-emissivity coatings in double glazed windows. Indium tin oxide (ITO) is mainly applied as transparent conductive coating in flat panel displays. Aluminium doped zinc oxide (ZnO:Al) has been developed for electronic applications such as transparent conductive oxide in thin-film solar cells [73] and has not yet been developed and applied as a low-emissivity coating. The optical properties of these doped semiconductor coatings are similar. They have a refractive index  $n$  of about 2 and an absorption coefficient  $\alpha$  that in the visible part of the spectrum is relatively low (in the order of  $5 \cdot 10^2 \text{ cm}^{-1}$ , depending on the doping level) but  $\alpha$  increases rapidly with increasing wavelength. In general a thicker and heavier doped coating will have a lower emissivity, but will also have a higher parasitic absorption. Because of the relatively high refractive index of doped semiconductor coatings they cause some extra reflection. So, when applied to the PV laminate, this extra reflection will reduce both the electrical efficiency and the absorption factor somewhat.

Because SnO:F is most widely used as low-emissivity coating it will be considered here. Haitjema has experimentally and numerically studied the optical properties of SnO:F in detail [96]. Applying a 300 nm thick SnO:F coating with a fluor doping concentration of  $3 \cdot 10^{20} \text{ cm}^{-3}$  will reduce the emissivity of the PV laminate from 85% to about 20%. Best SnO:F coatings prepared by Haitjema had an emissivity of 15% at a thickness of 620 nm.

#### Anti-reflective coatings

Both the front and back surface of the cover glass and the front surface of the PV laminate reflect about 4% of the incident irradiance each. This reflective loss can be reduced by means of anti-reflective coatings. Anti-reflective coatings have already been discussed in section 2.2.2. The anti-reflective coatings considered here are single layer porous SiO<sub>2</sub> coatings, deposited by a dip coating technique [60]. Because these anti-reflective coatings have a thickness of only 120 nm, they do not affect the



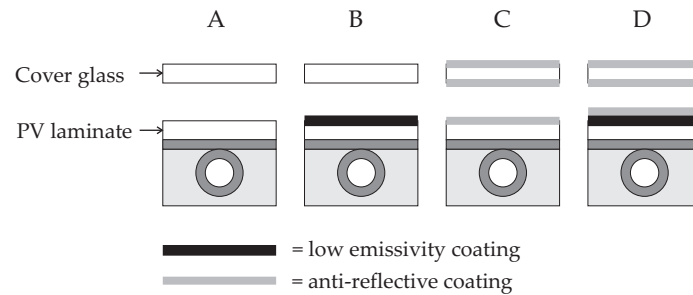


**Figure 5.11:** Four PVT collector configurations (drawing not to scale). A: Without coatings. B: low-emissivity coating on the laminate. C: AR coatings on both sides of the cover glass and on the PV laminate. D: AR coatings on both sides of the cover glass and a sandwich of low-emissivity coating and AR coating on the PV laminate.

emissivity of the substrate onto which they are deposited [60]. Anti-reflective coatings can be applied to the cover glass and on the PV laminate in the collector.

### Configurations

In this section PVT systems with collectors having c-Si PUM cells are considered again. However, this time the effect of the additional 300 nm SnO:F low-emissivity and/or 120 nm porous SiO<sub>2</sub> anti-reflective coatings described above, is investigated. The four configurations A to D that are considered are schematically shown in figure 5.11. Configuration A is the standard configuration, considered in section 5.4.2, without additional coatings. Configuration B has a low-emissivity coating on the PV laminate. Configuration C has an anti-reflective coating on both sides of the cover glass and on the PV laminate. In configuration D, the cover glass has anti-reflective coatings on both sides as well. In addition the PV laminate contains a sandwich of low-emissivity coating *and* anti-reflective coating.

The optical model described in chapter 2 is used to determine the electrical STC efficiency and the AM1.5 absorption factor of these configurations at collector level. Besides the effect of the cover glass and the packing density of the cells, the optical effects of the coatings have been taken into account. The results are given in the top half of table 5.6. The emissivity of the laminate  $\varepsilon$  is given in the final column. The effect of the addition of a low-emissivity coating can be seen by comparing configuration A and B. Because of increased reflection and because of parasitic absorption in the low-emissivity coating, the electrical STC efficiency has reduced from 12.97% to 11.84% and the absorption factor of the PV laminate has been reduced from 81.0% to 76.9%. This reflection and absorption will be discussed in more detail in section 5.5.

Comparing configurations A and C, it can be seen that the addition of the anti-reflective coatings has significantly increased the electrical STC efficiency of the lami-

**Table 5.6:** The electrical STC efficiency, the absorption factor and emissivity of a PV laminate with c-Si PUM cells, in a PVT collector with coating configuration A to D and in a PV module with coating configuration E and F. For a solar thermal collector with coating configuration G and H the absorption factor and emissivity of the absorber are given as well. Configurations E to H will be introduced in section 5.5.

conf.	system	$\eta_e^{\text{col,STC}}$ (%)	$A$ (%)	$\varepsilon$ (%)
A	PVT	12.97	81.0	85
B	PVT	11.84	76.9	20
C	PVT	14.19	87.9	85
D	PVT	13.67	86.7	20
E	PV	14.06	88.6	85
F	PV	14.71	91.2	85
G	thermal	-	86.6	12
H	thermal	-	91.4	12

nate from 12.97% to 14.19% and the absorption factor from 81.0% to 87.9%. In configuration D, both types of coating are combined. The low-emissivity coating reduces the emissivity of the PV laminate to 20% and the anti-reflective coatings increase the electrical STC efficiency and the absorption factor of the laminate, though not to the levels found for configuration C.

#### The effect on the annual yield

The laminate properties summarised for configurations A to D in table 5.6, are used as input parameters for the annual yield model. All PVT systems that have been considered in section 5.4.2, are considered here again, but with low-emissivity and/or AR coatings. These are the PVT systems for domestic hot water with collector areas of 3, 6 and 12 m<sup>2</sup> and systems for combined domestic hot water and room heating with collector areas of 6, 12 and 24 m<sup>2</sup>. In figure 5.12 the results are shown. In the left panel the results for the domestic hot water system are shown and in the right panel the results for the combined domestic hot water and room heating system are given. The annual thermal efficiency is plotted versus the annual electrical efficiency. The efficiencies of the 'A' configurations (without any additional coatings) were already given in table 5.5 and the fact that increasing the collector area results in higher annual yields, but lower thermal and electrical efficiencies has been discussed in section 5.4.2.

It can be seen in each case that the addition of a low-emissivity coating to the PV laminate (compare configurations A and B), increases the annual thermal efficiency somewhat, but reduces the annual electrical efficiency by more than 1% absolute. However, adding anti-reflective coatings (compare configurations A and C) is benefi-

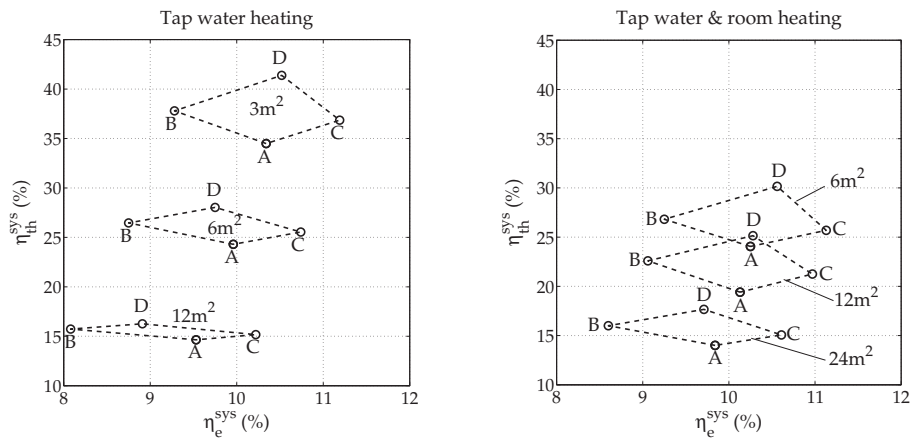


**Figure 5.12:** The annual electrical system efficiency versus the the annual thermal system efficiency for PVT systems with c-Si PUM cells and coating configurations A, B, C and D. Left: For PVT systems for domestic hot water with a collector area of 3, 6 and 12 m<sup>2</sup>. Right: For PVT systems for combined domestic hot water and room heating with a collector area of 6, 12 and 24 m<sup>2</sup>.

cial for both the annual electrical efficiency, *increasing* by almost 1% absolute, and the thermal efficiency. Having both a low emissivity coating and anti-reflective coatings (configuration D) results in the highest thermal efficiency. The electrical efficiency however, is not as high as the case with only anti-reflective coatings (configuration C) and may in some cases even be lower than the case without any coatings (configuration A).

Note that in systems with a high thermal efficiency, the extra heat collected because of the application of coatings is used most efficiently. The effect of these additional coatings on the thermal efficiency is therefore largest in these systems. For example consider the 3 m<sup>2</sup> collector for domestic hot water. Adding both low-emissivity and anti-reflective coatings increases the thermal efficiency from 34.5% to 41.4%. If the same coatings are applied to a 12 m<sup>2</sup> collector, the increase is only from 14.6% to 16.3%. Both in absolute and in relative terms the effect of the additional coatings is less in the system with the larger collector. This indicates that a complete system analysis, as performed here, is required to analyse the effect of the application of optical coatings.

### Thickness of the low-emissivity coating

Up till now for coating configurations B and D a low-emissivity coating with a thickness of 300 nm has been applied to the PV laminate, which is a standard thickness for low-emissivity coatings applied in double glazed windows [60]. Next the effect of the thickness of this coating on the annual system efficiencies is investigated.

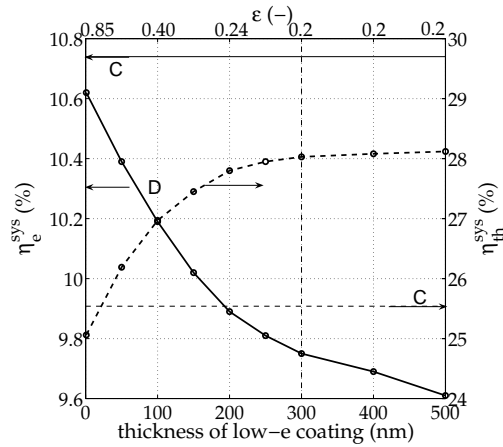


**Figure 5.13:** The electrical and thermal system efficiencies versus a the thickness of the SnO:F low emissivity coating applied to the PV laminate. A system for only domestic hot water with a  $6 \text{ m}^2$  collector is considered.

Haitjema presents the emissivity of SnO:F coated glass as a function of coating thickness [96]. The standard reference coating considered here has an emissivity of about 0.20 if the thicknesses is 300 nm or more. If the coating thickness is reduced, the emissivity increase to 0.24 at 200 nm and to 0.40 at 100 nm. A bare glass substrate, without low-emissivity coating has an emissivity of 0.85. This indicates that somewhat thinner coatings still reduce the emissivity significantly. At the same time thinner coatings give rise to less parasitic absorption. The resulting effect on the electrical STC efficiency of the PV laminate was investigated using the optical model presented in chapter 2.

The reference PVT system for domestic hot water with a  $6 \text{ m}^2$  PVT collector is considered and coating configuration D is used as starting point. The PV laminate's emissivity, electrical efficiency and absorption factor were determined for low-emissivity coating thickness ranging from 0 to 500 nm. These values were used as input for the annual yield model. The results are shown in figure 5.13. It can be seen that by decreasing the coating thickness below the standard value of 300 nm, the annual *electrical* system efficiency increases as a result of lower cell temperatures and the reduced parasitic absorption. The optical loss caused by additional reflection induced by the coating is not reduced. Therefore, the potential increase in electrical efficiency turns out to be limited. At the same time the annual *thermal* system efficiency is decreased. The optimal thickness of this coating for PVT applications will be discussed in section 5.5.5. The efficiencies of the same system, but with coating configuration C are also indicated. Note that because of the additional reflection inherently present in configuration D, the efficiencies for a low-emissivity coating thickness approaching 0, do not correspond to the efficiencies for configuration C.

## 5.5 PVT systems compared to separate PV and T systems

As with conventional PV systems and conventional solar thermal systems, the economy of the systems is strongly determined by the annual electrical and thermal efficiencies. In this section the annual *electrical* efficiency of PVT systems will be compared to the annual electrical efficiency of PV systems and the annual *thermal* efficiency of PVT systems is compared to the annual thermal efficiency of solar thermal collector systems. The objective of this comparison is to gain more insight in the performance of PVT systems and the specific loss mechanisms that are inherent to PVT systems. It will be convenient to express the efficiencies of a PVT system relative to the efficiencies of comparable conventional systems. Therefore the efficiencies of these conventional systems will be considered first.

### 5.5.1 The electrical yield of PV systems

To evaluate the performance of a PV system under the identical conditions used in the evaluation of the PVT systems, the PVT collector model was modified for modelling PV systems, i.e. the cover glass and heat collecting systems are removed. Again the Test Reference Year weather data is used (see section 5.3.2). For each time step, the energy balance in the PV module is solved to determine the cell temperature and the corresponding temperature induced electrical efficiency loss. Note that because of the absence of the cover glass and heat collecting system, the electrical efficiency of a PV module will deviate from the electrical efficiency of a PVT collector. Also note that because the PV module model is derived from the PVT collector model, a thermally well insulated back side was implicitly assumed. In reality the back side of a roof integrated PV cell is ventilated. This implies that the PV module model used here overestimates the cell temperatures and the corresponding electrical loss due to elevated cell temperatures. The model gives a loss of  $6.5\%_{\text{rel}}$ , while  $3.8-4.8\%_{\text{rel}}$  is more typical for a well ventilated, roof integrated PV module in Dutch climatological conditions [97]. The model results are therefore corrected, i.e. the temperature loss is reduced to a more realistic  $4.3\%_{\text{rel}}$ . Electrical losses due to high cell temperature, low irradiance, ohmic resistance and the inverter are determined by the same sub-models as in the PVT systems (see section 5.3.2).

A PV system with a module with c-Si PUM cells is considered without and with AR coating, as indicated by configurations E and F in in figure 5.14. The electrical STC efficiency, absorption factor and emissivity of the PV module are required input parameters. These parameters are given in table 5.6. The annual electrical efficiency of the PV system as determined by the PV module model is 11.6% for the system without additional anti-reflective coating (configuration E) and 12.1% for the system with additional anti-reflective coating (configuration F). These electrical system effi-

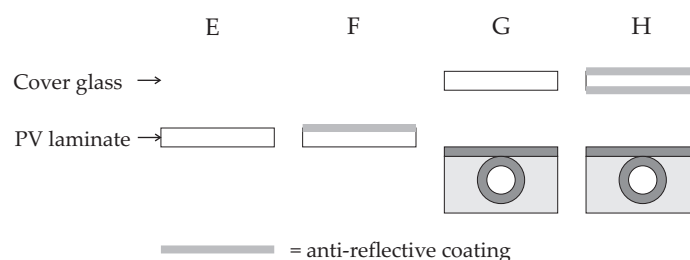


**Figure 5.14:** PV module configurations, E without AR coating and F with AR coating, and solar thermal collector configurations, G without AR coating and H with AR coatings.

iciencies are independent of the PV module surface area and will serve as reference values.

### 5.5.2 The thermal yield of solar thermal systems

A solar thermal collector system containing glazed flat-plate collectors with selective absorbers is considered. To evaluate the performance of this system under identical conditions as used in the evaluation of PVT systems, the thermal part of the PVT system model is used. In a solar thermal collector, a spectrally selective absorber is used instead of a PV laminate. It is assumed that this absorber has an emissivity of 12% and an absorption factor of 95%. Taking into account the effective transmittance of the cover glass without coating (configuration G in figure 5.14) an absorption factor of 86.6% is found. In case a double sided anti-reflective coated cover glass is used (configuration H), the absorption factor is 91.4%.

The annual thermal efficiency was determined of solar thermal systems for domestic hot water having a collector area of 3, 6 and 12 m<sup>2</sup> and of systems for combined domestic hot water and room heating having a collector area of 6, 12 and 24 m<sup>2</sup>. The volume of the heat storage tanks are again 200 l for domestic hot water and 40 m<sup>3</sup> for room heating in all cases. Both coating configuration G and H are considered. The annual thermal efficiencies for these solar thermal collector systems are summarised in table 5.7. These thermal system efficiencies will serve as reference values.

### 5.5.3 Relative efficiency of PVT systems

In section 5.4 the annual electrical and thermal efficiency of a range of PVT systems was presented. These are systems for domestic hot water or for combined domestic hot water and room heating, each for three different collector surface areas in combination with four different coating configurations. Relative system efficiencies will be considered here, i.e. the efficiency of PVT systems relative to the efficiency of

**Table 5.7:** Annual thermal system efficiency for solar thermal collector systems for domestic hot water (collector area 3, 6 and 12 m<sup>2</sup>) and combined domestic hot water and room heating (collector area 6, 12 and 24 m<sup>2</sup>).

	domestic hot water			Combined DHW & RH		
	3 m <sup>2</sup>	6 m <sup>2</sup>	12 m <sup>2</sup>	6 m <sup>2</sup>	12 m <sup>2</sup>	24 m <sup>2</sup>
configuration G	46.8%	30.1%	16.9%	36.1%	28.9%	15.5%
configuration H	48.4%	30.8%	17.1%	38.1%	30.2%	18.9%

conventional PV and solar thermal systems (see sections 5.5.1 and 5.5.2). Systems of equal collector or module surface area are compared and PVT systems with AR coatings are compared to conventional systems with AR coatings. To be more specific, regarding the *electrical* efficiency: PVT configurations A and B are compared to PV configuration E and PVT configurations C and D are compared to PV configuration F. Regarding the *thermal* efficiency: PVT configurations A and B are compared to solar thermal collector configuration G and PVT configurations C and D are compared to solar thermal collector configuration H.

In figure 5.15 the relative PVT system efficiencies are shown. From figure 5.15 it can be seen that the relative electrical and thermal efficiencies of all PVT systems are less than 100%. This indicates that both electricity and heat are generated less efficiently by glazed PVT systems than by the separate PV systems and solar thermal systems. The causes for this will be discussed in section 5.5.4. However, adding anti-reflective coatings to the PVT collectors increases both the relative electrical and relative thermal efficiency (compare configurations A and C or B and D). Adding a low-emissivity coating can significantly increase the relative thermal yield, but at the same time it decreases the relative electrical yield (compare system A and B or C and D). Roughly speaking, the systems reaching a high (>90%) relative thermal efficiency have low (<80%) relative electrical efficiency, and vice versa. Apart from these extremes there are systems having both a relative electrical and thermal efficiency of around 85%.

It can be seen that the systems with small collector areas obtain the highest relative electrical efficiencies. As mentioned in section 5.4.2, this is caused by the fact that these systems operate at a lower temperature, resulting in lower cell temperatures. As a result the temperature induced loss in electrical efficiency is lowest.

The explanation for the fact that the PVT systems with the larger collector areas have the highest relative thermal efficiency, is as follows. In a system with a large collector area, the thermal efficiency of the collector itself becomes less important for the thermal efficiency of the system as a whole. For example consider two systems for domestic hot water with large collectors, the first having an efficient collector and the second a less efficient one. On a sunny day, the efficient solar thermal collector may heat up the tank to its maximum temperature relatively quickly but then the

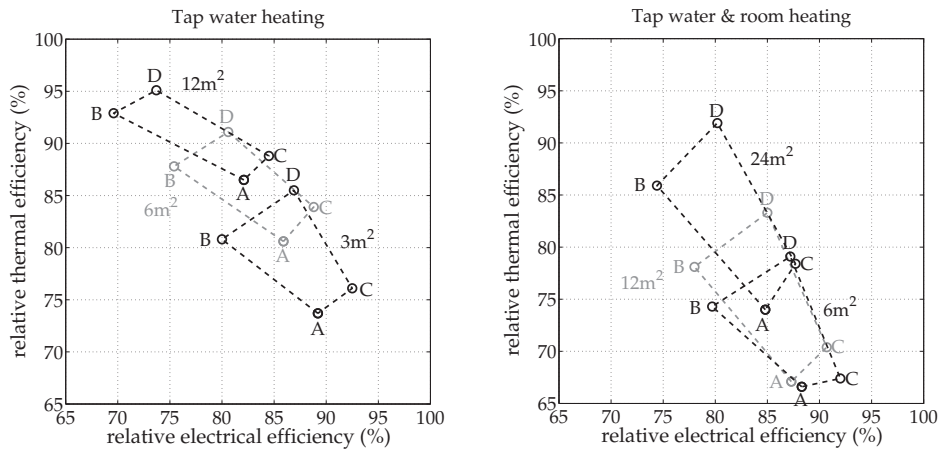


**Figure 5.15:** The relative electrical annual system efficiency versus the relative thermal annual system efficiency for PVT systems with c-Si PUM cells and coating configurations A, B, C and D. Left: For PVT systems for domestic hot water with a collector area of 3, 6 and 12 m<sup>2</sup>. Right: For PVT systems for combined domestic hot water and room heating with a collector area of 6, 12 and 24 m<sup>2</sup>.

pump has to be turned off to prevent boiling. On the other hand the less efficient collector will take more time to heat the tank but as a result it stays in operation during a larger part of the day before the water pump has to be turned off. At the end of the day both systems have generated the same amount of heat even though the collector efficiencies are different. Note that the heat demand is kept constant and only for systems with large collector areas these stagnation conditions occur. This explains why the difference between the annual yield of a solar thermal system and a PVT system tends to cancel out with increasing collector areas. In systems with small collector areas, the thermal efficiency of the collector remains very important.

#### 5.5.4 PVT specific efficiency loss mechanisms

In this section the causes for the somewhat lower annual electrical and thermal efficiency of the PVT systems compared to the reference systems are quantified.

##### Electrical efficiency

The causes for the lower electrical efficiency of a PVT system compared to a PV system are:

- cover glass transmission loss,
- additional temperature loss caused by higher cell temperatures induced by the cover glass.



In case a low-emissivity coating is applied on the PV laminate in the PVT collector, the additional causes are:

- increased reflection induced by the low-emissivity coating,
- parasitic absorption by the low-emissivity coating,
- additional temperature loss caused by higher cell temperatures induced by the low-emissivity coating.

By means of additional simulations, the relative importance of these causes is investigated. For example the cover glass transmittance loss is determined by relating the system efficiencies presented earlier to the efficiency of an imaginary system with a cover glass transmittance of 100%.

The results are shown in the top panel of figure 5.16. The systems for domestic hot water are considered in combination with coating configurations C (with anti-reflective coatings only, see figure 5.2) and D (with additional low-emissivity coating). It can be seen that the transmission loss of the cover glass with the anti-reflective coating on both sides is 3.5%, in all cases. In case a low-emissivity coating is applied (configuration D), there is an additional reflection loss of 2.8% and a parasitic absorption loss of 0.9%, as well. Because systems with a larger collector area operate at a higher temperature, the additional temperature losses increase with increasing collector area, as can be seen in the figure. Note that the additional temperature losses presented here are the additional temperature losses with respect to the PV reference system, i.e. it is the loss in electrical efficiency caused by the fact that cell temperatures of a PVT collector are higher than cell temperatures of the reference PV module. The additional temperature loss occurring in configuration C (without low emissivity coating) is induced by the cover glass and ranges from 4.2% to 12.2%. The temperature loss induced by the low-emissivity coating ranges from 1.8% to 7.1%.

Regarding the electrical efficiency of the PVT systems with AR coated cover glass, it can be concluded that the temperature induced efficiency loss is the major loss mechanism. Note that the magnitude of this temperature induced efficiency loss may be much lower in low temperature applications (e.g. pool heating) not considered here. However, independent of the temperature level of the cells, there are 3.5% and 3.7% optical losses caused by the limited transmittance of the cover glass and of the low-emissivity coating, respectively. Note that in PVT systems without additional AR coating, the optical losses would be much more severe.

### Thermal efficiency

The causes for the lower thermal efficiency of a PVT system compared to the reference solar thermal system are:

- higher emissivity of the absorber (85% (conf. C) or 20% (conf. D) versus 12% (conf. G and H)),

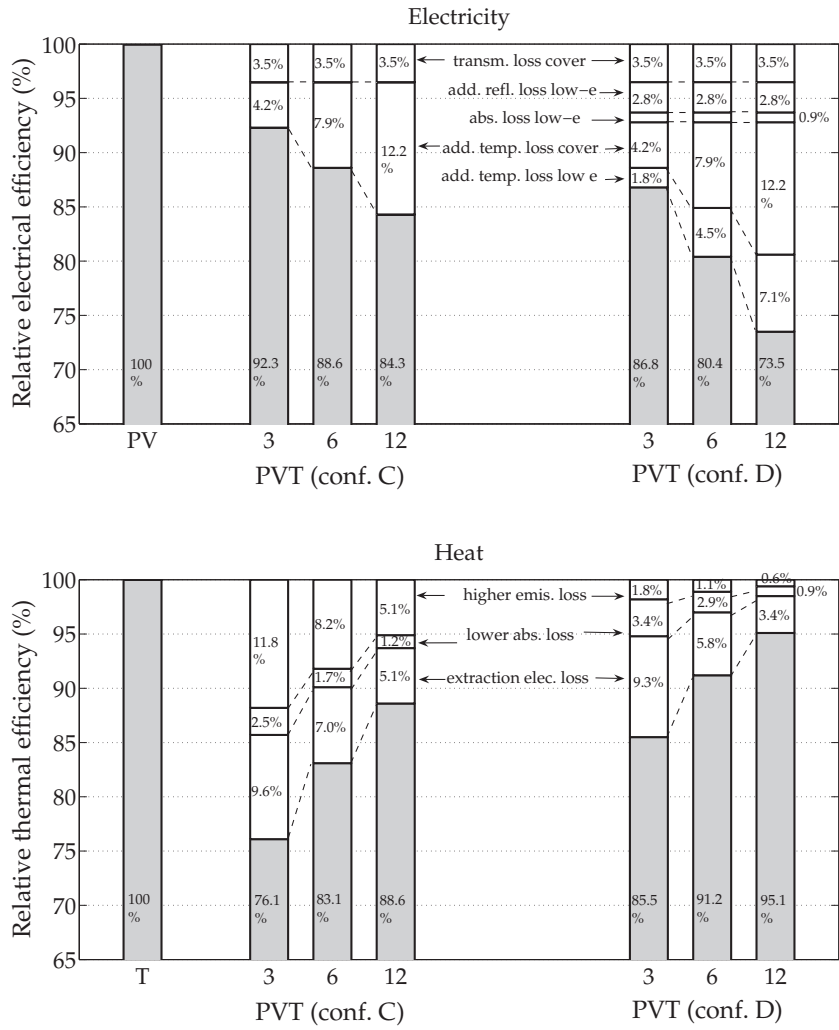


**Figure 5.16:** The relative electrical efficiency (top) and relative thermal efficiency (bottom) of PVT systems for domestic hot water with collector surface areas of 3, 6 and 12 m<sup>2</sup>. PVT configuration C has anti-reflective coatings and PVT configuration D has both a low-emissivity and anti-reflective coatings.

- lower absorption factor of the absorber (87.9% (conf. C) or 86.7% (conf. D) versus 91.4% (conf. H)),
- extraction of electrical energy (STC efficiency: 14.2% (conf. C) or 13.7% (conf. D) versus 0%).

In the lower panel of figure 5.16 these causes are quantified. As mentioned in section 5.5.3, in systems with a large collector, the efficiency of the collector itself becomes less important. As a consequence in relative terms, the losses in thermal efficiency are smallest for the systems with the largest collector areas. In case no low-emissivity coating is applied (configuration C), the loss caused by the higher emissivity of the absorber ranges from 11.8% to 5.1%. In case a low-emissivity coating is applied (configuration D) the loss is reduced to 1.8-0.6%. The somewhat lower absorption factor of the absorber is responsible for a loss of 3.4% to 0.9%. The fact that electrical energy is extracted, results in a loss of 9.6% to 3.4%. Note that from a thermal perspective the extraction of electricity can be considered to be a loss mechanism, the electricity itself however is used effectively.

### 5.5.5 Avoided primary energy

From the analysis presented in sections 5.4 and 5.5 it is clear that the electrical and thermal efficiencies of the glazed PVT systems considered here, are somewhat lower than the efficiencies of the separate PV and solar thermal systems, respectively. One should bear in mind however, that a PVT collector generates both electricity and heat simultaneously. Therefore, the *total* energy yield of a PVT system per  $\text{m}^2$  is higher than the yield of each of the reference systems per  $\text{m}^2$ .

In order to illustrate this the electrical and thermal yield of a PVT system are added. However, it should be taken into account that 1 kWh of electrical energy and 1 kWh of thermal energy represent a different 'value' and should not be added just like that. Coventry [98] attaches different weights to electric and thermal energy before adding them up. One possible way to determine these weights is by considering the avoided primary energy,

$$E_{\text{prim}} = \frac{E_e}{\eta_{\text{prim} \rightarrow e}} + \frac{E_{\text{th}}}{\eta_{\text{prim} \rightarrow \text{th}}}, \quad (5.13)$$

where  $E_e$  and  $E_{\text{th}}$  are the electrical and thermal yield of the PVT system and  $\eta_{\text{prim} \rightarrow e}$  and  $\eta_{\text{prim} \rightarrow \text{th}}$  are the efficiencies for converting primary energy into electricity and heat, respectively, in the conventional way. For  $\eta_{\text{prim} \rightarrow e}$  the power generation efficiency of a conventional power plant is used, which typically is 40% [98]. For  $\eta_{\text{prim} \rightarrow \text{th}}$  the thermal efficiency of a conventional gas fired domestic hot water system is used, which typically is 65% [99].

In trade-off considerations between the annual electrical and thermal efficiency of a PVT system, the consideration of avoided primary energy is a valuable tool. A

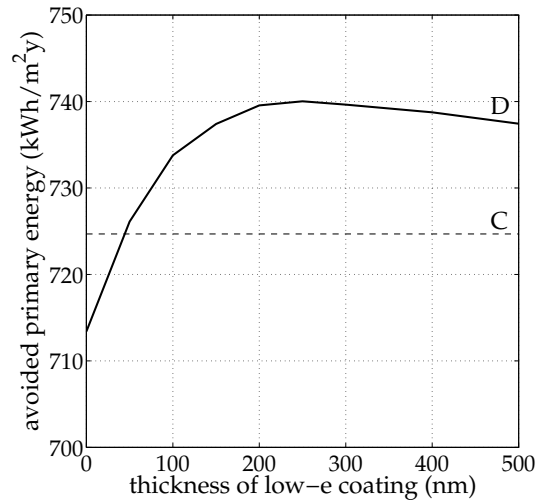


**Figure 5.17:** The avoided primary energy of a PVT system for domestic hot water with a 6 m<sup>2</sup> PVT collector with both AR and low-emissivity coatings (configuration D) versus the thickness of the low-emissivity coating. The avoided primary energy in case only AR coatings are applied (configuration C) is shown as well.

comparison between the avoided primary energy of a PVT system, a PV system and a solar thermal system, each having the same surface area, will be given as well. Such a comparison is interesting from a physical point of view, but one needs to be aware that from an economical point conclusions can not be drawn from this avoided primary energy alone.

#### Low-emissivity coating thickness

In section 5.4.3, a PVT system for domestic hot water with a 6 m<sup>2</sup> PVT collector with both AR and low-emissivity coatings (configuration D) was considered. The annual electrical and thermal efficiencies of this system were presented as a function of thickness of the low-emissivity coating. If the thickness of this coating is reduced below the standard thickness of 300 nm, the electrical efficiency increases, but the thermal efficiency decreases (see figure 5.13).

To investigate the optimum coating thickness with respect to the avoided primary energy, the results presented in section 5.4.3 are converted to avoided primary energy as shown in figure 5.17. It can be seen that for the standard low-emissivity coating thickness of 300 nm the avoided primary energy of the system is close to 740 kWh/m<sup>2</sup>·y. Though there is an optimum thickness of about 250 nm, in the range of 200-400 nm the avoided primary energy is almost constant, i.e. varying less than 1 kWh/m<sup>2</sup>·y. This indicates that within this range any increase in electrical efficiency

is cancelled by a decrease in thermal efficiency and vice versa. Only if the coating is thinner than 200 nm, the avoided primary energy is reduced somewhat. Because the avoided primary energy for configuration D is higher than for configuration C (without low-emissivity coating, also indicated), it can be concluded that in terms of avoided primary energy it is attractive to apply a low-emissivity coating. In other words, the gain in thermal efficiency outweighs the loss in electrical efficiency. However in relative terms the gain is a modest 2%<sub>rel</sub> (from 725 to 740 kWh/m<sup>2</sup>y).

Note that for a less than 40 nm thin low-emissivity coating, the avoided primary energy is lower than for the case without low-emissivity coating (configuration C). This is caused by the fact that this extremely thin low-emissivity coating does not increase the thermal efficiency sufficiently to compensate for the reflection loss it induces.

### PVT systems versus separate systems

In figure 5.18 a comparison is made between the avoided primary energy that can be reached per m<sup>2</sup> using various PVT systems (coating configurations A to D) and conventional PV and solar thermal systems. Again PVT systems for domestic hot water with a collector surface area of 6 m<sup>2</sup> are considered. Shown on the left are the avoided primary energy of the conventional PV and solar thermal systems, both with and without additional anti-reflective coating. The PV modules and solar thermal collectors considered here have a surface area of 6 m<sup>2</sup> as well.

It can be seen that the avoided primary energy of the conventional PV systems is about 300 kWh/m<sup>2</sup>y and of the conventional solar thermal systems it is about 500 kWh/m<sup>2</sup>y. The avoided primary energy of the PVT systems is much higher, about 700 kWh/m<sup>2</sup>y. This clearly demonstrates one of the main advantages of PVT systems over the conventional systems. Though the individual efficiencies of a PVT system are lower, the total avoided primary energy is higher for a given collector surface area.

## 5.6 Conclusion

In this chapter the annual electrical and thermal yield of PVT systems has been determined by means of numerical simulations. Systems with glazed PVT sheet-and-tube collectors have been considered for domestic applications. An existing PVT system model has been used and the heat storage model was refined to take into account stratified storage of heat. The absorption factors of solar cells resulting from the detailed analysis of chapters 3 and 4, have been used as input parameters for the system simulations presented in this chapter.

The annual electrical and thermal yield per unit of collector area of a PVT system is determined to a large extent by the type of PV cells used in the PVT collector.

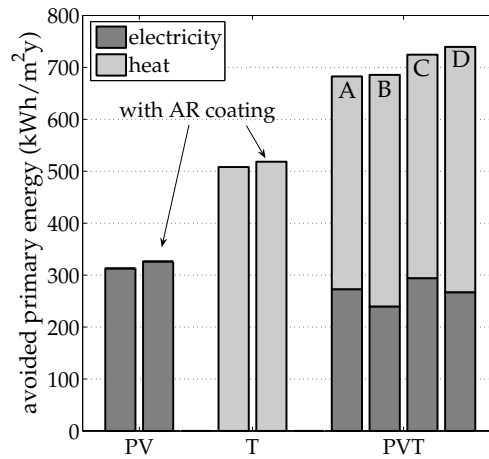


**Figure 5.18:** The avoided primary energy per  $\text{m}^2$  of PVT systems and of PV and solar thermal (T) reference systems. The reference systems are considered with and without anti-reflective coating and the PVT systems with coating configurations A to D. In all cases PV module or collector surface areas of  $6 \text{ m}^2$  are considered. The application for the heat is domestic hot water.

The annual yield was determined for systems with various cell technologies, i.e. c-Si cells (PUM and EWT), a-Si cells and CIGS cells. The system with c-Si EWT cells has the highest electrical yield because of the highest STC efficiency, while the system with CIGS cells has the highest thermal yield because of the most favorable effective absorption factor.

The PVT collector surface area has a large effect on the annual yield as well. The standard system for domestic hot water considered here has a collector area of  $6 \text{ m}^2$ . The standard system for combined domestic hot water and room heating considered here has a collector area of  $12 \text{ m}^2$ . If the collector area is increased (keeping the storage volume and demand constant) the system operates at a higher temperature. As a result, especially the thermal efficiency, but also the electrical efficiency are reduced.

Valuable solar energy is lost in the PVT collector because a part of the incident sunlight is reflected at the cover glass and the front of the PV laminate. Also because of the relatively high emissivity of the PV laminate, heat may escape by means of radiation. The application of anti-reflective and low-emissivity coatings to reduce the amount of energy lost in these ways has been investigated. It turns out that the application of anti-reflective coatings is beneficial for both the electrical and thermal yield. The application of a low-emissivity coating increases the thermal efficiency but unfortunately reduces the electrical efficiency. It turns out that some losses are inherent to PVT systems. Insight in these losses has been obtained. A feature of PVT

systems is that a higher avoided primary energy per  $\text{m}^2$  can be reached, compared to conventional PV and solar thermal systems.

# Assessment of PVT systems

In chapter 5 insight was gained in the mechanisms reducing the efficiency of PVT systems with respect to the separate reference systems. In this chapter these loss mechanisms and their fundamental limits are discussed in more detail. The focus is on glazed PVT systems for domestic hot water, but other PVT systems will be considered as well.

Though a detailed analysis of the investment cost and the related cost of energy produced with PVT systems is outside the scope of this thesis, one remark related to the investment cost will be made. From an investment point of view, a PVT system contains both the elements of a PV system (PV laminates, cabling, inverter) and most of the elements of a solar thermal system (cover glass, tubing, storage system). Therefore the investment cost of a PVT system will be close to the investment cost of two separate systems, each having the same surface area. In fact a thermal collector system needs to be installed with the selective absorber being replaced by a PV laminate incorporating the solar cells and the metal sheet for heat collection. This implies that the cost for the PV module frame and the installation cost of the PV module on the roof can be saved on the PV system side and the cost for the selective absorber coating on the thermal side.

Based on the cost break-down figures given by Jäger-Waldau [100] for 2 kW<sub>p</sub> c-Si PV systems (corresponding to a PVT collector area of about 20 m<sup>2</sup>) one can estimate that the total cost saving is about 10% for the PV part of a PVT system (5% because no frame is required and 5% because no separate installation on the roof is required). In case one considers a PVT system with a smaller collector area of 3 to 6 m<sup>2</sup> for



domestic hot water, then the *relative* cost of the installation labour for the PV modules on the roof and the project overhead cost will be higher. Therefore in smaller systems, the cost saving of a PVT system will be relatively higher.

Nevertheless, the cost savings are limited on both sides to at most 5 to 10% for larger area systems and 10 to 15% for small area systems. Therefore only slightly smaller electrical and thermal yields compared to separate reference systems will be acceptable from an economical point of view.

## 6.1 Electrical losses

Both in a PV system and in the PV part of a PVT system, the cost of the electricity produced is determined both by the investment cost and the annual yield, directly. The investment cost per watt peak ( $W_p$ ) installed, for PV systems with laminates with different solar cell technologies is more or less the same at the moment. Therefore the comparison is made on basis of the Performance Ratio (PR). The PR is the ratio of the annual electrical system efficiency and the *lamine* efficiency at STC. The PR is closely related to the losses that occur on the system level and make the comparison of various systems slightly easier. These loss mechanisms are:

- the optical loss, induced by the glass cover in case of a glazed PVT collector,
- the temperature loss, caused by the fact that the cell efficiency decreases with increasing cell temperature and deviates from the 25 °C STC cell temperature,
- the low irradiance loss, caused by the fact that the cell efficiency depends on the irradiance and deviates from the 1000 W/m<sup>2</sup> STC irradiance,
- the cable and inverter loss caused by the ohmic loss in cabling and the loss in the inverter.

Figure 6.1 summarises the losses for PV and PVT systems with c-Si and a-Si PV laminates.

The inverter and cable loss is about 7.5% in all cases. The low irradiance loss is 5% for the c-Si laminates and about 4% for the a-Si laminates. The optical loss and the temperature loss are the main causes for the difference in the annual electrical efficiency of PVT systems compared to PV systems. Both c-Si and single junction a-Si cells are considered in figure 6.1 because they represent the extreme cases with respect to the temperature coefficient of the electrical efficiency  $\beta$ . For c-Si solar cells  $\beta = -0.0045 / ^\circ\text{C}$  [23] and this value is known quite accurately. For silicon based thin-film cells this temperature coefficient is still subject of detailed investigation [101]. For single junction a-Si solar cells  $\beta = -0.002 / ^\circ\text{C}$  is used in this thesis [23].

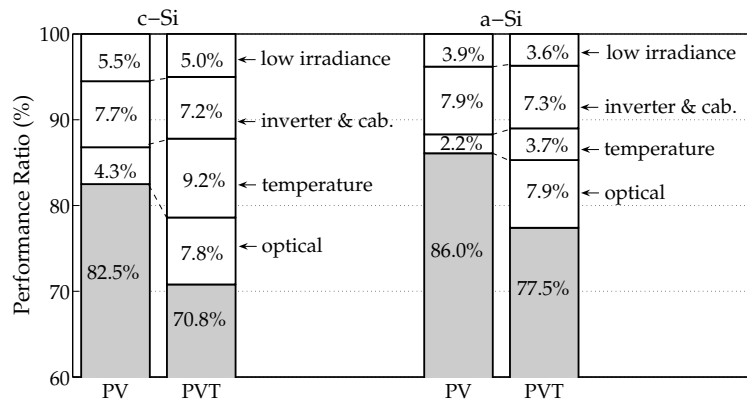


**Figure 6.1:** An overview of the performance ratio of a PV and a PVT system, both with c-Si and a-Si laminates. The loss mechanisms are indicated as well. A PVT system for domestic hot water with a collector surface area of 6 m<sup>2</sup> without additional coatings is considered. The PV module area is 6 m<sup>2</sup> as well.

### Optical loss

The optical loss induced by a cover glass is as much as about 8% if no coatings are applied, but as shown in section 5.4.3 this can be reduced to 3.5% by applying anti-reflective coatings on both sides of the cover. The magnitude of this optical loss is independent of the type of solar cells used or the sizing of the PVT collector. Note that an additional optical loss will occur if a low-emissivity coating is applied to the PV laminate, as will be discussed in section 6.2.

### Temperature loss

The temperature loss for the conventional PV system is 4.3% in case c-Si cells are used and 2.2% in case a-Si cells are used, see figure 6.1. In glazed PVT collectors the cells are operated at a higher average cell temperature in most cases, resulting in a higher temperature loss.

In the glazed PVT systems for domestic hot water with a collector surface area of 6 m<sup>2</sup> and a storage tank of 200 l, the temperature loss is 9.2% for this specific PVT system with c-Si cells and 3.7% for this system with a-Si cells. Using the numerical PVT system model, one can derive that the temperature loss ranges from 8 to as much as 20% for c-Si cells, depending on the sizing of the collector area and on the application of coatings. The comparable temperature loss for a-Si cells is 3 to 8%.

The magnitude of the temperature loss is determined by the temperature coefficient of the efficiency  $\beta$  on one hand and by the cell temperature on the other hand. Because the temperature loss is proportional to  $-\beta$  and because  $\beta$  is more or less

determined by the cell technology used, this loss can be minimised by using a cell technology with a small  $|\beta|$ , such as a-Si. It is an empirical fact that for single junction cells  $|\beta|$  is higher for cell technologies with a lower bandgap [23]. So far, a-Si single junction solar cells seem to have the most favourable temperature coefficient, being  $-0.002 / ^\circ\text{C}$  [23]. However, in increasing the efficiency of a-Si based solar cells, the tendency is to move from the single junction a-Si cells to multi-junction solar cells that include smaller bandgap semiconductors as well. Therefore one could expect that these solar cells have less favourable temperature coefficients. According to data sheet information, the Uni-Solar triple junction solar cell modules have a temperature coefficient of  $-0.0021 / ^\circ\text{C}$  [102] and the micromorph (a-Si/ $\mu\text{c-Si}$ ) modules delivered by Phoenix Solar of  $-0.0024 / ^\circ\text{C}$  [103] being close to the reported value of  $-0.0023 / ^\circ\text{C}$  for Kaneka micromorph modules [23]. In this respect modules based on HIT (Heterojunction with Intrinsic Thin Layer) solar cells are interesting. A HIT cell is composed of a thin single crystalline Si wafer sandwiched by ultra-thin a-Si layers. Sanyo reports a temperature coefficient  $\beta$  of  $-0.003 / ^\circ\text{C}$  for HIT cells, which is significantly lower than the value of  $-0.0045 / ^\circ\text{C}$  for traditional c-Si solar cells. The value of  $-0.003 / ^\circ\text{C}$  [104] corresponds well with results based on field measurements ( $\beta = -0.0025$  to  $-0.0034 / ^\circ\text{C}$ ) reported by Zinßer [101].

The second way to reduce the temperature loss is to reduce the solar cell temperature under operational conditions as much as possible. This can be done by reducing the temperature drop between the cells and the water and/or reducing the temperature of the water flowing into the collector. The temperature drop between the cells and the water is determined by a heat transfer coefficient and a heat flux. The effective heat transfer coefficient used in the model is  $70 \text{ W/m}^2\text{K}$  (based on the following heat transfer coefficients:  $120 \text{ W/m}^2\text{K}$  from cell to sheet,  $200 \text{ W/m}^2\text{K}$  along the sheet to the tube and  $700 \text{ W/m}^2\text{K}$  from the tube to the water, see section 5.2.2). In case of high solar irradiance ( $1000 \text{ W/m}^2$ ) and low collector inflow temperatures ( $20 ^\circ\text{C}$ ), the heat flux from cell to water can be as high as  $500 \text{ W/m}^2$ , implying a maximum temperature difference between cell and water of  $7 ^\circ\text{C}$ .

In the case of the  $6 \text{ m}^2$  PVT collector system for domestic hot water, the finite heat transfer coefficient between the cells and the water ( $70 \text{ W/m}^2\text{K}$ ) alone, causes a temperature loss of 1.0% (on an annual basis), to be compared to a total temperature loss of 9.2%. The temperature loss induced by the finite heat transfer coefficient could be reduced if this coefficient could be increased. It seems that doubling from  $70 \text{ W/m}^2\text{K}$  to  $140 \text{ W/m}^2\text{K}$  would be possible by increasing the heat transfer coefficient between the cells and the sheet from 120 to 250  $\text{W/m}^2\text{K}$  and the heat transfer coefficient along the sheet from 200 to 600  $\text{W/m}^2\text{K}$  by reducing the distance between the pipes and increasing the thickness of the sheet. Simulations show that increasing the heat transfer coefficient from 70 to  $140 \text{ W/m}^2\text{K}$  reduces the temperature loss induced by this heat transfer coefficient from 1.0% to 0.4% and the overall temperature loss from 9.2% to 8.6%.

The case described above shows that the temperature loss introduced by the heat resistance between the cells and the water is limited. The major part of the temperature loss is determined by the water temperature itself. Reducing the inflow temperature of the collector is therefore very important. The temperature of the water flowing into the collector can be kept low by using the PVT system in a low temperature application as will be discussed in section 6.3. However, if the application is fixed to medium temperature heat for domestic hot water, then the average solar cell temperature is mainly determined by the thermal solar fraction. From the result presented in section 5.4.2, it can be derived that by reducing the collector surface area from 6 to 3 m<sup>2</sup> (keeping heat demand constant) in the PVT reference system, the temperature loss is reduced from 9.2% to 7.8%.

It should also be noted that having a stratified storage tank, helps to reduce the average cell temperature. In chapter 5, a reasonably well stratified tank (FOM=0.78) was assumed, resulting in the above mentioned 9.2% temperature loss for the c-Si reference case. By means of additional simulations it was found that in case of a fully mixed tank (worst case, FOM=0.63) the additional temperature loss is increased to from 9.2 to 10.2% and in case of a very well stratified tank (FOM=0.94) it is slightly reduced to 8.7%.

### Conclusion

The optical and temperature loss are responsible for a lower Performance Ratio of glazed PVT systems compared to conventional PV systems. The optical loss is induced by the additional cover glass and is by definition 0% in PV systems. In PVT systems considered here, where no additional coatings are applied, the optical loss is 7.8%. This can be reduced to 3.5% by application of anti-reflective coatings to the cover glass. It is therefore recommended to apply anti-reflective coatings to minimise the optical loss.

In a conventional PV system in Dutch climatological conditions, the temperature loss is 4.3% for conventional c-Si cells and 2.2% for a-Si cells. In glazed PVT systems for medium temperature applications considered here, this temperature loss will be roughly twice as high. This illustrates that for these PVT systems, having a low  $|\beta|$  is very important. The exact magnitude of the temperature loss also depends on other systems design parameters as well. For the standard PVT systems for domestic hot water with a PVT collector of 6 m<sup>2</sup> with conventional c-Si cells, the temperature loss is 9.2%. This number increases strongly with increasing solar fraction. If a modest thermal solar fraction would be allowed, then the size of the collector can be reduced to 3 m<sup>2</sup> and the temperature loss would be reduced to 7.8%. Reducing the heat resistance between solar cell and water and having a more stratified heat storage tank can reduce the temperature loss only a little further.

Assuming that for c-Si cells the temperature loss can be reduced to about 7.3%, then this is still 3% higher than in the conventional PV system. Adding to that the

best case optical loss of 3.5%, it is concluded that with conventional c-Si cells in the best case the Performance Ratio of glazed PVT systems is about 6.5% lower than the Performance Ratio of a conventional PV systems.

## 6.2 Thermal losses

In section 5.4 the annual thermal yield of a PVT system for domestic hot water was considered. Compared to the reference solar thermal system, two main loss mechanisms were identified. They are both related to different thermal properties of the PV laminate in the PVT collector compared to the spectrally selective absorber in the reference system. Firstly, the PV laminate has an effective absorption factor of 71% (c-Si) compared to 95% for the spectrally selective absorber. Secondly, the PV laminate has a high emissivity of 85% compared to 12% for the spectrally selective absorber.

### Effective absorption factor

In table 6.1, the main results from chapters 3 and 4 regarding the effective absorption factor ( $A_{\text{eff}} = A - \eta_e$ ) of current and future solar cells are summarised. Note that table 6.1 is a very brief summary of table 4.7 and for a discussion of these numbers, please refer to section 4.6.

The PVT system for domestic hot water with a 6 m<sup>2</sup> PVT collector with conventional c-Si cells is considered. As a result of the lower effective absorption factor of the c-Si PV laminate (71% versus 95%), the thermal efficiency of the PVT systems is reduced by 8.7%<sub>rel</sub> with respect to a solar thermal system. This loss will be about 5.5%<sub>rel</sub> for PVT systems with thin-film PV laminates, because these have a somewhat higher effective absorption factor of approximately 80%.

The ongoing technological developments will lead to higher electrical cell efficiencies in future. Whether these developments increase or decrease the effective absorption factor, depends on the type of measures taken. A first kind of measures involves a reduction of reflective losses, e.g. reduction of the front side metallisation coverage (c-Si), improvement of incoupling and trapping of irradiance. In absolute terms, this kind of measures will always increase the absorption factor more than the electrical efficiency, thereby increasing the effective absorption factor.

Measures to improve the electrical cell efficiency of a second kind include the increase of the reflection coefficient of the back contact and a reduction of recombination of charge carriers in the bulk or at the interfaces of the PV cell. Though very important for the electrical efficiency, these measures reduce the effective absorption factor by at least the same amount as the electrical efficiency is increased. The reduction in effective absorption factor will lead to a reduction of the thermal yield of PVT

**Table 6.1:** The AM1.5 absorption factor  $A$ , the cell efficiency  $\eta_e$  and the effective absorption factor  $A_{\text{eff}}$  for c-Si cells and typical values for thin-film solar cells. Both current and expected future values are given for encapsulated cells without additional coatings. See also table 4.7.

	$A$ (%)	$\eta_e$ (%)	$A_{\text{eff}}$ (%)
<b>c-Si cells</b>			
PUM (current)	87	16	71
2030 design	91	25	66
<b>thin-film cells (typical values)</b>			
current	90	10	80
2030 design	91	16	75
<b>spectrally selective absorber</b>			
current and future	95	0	95

collectors. Note that in terms of avoided primary energy, the gain in electrical yield will in most cases outweigh the loss in thermal yield.

Because measures of the first kind have already been implemented for a large part, a further increase in absorption factor will for c-Si cells be limited to 4% (from 87 to 91%, see table 6.1) and for most thin-film cells it will be limited to about 1% (from 90 to 91%). In the long term (2030), the measures of the second kind are expected to increase the electrical efficiency of c-Si cells by 9% (from 16 to 25%) and for most thin film cells by about 6% (from 10 to 16%). As can be seen in table 6.1, the overall effect is a reduction of the effective absorption factor of c-Si PV cell from 71% to 66% and of thin-film PV cells from 80% to 75%. As a result the loss in thermal efficiency caused by the lower effective absorption factor is expected to increase slightly in the long term. However, although this will reduce the thermal efficiency of the PVT system, it will increase the electrical output.

### Emissivity

The loss in thermal system yield resulting from the high emissivity (0.85 versus 0.12) is generally quite high. In the PVT systems for domestic hot water considered in section 5.5.4 this loss ranges from as much as 11.8%<sub>rel</sub> in the system with a 3 m<sup>2</sup> PVT collector to 5.1%<sub>rel</sub> in the system with a 12 m<sup>2</sup> PVT collector. By applying a low-emissivity coating on the PV laminate, this loss can be reduced by 10.0%<sub>rel</sub> and by 4.5%<sub>rel</sub>, for the systems with the 3 and the 12 m<sup>2</sup> PVT collector areas, respectively. These values were derived in section 5.5.4 for a PVT collector with c-Si cells, but they are independent of the cell technology used.

However, at the same time, the low-emissivity coating reduces the *electrical* efficiency due to additional optical and temperature losses. Expressed in reduction

of Performance Ratio, as was done in section 6.1, the optical loss induced by the low-emissivity coating is 7.9%. In case an anti-reflection coating is applied to the low-emissivity coating the reduction in Performance Ratio due to the optical loss is 3.7%. The temperature loss induced by the low-emissivity coating for a PVT system with c-Si cells ranges from 1.8%<sub>rel</sub> in the system with a 3 m<sup>2</sup> PVT collector to 7.1%<sub>rel</sub> in the system with a 12 m<sup>2</sup> PVT collector. In case of a-Si cells the temperature loss will range from 0.8 to 7.1%<sub>rel</sub>.

It can be concluded that applying a low-emissivity coating to the PV laminate in a glazed PVT collector means that a higher thermal efficiency is obtained at the cost of a reduced electrical efficiency. Whether it is attractive to do so in terms of avoided primary energy depends mainly cell technology used. If a-Si cells are used it is attractive for the systems considered in this thesis to apply a low-emissivity coating. If conventional c-Si cells are used, it depends on the sizing of the PVT system. In the systems with a 3 m<sup>2</sup> PVT collector it is attractive, while in the systems with 12 m<sup>2</sup> collector it is not.

### Conclusion

The thermal efficiency of a glazed PVT system is significantly lower than of a solar thermal system because of losses induced by the lower effective absorption factor and the higher emissivity of the PV laminates compared to a spectrally selective absorber. The magnitude of these losses is very sensitive to the sizing of the PVT collector. For a PVT system with a 6 m<sup>2</sup> collector with c-Si cells the sum of these losses is about 17%<sub>rel</sub>. In case a-Si cells are used, these losses are slightly less. By application of a low-emissivity coating, the sum of these losses can be reduced to 9%<sub>rel</sub> at the cost higher optical and thermal losses at the electrical side. Whether it is attractive to apply this low-emissivity coating in terms of avoided primary energy, depends on the cell technology considered and on the sizing of the system.

## 6.3 Promising applications for PVT systems

For the glazed PVT systems for domestic hot water, both the electrical and thermal efficiency are significantly lower compared to separate PV and solar thermal systems. From an economical point of view, this annuls the modest saving in investment cost that can be obtained by combining the two separate systems. As a result the cost of energy supplied by the glazed PVT system will be somewhat higher. This may be different for some of the PVT systems briefly reviewed next.

### Glazed PVT systems for low temperature applications

The relatively high temperature loss of PVT collectors considered here is inherent to the application of domestic hot water, requiring a temperature level of 60 °C. By

means of additional simulations it was found that the inflow temperature of the PVT collector has to be reduced to as low as 15 °C to cool the PV cells down to an average temperature of 36 °C. Note that low flow rate 10 kg/m<sup>2</sup>h was assumed in combination with a 6 m<sup>2</sup> PVT collector. If this would be done, the temperature loss of the PVT collector would be equal to the temperature loss of the reference PV module, i.e. there would be no additional temperature loss for the PVT system. In practice this could be achieved by continuously pumping ground water through the PVT collector. However, unless there is a useful application for the large amount of low temperature heat being generated, this does not seem a very practical option.

#### **Unglazed PVT systems**

Both causes for the lower electrical efficiency of PVT systems (i.e. optical loss and temperature loss) would disappear if the cover glass is removed altogether, resulting in an unglazed PVT system. It is well known that unglazed thermal systems have a much lower thermal efficiency. In Dutch climatological conditions these collectors can be used only for low temperature applications. In sunnier climates, medium temperature applications may be possible as well.

#### **Applications with limited available roof area**

One of the main advantages of the PVT system over separate PV and solar thermal systems is the much higher total energy yield per unit of collector surface area. So in those cases where there is a demand for both electricity and heat, but the available roof surface area is the limiting factor, the application of a PVT system is attractive. Though the energy cost may be slightly higher, a system with PVT collectors covering the available area will have a higher electrical and thermal yield than two separate systems with PV modules and solar thermal collectors, each covering half of the available area.





# Conclusions and recommendations

## Conclusions

Regarding the numerical model for the absorption factor of solar cells, the following conclusions can be drawn:

- The net-radiation method was successfully extended to handle the *rough* interfaces found in solar cells as well.
- The extended net-radiation method allows a dedicated sub-model to be used for each type of interface found in solar cells.
- The model obtained is very suitable for determining the spectral absorption factor of a wide range of solar cells.

Regarding crystalline silicon solar cells the following conclusions can be drawn:

- Sub-bandgap irradiance ( $\lambda > 1.1 \mu\text{m}$ ) is mainly absorbed by free-carrier absorption in the very thin emitter.
- For most current and future c-Si cell designs the AM1.5 factor is as high as 87 to 91%, which is close to absorption factor of a spectrally selective absorber in a solar thermal collector (95%).
- Because electrical energy is extracted, the *effective* absorption factor of present c-Si solar cells is about 71%.

Regarding thin-film solar cells the following conclusions can be drawn:

- Most sub-bandgap irradiance is absorbed by free-carrier absorption in the transparent conductive oxide, provided optical confinement is good.
- The AM1.5 absorption factor of most thin-film solar cells (except the single junction a-Si cell) is very high, ranging from 88 to 93%.
- Because thin-film cells have a somewhat higher absorption factor and a lower electrical efficiency compared to c-Si cells, they have a higher effective absorption factor of about 80%, at present.

Compared to a conventional photovoltaic system (generating only electricity), the annual *electrical* efficiency of a glazed PVT system is somewhat lower because of:

- Optical losses induced by the additional cover glass (8%) and by an optional low-emissivity coating (8%). The application of anti-reflective coatings can halve these optical losses.
- High cell temperature induced losses (in case of c-Si solar cells: 8 to 20% for PVT systems versus 4% for PV systems). This loss is reduced if solar cells are used with a less negative temperature coefficient of the efficiency (e.g. single junction a-Si solar cells). The lower limit of the range given can be obtained if the cell temperature is kept as low as possible. The best way to achieve this is by reducing the inflow temperature of the PVT collector as much as possible.

Compared to a conventional glazed solar thermal system (generating heat only), the annual *thermal* efficiency of a glazed PVT system is somewhat lower because of:

- The lower effective absorption factor of a PV laminate compared to a spectrally selective absorber. For a PVT system with c-Si solar cells, this loss is 6 to 12%<sub>rel</sub> depending on the sizing of the system, but will be less if solar cells are used having a high effective absorption factor (e.g. CIGS solar cells).
- The higher emissivity of a PV laminate compared to a spectrally selective absorber. This loss is 5 to 12%<sub>rel</sub> depending on the sizing of the system, but can be reduced to less than 2%<sub>rel</sub> by application of a low-emissivity coating at the cost of a substantial reduction of the electrical efficiency.

Regarding the assessment of glazed PVT systems, the following conclusions can be drawn:

- Both the electrical and thermal efficiency of the PVT system are roughly 15%<sub>rel</sub> lower compared to separate PV and solar thermal systems. From an economical point of view this annuls the modest reduction in investment cost that could be obtained by combining two separate systems.
- Because the PVT system generates electricity and heat simultaneously, it has a higher energy yield per unit of collector area compared to the conventional systems.

## Recommendations

Regarding the numerical model for the absorption factor of solar cells, the following recommendation is made:

- The two-dimensional model for the absorption factor can successfully describe most optical effects occurring in solar cells. However, three-dimensional effects play a role when describing light-trapping. An escape factor was introduced to take this into account. In this thesis the required escape factor was derived from experimental results. It is recommended to investigate whether it is feasible to extend the numerical model to three dimensions and whether this would take away the need for a parameter that has to be derived from experiments.

Regarding the model for the annual yield of PVT systems, the following recommendations are made:

- In this thesis both the direct and diffuse components of the irradiance were considered as a normally incident beam. This introduces a small overestimation of the absorption factor for oblique incidence and therefore of the annual yield. As long as *differences* in annual yield are considered (as was done in this thesis), this overestimation hardly introduces an error. However, in case conclusions are based on the absolute value of the annual yield (e.g. for an economical analysis) it is recommended to take into account the effect of oblique incidence.
- In this thesis the focus has been on glazed PVT systems for medium temperature applications in Dutch climatological conditions. The research presented in this thesis indicates that the losses in annual yield occurring in these PVT systems (compared to conventional systems) are related to the cover glass and the system temperature. It is therefore recommended to widen the scope to include unglazed PVT systems, low temperature applications and other climatological conditions as well.



# Model for stratified thermal storage tanks

## A.1 Multinodel model

In the multinode approach [84, 94], a stratified heat storage tank is modelled as  $N$  fully mixed volume segments (nodes). If the total tank volume is  $V$ , then the volume of each segment is  $V/N$  and each segment has a uniform temperature  $T_i$ , where  $i = 1 \dots N$ . The top segment ( $i = 1$ ) has the highest temperature (lowest density) and the bottom segment ( $i = N$ ) has the lowest temperature (highest density). The degree of stratification is determined by the choice of  $N$ . Higher values of  $N$  can be used to simulate a higher degree of stratification. As shown in the left panel of figure A.1, the heat content of the storage tank is affected by two flows. At one side there is the collector loop with a flow rate  $\phi_c$ , taking water from the bottom segment and returning it at an elevated temperature  $T_c$ . At the other side there is the demand loop, with a flow rate  $\phi_d$ , taking water from the top segment and returning the same amount at a lower temperature. In this thesis the multinode model is used for both the domestic hot water tank and for the room heating tank. In case of the domestic hot water tank, the water returning at the demand side, is fresh water from the mains having a temperature of 10 °C. In case of the room heating tank, the water returning at the demand side, is returning from the underfloor heating system having a temperature of 25 °C.

As a result of buoyancy effects, water entering a stratified tank will rise or descend to match its density and thereby its temperature. In the numerical model it is assumed that water enters the tank in the segment of best matching temperature. If

the collector loop and/or the demand loop are active, water flows from one segment to the next as indicated by the vertical arrows in the left panel of figure A.1. In order to treat the collector and load loop simultaneously, the resultant flow between the segments is determined first. The next step is to write an energy balance for the  $i^{\text{th}}$  segment (also see description below)

$$Mc_p \frac{dT_i}{dt} = \alpha_i \phi_c c_p (T_c - T_i) \quad (\text{A.1})$$

$$+ \beta_i \phi_d c_p (T_{\text{mains}} - T_i) \quad (\text{A.2})$$

$$+ \delta_i \gamma_i c_p (T_{i-1} - T_i) \quad (\text{A.3})$$

$$+ (1 - \delta_i) \gamma_i c_p (T_i - T_{i+1}) \quad (\text{A.4})$$

$$- h_{\text{env}} (T_i - T_{\text{env}}), \quad (\text{A.5})$$

where the notation used by Kleinbach et al. [94] is used, in which

$\alpha_i = 1$ , if  $T_c$  best matches  $T_i$ , 0 otherwise,

$\beta_i = 1$ , if  $T_{\text{mains}}$  best matches  $T_i$ , 0 otherwise,

$$\gamma_i = \phi_c \sum_{j=1}^{i-1} \alpha_j - \phi_d \sum_{j=i+1}^N \beta_j,$$

$\delta_i = 1$ , if  $\gamma_i > 0$ , 0 otherwise.

Further  $M$  is the mass of the water in a single segment,  $c_p$  is the specific heat,  $h_{\text{env}}$  is the heat loss coefficient of the segment to the environment and  $T_{\text{env}}$  is the temperature of the tank's environment.

The five terms on the right hand side of equation A.1-A.5 are now briefly described. The first term represents the inflow of water returning from the collector into the segment of best matching temperature. The second term represents the inflow of cold water from the mains (in case of the domestic hot water tank) or from the return of the room heating system (in case of the room heating tank) into the segment of best matching temperature. The third term represents the resultant internodal flow into segment  $i$  coming from the higher segment  $i - 1$ . The fourth term represents the resultant internodal flow into segment  $i$  coming from the lower segment  $i + 1$ . The fifth term represents the heat lost to the environment. Note that  $\gamma_i$  is the resultant internodal flow, determined by adding the flows induced by the collector and the demand loop. Either the third or the fourth term is non-zero. Equation A.1-A.5 represents a set of  $N$  first-order ordinary differential equations that can be solved for the temperatures of the  $N$  segments as a function of time  $t$ .

## A.2 Figure of merit

The degree of stratification in a storage tank depends on the design of the inlets, on the flow rate and on the geometry of the tank. Van Berkel [93] uses a figure of merit (FOM) for indicating the degree of stratification. Similar to the definition of van

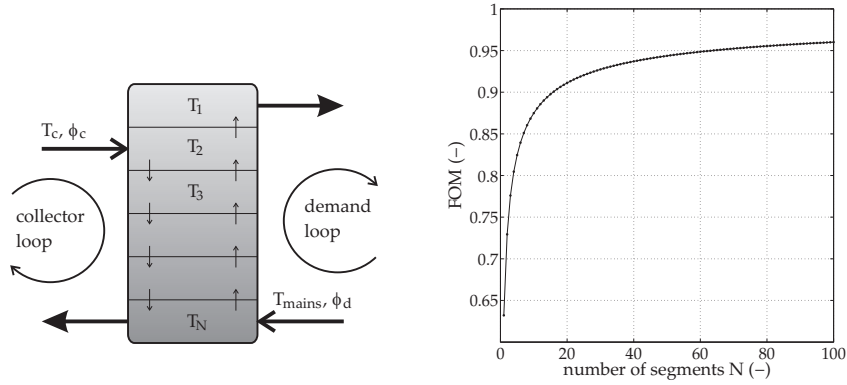


**Figure A.1:** Left: Schematic overview of the stratified heat storage tank divided into segments of uniform temperature. Inter-segment flows are indicated. Right: Figure of merit (FOM) versus the number of segments  $N$  used in the multinode model.

Berkel, the FOM is defined as the ratio of the actual and the maximum energy stored in a tank after a single charging cycle. In this charging cycle, a tank initially filled with cold water of temperature  $T_0$  is considered. Only the collector loop is active, the demand loop is inactive and the heat loss to the ambient is ignored. Under these assumptions only the first and third term of equation A.1-A.5 are non-zero and have to be taken into account. One tank volume of hot water of temperature  $T_c$  enters the tank at the top, displacing the cold water that can leave the tank from the bottom. In case there is perfect stratification, i.e. no mixing, at the end of the cycle all cold water is replaced by the hot water and the maximum amount of energy is stored in the tank (FOM=1). However, if mixing occurs, some of the hot water will leave the tank at the bottom and some of the cold water will remain inside the tank at the end of the cycle. In that case the mean tank temperature at the end of the cycle  $\bar{T}_e$  will be less than  $T_c$ . Therefore FOM, defined as

$$\text{FOM} \equiv \frac{\bar{T}_e - T_0}{T_c - T_0}, \quad (\text{A.6})$$

will be less than one.

The choice of the number of segments  $N$  determines the degree of stratification in the multinode model. The relationship between FOM and  $N$  can be derived by simulating the charging cycle. Because for the first segment ( $i = 1$ ) the inflow temperature is known, it is straightforward to solve equation A.1-A.5 for  $T_1$ , which in turn is the inflow temperature for the second segment. By consecutively solving A.1-



A.5 for  $i = 1 \dots N$  the temperature of each segment can be determined for  $t > 0$

$$T_i(t) = T_c + \sum_{j=0}^{i-1} \frac{1}{j!} \left(\frac{t}{\tau}\right)^j (T_0 - T_c) e^{-t/\tau}, \quad (\text{A.7})$$

where  $\tau = M/\phi_c$  is the segment turnover time. By evaluating this equation for each segment  $i$ , the temperature distribution after one *tank* turnover time  $t = N\tau$  is determined. By substituting the corresponding mean tank temperature  $\bar{T}_e = \sum T_i/N$  into equation A.6, the following relationship between FOM and  $N$  is found

$$\text{FOM} = 1 - e^{-N} \sum_{n=0}^{N-1} (N-n) \frac{N^{n-1}}{n!}. \quad (\text{A.8})$$

In the right panel of figure A.1, FOM is plotted versus  $N$ . In case only one segment is used ( $N = 1$ ) in the multinode model, this corresponds to a fully mixed tank with FOM=0.63. A very large number of segments is required to approach a perfectly stratified tank with FOM=1. By simulating the charging cycle with the multinode model and determining the heat content at the end of the cycle, the FOM was also determined numerically for  $N = 1 \dots 100$ . A perfect agreement of these numerical results was found with the analytical expression of equation A.8.

# Bibliography

- [1] Energy Information Administration, U.S. Department of Energy, "World consumption of primary energy by energy type and selected country groups, 1980-2004," 2006.
- [2] Intergovernmental Panel on Climate Change, "Climate change 2007: The physical science basis. Contribution of working group I to the fourth assessment report of the intergovernmental panel on climate change," 2007.
- [3] A. Luque and S. Hegedus, *Handbook of Photovoltaic Science and Engineering*. Chichester, England: John Wiley & Sons Ltd., 2003.
- [4] M. A. Green, *Silicon Solar Cells Advanced Principles & Practice*. Centre for Photovoltaic Devices and Systems, University of New South Wales, Sydney, 1995.
- [5] M. D. Archer and R. Hill, *Clean Electricity from Photovoltaics*. London, England: Imperial College Press, 2001.
- [6] R. E. I. Schropp and M. Zeman, *Amorphous and Microcrystalline Silicon Solar Cells: Modeling, Materials and Device Technology*. Kluwer Academic, Dordrecht, the Netherlands, 1998.
- [7] Photovoltaic Technology Platform, "A strategic research agenda for photovoltaic solar energy technology." [www.eupvplatform.org](http://www.eupvplatform.org), 2007.
- [8] C. Aubrey (editor), "Solar generation IV." Greenpeace and European Photovoltaic Industry Association, 2007.
- [9] D. De Ceuster, P. Cousins, D. Rose, D. Vicente, P. Tipones, and W. Mulligan, "Low cost, high volume production of >22% efficiency silicon solar cells," in *Proceedings of the 22nd European Photovoltaic Solar Energy Conference*, (Milan, Italy), pp. 816–819, 2007.
- [10] A. R. Burgers, *New Metallisation Patterns and Analysis of Light Trapping for Silicon Solar Cells*. PhD thesis, Utrecht University, the Netherlands, 2005.

- [11] J. H. Bultman, A. W. Weeber, M. W. Brieko, J. Hoornstra, A. R. Burgers, J. A. Dijkstra, and A. C. Tip, "Pin-up module: a design for higher efficiency, easy module manufacturing and attractive appearance," in *Proceedings of the 12th European Photovoltaic Solar Energy Conference, Amsterdam*, pp. 1210–1213, 1994.
- [12] A. W. Weeber, R. Kinderman, P. C. de Jong, and C. J. J. Tool, "17% cell efficiencies on large back-contacted multi-crystalline silicon solar cells," in *Proceedings of the 21st European Photovoltaic Solar Energy Conference and Exhibition, (Dresden, Germany)*, pp. 605–608, 2006.
- [13] J. M. Gee, M. E. Buck, W. K. Schubert, and P. A. Basore, "Progress on the emitter wrap-through silicon solar cell," in *Proceedings of the 12th European Photovoltaic Solar Energy Conference, Amsterdam*, pp. 743–746, 1994.
- [14] C. J. J. Tool, G. Coltti, J. Hoornstra, M. Koppes, E. J. Kossen, H. C. Rieffe, I. G. Romijn, and A. W. Weeber, "17% mc-Si solar cell efficiency using full in-line processing with improved texturing and screen-printed contacts on high-ohmic emitters," in *Proceedings of the 20th European Photovoltaic Solar Energy Conference and Exhibition, (Barcelona, Spain)*, pp. 578–583, 2005.
- [15] D. Kray, M. Hermle, and S. W. Glunz, "Theory and experiments on the back side reflectance of silicon wafer solar cells," *Progress in Photovoltaics*, vol. 16, pp. 1–15, 2008.
- [16] I. Romijn, M. Lamers, A. Stassen, A. Mewe, M. Koppes, E. Kossen, and A. Weeber, "Aspire: A new industrial MWT cell technology enabling high efficiencies on thin and large mc-Si wafers," in *Proceedings of the 22nd European Photovoltaic Solar Energy Conference, (Milan, Italy)*, pp. 1043–1049, 2007.
- [17] R. Hulstrom, R. Bird, and C. Riordan, "Spectral solar irradiance data sets for selected terrestrial conditions," *Solar Cells*, vol. 15, pp. 365–391, 1985.
- [18] W. G. J. van Helden, R. J. C. van Zolingen, and H. A. Zondag, "PV thermal systems: PV panels supplying renewable electricity and heat," *Progress in Photovoltaics*, vol. 12, pp. 415–426, 2004.
- [19] H. A. Zondag, "Flat-plate PV-thermal collectors and systems - a review," *Renewable and Sustainable Energy Reviews*, vol. 12, pp. 891–959, 2008.
- [20] D. W. Vries, *Design of a Photovoltaic/Thermal combi-panel*. PhD thesis, Eindhoven University of Technology, the Netherlands, 1998.
- [21] H. A. Zondag, D. W. de Vries, W. G. J. van Helden, R. J. C. van Zolingen, and A. A. van Steenhoven, "The yield of different combined PV-thermal collector designs," *Solar Energy*, vol. 74, pp. 253–269, 2003.

- 
- [22] S. A. Kalogirou and Y. Tripanagnostopoulos, "Industrial application of PV/T solar energy systems," *Applied Thermal Engineering*, vol. 27, pp. 1259–1270, 2007.
- [23] H. A. Zondag, M. Bakker, and W. G. J. van Helden, "PVT roadmap - a European guide to the development and market introduction of PV-thermal technology," 2005.
- [24] R. Siegel, "Net radiation method for transmission through partially transparent plates," *Solar Energy*, vol. 15, pp. 273–276, 1973.
- [25] S. Krauter and R. Hanitsch, "Actual optical and thermal performance of PV modules," *Solar Energy Materials and Solar Cells*, vol. 41/42, pp. 557–574, 1996.
- [26] N. Fraidenraich and O. C. Vilela, "Exact solutions for multilayer optical structures, application to PV modules," *Solar Energy*, vol. 69, pp. 357–362, 2000.
- [27] Z. H. Lu and Q. Yao, "Energy analysis of silicon solar cell modules based on an optical model for arbitrary layers," *Solar Energy*, vol. 81, pp. 636–647, 2007.
- [28] R. Platz, D. Fischer, M. A. Zufferey, J. A. Anna Selvan, A. Haller, and A. Shah, "Hybrid collectors using thin-film technology," in *Conference Record of the 26th Photovoltaic Specialists Conference*, pp. 1293–1296, 1997.
- [29] P. Affolter, A. Haller, D. Ruoss, and P. Toggweiler, "A new generation of hybrid solar collectors - absorption and high temperature behaviour evaluation of amorphous modules," in *Proceedings of the 16th European Photovoltaic Solar Energy Conference*, (Glasgow, UK), 2000.
- [30] D. A. Clugston, "PC1D version 5: 32-bit solar cell modeling on personal computers," in *26th IEEE Photovoltaic Specialist Conference, Anaheim*, 1997.
- [31] J. Krč, M. Zeman, F. Smole, and M. Topič, "Optical modelling of thin-film solar cells deposited on textured substrates," *Thin Solid Films*, vol. 451–452, pp. 298–302, 2004.
- [32] G. Tao, *Optical Modeling and Characterization of Hydrogenated Amorphous Silicon Solar Cells*. PhD thesis, Delft University of Technology, the Netherlands, 1994.
- [33] S. F. Rowlands, J. Livingstone, and C. P. Lund, "Optical modelling of thin-film solar cells with textured interfaces using the effective medium approximation," *Solar Energy*, vol. 76, pp. 301–307, 2004.
- [34] H. A. Macleod, *Thin-film optical filters*. Adam Hilger Ltd, Bristol, 2 ed., 1986.
- [35] E. Hecht, *Optics*. Addison Wesley Longman, Inc., 4 ed., 2002.

- [36] B. T. Phong, "Illumination for computer generated pictures," *Communications of the ACM*, vol. 18, no. 6, pp. 311–317, 1975.
- [37] J. Schumacher, S. Sterk, B. Wagner, and W. Warta, "Quantum efficiency analysis of high efficiency solar cells with textured surfaces," in *Proceedings of the 13th European photovoltaic solar energy conference*, (Nice, France), 1995.
- [38] J. D. Hylton, *Light Coupling and Light Trapping in Alkaline Etched Multicrystalline Silicon Wafers for Solar Cells*. PhD thesis, Utrecht University, the Netherlands, 2006.
- [39] P. Campbell and M. A. Green, "Light trapping properties of pyramidally textured surfaces," *Journal of Applied Physics*, vol. 62, no. 1, pp. 243–249, 1987.
- [40] P. Campbell, S. R. Wenham, and M. A. Green, "Light trapping and reflection control in solar cells using tilted crystallographic surface textures," *Solar Energy Materials and Solar Cells*, vol. 31, pp. 133–153, 1993.
- [41] A. W. Smith and A. Rohatgi, "Ray tracing analysis of the inverted pyramid texturing geometry for high efficiency silicon solar cells," *Solar Energy Materials and Solar Cells*, vol. 29, pp. 37–49, 1993.
- [42] R. Brendel, "SUNRAYS: A versatile ray tracing program for the photovoltaic community," in *Proceedings of the 12th European photovoltaic solar energy conference*, (Amsterdam, the Netherlands), pp. 1339–1342, 1994.
- [43] C. Haase, D. Knipp, and H. Stiebig, "Periodic pyramid texture for efficient light trapping in thin-film silicon solar cells," in *Proceedings of the 22nd European Photovoltaic Solar Energy Conference*, (Milan, Italy), pp. 2186–2189, 2007.
- [44] M. Schulte, S. Jorke, C. Zahren, J. Hüpkens, and H. Stiebig, "Analysis of the scattering properties of textured TCO structures for thin film silicon solar cells," in *Proceedings of the 22nd European Photovoltaic Solar Energy Conference*, (Milan, Italy), pp. 2190–2194, 2007.
- [45] C. K. Carniglia, "Scalar scattering theory for multilayer optical coatings," *Optical Engineering*, vol. 18, no. 2, pp. 104–115, 1979.
- [46] M. Schulte, C. Zahren, and H. Stiebig, "Light scattering of nano-textured substrates for solar cell application," in *Proceedings of the 21st European Photovoltaic Solar Energy Conference*, (Dresden, Germany), pp. 1703–1706, 2006.
- [47] M. A. Green and M. J. Keevers, "Optical properties of intrinsic silicon at 300K," *Progress in Photovoltaics*, vol. 3, pp. 189–192, 1995.
- [48] F. Bisschop, *Characterization and modelling of highly doped regions in silicon solar cells*. PhD thesis, University Utrecht, 1992.

- 
- [49] C. J. J. Tool, 2008. Private communication.
- [50] C. J. J. Tool, G. Coletti, F. J. Granek, J. Hoornstra, M. Koppes, E. J. Kossen, H. C. Riefe, I. G. Romijn, and A. W. Weeber, "Straightforward in-line processing for a 16.8% efficient mc-Si solar cell," in *Proceedings of the 31st IEEE PVSC*, (Orlando, US), pp. 1324–1327, 2005.
- [51] P. Lölgén, *Surface and volume recombination in silicon solar cells*. PhD thesis, University Utrecht, 1995.
- [52] S. W. Glunz, A. Grohe, M. Hermle, M. Hofmann, S. Janz, T. Roth, O. Schulz, M. Vetter, I. Martin, R. Ferré, S. Bermejo, W. Wolke, W. Warta, R. Preu, and G. Willeke, "Comparison of different dielectric passivation layers for application in industrially feasible high-efficiency crystalline silicon solar cells," in *Proceedings of the 20th European Photovoltaic Solar Energy Conference*, (Barcelona, Spain), pp. 572–577, 2005.
- [53] E. D. Palik, *Handbook of optical constants of solids*. Orlando, US: Academic Press Inc., 1985.
- [54] Swiss Federal Office of Energy, "New generation of hybrid solar PV/T collectors," 2000.
- [55] J. A. del Alamo, S. Swirhun, and R. M. Swanson, "Simultaneous measurement of hole lifetime, hole mobility, and bandgap narrowing in heavily doped n-type silicon," in *International Electron Device Meeting Technical Digest*, pp. 290–293, 1985.
- [56] B. Hoex, 2006. Private communication.
- [57] B. Hoex, *Functional Thin Films for High Efficiency Solar Cells*. PhD thesis, Eindhoven University of Technology, 2008.
- [58] "Product data and technical information of high efficient low-iron Centrosol glasses," 2006.
- [59] A. R. Burgers, 2006. Private communication.
- [60] E. Hammarberg and A. Roos, "Antireflection treatment of low-emitting glazing for energy efficient windows with high visible transmittance," *Thin Solid Films*, vol. 442, pp. 222–226, 2003.
- [61] Photovoltaic Technology Platform, "A strategic research agenda for photovoltaic solar energy technology." [www.eupvplatform.org](http://www.eupvplatform.org), 2007. p. 25.
- [62] Photovoltaic Technology Platform, "A vision for photovoltaic technology." [www.eupvplatform.org](http://www.eupvplatform.org), 2005. p. 20.

- [63] J. Krč, F. Smole, and M. Topič, "Analysis of light scattering in amorphous Si:H solar cells by a one-dimensional semi-coherent optical model," *Progress in Photovoltaics*, vol. 11, pp. 15–26, 2003.
- [64] J. Springer, A. Poruba, and M. Vanecek, "Improved three-dimensional optical model for thin-film silicon solar cells," *Journal of Applied Physics*, vol. 96, no. 9, pp. 5329–5337, 2004.
- [65] M. Zeman, 2006. Private communication.
- [66] M. I. Alonso, M. Garriga, C. A. D. Ricón, E. Hernández, and M. León, "Optical functions of chalcopyrite  $\text{CuGa}_x\text{In}_{1-x}\text{Se}_2$  alloys," *Applied Physics A*, vol. 74, pp. 659–664, 2002.
- [67] M. N. van den Donker, *Plasma Deposition of Microcrystalline Silicon Solar Cells: Looking Beyond the Glass*. PhD thesis, Eindhoven University of Technology, 2006.
- [68] M. Berginski, J. Hüpkes, M. Schulte, G. Schöpe, H. Stiebig, B. Rech, and M. Wuttig, "The effect of front ZnO:Al surface texture and optical transparency of efficient light trapping in silicon thin-film solar cells," *Journal of Applied Physics*, vol. 101, 2007.
- [69] "EAGLE2000." [www.corning.com](http://www.corning.com), 2008.
- [70] J. Krč, B. E. Pieters, M. Zeman, A. Campa, F. Smole, and M. Topič, "Optimisation and efficiency limits of amorphous silicon/amorphous silicon germanium/microcrystalline silicon triple-junction solar cell," in *Proceedings of the 21st European Photovoltaic Solar Energy Conference and Exhibition*, (Dresden, Germany), pp. 1684–1687, 2006.
- [71] T. S. Moss, *Handbook on Semiconductors*, vol. 2 of *Optical Properties of Solids*. Amsterdam, the Netherlands: North-Holland Publishing Company, 1980.
- [72] R. Groenen, *Remote Plasma Deposition of Textured Zinc Oxide with Focus on Thin Film Solar Cell Applications*. PhD thesis, Eindhoven University of Technology, 2005.
- [73] J. Löfler, *Transparent Conductive Oxides for Thin-Film Silicon Solar Cells*. PhD thesis, Utrecht University, 2005.
- [74] P. Lechner and H. Schade, "Thin-film technology based on hydrogenated amorphous silicon," *Progress in Photovoltaics*, vol. 10, pp. 85–97, 2002.
- [75] J. Krč, M. Zeman, B. E. Pieters, A. Campa, F. Smole, and M. Topič, "Optical and electrical analysis of tandem micromorph silicon solar cell to achieve record-high efficiency," in *Conference Record of the 2006 IEEE 4th World Conference on Photovoltaic Energy Conversion*, pp. 1529–1532, 2006.

- 
- [76] M. G. Sandoval-Paz, M. Sotelo-Lerma, A. Mendoza-Galvan, and R. Ramírez-Bon, "Optical properties and layer microstructure of CdS films obtained from an ammonia-free chemical bath deposition process," *Thin Solid Films*, vol. 515, pp. 3356–3362, 2007.
- [77] W. N. Shafarman and L. Stolt, *Cu(In,Ga)Se<sub>2</sub> Solar Cells*, ch. 13. In Luque and Hegedus [3], 2003.
- [78] U. Rau and H. W. Schock, *Cu(In,Ga)Se<sub>2</sub> Solar Cells*, ch. 7. In Archer and Hill [5], 2001.
- [79] A. V. Shah, H. Schade, M. Vanecek, J. Meier, E. Vallat-Sauvain, N. Wyrsh, U. Kroll, C. Droz, and J. Bailat, "Thin-film silicon solar cell technology," *Progress in Photovoltaics*, vol. 12, pp. 113–142, 2004.
- [80] H. A. Zondag, D. W. de Vries, W. G. J. van Helden, R. J. C. van Zolingen, and A. A. van Steenhoven, "The thermal and electrical yield of a PV-thermal collector," *Solar Energy*, vol. 72, pp. 113–128, 2002.
- [81] M. Bakker, H. A. Zondag, M. J. Elswijk, K. J. Strootman, and M. J. M. Jong, "Performance and costs of a roof-sized PV/thermal array combined with a ground coupled heat pump," *Solar Energy*, vol. 78, pp. 331–339, 2005.
- [82] J. Ji, T. T. Chow, and W. He, "Dynamic performance of hybrid photovoltaic/thermal collector wall in Hong Kong," *Building and Environment*, vol. 38, pp. 1327–1334, 2003.
- [83] S. Kalogirou and Y. Tripanagostopoulos, "Performance of a hybrid PV/T thermosyphon system," in *Proceedings of Regional World Renewable Energy Congress*, (Aberdeen, UK), 2005.
- [84] J. A. Duffie and W. J. Beckman, *Solar energy thermal processes*. New York, US: Wiley and sons, 1991.
- [85] K. Rajkanan, R. Singh, and J. Shewchun, "Absorption coefficient of silicon for solar cell calculations," *Solid-State Electronics*, vol. 22, p. 793, 1979.
- [86] W. Weiss, I. Bergmann, and G. Faninger, "Solar heat worldwide, markets and contribution to the energy supply." AEE - Insitute for Sustainable Technologies, 2008.
- [87] T. Schmidt, D. Mangold, and H. Müller-Steinhagen, "Central solar heating plants with seasonal storage in Germany," *Solar Energy*, vol. 76, pp. 165–174, 2004.



- [88] H. Lund, "Test reference years (TRY) weather data sets for computer simulations of solar energy systems and energy consumption (CEC R&D programme solar energy group F solar radiation data)," tech. rep., Technical University of Denmark (Hørsholm), 1984.
- [89] "Energieprestatie van woonfuncties en woongebouwen - bepalingsmethode (appendix D)." NEN 5128, 2001.
- [90] H. A. Zondag, M. J. M. Jong, and W. G. J. van Helden, "Development and applications for PV thermal," in *Proceedings of the 17th European Photovoltaic Solar Energy Conference*, (Munich, Germany), 2001.
- [91] NOVEM, "Referentiewoningen 1999," Tech. Rep. DV 1.2.183.99.09, NOVEM, Utrecht, the Netherlands, 1999.
- [92] SMA Solar Technology, "Sunny Boy SB 2500 and SB 3000 String Inverter for Photovoltaic Plants."
- [93] J. van Berkel, *Thermocline entrainment in stratified energy stores*. PhD thesis, Eindhoven University of Technology, 1997.
- [94] E. M. Kleinbach, W. A. Beckmann, and S. A. Klein, "Performance study of one-dimensional models for stratified thermal storage tanks," *Solar Energy*, vol. 50, pp. 155–166, 1993.
- [95] C. G. Granqvist, "Transparent conductors as solar energy materials: A panoramic overview," *Solar Energy Materials and Solar Cells*, vol. 91, pp. 1529–1598, 2007.
- [96] H. Haitjema, *Spectrally Selective Tin oxide and Indium oxide*. PhD thesis, Delft University of Technology, 1989.
- [97] C. W. A. Baltus, J. A. Eikelboom, and R. J. C. van Zolingen, "Analytical monitoring of losses in PV systems," in *Proceedings of the 14th European Photovoltaic Solar Energy Conference*, (Barcelona, Spain), 1997.
- [98] J. S. Coventry and K. Lovegrove, "Development of an approach to compare the 'value' of electrical and thermal output from a domestic PV/thermal system," *Solar Energy*, vol. 75, pp. 63–72, 2003.
- [99] L. Bosselaar and T. Gerlagh, "Protocol monitoring duurzame energie, update 2006," Tech. Rep. 2DEN0611, SenterNovem, 2006.
- [100] A. Jäger-Waldau, "Roadmap for European research and development for photovoltaics," Tech. Rep. EUR 21087 EN, PVNET, 2004.

- [101] B. Zinßer, M. B. Schubert, J. H. Werner, G. Makrides, and G. E. Georghiou, "Temperature and intensity dependence of 13 photovoltaic technologies," in *Proceedings of the 23rd European Photovoltaic Solar Energy Conference and Exhibition*, (Milan,Italy), 2008.
- [102] "Data sheet Uni-Solar Laminate PVL-Series, model PVL-136."
- [103] "Data sheet Phoenix Solar PHX-90."
- [104] "Data sheet Sanyo HIT photovoltaic modules, model HIP-210NKHE1 and HIP205NKHE1."



# Nomenclature

## Roman

$a$	relative surface area	[-]
$a^{\text{cell}}$	cell surface area	[m <sup>2</sup> ]
$a^{\text{col}}$	collector surface area	[m <sup>2</sup> ]
$A$	absorption factor	[-]
$c_{\text{p,n}}$	doping concentration	[cm <sup>-3</sup> ]
$C_{\text{p,n}}$	areal doping concentration	[cm <sup>-2</sup> ]
$d$	layer thickness	[μm]
$D$	minority carrier diffusion coefficient	[cm <sup>2</sup> /s]
$E$	energy	[J]
$E_{\text{ph}}$	photon energy	[eV]
$E_{\text{g}}$	bandgap energy	[eV]
$f_{\text{esc}}$	escape factor	[-]
$F$	loss cone fraction	[-]
FOM	figure of merit	[-]
$F_{\text{I}}$	irradiance factor for electrical efficiency	[-]
$F_{\text{T}}$	temperature factor for electrical efficiency	[-]
$G_{\lambda}$	spectral solar irradiance	[W/m <sup>2</sup> μm]
$h$	texture height	[μm]
$H$	haze parameter	[-]
$I$	intensity (power density)	[W/m <sup>2</sup> ]
$k$	extinction coefficient	[-]
$L$	diffusion recombination length	[μm]
$m$	Phong exponent	[-]
$n$	real refractive index	[-]
$N$	complex refractive index	[-]
$N$	number of storage tank segments	[-]
$P$	power	[W]
$q$	non-dimensional net-radiation flux	[-]
$\mathbf{q}$	non-dimensional net-radiation flux vector	[-]
$r$	reflection coefficient	[-]

$r$	reflection matrix	[-]
$R$	reflection factor	[-]
$R_{\text{sheet}}$	sheet resistance	$[\Omega_{\square}]$
$S$	surface recombination velocity	[cm/s]
SF	solar fraction	[-]
$t$	interface transmission coefficient	[-]
$\mathbf{t}$	interface transmission matrix	[-]
$T$	transmission factor	[-]
$T$	temperature	$[^{\circ}\text{C}]$
$T_{\text{red}}$	reduced temperature	$[^{\circ}\text{Cm}^2/\text{W}]$
$w$	texture width	$[\mu\text{m}]$

**Greek**

$\alpha$	absorption coefficient	$[\text{cm}^{-1}]$
$\beta$	temperature coefficient for electrical efficiency	$[^{\circ}\text{C}^{-1}]$
$\gamma$	texture steepness	$[^{\circ}]$
$\Delta\phi$	opening angle	$[^{\circ}]$
$\varepsilon$	emissivity	[-]
$\eta$	modified refractive index	[-]
$\eta_e$	electrical efficiency	[-]
$\eta_{\text{th}}$	thermal efficiency	[-]
$\eta_e^{\text{sys}}$	annual electrical system efficiency	[-]
$\eta_{\text{th}}^{\text{sys}}$	annual thermal system efficiency	[-]
$\lambda$	wavelength	$[\mu\text{m}]$
$\rho$	packing density	[-]
$\sigma$	root-mean-square roughness	$[\mu\text{m}]$
$\tau$	layer transmission coefficient	[-]
$\mathbf{\tau}$	layer transmission matrix	[-]
$\tau_b$	bulk minority carrier lifetime	$[\mu\text{s}]$
$\tau^*$	effective transmittance	[-]
$\phi$	angle of incidence (refraction)	$[^{\circ}]$
$\phi_c$	collector mass flow rate	$[\text{kg}/\text{h}]$
$\phi_s$	specific collector mass flow rate	$[\text{kg}/\text{m}^2\text{h}]$

**Subscripts**

ac	active area/layer
AM	air mass
amb	ambient
c	coating
col	collector
cr	critical

e	emitter
eff	effective
fc	free carrier
gr	grid area
in	incident
inv	inverter
ref	reflected
s	specular
STC	Standard Test Conditions
th	thermal
tr	transmitted
$\lambda$	spectral



# Summary

## Optical Absorption Factor of Solar Cells for PVT Systems

A two-dimensional optical model was developed to gain more insight in the absorption factor of solar cells. This model was validated by comparing its numerical results to results obtained by spectral reflection and transmission measurements performed on both crystalline silicon (c-Si) and thin-film solar cell samples. Using this detailed model, insight was gained in the spectral absorption factor of solar cells.

Regarding textured and anti-reflection coated c-Si solar cells it can be concluded that the major part of the irradiance with a wavelength less than  $1.1\ \mu\text{m}$  is absorbed by band-to-band absorption in the silicon wafer. The more weakly absorbed longer wavelength irradiance is trapped for multiple passes inside the wafer. As a result, a large part of this irradiance is absorbed by free-carrier absorption in the emitter. The AM1.5 absorption factor of c-Si cells was studied for a range of cell design parameters and lies between 87 and 91% for most current and future cell designs.

Thin-film solar cells, such as various amorphous silicon (a-Si) based single- and multi-junction solar cells and the copper indium gallium diselenide (CIGS) solar cell are considered as well. In these cells, reflection is reduced and light-trapping is improved by the roughness of the transparent conductive oxide (TCO). In multi-junction cells, each active layer absorbs a different part of the solar spectrum. The weakly absorbed sub-bandgap irradiance is mainly absorbed by free-carrier absorption in the TCO layer. It turns out that a-Si solar cells have the lowest absorption factor of around 81%, because of their relatively large bandgap. This value is very sensitive to the degree of optical confinement. Most other thin-film cells have an absorption factor of about 88%. The CIGS solar cell has a very high absorption factor of 94%, because of its relatively small bandgap.

The effective absorption factor of a solar cell is defined as the fraction of incident solar irradiance that is converted into heat and it is the AM1.5 absorption factor less the electrical efficiency. Currently, this value is about 71% for c-Si solar cells and about 80% for thin-film solar cells. In the long term (2030), these values will be reduced by about 5% each, as the electrical efficiency of the solar cells continues to increase.



In a PVT collector, a PV laminate generates electricity and functions as thermal absorber at the same time. The electrical and thermal yield of systems with covered sheet-and-tube PVT collectors were analysed in detail for Dutch climatological conditions. The effective absorption factors mentioned earlier were used as input.

Regarding the various solar cell technologies, it can be concluded that the annual electrical efficiency of PVT systems is mainly determined by the electrical efficiency of the specific cell technology used. Compared to conventional PV systems (generating electricity only) the following loss mechanisms occur, however. Firstly, there is an additional reflection loss, induced by the cover glass present in the glazed PVT collectors considered. This loss is about 8% and can be reduced to 3.5% by the application of anti-reflective coatings. Secondly, the cell efficiency is reduced by an additional 8 to 20% (in case of c-Si and depending on system sizing) because of higher cell temperatures in a glazed PVT collector, being mainly determined by the relatively high water temperatures on system level.

Compared to conventional solar thermal systems (generating heat only), the thermal efficiency of a PVT system is lower. This is caused by the fact that the PV laminate, used as absorber in the PVT collector, differs from the spectrally selective absorber normally used in solar thermal collectors. Firstly, it has a lower effective absorption factor, mainly because electrical energy is withdrawn. This reduces the thermal system efficiency by 6 to 12%<sub>rel.</sub> Secondly, it has a higher emissivity, implying that more heat is lost by radiation. This reduces the thermal system efficiency by an additional 5 to 12%<sub>rel.</sub> The radiative heat loss can be reduced by application of a low-emissivity coating on the PV laminate in the PVT collector. Though this increases the thermal system efficiency, the electrical system efficiency is reduced significantly as a result of additional optical and temperature losses. Whether it is attractive to apply such a coating depends on the exact PVT system configuration considered.

A modest part of the investment costs can be saved by combining a conventional PV and a conventional solar thermal system into a PVT system. However, in a system with glazed PVT collectors, these savings are in most cases annulled by the on average 15%<sub>rel.</sub> lower electrical and thermal efficiencies of the PVT system compared to the conventional systems. However, because the PVT system simultaneously generates electricity and heat, it has a higher energy yield per unit of collector area compared to conventional systems.

# Samenvatting

## Optische Absorptiefactor van Zonnecellen voor PVT-systemen

Een tweedimensionaal optisch model is ontwikkeld om meer inzicht te krijgen in de absorptiefactor van zonnecellen. Dit model is gevalideerd door de numerieke resultaten te vergelijken met resultaten verkregen met spectrale reflectie- en transmissiemetingen, uitgevoerd aan zowel kristallijn silicium (c-Si) als dunne-film zonnecel samples. Met behulp van dit gedetailleerde model, is inzicht verkregen in de spectrale absorptiefactor van zonnecellen.

Wat betreft c-Si zonnecellen met textuur en anti-reflectiecoating, kan geconcludeerd worden dat het grootste gedeelte van het zonlicht met een golflengte kleiner dan  $1.1 \mu\text{m}$  wordt geabsorbeerd door middel van band-band absorptie in de silicium wafer. Het zwakker geabsorbeerde langgolvlige licht wordt opgesloten in de wafer gedurende meerdere passages. Daardoor wordt een groot gedeelte van dit licht geabsorbeerd door vrije-ladingsdragersabsorptie in de emitter. De AM1.5 absorptiefactor van c-Si cellen is bestudeerd voor een range van cel-ontwerpparameters en ligt voor de meeste huidige en toekomstige celontwerpen tussen de 87 en 91%.

Ook zijn dunne-film zonnecellen beschouwd, zoals de verschillende op amorf silicium (a-Si) gebaseerde enkel- of multi-junctie zonnecellen en de koper-indium-gallium-diselenide (CIGS) zonnecel. In deze cellen wordt de reflectie gereduceerd en de lichtopsluiting verbeterd door de ruwheid van het transparante geleidende oxide (TCO). In multi-junctie zonnecellen, absorbeert iedere actieve laag een ander deel van het zonnenspectrum. Het zwak geabsorbeerde licht, met een fotonenergie kleiner dan de bandafstand, wordt voornamelijk geabsorbeerd door vrije-ladingsdragersabsorptie in de TCO laag. Het blijkt dat a-Si cellen, vanwege hun relatief grote bandafstand, de laagste absorptiefactor hebben van ongeveer 81%. Deze waarde is erg gevoelig voor de mate van lichtopsluiting. De meeste andere dunne-film cellen hebben een absorptiefactor van ongeveer 88%. De CIGS zonnecellen hebben een erg hoge absorptiefactor van 94% vanwege de relatief kleine bandafstand.

De effectieve absorptiefactor van een zonnecel is gedefinieerd als de fractie van het invallende zonlicht dat wordt omgezet in warmte en dit is de AM1.5 absorptiefactor verminderd met het elektrische rendement. Voor c-Si zonnecellen is deze

tegenwoordig ongeveer 71% en voor dunne-film cellen ongeveer 80%. Op de lange termijn (2030) zullen deze waardes met ongeveer 5% dalen, met het verder stijgen van het elektrische rendement van zonnecellen.

In een PVT-collector genereert het PV-laminaat elektriciteit en doet tegelijkertijd dienst als thermische absorber. De elektrische en thermische opbrengst van systemen met afgedekte 'sheet-and-tube' PVT-collectoren is in detail geanalyseerd voor het Nederlandse klimaat. De eerdergenoemde effectieve absorptiefactoren zijn gebruikt als input.

Wat betreft de verschillende zonneceltechnologieën kan geconcludeerd worden dat het elektrische jaarrendement van PVT-systemen voornamelijk bepaald wordt door het elektrische rendement van de gebruikte celtechnologie. Vergeleken met conventionele PV-systemen (die alleen elektriciteit produceren) treden echter de volgende verliesmechanismen op. Ten eerste is er een extra reflectieverlies, veroorzaakt door de glasplaat van afgedekte PVT-collectoren. Dit verlies is ongeveer 8% en kan gereduceerd worden tot 3.5% door de toepassing van anti-reflectiecoatings. Ten tweede wordt het celrendement met nog eens 8 tot 20% gereduceerd (in het geval van c-Si en afhankelijk van de systeemdimensionering) vanwege de hogere celtemperaturen in een afgedekte PVT-collector, voornamelijk veroorzaakt door de relatief hoge watertemperaturen op systeemniveau.

Vergeleken met conventionele zon-thermische systemen (die alleen warmte produceren) is het thermische rendement van een PVT-systeem lager. Dit wordt veroorzaakt door het feit dat het PV-laminaat, dat dienst doet als absorber in de PVT-collector, verschilt van de spectraal selectieve absorber die normaal wordt gebruikt in zonnecollectoren. Ten eerste heeft het PV-laminaat een lagere absorptiefactor, voornamelijk omdat elektrische energie wordt onttrokken. Dit reduceert het thermische systeemrendement met 6 tot 12%<sub>rel</sub>. Ten tweede heeft het PV-laminaat een hogere emissiecoëfficiënt, wat impliceert dat meer warmte verloren gaat door straling. Dit reduceert het thermische systeemrendement met nog eens 5 tot 12%<sub>rel</sub>. Het stralingsverlies kan worden gereduceerd door het toepassen van een coating met een lage emissiecoëfficiënt op het PV-laminaat in een PVT-collector. Hoewel dit het thermische systeemrendement verhoogt, wordt het elektrische systeemrendement verlaagd als gevolg van extra optische en temperatuurverliezen. Of het aantrekkelijk is om zulke coatings toe te passen hangt af van de precieze PVT-systeemconfiguratie die beschouwd wordt.

Een bescheiden besparing van investeringskosten is mogelijk door een conventioneel PV-systeem en een conventioneel zonnecollectorsysteem te combineren. Maar voor een PVT-systeem met afgedekte collectoren worden deze besparingen meestal tenietgedaan door de gemiddeld 15%<sub>rel</sub> lagere elektrische en thermische rendementen van het PVT-systeem ten opzichte van de conventionele systemen. Echter, omdat het PVT-systeem gelijktijdig elektriciteit en warmte levert, heeft het een hogere energieopbrengst per eenheid collectoroppervlak dan de conventionele systemen.

# Dankwoord

Op deze plaats wil ik een aantal mensen bedanken, die direct of indirect hebben bijgedragen aan de totstandkoming van dit proefschrift. Op de eerste plaats, bedank ik mijn eerste promotor professor Ronald van Zolingen, voor de uitstekende begeleiding en de verhelderende discussies over zonnecellen en aanverwante zaken. Zijn 'helicopterview' heeft me geholpen om tijdens het onderzoek het overzicht te behouden. Ook wil ik Herbert Zondag, van Energieonderzoek Centrum Nederland (ECN), bedanken voor zijn adviezen en voor het delen van zijn kennis op het gebied van PVT-systemen. Natuurlijk ben ik ook veel dank verschuldigd aan mijn copromotor Camilo Rindt en mijn tweede promotor professor Anton van Steenhoven die mij met hun enthousiasme hebben gestimuleerd, en ook steeds de grote lijn in de gaten hebben gehouden.

Verder wil ik ook de volgende afstudeerders bedanken: Pieter de Boer voor het testen van optische modellen, Sjoerd Keuren voor zijn activiteiten rond optische coatings, Jappe Goud voor zijn mooie werk op het gebied van dunne-film zonnecellen en Jeroen Reniers voor zijn inzet op het gebied van PVT-systeemmodellering.

Ik bedank ECN voor het beschikbaar stellen van de experimentele opstelling voor reflectie- en transmissiemetingen. Ook ben ik veel ECN-ers binnen de groep ZON dank verschuldigd: Arthur Weeber, John van Roosmalen, Kees Broek en Valentin Mihailtchi voor het produceren en doormeten van de door mij gewenste, soms wat ongebruikelijke, zonnecelsamples. Teun Burgers wil ik bedanken voor zijn hulp op het gebied van optische modellering van zonnecellen.

Miro Zeman (TU Delft) ben ik dankbaar voor het maken van verschillende dunne-film zonnecelsamples en voor het beschikbaar stellen van de optische eigenschappen van verschillende halfgeleidermaterialen. Bram Hoex (TU/e) bedank ik voor zijn nuttige opmerkingen aangaande siliciumnitride.

Het onderzoek is uitgevoerd in de sectie Energie Technologie (ET) van Thermo Fluids Engineering (TFE). Ik wil alle TFE-ers en in het bijzonder de ET-ers bedanken voor de ondersteuning en de prettige sfeer, vooral tijdens de koffie/thee/water- en lunchpauzes. Mijn kamergenoten, in chronologische volgorde: Svetlana, Srabon, Pieter en Ilhan, bedank ik voor hun gezelligheid. Ook de burens: Natascha, Henk, Srinidhi en Kiran, wil ik bedanken voor de vele leuke 'events' die onregelmatig wer-

den georganiseerd. I would like to thank also the visitors to our section from TU Liberec, Lucie and Petra, for introducing me to the Czech culture.

Ten slotte wil ik mijn familie, in het bijzonder mijn ouders en broers, bedanken voor hun steun. Kortom, het was een zonnige tijd!

Rudi Santbergen,

Valkenswaard, oktober 2008

# List of publications

## Journal papers

- R. Santbergen, R.J.Ch. van Zolingen, *Modeling the thermal absorption factor of photovoltaic/thermal combi-panels*, *Energy Conversion and Management*, 47 (2006) 3572-3581
- R. Santbergen, R.J.C. van Zolingen, *The absorption factor of crystalline silicon PV cells: A numerical and experimental study*, *Solar Energy Materials and Solar Cells*, 92 (2008) 432-444

## Conference proceedings

- R. Santbergen, R.J.Ch. van Zolingen, *Modeling the thermal absorption factor of photovoltaic/thermal combi-panels*, *Proceedings of the Heat SET conference*, Editor: B. Thonon, Grenoble, France (2005) 239-244
- R. Santbergen, R.J.Ch. van Zolingen, *An optical model for the absorption factor of textured crystalline silicon solar cells*, *Proceedings of the 21st European Photovoltaic Solar Energy Conference*, Editors: J. Poortmans, H. Ossenbrink, E. Dunlop, P. Helm, Dresden (2006) 416-421
- R. Santbergen, J.M. Goud, R.J.Ch. van Zolingen, *An Optical model for the absorption factor of thin-film photovoltaic cells*, *Proceedings of the 22nd European Photovoltaic Solar Energy Conference*, Editors: G. Willeke, H. Ossenbrink and P. Helm, Milan, Italy (2007) 265-270
- R. Santbergen, C.C.M. Rindt, R.J.Ch. van Zolingen, *Improvement of the performance of PVT collectors*, *Proceedings of the 5th European Thermal-Sciences Conference*, Editors: G.G.M. Stoffels, T.H. van der Meer, A.A. van Steenhoven, Eindhoven, the Netherlands (2008)



# Curriculum Vitae

- 9 March 1978 Born in Eindhoven
- 1990-1994 MAVO (school for lower general secondary education),  
St. Willibrordus, Valkenswaard
- 1994-1996 HAVO (school for higher general secondary education),  
Kempenpoort, Eindhoven
- 1996-1998 VWO (pre-university education), S.G. Were Di, Valkenswaard
- 1998-2004 M.Sc. Applied Physics, Eindhoven University of Technology
- 2004-2008 PhD student Mechanical Engineering, Eindhoven University  
of Technology